NOVEL FABRICATION OF A CALCIUM POLYPHOSPHATE DELIVERY MATRIX FOR TREATMENT OF OSTEOMYELITIS AND BONE REGENERATION

by

Patricia Comeau

Submitted in Partial Fulfilment of the
Requirements for the Degree of
Doctor of Philosophy

at

Dalhousie University
Halifax, Nova Scotia
June 2015

DEDICATION PAGE

For my parents, thank you for your continued love and support through this journey.

For my grandma, thank you for always inspiring me to dream big and achieve my goals.

TABLE OF CONTENTS

LIST OF TABLES

LIST OF FIGURES

ABSTRACT

Osteomyelitis is an inflammation of bone resulting from pyogenic organism activity. It affects patients of any age, impacts any bone and can lead to persistent morbidity. Local delivery systems have taken on a greater clinical focus for osteomyelitis therapy owing to their ability to overcome many disadvantages of systemic delivery. More appealing still is a device capable of eradicating infection *and* promoting bone regeneration. The overall aim of this research was to develop a clinically relevant, calcium polyphosphate (CPP) glass-based local delivery system for treatment of osteomyelitis and restoration of bone lost to the disease. Three specific approaches to manipulate CPP-based matrix functionality were evaluated - precipitation, strontium doping, and cold isostatic pressing.

CPP, with chain length as much as ~6X that of melt-derived CPP, was achieved following a sodium polyphosphate and calcium chloride precipitation reaction. However, this increased chain length reduced vancomycin loading efficiency of the disks and, largely owing to the presence of residual sodium in the precipitate, did not reduce early stage antibiotic release. Strontium doping of melt-derived CPP was found to increase the density and chain length of the glass. Subsequent *in vitro* analysis of these strontium doped CPP disks revealed greater structural stability compared to their undoped counterparts and a capacity to release greater fractions of vancomycin. Overall, observed changes in matrix hydration and vancomycin release in these first two approaches were largely attributed to differences in glass structure as a result of the presence of additional ions and their field strengths.

Finally, the capacity to predictably and reproducibly fabricate strontium-doped CPP beads using a cold isostatic pressing approach was demonstrated. In an *in vitro* analysis vancomycin-doped beads exhibited greater long-term structural stability compared to their blank counterparts. The vancomycin release from the beads was more controlled with detectable levels of vancomycin reported at least one week longer than for the disks. Lastly, the capacity for the strontium-doped beads to enhance osteoblast differentiation during a 12d *in vitro* study was demonstrated. Together these three approaches have provided evidence towards the enhanced clinical feasibility of a therapeutically loaded CPP bead-based local delivery system for osteomyelitis treatment.

LIST OF ABBREVIATIONS AND SYMBOLS USED

ALP	Alkaline Phosphate
ARS	Alizarin Red Solution
ATR-FTIR	Attenuated Total Reflectance – Fourier Transform Infrared Spectroscopy
BCA	Bicinchoninic Acid
BGP	Sodium β-Glycerophosphate
Ca	Calcium
CaSR	Cation Sensing Receptor
CIP	Cold Isostatic Pressing (or cold isostatically *pressed*)
CLSI	Clinical Laboratory Standards Institute
CPC	Cetylpyridinium Chloride
CPMM	Calcium Phosphate Monobasic Monohydrate
CPP	Calcium Polyphosphate
d_0	Original mold diameter (CIP)
d_1	Diameter of ungelled CIP bead
d_2	Diameter of gelled CIP bead
DMEM	Dulbecco's Modified Eagle's Medium
DMSO	Dimethyl Sulfoxide
DSC	Differential Scanning Calorimetry
F	Field strength
FBS	Fetal Bovine Serum
FCS	Fetal Calf Serum
FDA	Food and Drug Administration (USA)
FWHM	Full-width half maximum
ICP-OES	Inductively Coupled Plasma-Optical Emission Spectroscopy
L_{eff}	Loading efficiency (of VCM)
MAS	Magic Angle Spinning
MIC	Minimum Inhibitory Concentration
MTC	Maximum Tolerable Concentration
Na	Sodium
Na_2-EDTA	Disodium Ethylenediaminetetraacetate Dehydrate
NaPP	Sodium Polyphosphate
n_{ave}	Average chain length
NMR	Nuclear Magnetic Resonance
NWF	Network former
NWI	Network intermediate
NWM	Network modifier
OPG	Osteoprotegerin
P	Phosphorus
PGE2	Prostaglandin-E2
PMMA	Poly(methylmethacrylate)
Q^0	Orthophosphate (no bridging oxygen)
Q^1	End-chain phosphate (one bridging oxygen)
Q^2	Middle-chain phosphate (two bridging oxygen)
Q^3	Branching phosphate (three bridging oxygen)

r_c	Ionic radii of cation
r_{o-}	Ionic radii of oxygen ion
S.aureus	Staphylococcus Aureus
SEM	Scanning Electron Microscope
SFYS	SF Yellowish Solution
Sr	Strontium
TBS	Tris-Buffer Solution
T_c	Crystallization temperature
T_g	Glass transition temperature
TGA	Thermogravimetric Analysis
T_m	Melting temperature
TMA	Tetramethylammonium hydroxide
UV-VIS	Ultraviolet-Visible Spectrophotometer
VCM	Vancomycin
Z_c	Valency of cation
α-MEM	Alpha Minimum Essential Media
ρ_a	Apparent bulk density
ρ_t	Skeletal density

ACKNOWLEDGEMENTS

I would first like to thank my supervisor, Dr. Mark Filiaggi, for his support and guidance throughout this project. Thank you for challenging me to think of the 'big picture' and see beyond the tiny details. I would also like to thank my supervisory committee (Dr. Daniel Boyd, Dr. Michael Dunbar, and Dr. Kevin Plucknett) for their advice and input on my research design and analysis.

Thank you to Gordon Hall and Maxine Langman for your help in the lab, training me on equipment and protocols, and your continued encouragement. I have greatly appreciated your input on study design and allowing me to 're-organize' lab equipment.

For training me on the use of SEM and NMR I would like to acknowledge Pat Scallion and Dr. Ulrike Werner-Zwanziger, respectively. Thank you also to Chenxin Jin for training me on the use of CIP.

Lastly, I would like to thank my friends and colleagues from both the east and west coasts of Canada for their continued encouragement and support during my pursuit of this degree.

I gratefully acknowledge financial assistance from NSERC for supporting this project.

CHAPTER 1 INTRODUCTION

Osteomyelitis is an inflammation of bone due to pyogenic organism activity (Nandi *et al*., 2009; Abulfotooh *et al.*, 2003; Lew *et al*., 1997; Uckay *et al*., 2012). Unfortunately, despite continued progress towards understanding its pathophysiology and management, osteomyelitis still causes substantial morbidity worldwide and is a continuing concern for clinicians (Haas *et al*., 1996). Moreover, conventional systemic routes of therapy are currently unable to adequately resolve this infection (Nandi *et al*., 2009; Arruebo *et al*., 2010). To address this gap in the clinician's toolbox, this doctoral thesis describes the development of a novel calcium polyphosphate (CPP)-based local therapeutic agent delivery system for osteomyelitis treatment.

1.1 OSTEOMYELITIS

1.1.1 Etiology and Pathogenesis

Healthy bone is fairly resistant to infection. However, if a particularly virulent bacterial species gains access to bone through tissue trauma, the introduction of implant devices (eg, joint replacement), and/or if the patient has a pre-disposing disease (e.g. peripheral vascular disease and diabetes), osteomyelitis may develop (Brady *et al*., 2006; Haas *et al.,* 1996; Caputo *et al*., 1994; Calhoun et al., 1988; Lew *et al*., 2004). After inflammation has taken hold, infection may then advance through the Haversian and Volkmann canal systems (Brady *et al*., 2006). This spread of infection and the rigid limitations of the marrow space act together to reduce blood flow, provide an ideal site for bacteria to settle, and will eventually lead to local vascular occlusion and thrombosis as the inflammatory response grows (Lew *et al.,* 1997). A compromise, and in some cases full obliteration, of vascular channels contributes to the observed

bone necrosis and development of local sequestra (Soontornvipart *et al.,* 2003; Larsen, 1934; Lew *et al.,* 1997; Parsons *et al*., 2004). The formation and avascular nature of sequestra are the leading *anatomical* reasons why osteomyelitis is so difficult to treat, as neither the individual's own white blood cells nor the systemically supplied antibiotics may penetrate the area sufficiently. Over time the infected foci will become surrounded by sclerotic, avascular bone that is itself covered by a thickened periosteum, scarred muscle and subcutaneous tissue (Lew *et al*., 2004). As infection progresses purulent material (e.g. bacteria, pus cells, and necrotic debris) may penetrate the periosteum as a sinus tract and cause a soft tissue abscess (Parsons *et al*., 2004).

The identity of the pathogen(s) responsible for osteomyelitis is dependent on host factors such as geographic location, immune status, and age of the patient, as well as the pathophysiologic circumstance that allowed bacterial access to bone (Haas *et al*., 1996; Lew *et al*., 2004; Soontornvipart *et al*., 2003). Whether these microorganisms reach the bone by hematogenous travel of bacteria from elsewhere in the body, by spreading from a contiguous focus secondary to vascular insufficiency (e.g. diabetes), or by a penetrating wound, they are most likely *Staphylococcus Aureus* (*S.aureus*) (Bamberger, 2000). Unfortunately*, S.aureus* has an array of extracellular and cell-associated virulence factors that assist in its infectious role and are responsible for its adherence, direct host damage, and immune-avoidance (Brady *et al*., 2006; Lew *et al.,* 2004, Kluin *et al.,* 2013). In addition, the biofilms that form on the necrotic bone and foreign bodies as a result of *S.aureus* and other pathogens provide additional antibiotic resistance. Biofilm organisms are up to 800-fold less susceptible to antibiotics than those that are planktonic (Kluin *et al.,* 2013). Altogether, these *biochemical* factors provide yet another

challenge towards the treatment of this disease and the body's own attempt at healing following injury.

Inadequate acute osteomyelitis therapy encourages the infection to persist and either recur at a later time or become chronic (Kluin *et al.,* 2013). This in turn leads to prolonged hospitalization, poor functional outcome, sepsis and a significant reduction in quality of life (Lucke *et al*., 2003). Local therapy using a biodegradable system has shown great potential to improve treatment outcome (Kluin *et al.,* 2013).

1.1.2 Treatment

Effective treatment of osteomyelitis relies heavily on addressing three interacting components: 1) anatomic stability, 2) microbiological virulence, and 3) host physiology (Mast *et al*., 2005). Though acute cases may require a less rigorous approach than one with increased chronicity, a combination of antibiotic delivery and surgical approaches should be considered for all osteomyelitis cases. (Bamberger, 2000; Lew *et al*., 2004; Gentry, 1997).

The current standard of osteomyelitis therapy consists of debridement, dead space management, and a lengthy regimen of parenteral antibiotics. Surgical debridement is an essential first step in treating this disease. It reduces bacterial load, removes necrotic tissue and visible sequestra, and potentially allows for the apposition of healthy bone, though not without temporarily causing some destabilization of the site (Mast *et al.*, 2005). Following surgical debridement and dead space management, antibiotics are traditionally administered systemically for at least six weeks (Gentry, 1997; Lew *et al*., 2004; Haas *et al*., 1996). However, as 6 weeks of systemic antibiotic

administration is insufficient in many cases of chronic osteomyelitis (Garcia-Lechu *et al*., 2009; Lucke *et al*., 2003) and there is a growing concern over antimicrobial resistance development with prolonged antibiotic presence (Bamberger, 2000), an alternative delivery strategy needs to be considered.

The management and treatment of chronic osteomyelitis using local drug delivery systems is one novel approach that has already shown positive treatment outcomes (Klemm *et al.,* 2001; Chang *et al.,* 2007; Heijink *et al.,* 2006; Gitelis *et al*., 2002). For example, this strategy may achieve elevated antibiotic concentrations at the site of infection and limit the side effects and risk of overdose otherwise seen with systemically administered therapeutics, as well as offer additional therapeutic value by supporting bone restoration. ***The overriding objective of this research is to develop a local delivery system for treatment of osteomyelitis and restoration of any bone lost to the disease***.

1.2 CARRIER MATERIALS STUDIED FOR LOCALIZED OSTEOMYELITIS THERAPY

The body of literature regarding controlled drug delivery research and applications continues to grow, yet only a few local delivery products have reached the commercial stage (Ahola *et al*., 2014; Kluin *et al.,* 2013; Heijink et al., 2006). This difficulty in achieving idea-to-market translation is largely attributed to the various factors that influence the release of drug molecules from these systems and increase design complexity. These design factors include those related to the nature of the drug itself (e.g. molecular weight, drug solubility, and drug dose), the delivery matrix (type, molecular weight), drug-material interactions, and the size, shape and porosity of the device (Ahola *et al*., 2014; Kluin *et al*., 2013; Maderuelo *et al.,* 2011). These

factors cannot be considered individually as they are very interdependent; as a result, the tuning of any delivery system is multi-faceted. Together these factors will contribute to the design of a delivery system that must be able to load a sufficient amount of agent, to fill the dead space following surgical debridement of the infected area, and to release an effective dose of agent above the minimum inhibitory concentration (MIC) but below the maximum tolerable concentration (MTC) for the necessary release period (Figure 1.1) (Mourino *et al*., 2010; Gitelis *et al*., 2002; Nandi *et al*., 2009; Dion *et al*., 2005b).

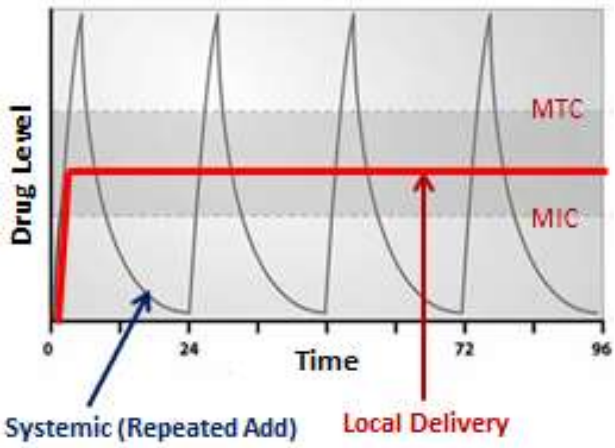

Figure 1.1: Drug level at site of infection when delivered systemically (cyclic grey line) and locally (bold red line) (adapted from Ahola (2014)).

The goal of local delivery is to achieve zero-order release as quickly as possible (while limiting burst release) and to sustain this release for a sufficient period of time in the therapeutic range in order to eradicate the infection. The carrier material employed to address these design requirements may be generally classified as either non-biodegradable or biodegradable. The significant advantages and potential disadvantages of the materials most commonly studied as local antibiotic carriers are listed in Table 1.1 with the following sections providing further details (see sections 1.2.1 and 1.2.2).

Table 1.1: Commonly studied materials for local delivery in osteomyelitis therapy.

Material	Advantages	Potential Disadvantages	*In Vivo* Models	Clinical Studies	Examples
Non-biodegradable					
Hand-mixed Poly(methyl methacrylate)	Ease of preparation Readily customizable	Unpredictable release Requires surgical removal after treatment Lower antibiotic availability	Holcombe et al (1997) Trostle et al. (1996)	Ozaki et al (1998) McFadden (1998) Cho et al (1997)	Fresh spacers Fresh beads
Pre-made Poly(methyl methacrylate)	Sustains high level of release	Few antibiotics suitable Requires surgical removal after treatment Incomplete release	Giuliano et al (1986) Faber et al (2004)	Klemm (1979) Neut et al (2003) Evans et al (1993) Nelson et al. (1993)	Septopal® Spacer G Vancogenx™
Biodegradable					
Calcium Sulphate	Historic bone void filler Low cost	High burst release Seroma formation	Turner et al. (2005) Turner et al. (2001) Jia et al (2010) Nelson et al (2002)	McKee et al. (2002) Gitelis et al. (2002)	Herafill® Osteoset® T
Calcium Phosphates	Superior biocompatibility Assists in bone repair	Low-to-medium burst release Incomplete release from cement	Shinto et al. (1992) Nandi et al. (2009) Lambotte et al. (1998)	Yamashita et al (1998) Kawanabe et al (1998)	Calcibon® Bonesource® Vitoss® Cerasorb®
Collagen	Superior biocompatibility Low cost	Very high burst release Seroma formation	Phienney et al (1988) Mehta et al (2005)	Ipsen et al (1991) Ascherl et al (1986)	Collatramp G® Septocoli®
Aliphatic Polyester Polymers	Readily sustains release	Inflammatory foreign-body reactions and bone resorption	Ambrose et al. (2003) Makinen et al. (2005) Garvin et al. (1994) Liu et al (2002)	Bostman et al (1990)	PLA, PLGA implants
Bioactive Glass	Assists in bone repair	Processing control more complex (e.g. control of crystallization, porosity)	Zhang et al (2010) Xie et al (2009)	Lindfors et al (2010) Drago et al (2013) McAndrew et al (2013)	Bioglass® (45S5) BonAlive® (S53P4)

Additional references for Table 1.1: Nandi *et al*., (2009); Schlickewei *et al*., (2014); Gomes *et al*., (2013); Kluin *et al*., (2013); Maier *et al*. (2013); Romano *et al*. (2014); Garvin *et al*. (1994); Jones (2013).

1.2.1 PMMA-Based Carriers

In the 1970's non-biodegradable poly(methyl methacrylate) (PMMA) cement containing an antibiotic was first used in orthopedic surgery as a prophylactic agent against deep bone infections (Buchholz *et al*., 1984). Since then antibiotic-impregnated PMMA has existed in two forms: as a bone cement in arthroplasties and as beads for musculoskeletal infections (Nandi *et al.*, 2009). Over the last forty years, various antibiotics including aminoglycosides, gentamicin, vancomycin, tobramycin, penicillins, cephalosporins, and clindamycin have each been proven to effectively elute from this carrier (Nandi *et al*., 2009; Haas *et al*., 1996). Under the trade name Septopal®, PMMA beads containing gentamicin have been used in treatment of osteomyelitis and on the market for more than 30 years in Europe (Nandi *et al*., 2009; Garcia-Lechu *et al*., 2009; Haas *et al*., 1996; Arruebo *et al*., 2010; Cierny *et al*., 2003; McHugh *et al*., 2011). Unfortunately, these beads are still not accepted by the Food and Drug Administration (FDA) in the USA. In North America non-commercial preparations of the PMMA-based beads are, instead, made in many operating rooms by the surgeons themselves; commercially available PMMA is mixed with powdered antibiotic shortly before the operation (Nandi *et al*., 2009; Gomes *et al*., 2013). The overall clinical success of these beads in carrying therapeutics has been attributed primarily to the absence of any significant immune response being triggered from the host, and to a bead format that confers a wide surface area for rapid therapeutic release (Nandi *et al*., 2009). However, a major disadvantage of the PMMA beads is the need for their surgical removal within two to four weeks (followed by replacement with cancellous bone grafts) (Nandi *et al*., 2009). Additional disadvantages include a limited cumulative elution of antibiotics from the PMMA such that a good portion of drug is unused, as well as the fact that this material will not aid in bone regeneration (McLaren, 2004). Furthermore, antibiotics loaded

into PMMA need to be chemically stable during the polymerization of PMMA (which can reach temperatures greater than 80^0C) (Kluin *et al*., 2013).

1.2.2 Biodegradable Carrier Materials

Biodegradable delivery vehicles have been the focus of recent local therapy research and are of interest in the doctoral research presented here largely as they eliminate the need for reoperation and removal following treatment (Lucke *et al*., 2005; Gitelis *et al*., 2002; Nandi *et al*., 2009; Wang *et al*., 2003; Jarcho, 1981; Dion *et al*., 2005b; Wang, Q *et al*., 2009). Also owing to its eventual degradation, a biodegradable carrier is not as limited by the size or type of antibiotic that may be loaded and offers greater antibiotic availability than that possible with PMMA. Biodegradable carrier materials of interest include natural polymers such as collagen (e.g. CollatrampG® and Septocol®E), and bone graft substitutes including calcium sulphate (e.g. Herafill®, Osteoset®T), bioactive glass (e.g. Bioglass®, BonAlive®), and calcium phosphate (e.g. Vitoss®, Bonesource®) (Kluin *et al*., 2013). Disadvantages of collagenous and calcium sulphate carriers include the high risk of seroma formation (i.e. an accumulation of serum) and burst release owing to a ready absorption of large amounts of water into these materials (Ziran *et al*., 2007; Lee *et al*., 2001; Kluin *et al*., 2013; Schlickewei *et al*., 2014). For synthetic aliphatic polyester polymers the most significant disadvantage is the potential for bone resorption during carrier degradation (Schlickewei *et al*., 2014). With bioactive glass matrices the processing control is more complex and has, to date, limited their application for drug delivery (Schlickewei *et al*., 2014; Jones, 2013). For example, conventional organic compounds used to create porosity within the Bioglass® matrices cannot be readily removed upon heat treatment (Chevalier *et al.,* 2009). Furthermore, despite the relative interest in many of the aforementioned carriers, there is

a lack of large randomized controlled trials to evaluate their relative value in treating chronic osteomyelitis (Kluin *et al*., 2013). As a result, there are still many carriers awaiting FDA approval for use as an antibiotic delivery vehicle. *Commercially available applications in osteomyelitis treatment remain sparse and much research is still required in this field*.

Of the carriers studied, biodegradable calcium phosphates offer superior biocompatibility (owing to a chemistry resembling the mineral phase of bone) and, in many instances, a more readily controlled antibiotic release (Kluin *et al*., 2013). Therefore, for the purposes of osteomyelitis therapy and subsequent recovery of bone there is strong interest in calcium phosphate-based carrier development. A unique class of calcium phosphate, calcium *poly*phosphate (CPP) may offer an advantage in this regard as it possesses some potentially unique drug delivery-relevant attributes of its own.

Owing to its biocompatible, osteoconductive and biodegradable nature (Kandel *et al*., 2006; Wang, F. *et al*., 2006; Comeau *et al*., 2010; Kim *et al*., 2008), CPP has been studied for use in cartilage and bone repair, as well as for angiogenesis (Baksh *et al*., 1998; Kandel *et al*., 2006; Lee *et al*., 2000; Park *et al*., 2004; Chen *et al*., 2008). In addition, recent progress in the development of low-temperature fabrication protocols for inclusion of thermal-labile biological agents in CPP has further supported the potential of this material for local drug delivery (Dion *et al.*, 2005a; Dion *et al*., 2005b; Petrone *et al*., 2008). The next section highlights some of the structural and *in vitro* properties of CPP that may impact its potential to serve as a carrier in a local delivery system. *Owing to their long-term success in Europe, commercially available*

PMMA beads are the current clinical gold standard for local osteomyelitis therapy and will be treated as the benchmark for the design of the CPP-based system.

1.3 CALCIUM POLYPHOSPHATE - THE CARRIER MATERIAL FOR LOCALIZED OSTEOMYELITIS THERAPY

1.3.1 CPP Structure

Any structural description of a phosphate should consider both short-range (i.e. immediate coordination environment of an ion) and longer-range information (i.e. how the polyhedral are themselves linked), before it is considered complete. For example, in many cases the properties of polyphosphate glasses are more dependent on the P-O-cation interchain bonding than the nature of the P-O-P bonds that form the phosphate chain (Brow *et al*., 2000).

The phosphate structure consists of phosphorus atom (of sp^3 hybrid orbital bonding) surrounded by four oxygen atoms arranged at corners of a tetrahedron; this satisfies Zachariasen's criteria (Van Wazer, 1958; Brow *et al*., 2000). Interconnected PO_4 tetrahedra are then produced when these oxygen atoms are shared via covalent bonds (Van Wazer, 1958). These basic building blocks of phosphate are classified following Q^i terminology, where "i" indicates the number of bridging oxygen per tetrahedral (Figure 1.2).

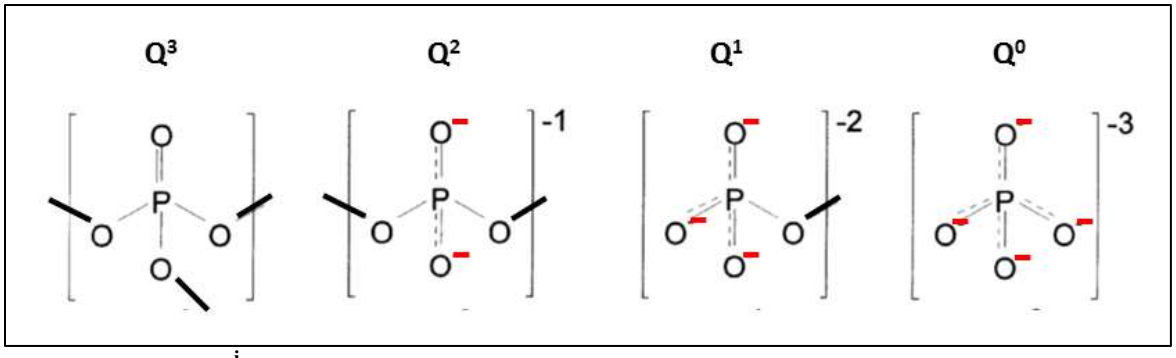

Figure 1.2: Q^i phosphate tetrahedral species (adapted from Brow *et al.* (2000)).

The phosphate species include: Q^0 as an orthophosphate ion, Q^1 as a pyrophosphate or chain end group, Q^2 as an internal phosphate group, and Q^3 as a branched phosphate group. By combining the end groups, middle groups, and branching points a number of different phosphate networks can be formed. Of interest in this thesis is a linear long-chain phosphate structure that consists mainly of the Q^2 species.

As a result of the high charge associated with the tetrahedral anions, phosphates tend to associate strongly with cations under most conditions (Van Wazer, 1958). CPP itself consists of long polymeric chains of phosphate connected via covalent bonds and "chelated" calcium (Ca) ions as network modifiers/connectors between chains (Wang, K. *et al*., 2008; Kasuga *et al*., 2001). The molecular structure of CPP (i.e. $[Ca(PO_3)_2]_n$) is shown in Figure 1.3.

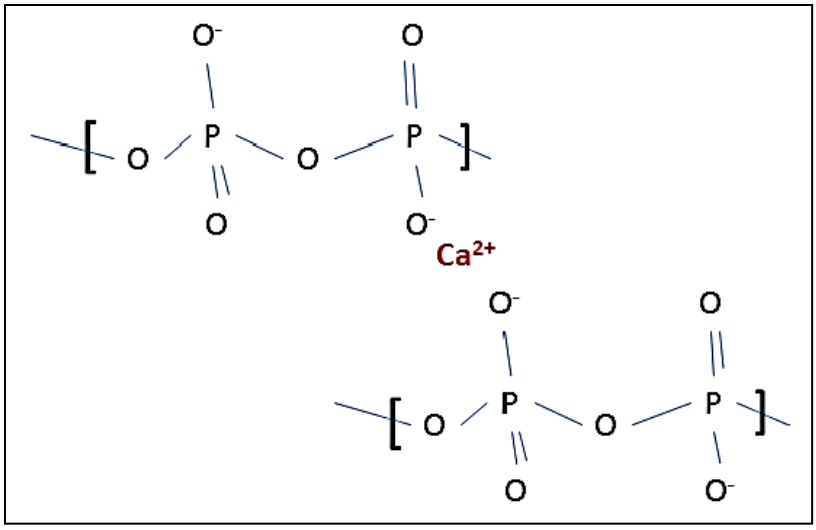

Figure 1.3: Molecular schematic of CPP.

In CPP *each* phosphate tetrahedral has on average two bridging oxygen serving to link the phosphate units, as well as two non-bridging oxygen atoms available for calcium coordination (Wetherall *et al*., 2009). As the coordination number of calcium ions in CPP glass is reportedly ~7, 3 out of 4 non-bridging oxygen atoms are required to form two Ca-O bonds (Wetherall *et al.,* 2009; Hoppe *et al*., 1996). In other words, as the mean coordination number of calcium exceeds unity around the terminal oxygen atoms, most non-bridging oxygen atoms are each coordinated to two calcium atoms (Wetherall *et al*., 2009). This sharing of available oxygen atoms distorts the coordination environment around the calcium ions and is expected to play a role in CPP hydration and the resulting hygroscopic nature of the glass.

1.3.2 CPP *In Vitro* Properties

The sharing of available oxygen atoms distorts the coordination environment around the calcium ions in such a way that, upon contact with moisture, there is a competition between the oxygen from terminal phosphate groups and water to bond with calcium ions. Continued exposure to

aqueous media encourages the gradual degradation of CPP by two interdependent steps: (1) the exchange of calcium ions in CPP with hydrogen ions from the media, resulting in the formation of a hydrated layer at the interface between CPP and media, and (2) the network breakage of P-O-P bonds under the attack of hydrogen ions and water molecules (Wang, Q. *et al.*, 2009; Omelon *et al.*, 2008; Balamurugan *et al.*, 2011; Kasuga *et al.*, 2001; Porter *et al*., 2001; Clement *et al.*, 1999). Totally hydrated phosphate chains disentangle from partially hydrated chains still attached to the surface and leach into the solution (Clement *et al.*, 1999). Hydrolytic degradation in the presence of calcium occurs significantly at the inner P-O-P linkages and continues to produce shorter and shorter polyphosphate chains (Delahaye *et al*., 1999; Huffman, 1960). However, alternative degradation paths include splitting of end PO_4 groups and, to a lesser degree, ring formation (e.g. tri- and tetra-metaphosphate) (Umegaki *et al*., 1979, Huffman, 1960). Depending on the solution pH, as CPP degradation continues beyond several days precipitates such as $Ca_3(HP_2O_7)_2*4H_2O$ and $Ca(H_2PO_4)_2$ start to form (Umegaki *et al*., 1979). Overall, longer chains will not release the orthophosphate as quickly as shorter chains, pH will not drop as quickly, and there will be fewer preferable sites for chain scission with a reduced degradation rate compared to short molecular chains (Balamurugan *et al*., 2011; Qiu, K.(a) *et al*., 2006; Ding *et al*., 2008). *Increasing the chain length of CPP, then, may be one useful approach to further control the degradation of the carrier and release of the loaded antibiotic in vitro*.

Some of the environmental factors that influence phosphate chain degradation in aqueous solution are shown in Table 1.2 (Van Wazer, 1958).

Table 1.2: Approximate effect of different environmental factors on hydrolytic phosphate chain degradation (adapted from Van Wazer, 1958).

	Factor	Approximate effect on rate
1	Temperature	Boiling is 10^5 – 10^6 faster than freezing
2	pH	Strong base is 10^3 – 10^4 slower than strong acid
3	Enzymes	As much as 10^5 – 10^6 faster
4	Colloidal gels	As much as 10^4 – 10^5 faster
5	Complexing cations	Vary many-fold faster in several cases
6	Concentration	Approximately Proportional
7	Ionic environment in the solution	Several-fold change

The activation energy for the splitting of P-O-P linkages in phosphate chains is on average 25kcal/mole in a neutral solution and drops roughly 12-17kcal/mole in the presence of strong acids (Van Wazer, 1958). Thus, in a neutral aqueous solution absent of cations and at room temperature, the half-life of P-O-P linkages is several years (Van Wazer, 1958). In the presence of calcium (i.e. CPP) the half-life of *dissolved* phosphate chains in a near-neutral aqueous solution drops to roughly 180 days (Huffman *et al.,* 1960). The success of maintaining the CPP linkages for even that long is partly owing to its polyelectrolytic nature (Callis *et al*., 1954). While low molecular weight electrolytes may readily disperse in solution, the high concentration of charge in the vicinity of polyelectrolytes (i.e. phosphate anions) attracts most of the counter-ions to their environment (Manning, 1969). The gradual accumulation of ions in the test solution towards CPP increases the electrostatic interactions in the hydrated layer of the glass and eventually hampers further dissolution (Balamurugan *et al.*, 2011; Ding *et al*., 2008b; Manning, 1969).

1.3.3 CPP Processing

CPP can be readily fabricated to give phosphate glass or crystalline material by manipulating the processing parameters and starting compounds used. Of interest in this thesis is the processing

of *CPP glass*. According to the literature, the most common method for fabricating amorphous CPP is directly from phosphate melts following prior condensation of a starting calcium phosphate hydrate (as described in Pilliar *et al*. (2001)). The heat ramp rates, temperatures, and dwell times of calcination are important parameters to consider when synthesizing CPP from a calcium phosphate monobasic monohydrate (CPMM) (i.e. $Ca(H_2PO_4)_2*H_2O$). These parameters need to be of sufficient magnitude in order to drive off the crystalline water and initiate condensation and to, subsequently, further polymerize the phosphates in accordance with equation 1.1 (Balamurugan *et al*., 2011; Pilliar *et al*., 2001).

$$nCa(H_2PO_4)_2*H_2O \rightarrow [Ca(PO_3)_2]_n + 3nH_2O \qquad \textbf{[Equation 1.1]}$$

To date, there is little variation in the reported heat ramp rates, temperatures, or duration of CPMM calcination. For example, CPMM is typically calcined at a temperature of 500°C for 10 or 15hrs (Porter *et al*., 2009; Qiu, K.(a) *et al*., 2006; Pilliar *et al*., 2001; Petrone *et al*., 2008; Dion *et al*., 2005; Dion *et al*., 2005b; Wang, K. *et al*., 2008; Kandel *et al*., 2006; Schofield *et al*., 2006; Omelon *et al*., 2008; Balamurugan *et al.*, 2011; Chun *et al*., 2001; Grynpas *et al*., 2002; Waldman *et al*., 2002; Guo *et al*., 2004; Ding *et al*., 2008; Chen, F. *et al*., 2008). Meanwhile, melting is commonly carried out at 1100 – 1200°C with a 1- 2hr dwell (Porter *et al*., 2009; Qiu, K.(a) et al., 2006; Pilliar *et al*., 2001; Petrone *et al*., 2008; Dion *et al*., 2005; Dion *et al*., 2005b; Wang, K. *et al*., 2008; Kandel *et al*., 2006; Schofield *et al*., 2006; Omelon *et al*., 2008; Balamurugan *et al*., 2011; Chun *et al*., 2001; Grynpas *et al*., 2002; Waldman *et al*., 2002; Guo *et al*., 2004; Ding *et al*., 2008; Chen, F. *et al*., 2008). The literature is largely devoid of any studies linking the choice of melt protocol parameters to the properties of CPP. However, two

independent studies, by Qiu *et al*.(2006) and Ding *et al*.(2008), did vary calcine duration from 0-10hrs in order to determine the impact of different calcination dwell times on polymerization degree. They found that a minimum of 3hrs of calcination was necessary in order to produce any noticeable change in polymerization and that the degree of polymerization increased with calcine duration (Qiu *et al*., 2006; Ding *et al*., 2008). Unfortunately, more recent work by Wu *et al* (2012) somewhat contradicts these linear results; in their study there was a lack of consistent increase or decrease in chain length as calcine time increased. In practice it is very difficult to remove the last trace of water from the CPP melt, and furnace conditions (which were not reported in the three aforementioned studies) may play a role in the ease with which water is removed (Callis *et al*., 1954). In fact, CPP glass chain length is likely a result of the competition between the hydrolysis reaction and condensation that occurs during the melt steps (Ue, 2009). *Further refinement of the melt protocol parameters to increase the chain length of CPP may, as a result, be limited*.

As an alternative processing strategy amorphous CPP may be fabricated from water-soluble polyphosphates such as sodium polyphosphate (NaPP) by precipitation from solution (Sinyaev *et al*., 2001; Squali *et al*., 1991; Gomez *et al*., 1997; Kasuga *et al*., 2001). Unlike CPP, in NaPP each phosphate is bound to only one cation (i.e. sodium). The dissociation constant for calcium and the complexing ability of the phosphate for calcium are, as a result, both greater than that for sodium (Van Wazer, 1958; Callis *et al*., 1954). The reaction between NaPP ($NaPO_3$) and calcium chloride ($CaCl_2$) to precipitate out CPP occurs in accordance with equation 1.2 (Masson *et al.,* 1997; Sinyaev *et al*., 2001):

$$2NaPO_{3(aq)} + CaCl_{2(aq)} \rightarrow Ca(PO_3)_{2(s)} + 2NaCl_{(aq)} \quad \textbf{[Equation 1.2]}$$

In a single study by Sinyaev *et al*. (2001), the addition of calcium chloride to NaPP was found to precipitate a CPP with a chain length only slightly lower than that of the starting sodium polyphosphate. As this study did not measure the residual sodium nor study the *in vitro* degradation of the resulting material, there is much still to explore with this methodological approach. Unfortunately, few reports have indicated – let alone studied – the impact of different precipitation factors on the chain length of the resulting amorphous CPP. In addition, despite a slower dissolution rate, the activation energy of polyphosphate in the presence of calcium is 6kcal/mole lower than that in the presence of sodium and so any *dissolved* CPP will then degrade 5-10 times faster under similar conditions (Huffman *et al*., 1960; Bhargava *et al*., 1970). These degradation differences are explained by the closer approach of the water dipole in the less ionized (and more nearly neutral) phosphate structure when calcium is present (Huffman *et al*., 1960). *The presence of residual sodium may then influence how quickly the carrier material degrades and releases the loaded antibiotic*.

As is evident from the literature, despite successful fabrication of CPP by both high and low temperature routes, the rationale behind the different processing parameters chosen and their potential impact on the resulting glass structure and properties has not been systematically studied. *This thesis seeks to add to the body of knowledge surrounding these processing-structure-property relationships while exploring novel CPP glass fabrication strategies*.

1.4 STRUCTURAL THEORIES OF GLASS FORMATION

There are two categories of glass formation theories: structural and kinetic. Kinetic theories largely assume that any melt can be vitrified provided the cooling rate is fast enough to avoid crystallization (Varshneya, 1994). Given that the cooling rate of the melt is not a parameter studied in this thesis, with no indication in the available literature that unreasonable cooling rates are necessary to produce CPP glass, structural theories may be of more use for the assessment of a CPP-based glass suitable as a carrier material. Two structural theories in particular have earned academic support for their predictive nature towards glass formation and properties: (1) Zachariasen's random network theory, and (2) Dietzel's field strength criterion (Varshneya, 1994). This section briefly summarizes these theories with emphasis on the components that make up CPP glass.

Work by Zachariasen has arguably had the most impact on glass science (Varshneya, 1994). His theory stems from two key observations: (1) that the mechanical properties of glasses are similar to those of the corresponding crystals, and (2) that the x-ray diffraction spectra for glasses have a diffuseness that is indicative of an infinitely large unit cell (Varshneya, 1994). The glass must then consist of a 3D random network that, as Zachariasen proposed, requires the corners being shared in the polyhedral structure. His four rules for formation of a hypothetical glass A_xO_y are: (1) an oxygen atom is linked to at most two atoms of A, (2) the oxygen coordination around A is small (e.g. 3 or 4), (3) the polyhedral of A can only share corners, and (4) at least three corners of each polyhedral are shared (Varshneya, 1994). From this theory oxides of alkali or alkaline earth metal cations (e.g. sodium, calcium, strontium) alone will not form glass successfully. However,

group IV oxides ("AO_3") and group V oxides ("A_2O_5") will be glass formers if the oxygen atoms form tetrahedral around the cations – P_2O_5 is a good example of the latter.

Dietzel's theory separates oxides into three classes using their field strengths (see equation 1.3):

$$F = \frac{Z_c}{(r_c + r_{o-})^2} \qquad \textbf{[Equation 1.3]}$$

Here, Z_c is the valency of the cation, while r_c and r_{o-} are the ionic radii of the cation and the oxygen ion, respectively, in Angstrom units. Network-forming (NWF) cations have high field strengths (~1.3 – 2.0), network-modifying (NWM) cations have low field strengths (0.1 – 0.4), and intermediates (NWI) have field strengths in-between the other two (Varshneya, 1994). In CPP glass, phosphorus is a network former while calcium is a network modifier (as are sodium and strontium).

As will become even more apparent in later chapters describing the thesis research glass properties are highly dependent on the elements used to form the glass and the ratio of NWF to NWM within the composition.

1.5 THERAPEUTIC AGENTS STUDIED FOR LOCALIZED OSTEOMYELITIS TREATMENT

1.5.1 Antibiotics

The majority of osteomyelitis cases present with gram-positive *S. aureus* bacteria and, as a result, most drugs studied for addition to an osteomyelitis-specific local delivery device have been selectively chosen for their effectiveness against this microorganism. These antibiotics

include penicillins, vancomycin (VCM), rifampin, aminoglycosides, fluoroquinolones, daptomycin, and tigecycline (Mader *et al*., 1999; Lucke *et al*., 2005; Arruebo *et al*., 2010; Nandi *et al.*, 2009). VCM with a MIC of 1ug/mL, a MTC of 0.05mg/mL (White *et al*., 1988), and both water-soluble and stable at body temperature (Petrone *et al*., 2008; Dion *et al*., 2005b), will be the antibiotic of choice in this thesis work (see Figure 1.4 for molecular structure). As a tricyclic glycopeptide antibiotic, VCM reportedly inhibits cell wall peptidoglycan synthesis in gram-positive bacteria (Reynolds, 1989); by preventing DNA, RNA, and protein synthesis it will in time lead to death of the bacterial cell. This antibiotic has been of particular interest in the development of carrier systems due to such properties and its effectiveness against *S.aureus* and various other osteomyelitis associated bacteria. In addition, VCM is used clinically to treat patients with osteomyelitis infections who are allergic to penicillins or have a methicillin-resistant form of *S.aureus* infection (Ma *et al*., 1994). Furthermore, VCM has shown *fewer* negative effects on osteoblasts *in vitro* and should be less likely to impede bone growth than other commonly used antibiotics (Edin *et al*., 1996; Antoci *et al*., 2007; Haleem *et al.*, 2004; Li *et al*., 2010).

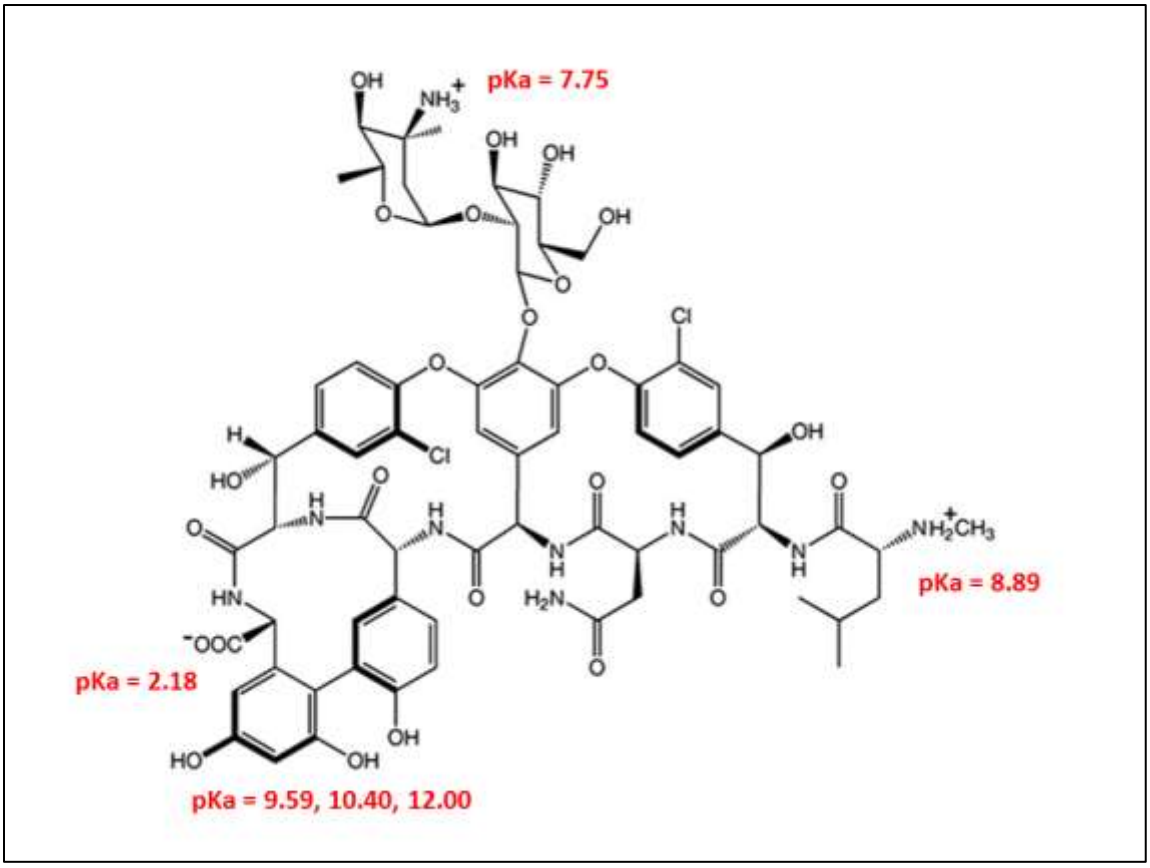

Figure 1.4: Molecular schematic of VCM: $C_{66}H_{75}Cl_2N_9O_{24}$ (adapted from Li et al (2010)).

The molecular structure of VCM consists of 18 chiral centers surrounding three "cavities" that are bridged by five aromatic rings (Vijan *et al*., 2009). This antibiotic is able to have strong polar interactions with solutes likely as a result of the strong polar groups proximate to the ring structures. The six functional groups that exhibit dissociable hydrogen atoms at specific pH values are highlighted in Figure 1.3 (Li *et al*., 2010; Vijan *et al*., 2009). These groups include a carboxyl group (pKa of 2.18), a primary amino group (pKa of 7.75), a secondary amino group (pKa at 8.89) and three phenol groups (pKa of 9.59, 10.40, 12.00) (Vijan *et al*., 2009). The two amino groups have basic properties, while the carboxyl and phenol groups are more acidic. The net positive charge of VCM across a 0 to 13 pH range is varied: it is +2.1 at pH of 2, +0.7 at a pH of 3-7.4, and +4.0 at a pH of 13 (Vijan *et al*., 2009). The unique size and structure of VCM

may impact how this antibiotic is loaded and released from the CPP-based local delivery system. For example, owing to VCM being a large molecule and potentially having some chemical steric hindrance, strong evidence has been presented that any chemical interaction between this antibiotic and calcium phosphate materials is limited (Stigter *et al*., 2004; Pacheco *et al*., 2014; Ooya *et al*., 2002; Kriwet *et al*., 1996). Instead, the loaded VCM interacts with calcium phosphate materials via physical adsorption and, as a result, the manner in which VCM is incorporated into a calcium phosphate material is of particular importance (Del Valle *et al*., 2011; Verron *et al*., 2012).

An important consideration in localized delivery of a therapeutic of choice is the mechanism or mechanisms guiding its release. Drug release kinetics may be affected by many factors including those linked to the matrix material (e.g. composition, structure, swelling, degradation), release medium (e.g. pH, temperature, ionic strength, enzymes), and drug compounds (e.g. solubility, stability, charges, interaction with matrix) (Fu et al., 2010). These factors contribute to the release of the loaded drug by three main mechanisms (Arifin *et al*., 2006):

(1) Diffusion-controlled mechanism, in which drug diffusion occurs through water-filled pores or through the macromolecular mesh,

(2) Swelling-controlled mechanism, whereby enhanced drug diffusion is observed due to polymer hydration and subsequent swelling, and

(3) Erosion-controlled mechanism, in which the drug entrapped within macromolecules is released as the molecules degrade to smaller molecular weight species.

As a result of the polymeric nature of CPP, the hydrolytic dissolution and degradation of the phosphate chains in CPP will lead to some degree of swelling- and/or erosion-based drug release mechanisms. However, diffusion may still be dominant if the two other processes are slow (Arifin et al., 2006). For example, insignificant water penetration results in a limited polymer relaxation and a Fickian diffusion-controlled release. In contrast, if water penetration is significant drug release will be controlled by the polymer dissolution process at the moving carrier-solution interface (i.e. non-Fickian case-II transport) (Arifin et al., 2006). In between these extreme cases, an intermediate "anomalous transport" is often typified by indistinguishable diffusion *and* dissolution processes. *The degree of water penetration into the carrier material is, therefore, one significant factor for determining which mechanism(s) will dominate drug release*.

1.5.2 Therapeutic Ions

Doping a phosphate glass with additional elements via ion substitution is a common approach to modify glass properties and, with therapeutic ions involved, is of particular interest in the application of local delivery devices for ion-based therapy. In the last few years there has been a dramatic increase in the number of reports published on the ability of *crystalline* CPP to be doped with ions such as strontium, potassium, zinc, sodium, and magnesium (Chen *et al.*, 2008; Song *et al*., 2011; Chen, Y(b). *et al*., 2008; Tian *et al.,* 2009; Kanchana *et al*., 2010; Ue, 2009; Qiu, K.(b) *et al*., 2006; Song *et al*., 2008). *The impact of doping <u>amorphous</u> CPP glass with strontium on glass structure and in vitro degradation will be addressed for the first time in this thesis*.

Like calcium, the structural glass theories predict strontium oxide will act as a network modifier, an attribute that has been supported by available phosphate-glass literature. With a slightly larger ionic radius than calcium (i.e. 1.27 vs 1.06A) the field strength of strontium is, however, lower than that for calcium – a difference that may be sufficient to impact glass properties (Varshneya, 1994). For example, Fletcher *et al*. (1993) used field strength values to describe the relative polymerization states of phosphate-based glass with different cations. They claimed that a cation with a greater field strength will drive the equilibrium of Q^i species (i.e. $2Q^2 = Q^1 + Q^3$) to the right with an increased range of polymerizations (and de-polymerizations) of the P tetrahedral (Fletcher *et al.,* 1993). If the opposite holds true, then by substituting calcium for strontium (and decreasing field strength) the equilibrium may be pushed to the left and there will be a more narrow distribution of phosphate anions in the glass. In addition, with a slightly lower electronegativity than calcium, strontium ions may decrease both the covalency of the cation – to – non-bridging oxygen atom and the ionicity of the opposing P-O bond (Brow *et al*., 1991). This latter theory could then predict that by increasing the electron density on phosphorus, the replacement of calcium by strontium results in a phosphate structure that is more ionized. As a result, the water dipole should then be less able to approach the phosphate backbone and degradation of the dissolved phosphate chain will be slightly slower with strontium present.

Although limited to analysis of the *crystalline* state, the *in vitro* degradation of strontium-doped CPP has been previously characterized. For example, Song et al. (2008) observed through much of their four week *in vitro* study in SBF that incorporation of strontium decreased CPP degradation to a small extent. In a parallel study by Chen, Y. et al. (2008), strontium doped-CPP was again shown to have a reduced rate of *in vitro* degradation compared to undoped CPP over 3

months in physiological saline solution. However, one distinction not made in either of these studies is the extent to which different strontium concentrations impacts degradation. For example, Song et al. (2008) added 8mol%, while Chen, Y et al. (2008) added only 1mol% strontium. As a result, the amount of therapeutic ion added was one of the design parameters considered in this thesis project.

Largely owing to the development of the drug strontium ranelate (Protelos®) for treatment of osteoporotic patients, there has been an increased interest in strontium as a therapeutic agent in hard tissue engineering (Marie, 2005; Marie, 2005-b; Ammann, 2005; Ammann et al., 2004; Hott *et al.,* 2003; Bonnelye *et al*., 2008; Li *et al*., 2010; Marie, 2006; Reginster *et al*., 2008). Growing evidence that strontium has a beneficial effect on bone by increasing both its density and strength suggests the potential for the release of this ion from hard tissue biomaterials in treating metabolically damaged bone (Qiu, K.(b) *et al*., 2006; Song *et al*., 2011; Chen, Y(b). *et al*., 2008; Tian *et al*., 2009; Zhang *et al*., 2011; Christoffersen *et al*., 1997; Dahl *et al*., 2001; Marie *et al.*, 2001; Buehler *et al*., 2001; Hott *et al*., 2003; Takahashi *et al*., 2003).

Several reports have suggested a definitive biochemical linkage between strontium ion and the cascade of events involved in bone resorption and formation. For example, it has been shown that, like calcium, strontium is able to activate the cation-sensing receptor (CaSR) in bone cells and indirectly promotes osteoblast replication (Marie, 2007; Caverzasio, 2008; Quarles, 1997; Brown *et al*., 2001; Yamaguchi *et al*., 2000). In addition, strontium may be able to influence osteoblastic cell replication as well as inhibit bone resorption by increasing osteoprotegerin (OPG) (Tian *et al*., 2009). Furthermore, strontium may act on bone cells to increase

prostaglandin-E2 (PGE2) production by osteoblasts and aid in osteoblast differentiation (Marie, 2007). Based on prior *in vitro* and *in vivo* studies of strontium-based salts the recommended strontium therapeutic trough is 2-20ug/mL; concentrations much higher than this may lead to deleterious effects (Verberckmoes *et al.*, 2004; Qiu, K(b) *et al*., 2006; Tian *et al*., 2009; Omdahl *et al.,* 1972; Ozgur *et al*., 1996; Shrooten *et al*., 2003; Schrooten *et al*., 1998).

An early study by Qiu, K.(b) *et al*. (2006) found that replacing 1-20% of calcium in *crystalline* CPP with strontium (i.e. CPP of 0.5-10mol% strontium) was optimal for osteoblast proliferation and differentiation based on their direct-contact study. Further support of this low strontium level doping impact on cell proliferation on *crystalline* CPP has since been provided by both Chen *et al*., (2008) and Song *et al*. (2011). This thesis project considered the osteo-promotive potential of *amorphous* strontium-doped CPP matrices compared to the undoped matrices.

To date, the most common method for producing ion-doped CPP has involved phosphoric acid flux (i.e. ion-carbonate, or ion-dihydrogen phosphate, and calcium-carbonate added to phosphoric acid) and the creation of an ion-doped CPMM precipitate (Chen *et a*l., 2008; Song *et al.*, 2011; Chen, Y(b). *et al*., 2008; Tian *et al*., 2009; Song *et al*., 2008). This precipitate is then calcined, melted, and quenched as per the methodology of Pilliar *et al*. (2001). One less frequently used alternative method reported by Chun *et al*. (2001; 2006) involves the dry-powder mixing of ion-H_2PO_4*$2H_2O$ (or ion-H_2PO4) and CPMM, followed by calcining for 12hrs and further heat treating for 3hrs. Ue (2009) similarly used CPMM as the calcium source but, instead of a solid-state reaction, mixed the soluble salts of NaOH, NaH_2PO_4, or Na_2CO_3 with the CPMM crystallite in a slurry-form, dried the slurry until viscous, and then followed the calcine-melt-

quench protocol described by Pilliar *et al*. (2001). As these studies have gone on to study the crystalline nature of the ion-doped CPP, the amorphous ion-doped CPP is further heat treated to create a crystalline ion-doped CPP. Any impact of ion doping on CPP has largely, then, been focused on its crystalline structure. *To what extent these results can be applied to amorphous CPP and the design of a local delivery system was considered in the present thesis*.

1.6 MATRIX FABRICATION STRATEGY FOR LOCALIZED OSTEOMYELITIS THERAPY

1.6.1 Current Status in the Literature

One of the greatest challenges in designing drug delivery systems is how to best load the drug without de-activating it and, simultaneously, maintain all necessary carrier characteristics for optimal elution. As traditional ceramics processing involves the consolidation of powders by molding and sintering, the high temperatures involved prevent the loading of drug until shaping of the final implant has been completed (Tadic *et al*., 2004). Various techniques have been used to incorporate a therapeutic agent with a pre-made calcium phosphate biomaterial (Del Valle *et al*., 2011). These techniques include powder-powder mixing (Yu *et al*., 1992; Hamanishi *et al*., 1996; Gautier *et al*., 2000a), adsorption of agent on the biomaterial following some degree of solution soaking (Hasegawa *et al*., 2004; Baradari *et al*., 2012; Makarov *et al*. 2010), and centrifugation of solution into porous construct (Itokazu *et al*., 1996). The relatively rapid therapeutic release common to many of these approaches limits their use in fabricating any sustainable local delivery system for long-term osteomyelitis therapy. *The matrix design presented in this thesis takes advantage of both the hygroscopic and moldable tendencies of the amorphous CPP powder to create a more suitable delivery device.*

For several years our research group has sought to exploit the unique gelling characteristics of CPP glass in conjunction with secondary processing methods to achieve more robust therapeutic loading with more controllable and sustained antibiotic release. Due to the chelation of calcium ions to the phosphate chains of CPP, any exposure to water molecules is believed to cause a preferential bonding of hydrogens to the protons already connected to the non-bridging-oxygen atoms (Wang, K. *et al*., 2008; Kasuga *et al*., 2001). One early theory, based on this behaviour of CPP in high humidity, suggested that the solvation or hydrolysis, then condensation, and, lastly, drying steps involved in gelling of CPP could create an altered polyphosphate structure (Dion *et al*., 2005). This altered structure is then more capable of encapsulating the dissolved drug and exhibiting appropriate delivery characteristics. Carrying this theory forward, a low temperature gelling and drying ("G1") protocol developed by Dion *et al* (2005; 2005b) was able to reduce the burst release of VCM from the gelled amorphous CPP disks and extend the therapeutically-relevant release period compared to un-gelled disks to six days. However, despite greater sample densities observed in the internal regions of the gelled samples compared to non-gelled samples, the disk tensile strength decreased with increased gelling time until a minimum of 0.411MPa was reached following 48 hours of gelling (Dion *et al.*, 2005; Dion *et al*., 2005b). This was believed to be due to the congruent creation of larger pores at the surface of the disks with longer exposure to humidity, and the changing distribution of pores and pore sizes throughout the bulk of the disk. The uneven distribution of pores also likely contributed to the still present, though reduced, burst release. A subsequent study by our group explored the interaction of amorphous CPP with water and suggested that extending gelling time during VCM loading (i.e. increased exposure to humidity) resulted in decreased chain length, improved the ease with which VCM

could diffuse out, but also increased the likelihood of an initial burst release of the drug (Filiaggi *et al*., 2011). VCM itself is not believed to have any effect on the length of CPP chains in the disk (Dion *et al*., 2005).

To improve upon these G1 studies, a subsequent G2 protocol was developed by Petrone *et al* (2008). Several compaction approaches exist, yet few have utilized the relatively straightforward uniaxial compression or pelleting technique used in the pharmaceutical industry. The G2 protocol translated some of this compaction potential and involved comminution of drug-loaded G1 disks and subsequent uni-axial compaction, re-gelling and drying. Using this G2 protocol, VCM burst release was mostly eliminated, with release extended out to three weeks *in vitro* (Petrone *et al*., 2008). In addition, the released VCM was shown to be capable of inhibiting the growth of *S. aureus* at the standardized MIC (Petrone *et al*., 2008).

Unfortunately, secondary processing utilizing uniaxial processing has limited diversity in geometrical design of delivery systems. In addition, as the applied pressure involved in uniaxial pressing is not transmitted uniformly to the powder due to friction between particles and the die wall as well as amongst the particles themselves, there is difficulty in maintaining uniform density through even the most simple shape design (Stienstra *et al*., 2003). *As an alternative compaction strategy, CIP cold isostatic pressing (CIP) may offer greater dimensional uniformity and geometrical versatility for the therapeutically-loaded device.*

1.6.2 Novel CIP Fabrication Strategy

CIP involves the uniform application of high pressures transmitted by a liquid in all directions within a powder-containing sealed mold and is frequently used in the food industry to produce effects close to those obtained with heat (Gautier *et al*., 2000). Prior studies on other materials have shown isostatic pressing to be more adept at compressing ceramic mixtures and increasing the degree of contact, and therefore density, of the resulting matrix compared to uniaxial pressing (Ani, 2006; Itoh *et al*., 1994; Figure 1.5). Today CIP is used in the commercial production of various components including filter elements, milling or bearing balls, and threaded structural parts (Oberacker, 2011).

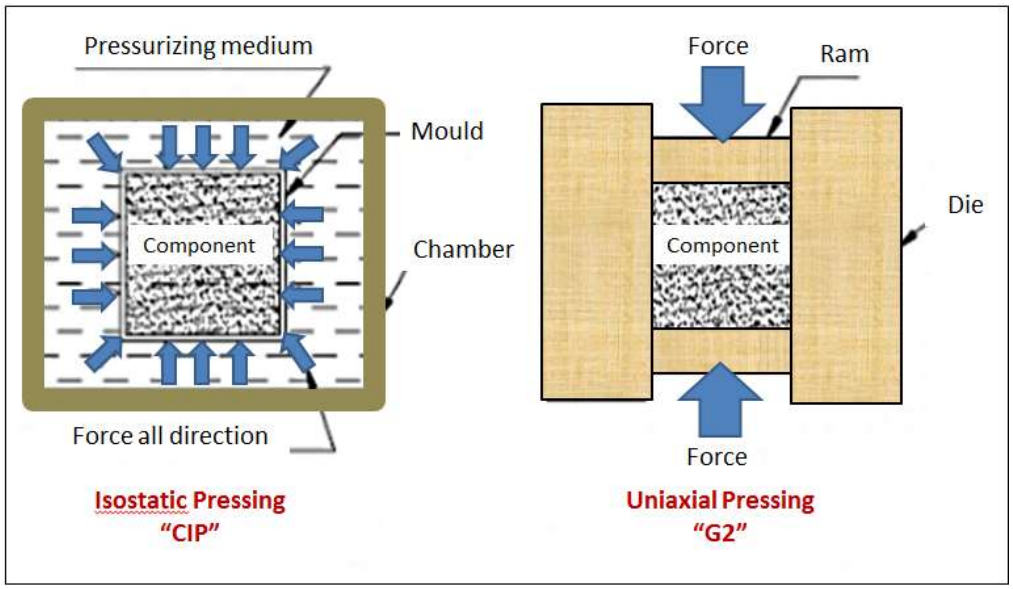

Figure 1.5: Schematic of (left) CIP and (right) uni-axial pressing (adapted from Ani, 2006).

In either case the compaction process for powders during pressing consists of two main overlapping stages (Koizumi *et al*., 1991; Kong *et al*., 2000; Eksi *et al*., 2002):

(1) Stage I: Rearrangement of the particles, and

(2) Stage II: Elastic and plastic deformation of the particles, or fracture.

Compaction curves are often used to describe the response of ceramic powder under compaction and, by reporting density as a function of pressure, can provide information on the transition between the two stages. The linear region at low pressures is thought to be dominated by stage I and be highly dependent on inter-particle friction, while the second linear region at intermediate pressure (stage II) is more dependent on particle strength (Kong *et al*., 2000). Where these two linear regions intersect marks the point where the inter-particle interfaces unite to form a planar layer of uniform density and the net directional transmission of pressure starts to become more effective (i.e. stage I-II transition) (Kong *et al*., 2000). Density will continue to increase in the construct in a more stepwise fashion at pressures above this point. Overall, the compaction curves are useful for providing some insight into the relative dependence of densification on variables such as particle size and shape, as well as pressing conditions (e.g. pressure magnitude, humidity) (Kong *et al*., 2000).

By more efficiently addressing dimensional uniformity and construct densification than uni-axial pressing, CIP may positively influence drug release. For example, Gautier *et al* (2000) showed that CIP of VCM-loaded biphasic calcium phosphate granules resulted in a matrix with decreased drug release with increasing isostatic compression from 100 to 200MPa, as well as no denaturing of the VCM within this pressure range. *In fact, by decreasing the porosity of the CPP construct by CIP relative to uniaxial pressing, fluid exchange across the accessible surface may be reduced and the drug more controllably delivered*.

CIP also allows for the creation of complex geometries such as spheres or rods (Camire *et al*., 2006), and is of interest here for evaluating the optimal design (related to surface area to volume ratios) for treating of osteomyelitis. *With consideration to Septopal® beads as a clinical benchmark for our design, this project sought to utilize the CIP process for fabricating CPP beads that will further improve control over the elution properties and therapeutic potential of the CPP-based delivery system*.

1.7 SUMMARY

Osteomyelitis is a disease that can affect patients of any age, impact any bone and lead, in time, to persistent morbidity. Conventional systemic administration of antibiotics following surgical debridement is currently unable to adequately resolve osteomyelitis. To address this gap in the clinician's toolbox, this doctoral thesis describes the development of a novel local delivery system for osteomyelitis treatment.

To further harness the delivery potential of a CPP-based delivery system there is still a need to make appropriate CPP structure-property connections and improve geometrical versatility. The guiding objective in this thesis, then, was to pursue different functionally driven processing strategies in order to achieve a local delivery system that can be tuned for the appropriate release behaviour, while enhancing the osteo-promotive potential of the amorphous CPP matrix. The delivery system designed here will be ultimately capable of both treating the infection and providing an osteo-promotive matrix for further bone regeneration.

CHAPTER 2 THESIS OBJECTIVES & HYPOTHESES

The overarching objective of this thesis project was to develop a novel amorphous CPP-based local therapeutic agent delivery system for osteomyelitis treatment that can be tuned for the appropriate release behaviour using functionally driven fabrication strategies, while enhancing the osteo-promotive properties of the CPP matrix. Three specific approaches were evaluated, namely CPP precipitation, strontium doping, and cold isostatic pressing of CPP-based matrices, each with a guiding set of hypotheses.

In Chapter 3, CPP precipitation is examined as a strategy to tune the chain length of the glass and subsequent release of VCM *in vitro*.

- Objective 1.1 - **to compare the molecular nature of precipitated CPP to that of the conventional melt-derived CPP glass**
  - *Hypothesis 1.1a: A precipitation strategy can be optimized to create a CPP with significantly greater chain length than that achieved through the conventional melt approach*

- Objective 1.2 - **to compare the *in vitro* elution of VCM from the CPP glass matrices achieved using CPP obtained from either a conventional melt approach or by the new precipitation protocol**
  - Hypothesis 1.2: A*n increase in chain length resulting from this alternative precipitation protocol will enhance the sustained delivery of VCM from the CPP-based G2 matrices*

In Chapter 4 the impact of strontium doping on the structural characteristics of CPP glass and the capacity of the CPP glass-based local delivery system to release VCM *in vitro* is examined. The cytocompatibility and VCM efficacy of the CPP glass-based local delivery system is also evaluated.

- Objective 2.1 - **to determine the impact of strontium on the powder density, chain length, and crystallization, melting and glass transition temperatures of the CPP glass**
  - *Hypothesis 2.1a: Increasing strontium doping to 10 mol% will increase the density and chain length of the CPP glass while reducing the crystallization, melting, and glass transition temperatures of the glass*
  - *Hypothesis 2.1b: The powder density, chain length, and crystallization, melting, and glass transition temperatures of the strontium-doped CPP glass will not be dependent on the type of strontium salt used in fabrication*

- Objective 2.2 - **to determine the impact of strontium doping on the gelling capacity and overall stability of CPP glass *in vitro***
  - *Hypothesis 2.2a: The addition of 10 mol% strontium to CPP will not impact the ability of this material to gel and form blank CPP-based G1 disks*
  - *Hypothesis 2.2b: The structural stability of the blank CPP-based G1 disks in vitro will be improved with strontium doping, with less ion release and greater retention of disk shape*

- *Hypothesis 2.2c: The structural stability of the blank CPP-based G1 disks in vitro will not be dependent on the type of strontium salt used in fabrication*

- Objective 2.3 - **to determine the impact of strontium doping on ion and VCM release from the CPP glass-based local delivery system**
  - *Hypothesis 2.3a: 10 mol% strontium doping will reduce the degradation of the CPP G2 matrices and release of calcium and phosphorus ions, as well as delay VCM release from the CPP-based G2 matrices in vitro*

- Objective 2.4 - **to determine the impact of strontium doping on the cytocompatibility and VCM efficacy of the CPP glass-based local delivery system**
  - *Hypothesis 2.4a: 10mol% strontium doping will not change the cytocompatibility or VCM efficacy of the therapeutically-doped CPP G2 matrices relative to test controls*

In Chapter 5, the development of a cold isostatic pressing design is highlighted as a strategy to increase matrix structural stability, modify VCM release and enhance clinical applicability.

- Objective 3.1 **– to reproducibly form therapeutically-loaded CPP beads using a novel cold isostatic pressing and gelling protocol**
  - *Hypothesis 3.1a: After removal from the CIP molds and subsequent gelling the beads will maintain their uniform and spherical shape*

- Objective 3.2 - **to determine the impact of strontium doping and G1 CPP glass particle size on the porosity and gelling ability of the CPP CIP beads**

- *Hypothesis 3.2a: A smaller overall G1 CPP glass particle size will reduce the porosity of the CPP-based beads but not impact the ability of the beads to gel*
- *Hypothesis 3.2b: 10 mol% strontium doping will not impact the porosity or gelling ability of the CPP-based beads*

- Objective 3.3 - **to determine the impact of strontium doping and G1 CPP glass particle size on ion and VCM release from the CPP CIP bead-based local delivery system *in vitro***
  - *Hypothesis 3.3a: A smaller overall G1 CPP glass particle size will delay VCM release and slow CPP CIP bead degradation.*
  - *Hypothesis 3.3b: 10 mol% strontium doping will delay CPP CIP bead degradation and VCM release in vitro.*

- Objective 3.4 - **to compare the release of VCM from the CPP G2 disk- and CPP CIP bead-based local delivery systems**
  - *Hypothesis 3.4a: CIP beads will extend the period of measurable VCM release beyond that achieved with G2 disks in vitro.*

- Objective 3.5 - **to assess the clinical feasibility of the newly designed therapeutically-loaded CPP CIP beads for supporting bone tissue recovery using an *in vitro* model**
  - *Hypothesis 3.5a: 10 mol% strontium doping will improve pre-osteoblastic cell response to bead extracts, while VCM loading will not negatively impact this same response relative to the study controls.*

The ultimate goal of this thesis work is to design a therapeutically loaded CPP-based delivery system capable of treating a bone infection by releasing an antibiotic in a controllable manner while providing therapeutic ions capable of supporting subsequent bone regeneration.

CHAPTER 3 CALCIUM POLYPHOSPHATE PRECIPITATION – A STRATEGY TO TUNE THE CHAIN LENGTH OF THE GLASS AND RELEASE OF VCM *IN VITRO*[1]

3.1 INTRODUCTION

Chain length is expected to be a key driver of CPP glass properties, with an anticipated impact on the drug delivery and matrix stability of the CPP-based system *in vitro*. In order to observe these structure-property relationships, CPP of varying average chain length was created by manipulating CPP processing parameters.

A number of different routes exist for processing calcium phosphates, including precipitation, hydrothermal, and sol-gel techniques (Salma *et al*., 2010). However, in the literature, CPP is most commonly processed using a thermal processing route in which calcium phosphate monobasic monohydrate powders are heated to a sufficient temperature to allow for polycondensation reactions prior to melting and quenching to produce an amorphous glass, with subsequent heating of the glass to obtain a crystalline form (Pilliar *et al*., 2001; Willot *et al*., 2002). Only a few studies have examined chain length as a function of furnace conditions for producing these CPP, with some contradictory results (Wu, 2012; Qiu, K.(a) *et al*., 2006; Ding *et al.*, 2008). For example, Ding *et al* (2008) reported that increasing the calcining dwell up to 10hrs at 500^0C would increase the chain length of the CPP, while Wu *et al* (2012) did not observe any linear trend (e.g. a consistent increase or decrease) in chain length when calcining

[1] Significant portions of this chapter are reported in: Comeau, P. A., and M. J. Filiaggi. "Calcium polyphosphate precipitation–A strategy to tune the chain length of the glass and control the subsequent release of vancomycin." *Materials Chemistry and Physics* (Online April 1 2015).

for the same duration and temperature. Early exploratory work on thermal manipulation of CPP chain length carried out in this thesis project revealed a decrease in chain length with calcining longer than 10hrs. This exploratory work also showed that increasing melting time from 2 to 10hrs, or increasing melting temperature from 1100^0C to 1500^0C, resulted in a decrease in CPP glass chain length. As a result of this exploratory work, and given the inherent limitations of a thermal processing route, a decision was made to pursue an alternative fabrication strategy.

Earlier reports by Masson *et al* (1997) and Sinyaev *et al* (2001) revealed that CPP could be precipitated starting with a monovalent polyphosphate in accordance with the following aqueous reaction:

$$2MPO_{3(aq)} + CaCl_{2(aq)} \rightarrow Ca(PO_3)_{2(s)} + 2MCl_{(aq)}$$

where M is a monovalent cation (e.g. Na^+). Such a precipitation strategy may be able to take advantage of the pre-existing chain structure of the starting polyphosphate reactant. NaPP, for example, has been reported to have a chain length much greater than that of the standard melt-derived CPP glass (Mehrotra, 1988). However, the extent to which the greater chain length of NaPP can be converted to that of CPP has not been previously pursued.

Precipitation studies of other calcium phosphates have indicated that a number of factors, including solution pH, temperature, the Ca/P ratio, ionic strength and concentration of the reagents, may influence the nature of the final precipitate (Salma *et al*., 2010; Chen, J. *et al*., 1996; Zauner *et al*., 2002; Benet *et al*., 2002; Montastruc *et al*., 2003). However, no studies have yet been published on the impact of these factors on *CPP* precipitation specifically. **The**

primary objective of this study was therefore to compare the molecular nature of precipitated CPP to that of the conventional melt-derived CPP glass. As part of this objective the impact of such fabrication variables as drying protocol, aqueous NaPP concentration, buffer conditions, order of reactant addition, aqueous solution mixing time, reaction temperature, Ca/P mix ratio of reactants, and impeller speed was first assessed using single-variable analysis. The first hypothesis was that *this precipitation strategy could be optimized to create a CPP with significantly greater chain length than that achieved through the conventional melt approach.*

In addition, little data exists on how such alternative strategies may be of use to further tune the performance of the therapeutically loaded amorphous CPP *in vitro*. Dion *et al* (2005a; 2005b), for example, found that increasing CPP glass exposure time to humidity from 5 hours to 24 hours resulted in a small reduction in average chain length, and a subsequent increase in the therapeutic burst release coupled with a decrease in the duration of sustained antibiotic release *in vitro*. The second objective then was **to compare the *in vitro* elution of an antibiotic from the CPP glass matrices achieved using CPP from either a conventional melt approach or by the new precipitation protocol.** As a corollary to observations noted above**,** the corresponding hypothesis here was *that an increase in chain length resulting from the alternative precipitation protocol will enhance the sustained delivery of VCM from the CPP-based G2 matrices*.

In the first section of this chapter an investigation of how nine different variables individually impact the precipitation of CPP is described, followed by a multi-variable assessment of the three principal variables that made the greatest single-variable impact on amorphous CPP chain

length. The CPP precipitate was considered optimal when it had a significantly greater chain length but similar basic chemistry to that of melt-derived CPP. Lastly, an *in vitro* elution study was performed using CPP matrices derived from these optimized precipitation conditions.

3.2 MATERIALS AND METHODS

3.2.1 Material Processing and Matrix Fabrication

3.2.1.1 Standard Melt-Derived CPP (Reference)

The standard melt-derived CPP glass, which was used as a reference in all subsequent studies, was produced following the protocol reported by Pilliar *et al* (2001). Briefly, CPMM ($Ca(H_2PO_4)_2*H_2O$) was calcined at 500°C for 10 hrs to produce CPP via a condensation reaction as shown in equation 3.1 (previously equation 1.2).

$$nCa(H_2PO_4)_2*H_2O \rightarrow [Ca(PO_3)_2]_n + 3nH_2O \qquad \textbf{[Equation 3.1]}$$

The resulting powder was then melted at 1100°C for 2 hrs and quenched in distilled water. After washing the resulting amorphous CPP frit in 100% ethanol, the frit was milled at speed 7 for 7mins using a Fritsch Planetary Mill with alumina mortars and balls, and subsequently sieved in 5min increments on an Octagon Digital sieve shaker with Laboratory Test Sieves (Fisher Scientific) to obtain <45μm particle size distribution.

3.2.1.2 CPP Precipitation

NaPP was obtained by heating sodium phosphate monobasic monohydrate in a Pt crucible at 800°C for 20 hours in a protocol similar to Strauss *et al* (1953-I). The melt was then rapidly

quenched on a copper plate and cooled to room temperature. Aqueous solutions of this NaPP were subsequently mixed with 10% (w/v) aqueous solutions of $CaCl_2*2H_2O$ in order to form a CPP precipitate (as shown in Figure 3.1).

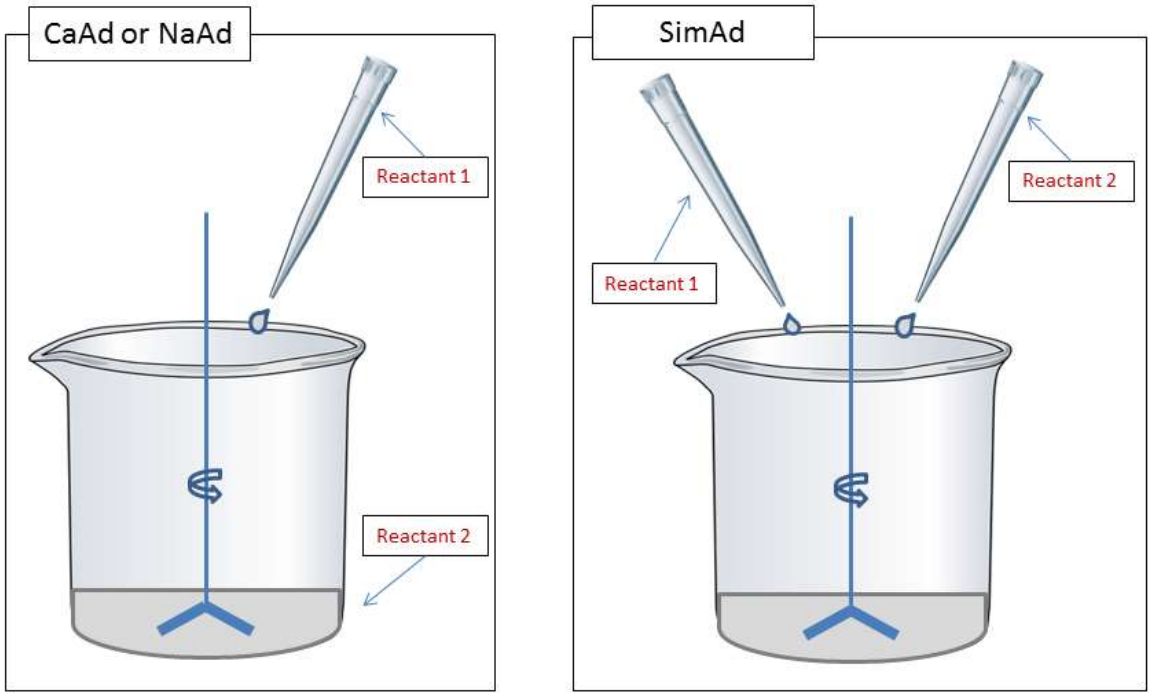

Figure 3.1: Precipitation set-up. Under 'CaAd' conditions calcium chloride was added to NaPP, while under 'NaAd' conditions NaPP was added to calcium chloride (left). Under 'SimAd' conditions (right), calcium chloride was added to the beaker at the same time as NaPP.

In accordance with the 'stirred tank' model, the reactants were added near the blade of a continuously rotating mixer impeller within a rigidly contained beaker (Benet *et al*., 2002). From available literature on phosphate precipitation (Salma *et al*., 2010; Ferguson *et al*., 1973; Kind, 2002; Chen *et al*., 1996; Zauner *et al*., 2002; Benet *et al*., 2002; Montastruc *et al*., 2003) factors that influence feed blending, such as the bulk and local concentrations of chemical species, duration of solution exposure (i.e. precipitate collection time), impeller speed, buffer conditions and order of reactant addition, may be of particular significance. In contrast, a design

variable such as drying protocol (a process following sample collection) was not expected to have as great an impact on the optimization of the final precipitate. As the CPP precipitate dries the water that still remains continues to hydrolyze the polyphosphate species into calcium mono- and diphosphate at a rate directly proportional to temperature (Sinyaev et al., 2001; Huffman et al., 1960). The drying condition that produces the *smallest* decrease in chain length will be recommended for further study. The variables evaluated, including the defined levels for each variable, are detailed in Table 3.1. The different levels for each variable are represented accordingly as Level 1 (L1), Level 2 (L2), Level 3 (L3), and Level 4 (L4).

Table 3.1: Variables considered in single-variable precipitation of CPP.

Single Variable	Values Studied
Reactant Order	L1: $CaCl_{2(aq)}$ added to $NaPP_{(aq)}$ ("CaAd"), **L2: $NaPP_{(aq)}$ added to $CaCl_{2(aq)}$ ("NaAd"),** L3: $CaCl_{2(aq)}$ and $NaPP_{(aq)}$ added simultaneously ("SimAd")
NaPP Concentration	L1: 0.1%, L2: 1%, L3: 5%, **L4: 10%**
Drying Protocol	L1: Oven Dried, **L2: Freeze Dried**, L3: Room Temperature Dried
Buffer Presence	**L1: No**, L2: Yes
Precipitate Collection Time	**L1: 2min**, L2: 40min
Reaction Temperature	L1: 5°C, **L2: 20°C**
Pre-Dry Technique*	L1: None, **L2: EtOH rinse**, L3: liquid N_2 rinse
Impeller Speed**	**L1: 190rpm**, L2: 800rpm
Ca/P Mix Ratio of Reactants**	L1: 0.5, **L2: 1.0**

*Note 1: Levels in **Bold Font** Represent Standard Precipitation Conditions (i.e. Conditions Kept Constant Unless Varied for Study).*
*Note 2: *Indicative of Variables Studied With 5 ^{0}C Reaction Temperature Conditions.*
*Note 3: **Indicative of Variables Studied With 'SimAd' Reactant Order Conditions.*

Unless otherwise varied, *standard* precipitation conditions consisted of addition of unbuffered 10% (w/v) $NaPP_{(aq)}$ to a 10% (w/v) $CaCl_2*2H_2O_{(aq)}$ maintained at 20°C and stirred at a continuous speed of 190rpm to closely resemble prior precipitation studies (Umegaki *et al*.,

1975; Umegaki *et al*., 1976; Sinyaev *et al*., 2001). The Ca/P mix ratio of the two reactants was kept at 1.0 in accordance with the concern reported by Sinyaev *et al* (2001) that excess calcium is necessary to encourage the reaction. After no further precipitation from solution was observed (which occurred after approximately 2 mins), the precipitate was rinsed three times with cold distilled water in order to remove as much of the co-precipitated chlorides as possible (Sinyaev *et al*., 2001) and stored in ethanol (Pfanstiel *et al*., 1956) for a minimum of 30 minutes prior to transfer of the samples to fresh tubes. Samples were frozen overnight (-18°C) before proceeding with freeze drying (Labconco® Freeze Dry System) for a minimum of 48hrs until the change in weight loss was less than 1% of total sample weight. Collected samples were then milled and sieved similar to melt-derived CPP glass to obtain a <45μm particle size distribution.

Previous reports on calcium phosphate precipitation have suggested that a pH near 8 would improve the degree to which phosphate reacted and remained within the precipitate (Ferguson *et al*., 1973), as well as create an amorphous calcium phosphate (Amjad *et al*., 2002). A further consideration in choosing the pH level to be maintained was the impact of acidity on chain length. It is believed that a very acidic pH destabilizes the chain structure (Willot *et al*., 2002; Gupta *et al*., 1995). As a result, when the precipitation reaction was buffered a pH of 8 was maintained. 0.2M tetramethylammonium hydroxide (TMA) was chosen as the buffer as it has been found to not associate as strongly to polyphosphates as metal ions, and was therefore not expected to interfere with the composition of the resulting precipitate (Strauss *et al*., 1957; Strauss *et al*., 1959).

The goal in fabricating CPP glass from the NaPP was to achieve a greater chain length than the melt-derived CPP but still maintain its basic chemistry. To this end, the primary design condition was a greater chain length, while secondary design constraints were met by a precipitate with a Ca/P molar ratio close to 0.50 and as low of a residual sodium content as possible. All precipitates were therefore assessed for chain length, Ca/P ratio, and residual sodium content.

From the analysis of the nine fabrication variables indicated in Table 3.1, the three variables having the greatest capacity to increase chain length while maintaining low residual sodium and Ca/P molar stoichiometry were further studied in a multi-variable design across two levels for each variable. This multi-variable analysis included evaluation of any interaction effects as well as additional structural and functional analysis of the resulting material not observed in single-variable analysis.

3.2.1.3 CPP Matrices

Based on this multi-variable analysis, the precipitation condition that best met the design criteria was further evaluated against the melt-derived CPP for drug loading and subsequent *in vitro* elution of the antibiotic VCM. VCM – loaded CPP disks were fabricated following the protocol reported by Petrone *et al* (2008) and shown in Figure 3.2. Briefly, distilled water with or without VCM was added to CPP powder in a ratio of 150mg CPP: 0.0602mL distilled water: 7.5mg VCM, and mixed well. The resulting paste was transferred into disk-shaped polyvinylsiloxane molds until flush with the top surface, then placed in a sealed vessel containing water at 37°C in order keep the samples at ~100% relative humidity. After 2 hrs the samples were removed from humidity and left to dry at 37°C in atmospheric air for a minimum of 24 hrs. The resulting "G1"

disks were milled and sieved to obtain <45μm G1 powders. Roughly 135mg of this G1 powder was placed in individual 8mm diameter chambers of a punch-die system and a 113MPa stress applied for 5 mins with a Carver manual, 25 ton, 2-column hydraulic press. The compacted G1 powder was placed in a sealed vessel maintained at 37°C and ~100% relative humidity for an additional gelling time of 3 hrs prior to drying. These final "G2" disks were then used in the *in vitro* elution study.

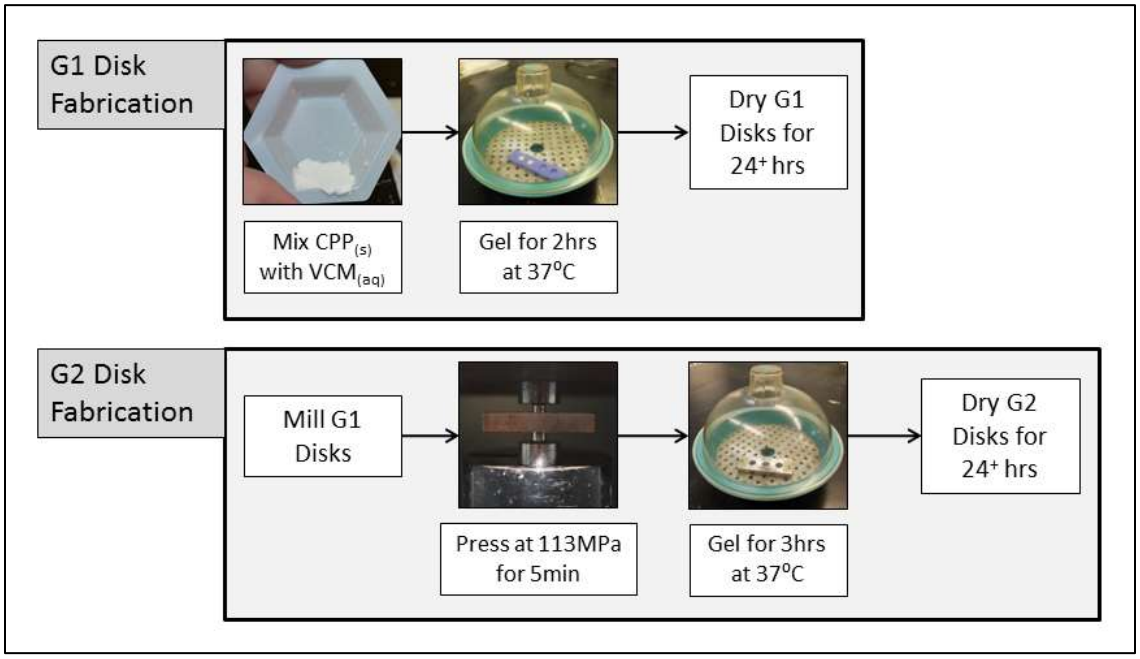

Figure 3.2: Schematic of G2 disk fabrication consisting of two different stages.

3.2.2 Material Characterization

3.2.2.1 CPP Powder

The composition of the CPP powder was confirmed after dissolution in an equi-volume mixture of 6N $HCl_{(aq)}$ and 15N $HNO_{3(aq)}$ at 80^0C for 12hrs followed by assessment with Inductively Coupled Plasma-Optical Emission Spectroscopy (ICP-OES) (PerkinElmer Optima8000). Calcium, phosphorus, and sodium were measured at wavelengths of 317.933nm, 213.617nm, and

589.592nm, respectively, and reported in units of ppm (i.e. mg/L). The molar Ca/P ratio and % residual Na was then calculated.

To determine chain length of the starting soluble NaPP, acid-base titration was used to obtain the number-average value in accordance with Mehrotra [1988]. Here, 10% (w/v) NaPP solutions were mixed until all material was dissolved before diluting by a further factor of 2. Using 0.1M $HCl_{(aq)}$ the pH of the NaPP solution was dropped below 4.5. Next, 1.0M $NaOH_{(aq)}$ was added in 2.5 µL increments until a pH above 9.5 was achieved. Chain length (n) was determined from the volume necessary to go from a pH at the early inflection point (a pH of ~4.5) to the latter inflection point (a pH of ~9.0) in accordance with Equation 3.2 [Mehrotra, 1988];

$$n = \frac{2000*(weight\ of\ polymer\ dissolved\ in\ solution)}{(Molecular\ Weight)*(Volume\ of\ NaOH\ between\ inflections)} \qquad \textbf{[Equation 3.2]}$$

Average chain lengths (n_{ave}) of the melt-derived CPP samples were analyzed by both solid-state and liquid-state ^{31}P NMR experiments. Solid-state NMR was performed using a Bruker Avance NMR spectrometer with a 9.4T magnet (162.02 MHz ^{31}P Larmor frequency) and 2.5 mm diameter rotors (as shown in Figure 3.3).

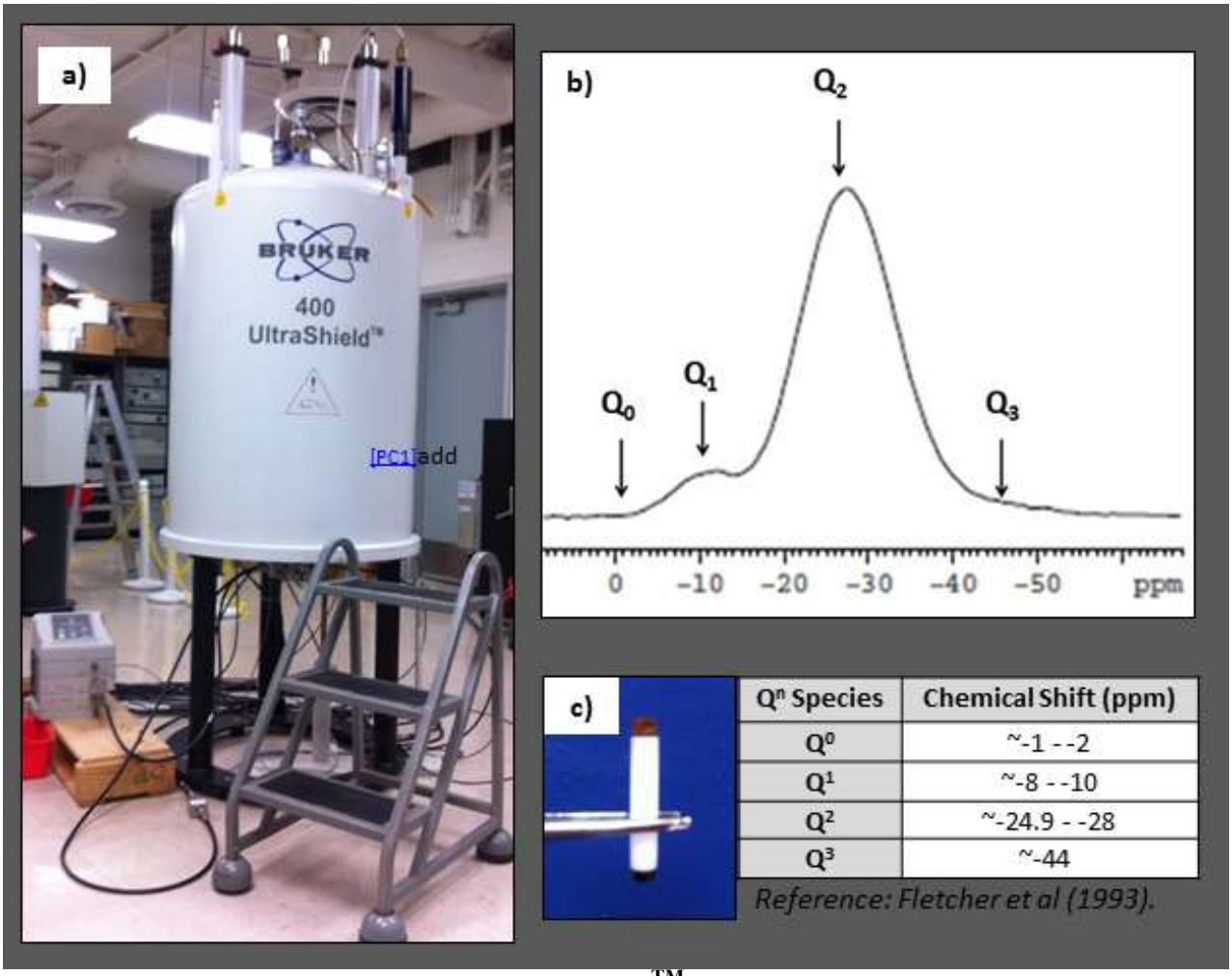

Figure 3.3: (a) Solid state NMR 400 UltraShield™, (b) NMR spectra of a reference melt-derived CPP, (c) 2.5mm ID NMR rotor, table of Q^n species and expected chemical shifts.

The ^{31}P NMR chemical shift scale was referenced externally against $NH_4H_2PO_3$ at 0.81ppm as a secondary reference. For these spectra, the samples were spun at 25.0 kHz. In addition, liquid-state ^{31}P NMR was carried out on samples dissolved in 200mM disodium ethylenediaminetetraacetate dehydrate (Na_2-EDTA) using a Bruker AV500 MHz NMR spectrometer. Spectra are reported using an 85% solution of H_3PO_4 in H_2O as a reference. For liquid state NMR the Q^2 peaks can be resolved into linear (polyphosphate) and ring (metaphosphate) structure chemical shifts at ~-20ppm and ~-22ppm, respectively (Dion et al., 2005a).

Line shape simulations were subsequently performed using DMFit 2010 Software for each phosphorus species shown in Figure 2.1 (i.e. Q^1, Q^2, Q^3). The integrated peak areas (%) for each species were subsequently entered into Equation 3.3, adapted from Kulaev *et al*. (2005) to include the Q^3 term when calculating average chain length (n_{ave}):

$$n_{ave} = \frac{2*[Q^1+Q^2+Q^3]}{[Q^1-Q^3]} \qquad \textbf{[Equation 3.3]}$$

The percentage deviation for chain length and Ca/P molar ratio of the precipitated CPP relative to the melt-derived CPP reference was calculated as "(precipitate value – reference)/reference".

Precipitated CPP samples resulting from the multi-variable assessment were further characterized by thermal analysis using simultaneous differential scanning calorimetry (DSC) and thermogravimetric analysis (TGA) (Netzsch Luxx 409 PC), and Attenuated Total Reflectance – Fourier Transform Infrared spectroscopy (ATR-FTIR) (Tensor 27, Bruker) with OPUS-7.2 (Bruker) software to further elucidate structural characteristics. The DSC/TGA instrument was controlled by an external PC using the software package provided by Netzsch (Netzsch STA 409PC). Approximately 20-30mg of each powder sample was placed in covered Pt crucibles before placing the crucible on the sample holder within the DSC/TGA unit. Samples were heated at a rate of 10K/min from 20°C to 1100^0C in a Pt pan. A constant flow of N_2 gas was blown over all samples for the duration of the experiment in order to maintain an inert environment. The TGA curves were analyzed for mass loss using the software package Proteus Thermal Analysis 4.8.4. For ATR-FTIR analysis, the background spectrum was first collected

with no sample powder present on the crystal. Material was then added on the ATR crystal surface and the unit arm pressed into place to create good contact between the powder and crystal surface. The functional groups were analyzed with a series of 200 scans run from 4000 to 700cm^{-1} at a resolution of 1cm^{-1}. The crystal surface was cleaned between each sample with ethanol and tissue paper (KIMTECH Sciences). The average of the recorded absorbance for each wavelength during the scans was presented in this document.

3.2.2.2 CPP Matrices

To determine the amount of VCM successfully loaded, G1 powder was dissolved in 200mM Na_2-EDTA and the VCM in the Na_2-EDTA measured using an ultraviolet-visible spectrophotometer (UV-Vis) (BioTek Instruments Synergy HT) at a wavelength of 280nm. VCM loading efficiency (L_{eff}) was then calculated as per Equation 3.4:

$$L_{eff}(\%) = \frac{VCM\ measured\ from\ disk\ dissolved\ in\ Disodium\ EDTA}{VCM\ available\ for\ loading\ during\ disk\ fabrication}\ x\ 100\% \qquad \textbf{[Equation 3.4]}$$

For the *in vitro* elution study, 15mL of 0.1M *tris*-buffered saline (TBS) was added to each G2 disk within a 20mL glass vial on a horizontally rotating plate at 100rpm and kept at 37°C. At established time points over a span of 15 days, 7mL of elution media was removed for measurement of the release of VCM, calcium, and phosphate. A fresh 7mL of elution media was then added to each disk to maintain the elution volume. Phosphate and calcium release were analyzed as previously reported (see 3.2.2.1). VCM release was measured using a UV-Vis (BioTek Instruments Synergy HT) at a wavelength of 280nm, with the measured absorbance of blank samples subtracted from that of the VCM-containing samples in order to compensate for

any potential interference of calcium and phosphorus ions in the media with VCM detection. Adjustments were also made for the VCM and ion concentrations present at the previous time point and taking into consideration the dilution of the sample upon addition of fresh TBS at each time point. Images of the disks were captured with a Nikon D3100 camera.

3.2.3 Statistics

A power analysis was initially performed in order to estimate the required sample size for detection of reasonable departures from the null hypothesis. Based on preliminary studies a sample size of 3 in single-variable analysis of CPP precipitates was found to be sufficient, while in multi-variable (and dual-level) analysis a sample size of 4 was required for a power greater than 95%. Elution studies designed to match prior work (Petrone *et al*., 2008) sought a power greater than 98% and required a sample size of 6.

Differences in means of study outcomes were analyzed using Minitab15.0, a statistics software program, and either a one-way analysis of variance (for single-variable study, elution study) or a 3-factor modified general linear model (for multi-variable study) was used with a significance value of $p=0.05$. In addition a post-hoc pairwise Tukey analysis was performed. Lastly, study outcomes were compared with Pearson correlation to determine any significantly related trends ($p<0.05$).

3.3 RESULTS

There are few reports on the precipitation of CPP from a monovalent polyphosphate such as NaPP (Masson *et al*., 1997; Sinyaev *et al*., 2001; Umegaki *et al*., 1975). In particular, the extent

to which the greater chain length of NaPP can be converted to that of CPP has not been previously pursued. Here we sought to elucidate what key precipitation parameters, including some of their potential interactions, most significantly contributed to increasing chain length of the precipitated CPP while achieving the expected chemical composition of this material (i.e. $Ca(PO_3)_2$). Indicators of the success of this approach were increased chain length, a Ca/P ratio of precipitate of approximately 0.50, and residual sodium levels approaching 0 mol%.

3.3.1 Melt-Derived CPP

Figure 3.4 depicts a fitted ^{31}P MAS NMR curve for CPP obtained using the furnace protocol previously established by Pilliar *et al* (2001). This sample will serve as the reference in all subsequent precipitation results presented here.

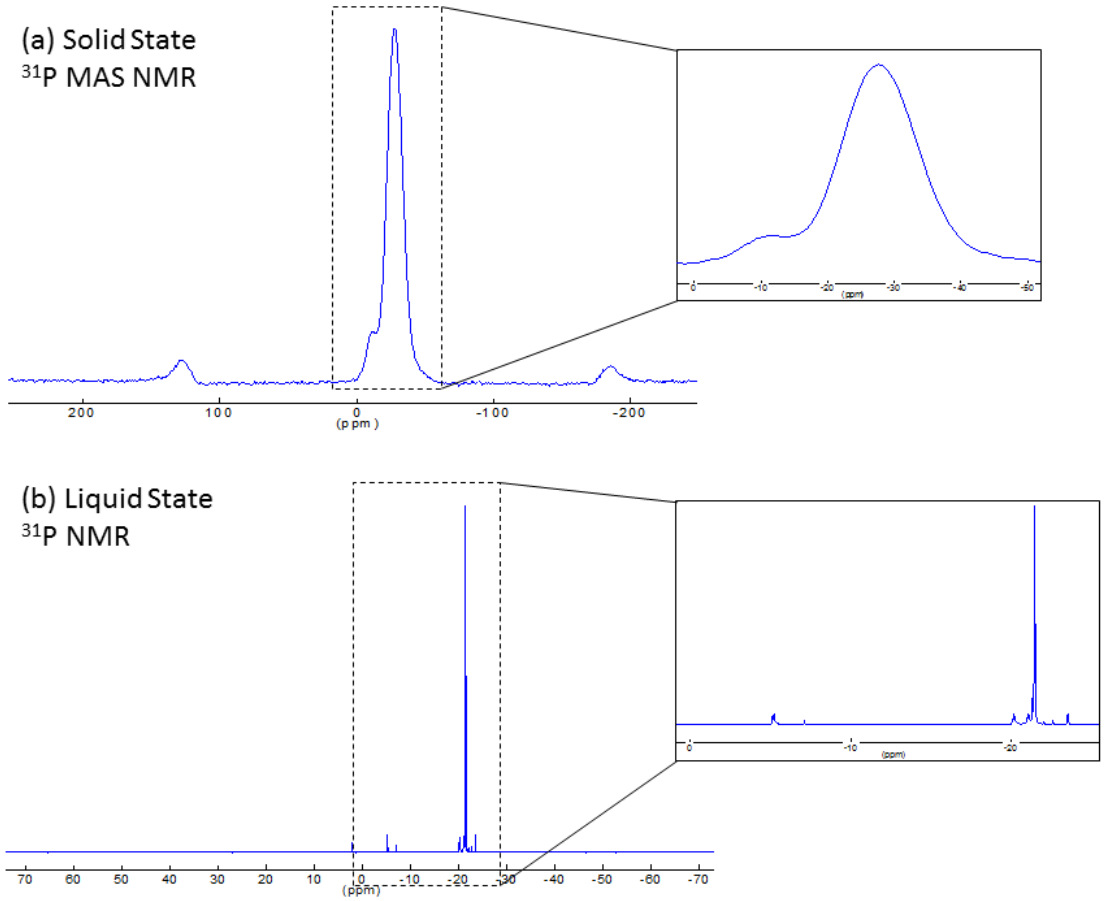

Figure 3.4: (a) Solid state MAS and (b) Liquid state ^{31}P NMR of melt-derived CPP. Note that NMR plots will be shown as the zoomed-in image for the rest of this document.

The average chain length of the CPP reference was found to be 52±3 and 19±1 using solid state and liquid ^{31}P NMR, respectively; both measurements are comparable to previous reports (Filiaggi *et al*., 2011; Dion *et al*., 2005; Petrone *et al*., 2008). As shown in Figure 3.4 solid state NMR profiles are much broader than those acquired using liquid NMR. In mobile fluids the nuclei isotropic motions are more rapid and the anisotropic interactions average such that they are removed from the spectrum – but this does not occur naturally in solid state NMR (Andrew *et al*., 1981). To best improve the resolution of solid state NMR, current commercial equipment (such as that used in this work) includes a magic angle spinning facility in order to impose an

improved spin on the nuclei within the solid and better match liquid profile resolution (Andrew *et al*., 1981). There still remains a noticeable difference in the two types of NMR spectra, but in each case most of the phosphorus atoms could be found in the Q^2 position. This difference is attributed to the additional sample preparation steps of liquid compared to solid state NMR. In liquid NMR the CPP samples are dissolved in in Na_2-$EDTA_{(aq)}$; some chain lysis is likely observed as a result of aqueous exposure prior to measurement. ICP analysis confirmed a nominal Ca/P molar ratio of 0.50 for the melt-derived CPP.

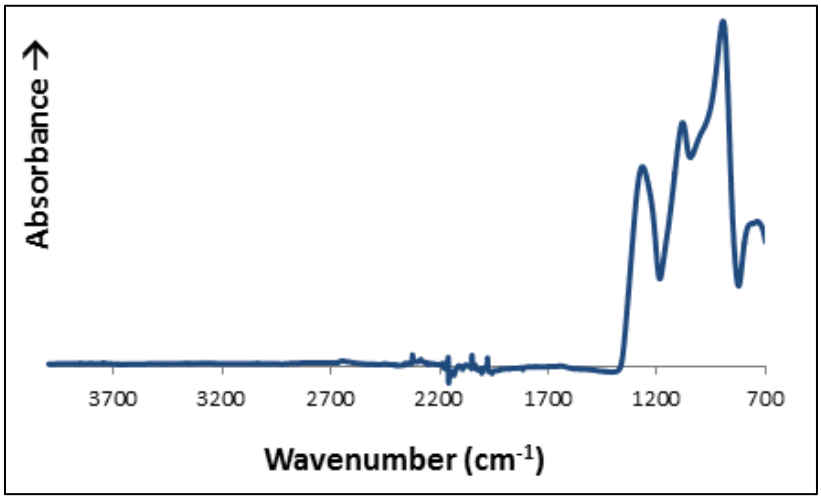

Figure 3.5: ATR-FTIR spectrum of melt-derived CPP powder.

The ATR-FTIR profile for melt-derived CPP (Figure 3.5) closely matched that previously reported for amorphous CPP (Jackson *et al*., 2005). The band in the region 850-920cm^{-1} can be assigned to the antisymmetric stretching vibration of the P-O-P bonds. Similarly, the band in the region 1080-1110cm^{-1} can be assigned to the symmetric stretching vibration of the bridging PO_2, with an additional band in the 1230-1270cm^{-1} region reflecting antisymmetric stretching of these same bridging PO_2. The band in 940-1020cm^{-1}, though not as strong as the others previously mentioned, can be attributed to symmetric PO_3 stretching vibration.

Figure 3.6 shows the thermal analysis profile of melt-derived CPP.

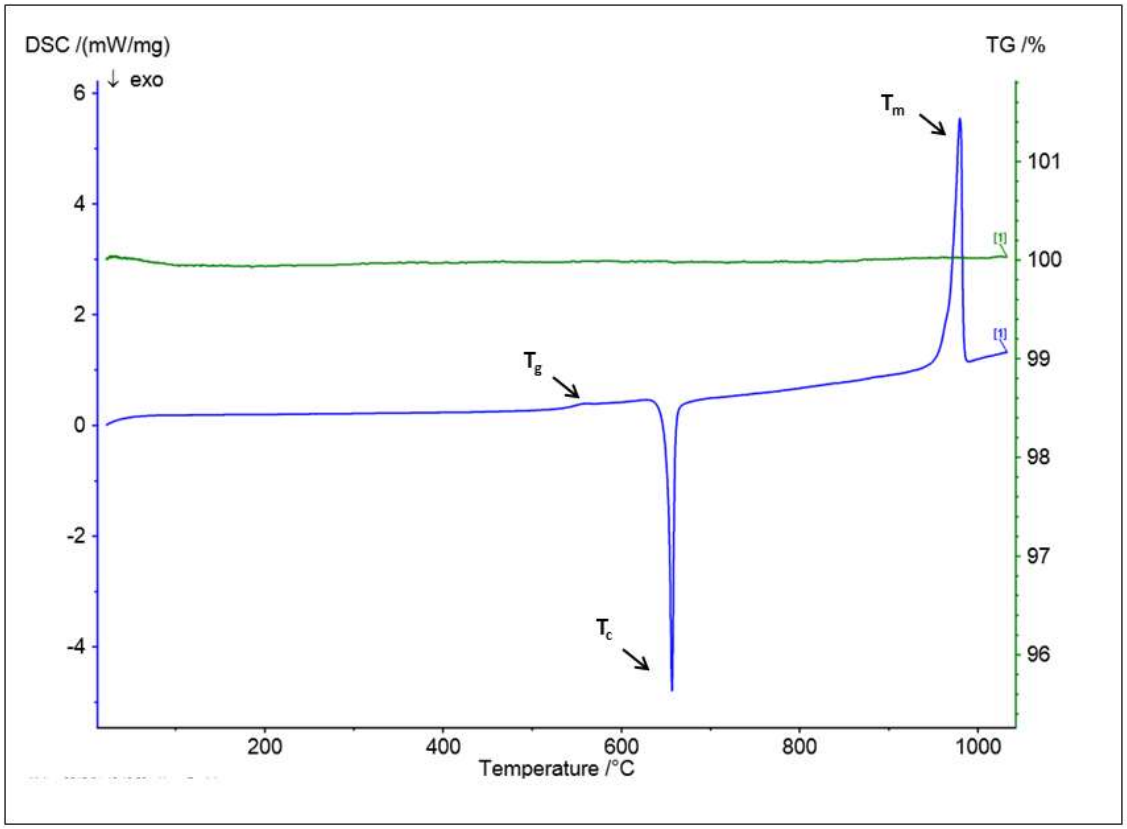

Figure 3.6: DSC (blue line) and TG (green line) of melt-derived CPP.

A glass transition temperature (T_g) of ~540^{0}C, a crystallization temperature (T_c) of 652^{0}C, and a melting temperature (T_m) of 969^{0}C for this melt-derived CPP closely match those previously reported for this glass (Wang, K. *et al*., 2008). TGA also confirmed that following thermal processing no significant amount of water remained and the polycondensation should be largely complete (i.e. no further weight loss occurs upon heating glass samples during thermal analysis).

3.3.2 Precipitated CPP

The average chain length of the starting aqueous NaPP solution to be used in all precipitation studies was found to be 219±14 (n=4). Figure 3.7 shows an acid-base titration profile of one of the NaPP melts.

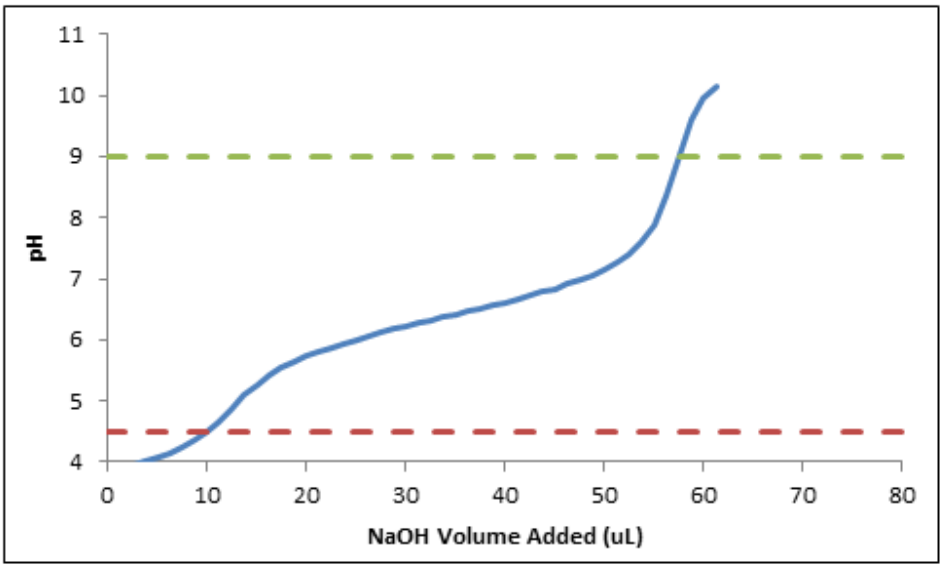

Figure 3.7: Acid-base titration profile of a NaPP melt prior to reacting with $CaCl_{2(aq)}$ to precipitate CPP.

Figures 3.8 to 3.16 show the solid state ^{31}P MAS NMR profiles, chain length, Ca/P molar ratio, and residual sodium for each precipitate in accordance with the different precipitation factors studied.

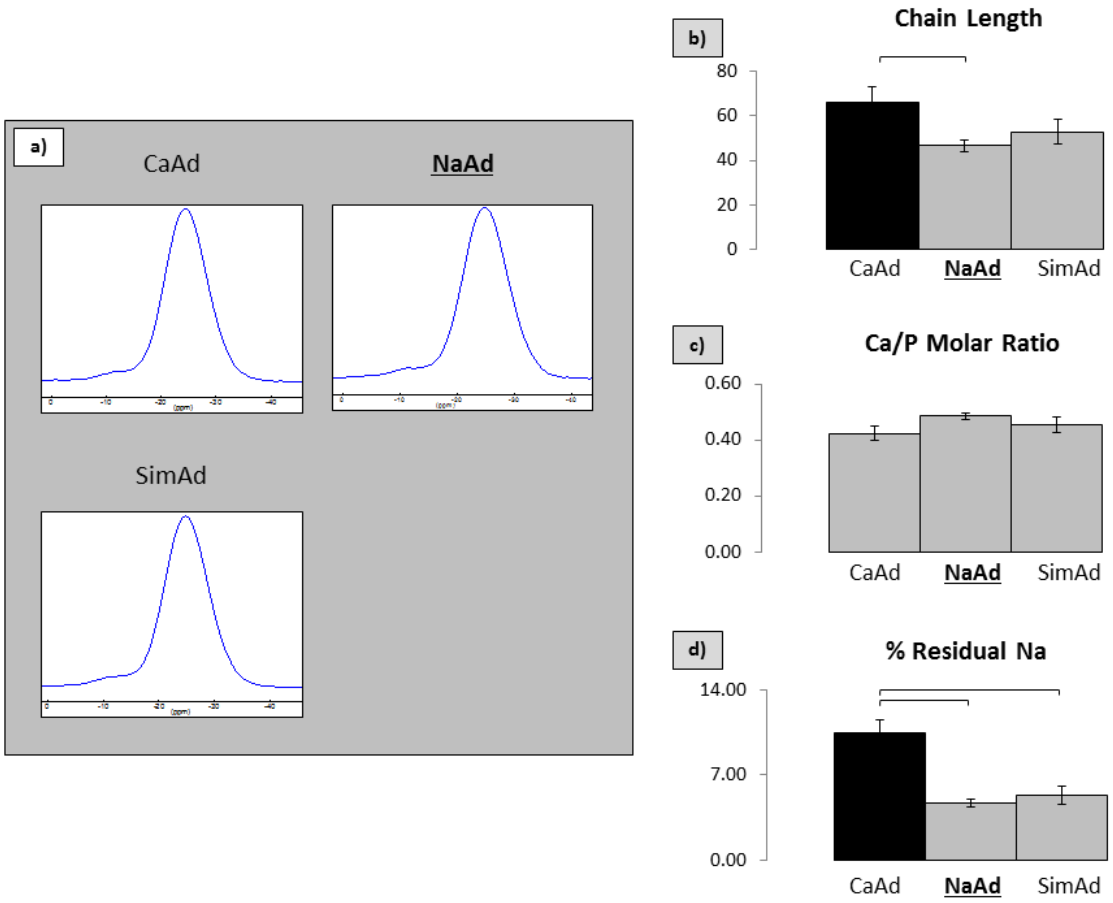

Figure 3.8: (a) Solid state ^{31}P NMR profiles, (b) Chain length, (c) Ca/P molar ratios, (d) Residual Na for precipitation carried out under different reactant order conditions. Values reported as average ± one standard deviation. Horizontal bars represent significant difference ($p<0.05$) (n=4). Standard condition in this subset of data is labelled "NaAd"; Black column indicates a significantly greater value and a white column significantly lower value, while a grey column is not significantly different relative to standard condition ($p<0.05$).

In precipitating CPP under the "CaAd" condition both the chain length and residual sodium of the precipitate was significantly increased ($p<0.05$) compared to the other reactant order conditions. The Ca/P molar ratio of the collected precipitates was not significantly impacted by reactant addition order.

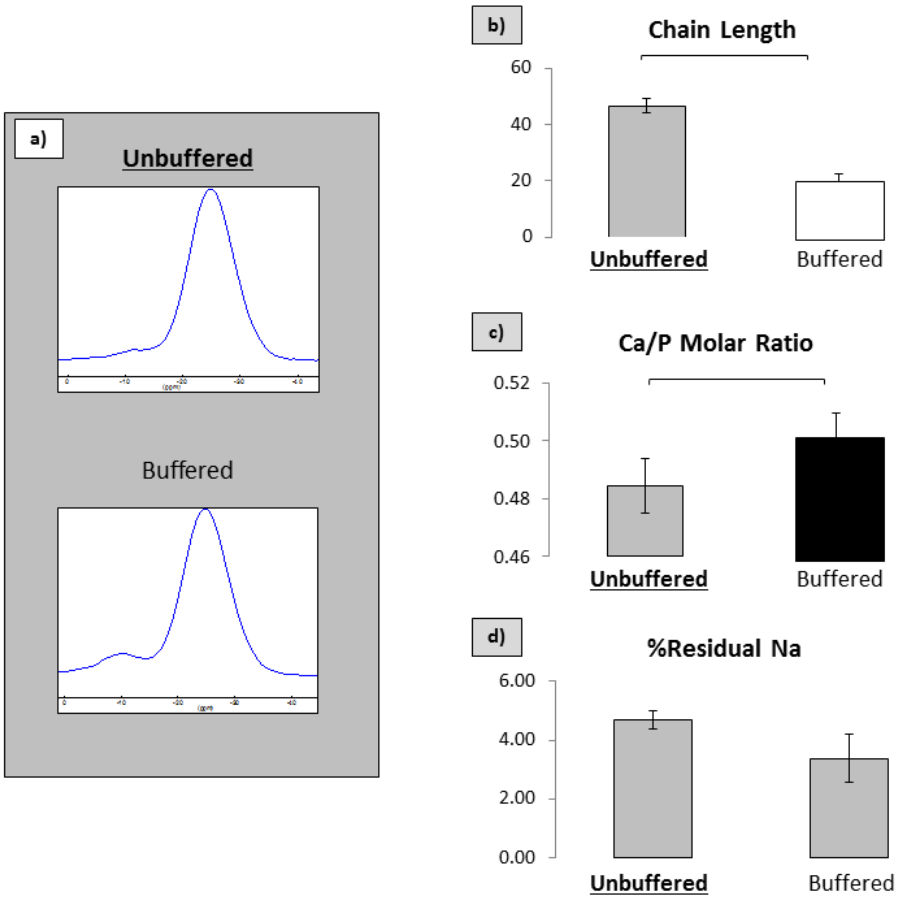

Figure 3.9: (a) Solid state ^{31}P NMR profiles, (b) Chain length, (c) Ca/P molar ratios, (d) Residual Na for precipitation carried out with and without buffering. Values reported as average ± one standard deviation. Horizontal bars represent significant difference ($p<0.05$) ($n=4$). Standard condition in this subset of data is labelled "Unbuffered"; Black column indicates a significantly greater value and a white column significantly lower value, while a grey column is not significantly different relative to standard condition ($p<0.05$).

As shown in Figure 3.9, the use of a buffer increased the proportion of end-phosphate (Q^1) groups present compared to middle-phosphate (Q^2) groups, with a significant drop in chain length ($p<0.05$). In addition, a higher Ca/P molar ratio with correspondingly lower residual sodium was achieved under these buffered conditions.

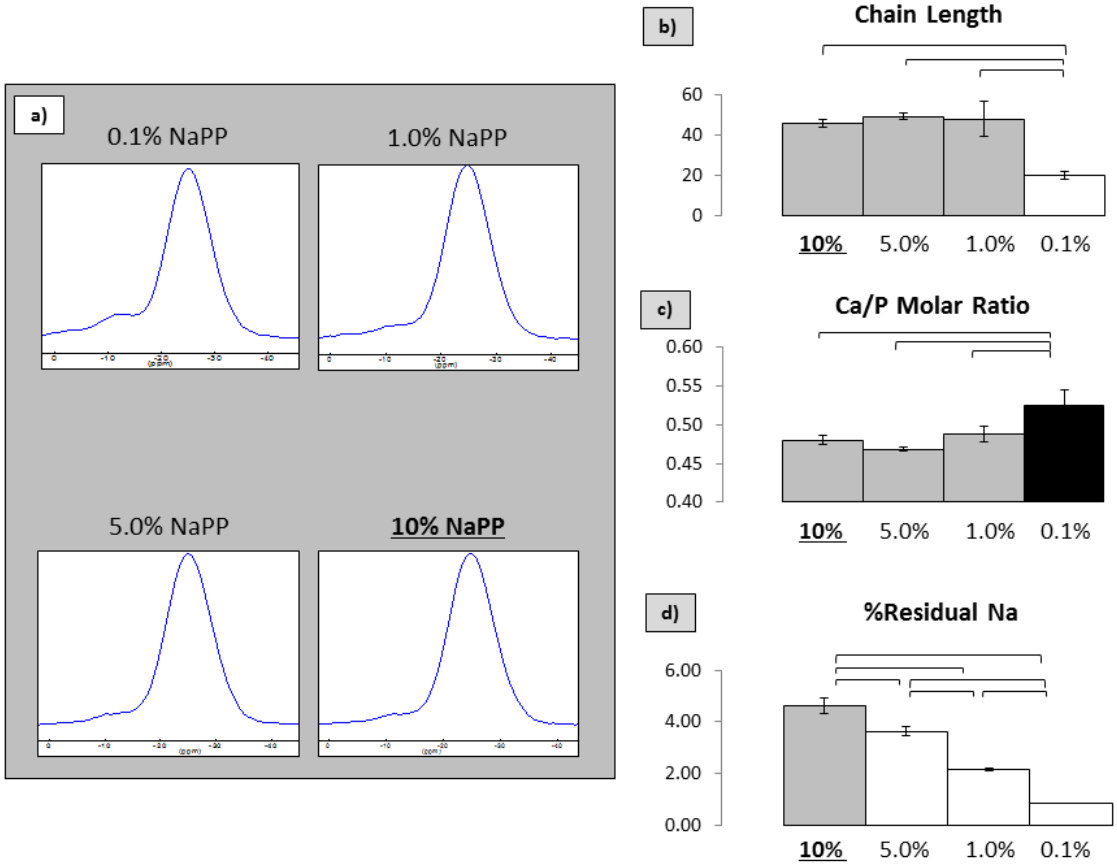

Figure 3.10: (a) Solid state ^{31}P NMR profiles, (b) Chain length, (c) Ca/P molar ratios, (d) Residual Na for precipitation carried out using different $NaPP_{(aq)}$ concentrations. Values reported as average ± one standard deviation. Horizontal bars represent significant difference ($p<0.05$) (n=3). Standard condition in this subset of data is labelled "10% NaPP"; Black column indicates a significantly greater value and a white column significantly lower value, while a grey column is not significantly different relative to standard condition ($p<0.05$).

Overall, the NMR profiles for 1.0, 5.0, and 10% NaPP were not significantly different (Figure 3.10). However, decreasing NaPP concentration even further to 0.1% NaPP resulted in an increase in the relative proportion of Q^1 species present and a significantly lower average chain length than the other sample groups ($p<0.05$). A significantly lower residual sodium level ($p<0.05$) and higher Ca/P molar ratio ($p<0.05$) were also obtained at this low concentration compared to the other groups, which yielded Ca/P molar ratio values closer to the reference CPP.

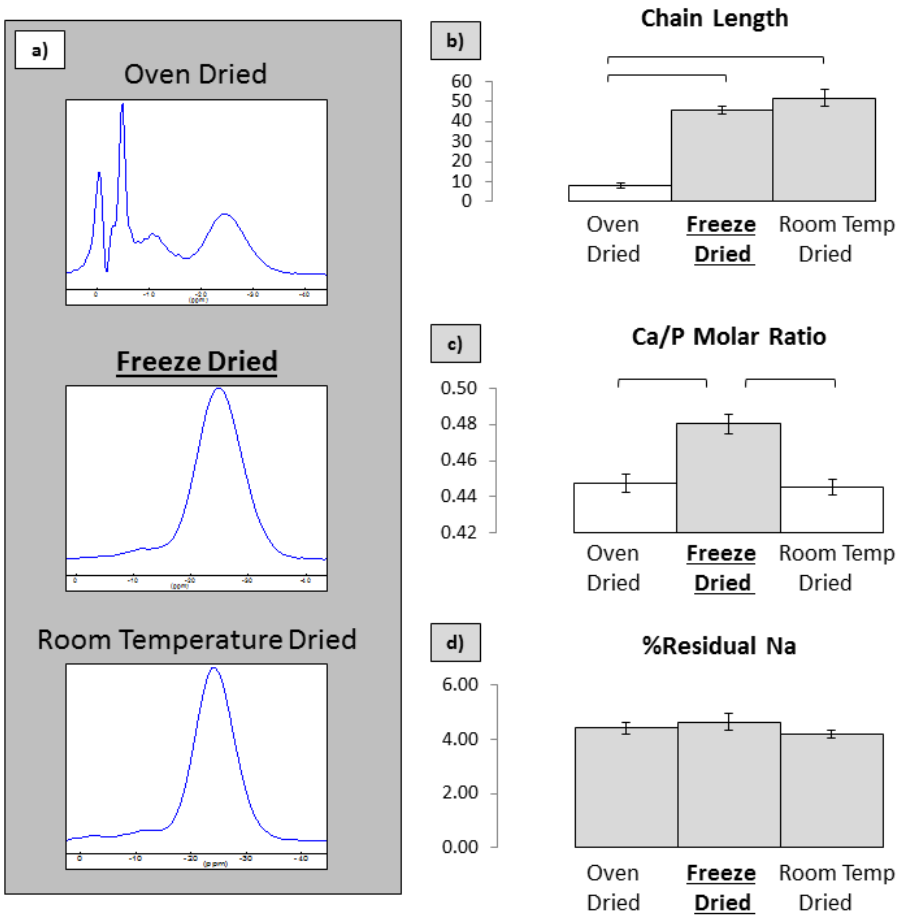

Figure 3.11: (a) Solid state ^{31}P NMR profiles, (b) Chain length, (c) Ca/P molar ratios, (d) Residual Na for precipitates exposed to different drying conditions. Values reported as average ± one standard deviation. Horizontal bars represent significant difference ($p<0.05$) (n=3). Standard condition in this subset of data is labelled "Freeze Dried"; Black column indicates a significantly greater value and a white column significantly lower value, while a grey column is not significantly different relative to standard condition ($p<0.05$).

Freeze drying and room temperature drying of the precipitates yielded similar NMR profiles and resultant chain lengths (Figure 3.11). However, oven drying the precipitates resulted in a significant proportion of Q^0, and Q^1 species present in the precipitate, with a corresponding drop in Q^2 species. Freeze dried precipitates also had a significantly higher Ca/P molar ratio ($p<0.05$) than for those exposed to other drying conditions.

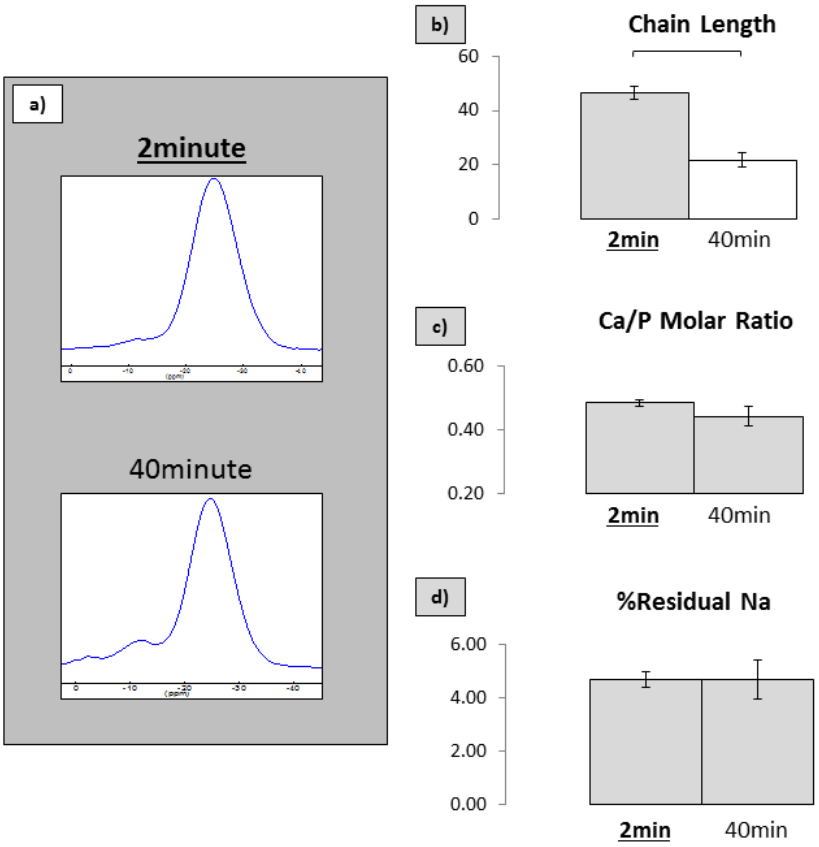

Figure 3.12: (a) Solid state ^{31}P NMR profiles, (b) Chain length, (c) Ca/P molar ratios, (d) Residual Na for precipitates collected after 2 or 40minutes in an aqueous environment. Values reported as average ± one standard deviation. Horizontal bars represent significant difference ($p<0.05$) (n=4). Standard condition in this subset of data is "2min"; Black column indicates a significantly greater value and a white column significantly lower value, while a grey column is not significantly different relative to standard condition ($p<0.05$).

Increasing the precipitate collection time from 2 to 40mins prior to drying resulted in a significant increase in the proportion of Q^1 species and a resultant drop in chain length ($p<0.05$). However, having the precipitate spend an additional 38mins in the aqueous environment did not significantly impact the Ca/P molar ratio or residual sodium of the resulting precipitates.

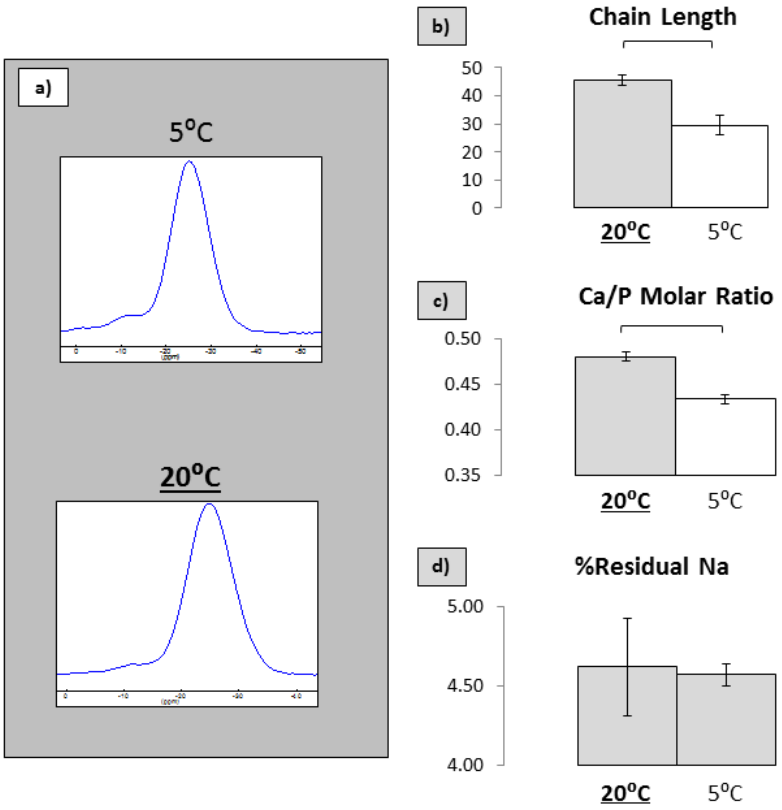

Figure 3.13: (a) Solid state ^{31}P NMR profiles, (b) Chain length, (c) Ca/P molar ratios, (d) Residual Na for precipitated at either 5°C or 20°C. Values reported as average ± one standard deviation. Horizontal bars represent significant difference ($p<0.05$) (n=3). Standard condition in this subset of data is labelled "20^{0}C"; Black column indicates a significantly greater value and a white column significantly lower value, while a grey column is not significantly different relative to standard condition ($p<0.05$).

A lower reaction temperature resulted in a significant 30% decrease in chain length ($p<0.05$) (as measured with solid state ^{31}P NMR), with a corresponding significant decrease in the Ca/P molar ratio ($p<0.05$).

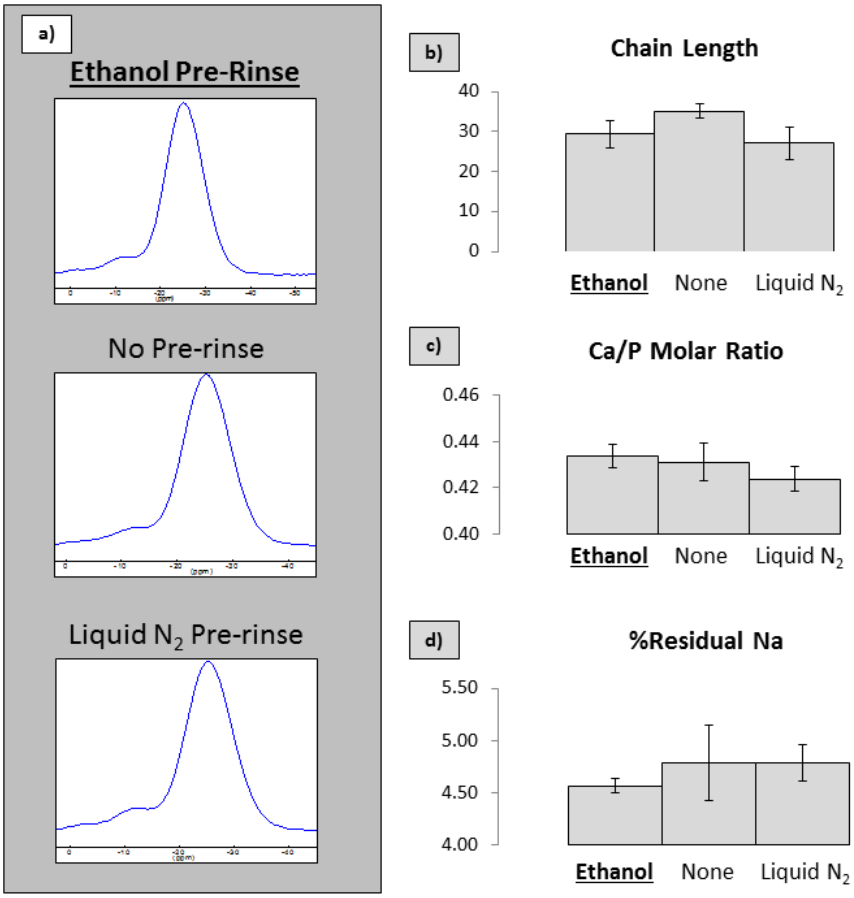

Figure 3.14: (a) Solid state ^{31}P NMR profiles, (b) Chain length, (c) Ca/P molar ratios, (d) Residual Na for precipitates exposed to different pre-drying conditions. Values reported as average ± one standard deviation. Horizontal bars represent significant difference ($p<0.05$) ($n=3$). Note that this set of sample was collected at 5^{0}C (not 20^{0}C). Standard condition in this subset of data is labelled "Ethanol Pre-Rinse"; Black column indicates a significantly greater value and a white column significantly lower value, while a grey column is not significantly different relative to standard condition ($p<0.05$).

The conditions for pre-drying the precipitates prior to final drying did not have a significant impact on chain length, Ca/P molar ratio, and residual sodium of the precipitate. It is important to note that for this variable the reaction temperature was kept at 5°C. After pre-drying all precipitates underwent the same final freeze-drying steps; the reported chain length, Ca/P molar ratio, and residual Na are for the final, dried products.

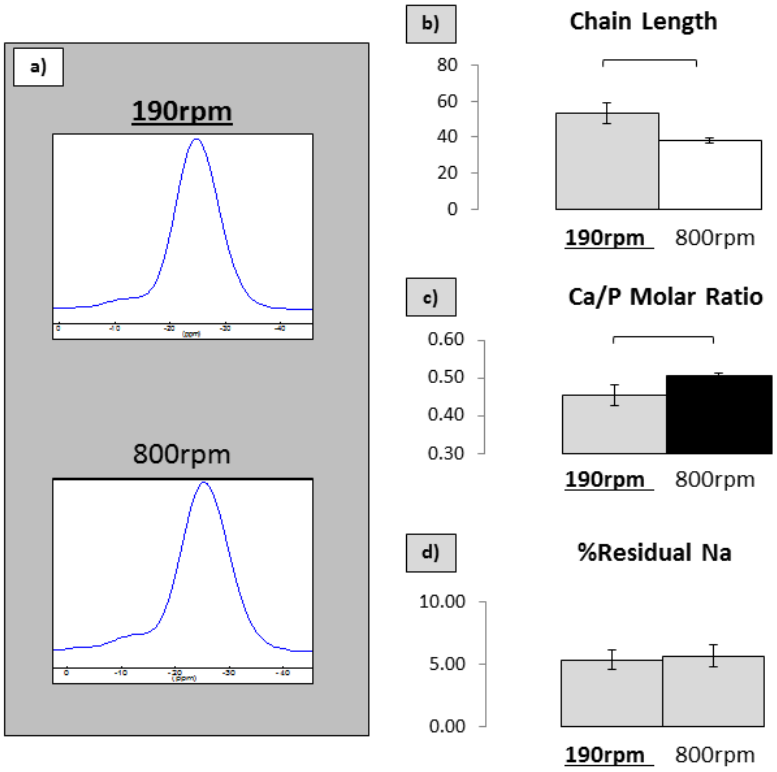

Figure 3.15: (a) Solid state ^{31}P NMR profiles, (b) Chain length, (c) Ca/P molar ratios, (d) Residual Na for precipitation carried out with an impeller speed of 190rpm or 800rpm. Values reported as average ± one standard deviation. Horizontal bars represent significant difference ($p<0.05$) (n=4). Note that this set of sample was precipitated under SimAd conditions (not NaAd). Standard condition in this subset of data is labelled "190rpm"; Black column indicates a significantly greater value and a white column significantly lower value, while a grey column is not significantly different relative to standard condition ($p<0.05$).

The chain length decreased significantly ($p<0.05$) when the impeller speed was increased from 190 to 800rpm. However, increasing impeller speed also brought the Ca/P molar ratio significantly closer to 0.50. The residual sodium content of the precipitates was not significantly impacted by the impeller speed.

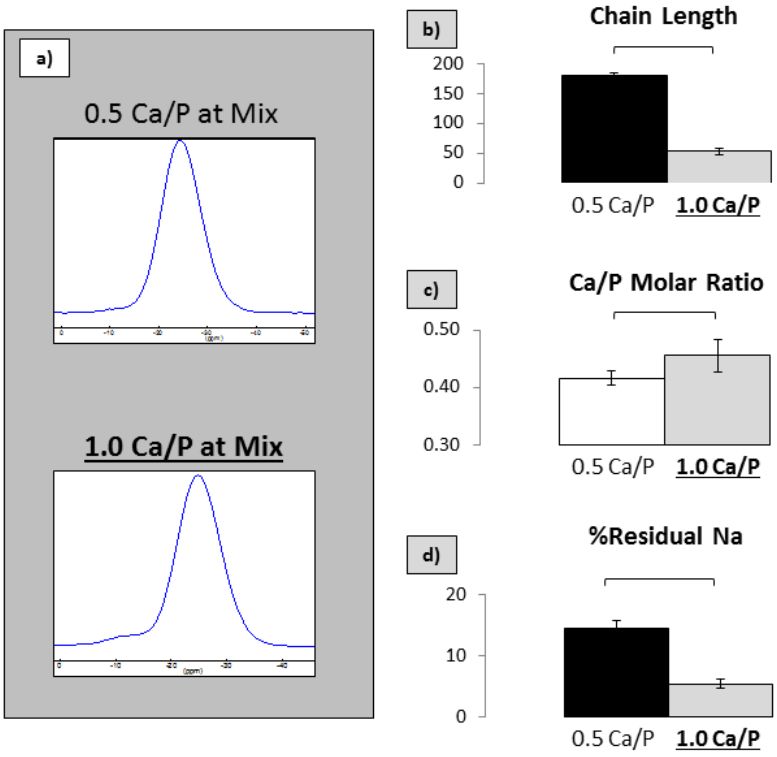

Figure 3.16: (a) Solid state ^{31}P NMR profiles, (b) Chain length, (c) Ca/P molar ratios, (d) Residual Na for precipitates obtained using a 0.5 or 1.0 Ca/P molar mix ratio of reactants. Values reported as average ± one standard deviation. Horizontal bars represent significant difference ($p<0.05$) ($n=4$). Note that this set of sample was precipitated under SimAd conditions (not NaAd). Standard condition in this subset of data is labelled "1.0 Ca/P at Mix"; Black column indicates a significantly greater value and a white column significantly lower value, while a grey column is not significantly different relative to standard condition ($p<0.05$).

Decreasing the Ca/P molar mix ratio from 1.0 to 0.5 saw the relative area under the Q^0 and Q^1 peaks in the NMR profile approach zero. As a result, the chain length of the precipitate significantly increased almost 3-fold ($p<0.05$). However, the residual sodium significantly increased ($p<0.05$) and Ca/P molar ratio significantly decreased ($p<0.05$) for the corresponding precipitate.

In the single-variable analysis little difference was observed between the addition of $NaPP_{(aq)}$ to Ca salt ("NaAd") and simultaneous additions of both reagents ("SimAd"), with both groups achieving a lower chain length but more acceptable Ca/P ratio and sodium residual level than that for the addition of calcium salt ("CaAd"). There was also very little difference between precipitates obtained using 10%$NaPP_{(aq)}$, 5% $NaPP_{(aq)}$, or 1% $NaPP_{(aq)}$. However, the samples produced using 0.1% $NaPP_{(aq)}$ had a significantly shorter chain length than the other precipitated sample groups. The residual sodium content decreased significantly with decreasing aqueous sodium concentration as expected. Meanwhile, reducing the Ca/P ratio at mix for the reactants from 1.0 to 0.5 significantly increased the chain length, but also prompted a significant increase in residual sodium content. Lastly, buffering at a pH of 8, oven drying, increasing precipitate collection time, decreasing reaction temperature, and increasing impeller speed were found to significantly decrease chain length. Pearson correlation analysis confirmed that a precipitate with a greater chain length and/or lower Ca/P molar ratio was strongly likely to have a higher residual sodium content ($p<0.05$).

In accordance with the design criteria, the chain length and residual sodium of the precipitated CPP described as a deviation from the melt CPP reference are given in Figure 3.17 and Table 3.2.

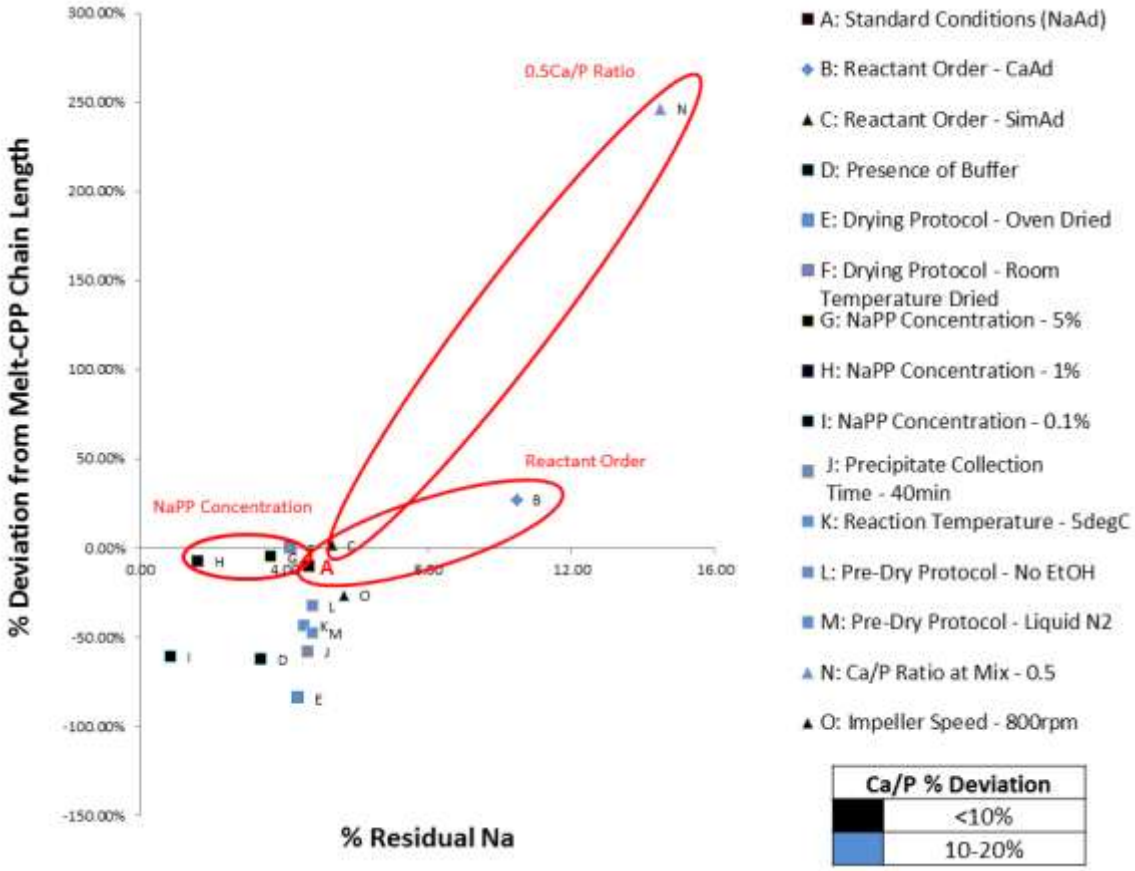

Figure 3.17: Multi-response deviation plot of CPP precipitates relative to design criteria. Average values reported. "A" on the plot indicates the standard precipitate condition.

As the design constraints consist *primarily* of an increased chain length while *secondarily* maintaining CPP chemistry (i.e. 0.50 molar Ca/P ratio, as low a residual sodium as possible), samples that best match this criteria should be found in the upper quadrant and as near the y-axis line as possible (corresponding to 0% residual sodium). As indicated by the red circles, three groups of design factors best met the *primary* design condition of greater chain length. The secondary design constraints of precipitate Ca/P molar ratio and residual sodium were not as well met in this single-variable study. In fact, a greater chain length was strongly correlated with greater residual sodium in the single-variable study precipitates. A multi-variable analysis of these three design factors may help optimize primary *and secondary* design constraints.

Table 3.2: Precipitate characterization following single-variable analysis. Refer to Table 3.1 for level descriptors.

	% Deviation from Melt-Derived								% Residual			
	Chain Length				Ca/P Precipitate Ratio				Sodium			
Level	**1**	**2**	**3**	**4**	**1**	**2**	**3**	**4**	**1**	**2**	**3**	**4**
Reactant Order	27±14	-10±4.8	1.7±11		17±5.2	5.0±1.8	11±5.5		10±1.1	4.7±0.3	5.3±0.8	
NaPP Concentration	-61±3.8	-7.7±17	-5.1±3.3	-10±4.8	3.1±3.7	4.3±2.0	8.1±0.6	5.0±1.8	0.8±0.0	1.6±1.1	3.6±0.2	4.7±0.3
Drying Protocol	-84±2.4	-10±4.8	-0.4±8.3		12±0.9	5.0±1.8	13±0.8		4.4±0.2	4.7±0.3	4.2±0.1	
Buffer Presence	-10±4.8	-62±5.8			5.0±1.8	2.1±1.3			4.7±0.3	3.4±0.8		
Precipitate Collection Time	-10±4.8	-58±4.9			5.0±1.8	13±6.2			4.7±0.3	4.7±0.7		
Reaction Temperature	-43±6.8	-10±4.8			15±1.0	5.0±1.8			4.6±0.1	4.7±0.3		
Pre-Dry Technique	-32±3.4	-43±6.8	-48±7.7		15±1.6	15±1.0	17±1.0		4.8±0.4	4.6±0.1	4.8±0.2	
Impeller Speed	1.7±11	-26±3.0			11±5.5	1.4±0.7			5.3±0.8	5.7±0.9		
Ca/P Ratio of Reactants	247±7.6	1.7±11			18±2.2	11±5.5			14±1.2	5.3±0.8		

The design variables of Ca/P ratio of reactants, reactant order, and NaPP concentration were evaluated in a subsequent multi-variable interaction study in order to further optimize the precipitates against *all* of the design criteria. The defined levels for each of these three variables are shown in Table 3.3.

Table 3.3: Fabrication variables and levels considered in precipitation of CPP.

	Variable	Level One	Level Two	Level Three
1	NaPP Concentration (w/v)	1%	10%	
2	Ca/P Molar Mix Ratio of Reactants	0.5	1.0	
3	Reactant Order	$CaCl_{2(aq)}$ added to $NaPP_{(aq)}$ ("CaAd")	$NaPP_{(aq)}$ added to $CaCl_{2(aq)}$ ("NaAd")	$CaCl_{2(aq)}$ and $NaPP_{(aq)}$ added simultaneously ("SimAd")

To facilitate the analysis, samples were divided into four groups as shown in Table 3.4, with each group consisting of three levels of reactant order (Variable 3).

Table 3.4: Sample Sets for Multi-variable CPP Precipitate Analysis

Group	Variable 1	Variable 2
S1	1% NaPP	0.5 Ca/P
S2	1% NaPP	1.0 Ca/P
S3	10% NaPP	0.5 Ca/P
S4	10% NaPP	1.0 Ca/P

CaAd
NaAd
SimAd

As the liquid NMR profiles show (see Appendix A: Figures A1-A4), there was generally little difference in the relative area proportions of each peak for samples sets 1, 2 and 3.

However, the relative proportion of Q^1 was significantly greater for sample set 4 (i.e. S4). As a result, the chain length of the precipitates in sample set 4 are significantly less than those for the precipitates corresponding to the other sample sets (Figure 3.18).

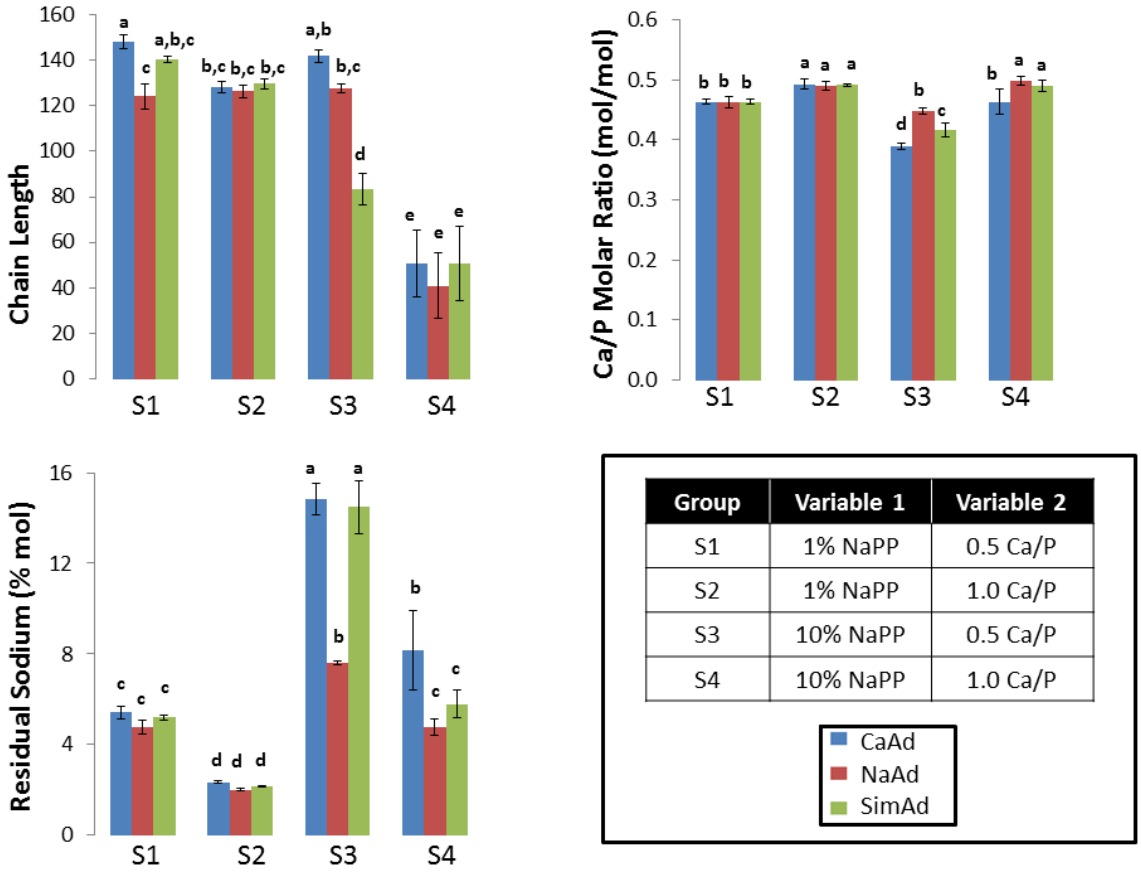

Figure 3.18: The impact of reaction order, NaPP concentration, and Ca/P ratio at mix on (top left) Chain length, (top right) Ca/P precipitate ratio, and (bottom left) Residual sodium content of the CPP precipitates (n=4). Values reported as average ± one standard deviation (means that do not share a letter are significantly different, $p<0.05$). Recall that the chain length of melt-derived CPP is 19±1 as determined by liquid ^{31}P-NMR.

From this multi-variable analysis, it was revealed that chain length could be increased to roughly six times that of melt-derived CPP while maintaining the residual sodium content below 5mol% (see group "S2").

Increasing the Ca/P molar ratio at mix from 0.50 to 1.00 while maintaining NaPP concentration resulted in a significant decrease ($p<0.05$) in precipitate chain length and residual sodium. In addition, by increasing NaPP concentration from 1 to 10% (w/v) and keeping the Ca/P molar ratio of mix constant at 1.0 there was a significant reduction ($p<0.05$) in chain length and increase in residual Na of the precipitates. However, this drop in chain length was not similarly observed at a Ca/P molar ratio of mix of 0.5. In addition, it is important to note that in the single-variable analysis of NaPP concentration, the difference in chain length of CPP from 1% NaPP or 10% NaPP was not significant. These observed differences could be the result of inherent variability in batches, or perhaps may be attributable to the greater sensitivity of liquid NMR to small changes in chemistry (i.e. residual sodium). With few exceptions, the order of reactant addition during the precipitation reaction did not have a significant impact on the measured outcomes. The Ca/P molar ratio of the collected precipitates, though found to be significantly impacted by the different conditions studied, still largely met the design criteria of 0.50. The interaction of the three design variables was found to be significant for the measured outcomes of chain length and residual sodium. Pearson correlation analysis of the multi-variable study outputs once again confirmed that a precipitate with a greater Ca/P molar ratio was strongly likely to also have a lower residual sodium content ($p<0.05$).

To gain a better understanding of the chemistry of the precipitates collected in the multi-variable analysis, they were further characterized by TGA and ATR-FTIR and compared to the reference melt-derived CPP (as previously shown in Figures 3.5 and 3.6). The ATR-FTIR spectra of CPP precipitates are shown in Figures 3.19, 3.20, and 3.21.

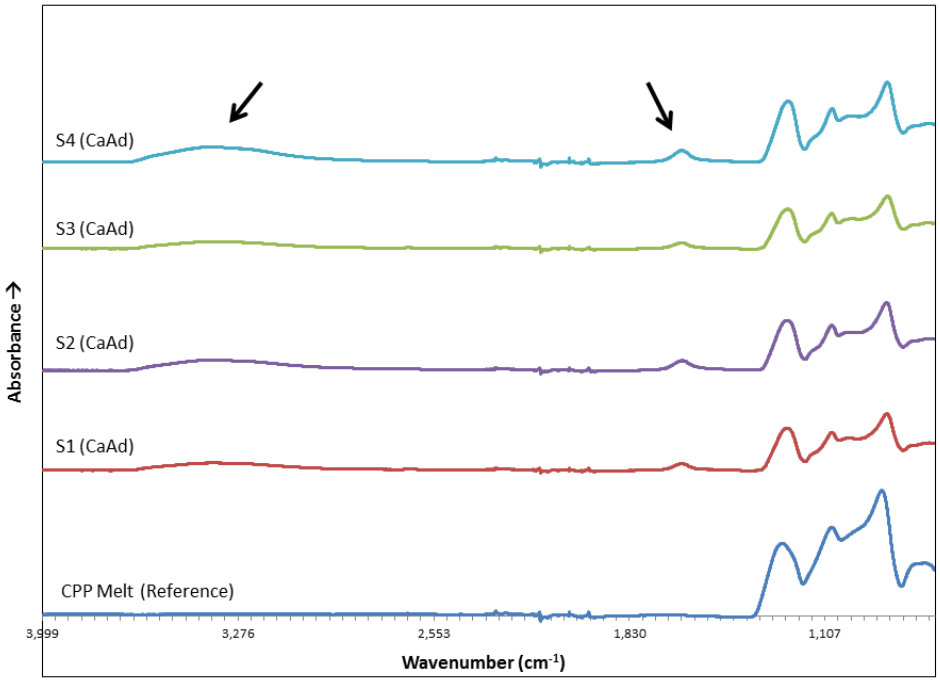

Figure 3.19: ATR-FTIR spectra of CPP precipitates from "CaAd" sample subsets and melt-derived CPP. Black arrows indicate peaks attributed to residual water.

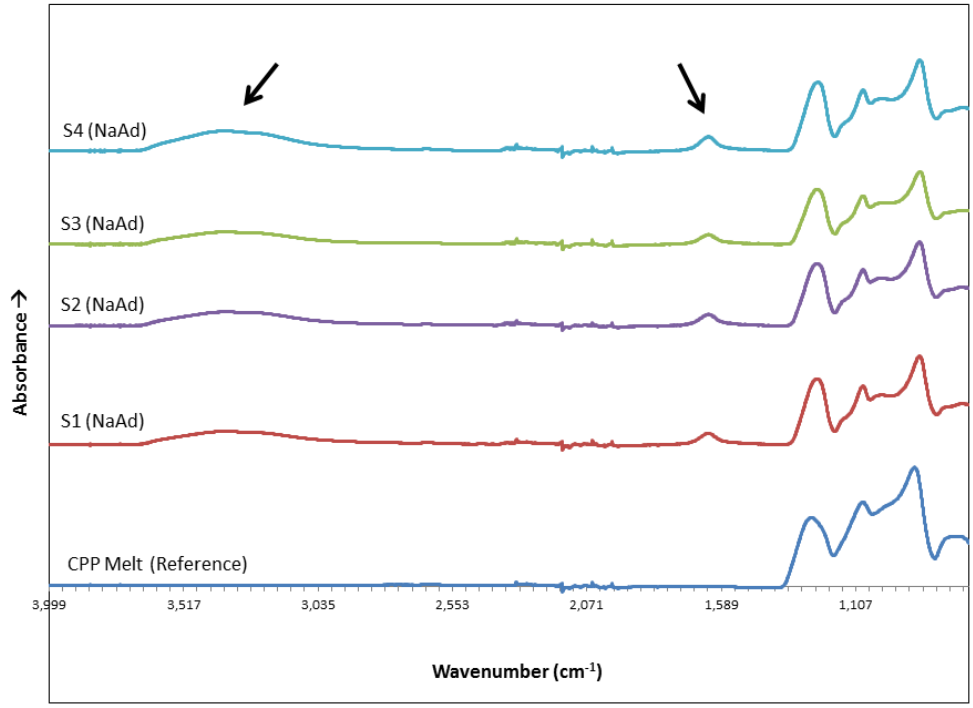

Figure 3.20: ATR-FTIR spectra of CPP precipitates from "NaAd" sample subsets and melt-derived CPP. Black arrows indicate peaks attributed to residual water.

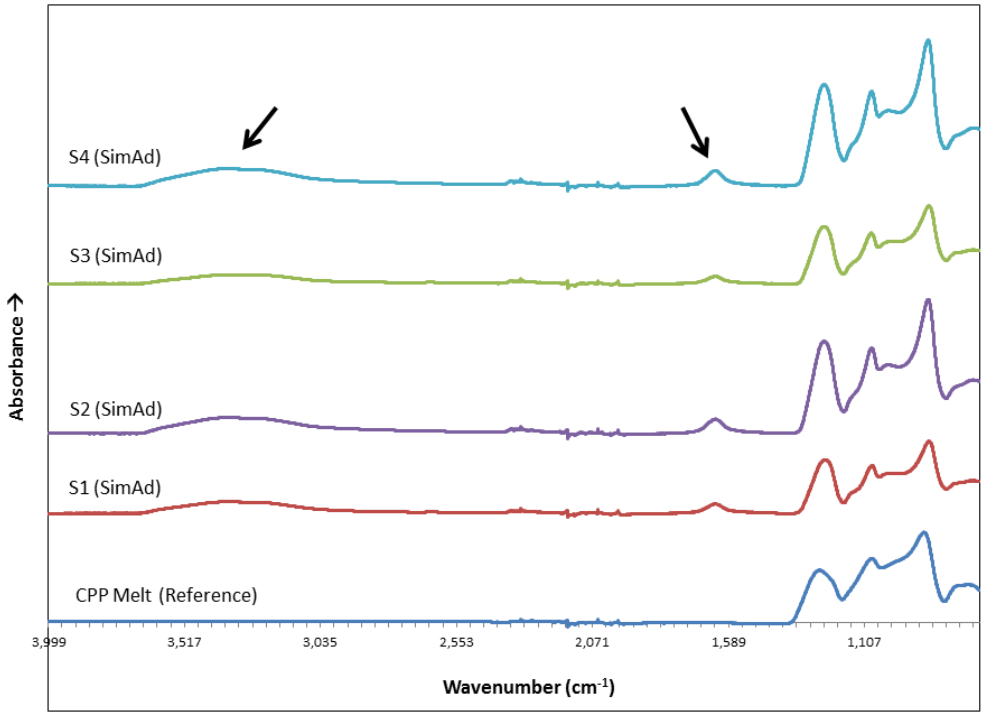

Figure 3.21: ATR-FTIR spectra of CPP precipitates from "SimAd" sample subsets and melt-derived CPP. Black arrows indicate peaks attributed to residual water.

The ATR-FTIR spectra of the precipitates closely matched that of the melt-derived CPP – particularly for the 1500 – 700cm^{-1} region, but with, a few noticeable differences as well. The broad absorption peak observed for the precipitate CPP samples between 3100 and 3700cm^{-1} is believed to be a result of water/-OH groups (Omelon *et al*., 2008). The small peak at ~1600cm^{-1} may also be attributed to the bending mode of absorbed water (Ataka *et al*., 1996). Altogether, ATR-FTIR spectroscopy further supports the previously presented NMR work indicative of a polymeric phosphate-based structure, while also providing evidence that residual water is present in the precipitated CPP; a 12-15% mass loss during concurrent TGA analysis of the CPP precipitates was consistent with the observation of residual water. In contrast, the lack of significant peaks at 3100-3700cm^{-1} and ~1600cm-1 in ATR-FTIR, as well as the lack of any significant mass loss during heating in TGA, indicated that melt-derived CPP does not have any residual water present.

3.3.3 Elution Study

Recalling that the guiding objective of this thesis project was to develop a local delivery system better tuned towards the treatment of osteomyelitis, the next aim of this research was to fabricate therapeutically loaded disks and study their elution behaviour *in vitro*. Based on the results reported in Figure 3.18 and how well the different sample groups met the design criteria, one of the precipitate conditions that best met (e.g. SimAd-S2) and one that showed the smallest change in chain length relative to melt-derived CPP (e.g. SimAd-S4) were further evaluated against the melt-derived CPP for drug loading and subsequent *in vitro* elution of VCM. The physical characteristics for these two

precipitation groups and for the melt-derived CPP are summarized in Table 3.5 and Figure 3.22 along with their respective VCM loading efficiencies; images of the resulting G1 and G2 disks are shown in Figure 3.23.

Table 3.5: VCM loading efficiencies of sample G1 powder.

				Outcome
Sample	**Chain Length**	**Ca/P Ratio (mol/mol)**	**Residual Na (mol %)**	**% VCM Loading**
Melt CPP	19±1	0.50±0.00		99.69±2.63^{A}
SimAd (S2) Precipitate	130±2	0.49±0.00	2.16±0.05	78.30±3.12^{C}
SimAd (S4) Precipitate	51±16	0.49±0.01	5.78±0.60	93.83±1.98^{B}

Note: Means that do not share a letter are significantly different ($p<0.05$).

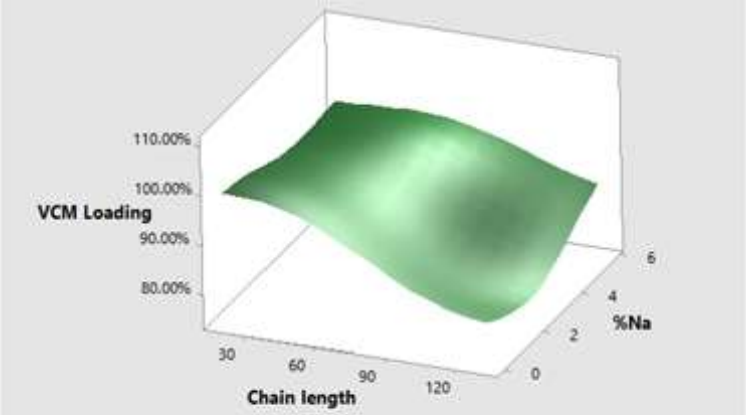

Factor	Pearson Correlation	*p*
Chain length	-0.905	0.000
Residual Na	0.005	0.983

Figure 3.22: Surface plot of VCM loading and Pearson correlation values between VCM loading and either chain length or residual Na (n=6).

The loading efficiency of CPP precipitate fabricated with 10% $NaPP_{(aq)}$ (i.e. SimAd (S4)) was found to be significantly greater than that with 1% $NaPP_{(aq)}$, and significantly less than that for melt-derived CPP ($p<0.05$). As shown in Figure 3.22, a Pearson correlation analysis found that there is a significant ($p<0.05$) and strong opposing correlation between chain length and VCM loading efficiency. The ANOVA and Pearson correlation analysis together suggest that CPP with a greater chain length had a lower VCM loading efficiency.

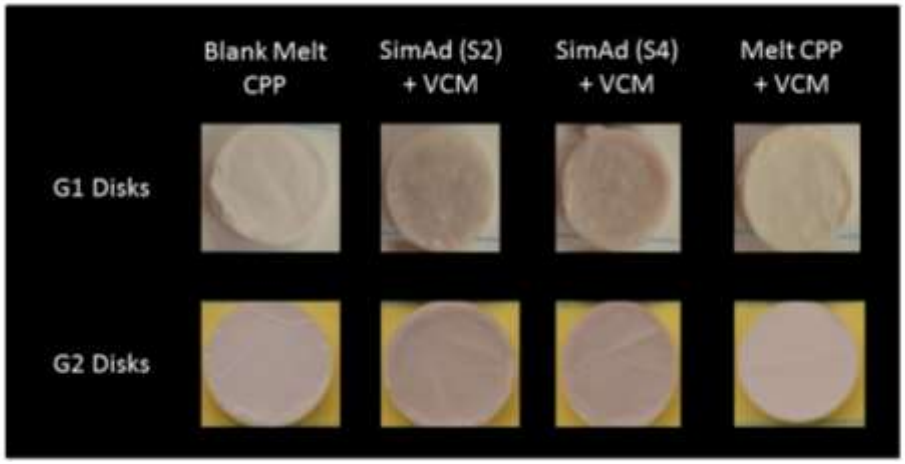

Figure 3.23: G1 and G2 disks for each sample group studied.

As Figure 3.23 shows, disks made from precipitated CPP are slightly more pinkish and glassy in appearance, but otherwise appeared similar prior to carrying out the elution study. The appearance of G2 matrices at different elution time points is shown in Figure 3.24.

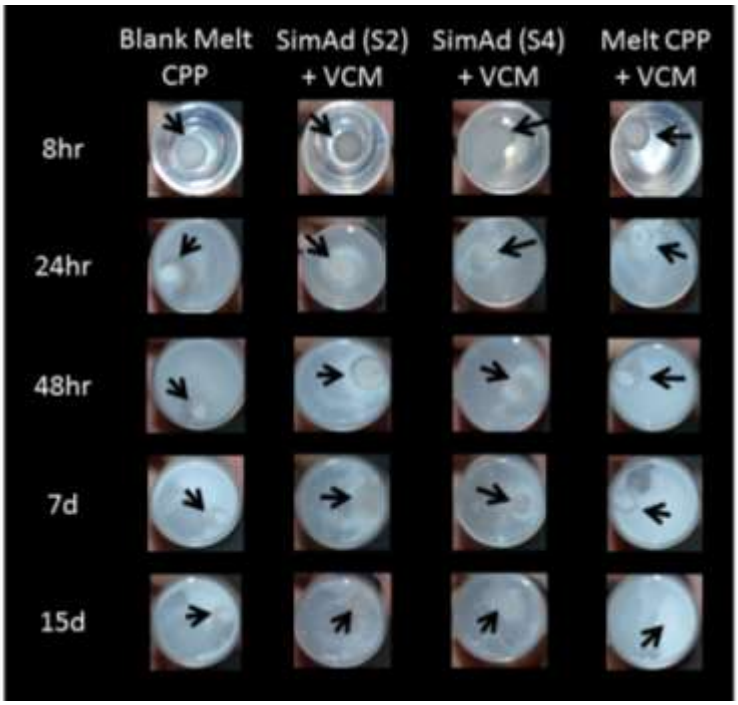

Figure 3.24: Appearance of representative G2 disks at select elution time points. Black arrows indicate position of disk in vial.

At the end of the elution study, the media was removed from the disks and they were allowed to dry (as shown in Figure 3.25).

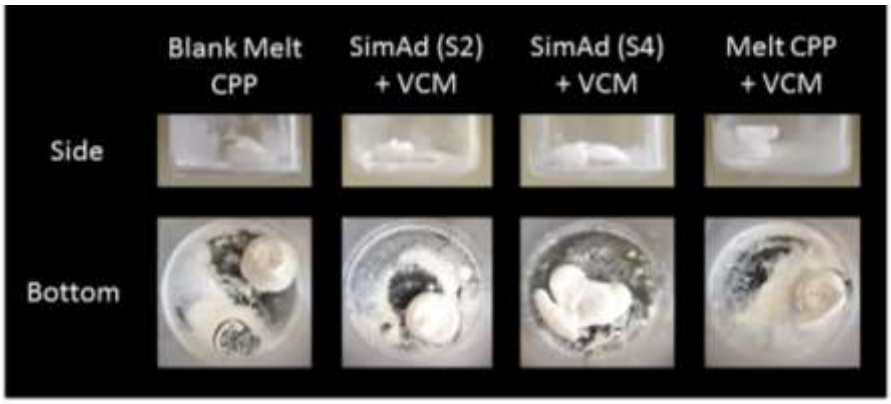

Figure 3.25: Appearance of the G2 disks at end of elution study and following media removal.

The G2 disks made from precipitated CPP were more likely to spread across the bottom of the glass scintillation vial during elution (particularly SimAd-S4) than the melt-derived CPP. The melt-derived CPP disks also typically expanded more in height and had more powdery debris collected near the dried disk.

Accompanying profiles of cumulative calcium ion, phosphorus ion, and VCM release are shown in Figure 3.26, 3.27, and 3.28, respectively.

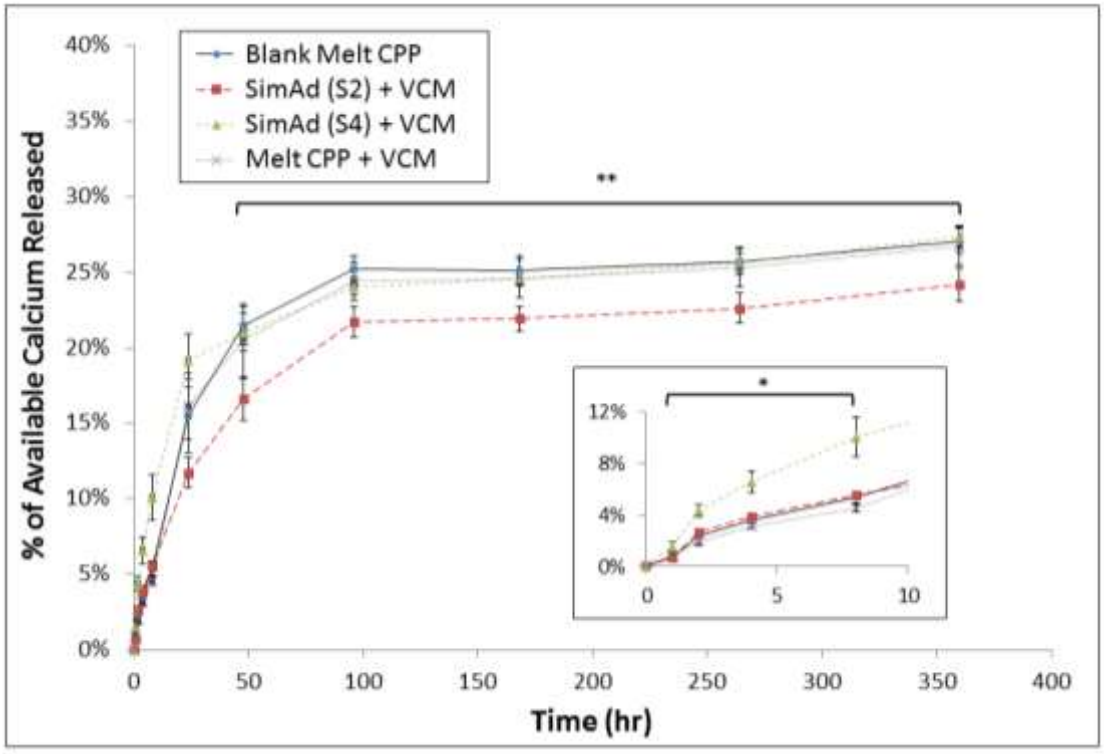

Figure 3.26: Cumulative release of calcium during first 8 hours (insert) and entire 15d study (n=6). Values reported as average ± one standard deviation. SimAd (S4) released significantly higher % of available calcium at early time points (*), while SimAd (S2) released significantly lower % of available calcium than other groups at later time points (**) ($p<0.05$).

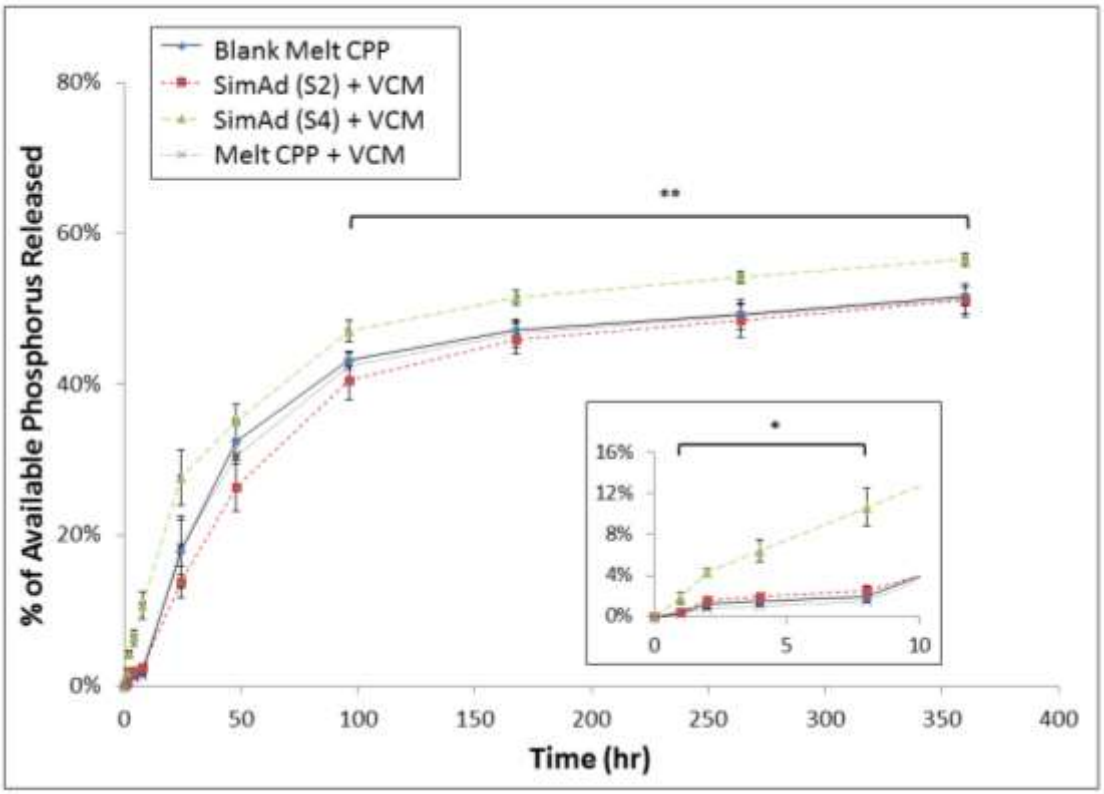

Figure 3.27: Cumulative release of phosphorus during first 8 hours (insert) and entire 15d study (n=6). Values reported as average ± one standard deviation. SimAd (S4) released significantly higher % of available phosphorus at early time points (*), while SimAd (S2) released significantly lower % of available phosphorus than other groups at later time points (**) ($p<0.05$).

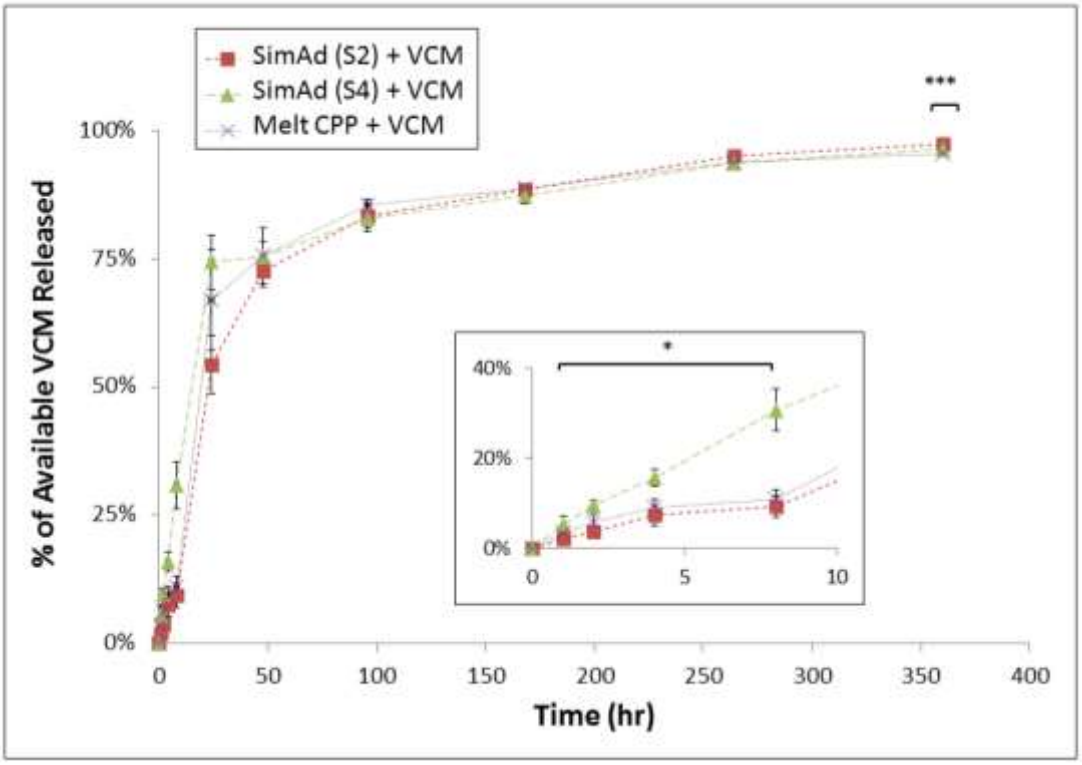

Figure 3.28: Cumulative release of VCM during first 8 hours (insert) and entire 15d study (n=6). Values reported as average ± one standard deviation. SimAd (S4) released significantly higher % of available VCM at early time points (*), while final cumulative VCM released is significantly different for each group (***) ($p<0.05$).

CPP precipitated with 10% $NaPP_{(aq)}$ (SimAd-S4), for which there was significantly more residual sodium, released significantly more calcium ions, phosphorus ions, and VCM within the first 8 hrs of elution study in TBS than the other sample groups ($p<0.05$). Matrices derived from CPP precipitated at 1% $NaPP_{(aq)}$ (SimAd-S2), for which there was significantly greater chain length, released essentially the same amount of ions and VCM as that by the melt-derived CPP during this same period of study. Although the 10% $NaPP_{(aq)}$-precipitated CPP group released significantly more calcium and phosphorus ions than the 1% $NaPP_{(aq)}$-precipitated group after 168 hours in elution media ($p<0.05$), the cumulative release of VCM after 168 hours did not differ between these two groups by

more than 3% of the total VCM available. By this time point, the melt-derived CPP group released significantly more calcium than the 1% $NaPP_{(aq)}$-precipitated CPP group ($p<0.05$) and significantly less phosphorus than the 10% $NaPP_{(aq)}$-precipitated CPP group ($p<0.05$). In addition, after 264 hours (i.e. 11 days) the 1% $NaPP_{(aq)}$-precipitated CPP matrices released significantly more VCM than those made with 10% $NaPP_{(aq)}$ ($p<0.05$); by the end of the study, both precipitated CPP groups had released cumulatively more VCM than the melt CPP group. The Pearson correlations between the total fraction of VCM released at 8hr and at the conclusion of the elution study, with sample chain length or residual sodium are shown in Figure 3.29.

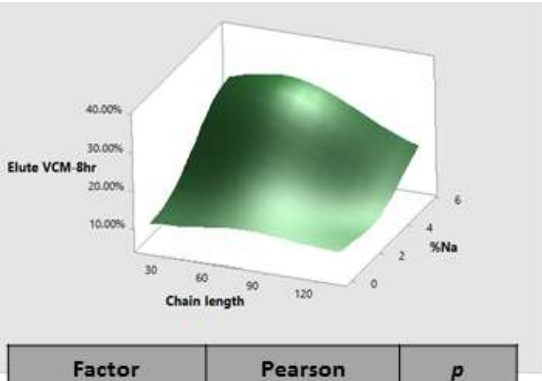

Factor	Pearson Correlation	p
Chain length	-0.287	0.248
Residual Na	0.864	0.000

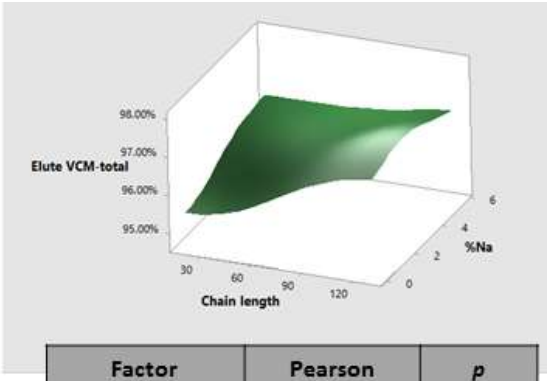

Factor	Pearson Correlation	p
Chain length	-0.852	0.000
Residual Na	0.341	0.166

Figure 3.29: Surface plot of total fraction of VCM released at (left) 8hr, and (right) end of study. The corresponding Pearson correlation values between total fraction of VCM released and either chain length or residual Na are given in corresponding table (n=6).

Pearson correlation analysis confirmed that the correlation between fraction of VCM released and residual Na was positively significant at 8hr, while at the end of the study the correlation between fraction of VCM released and chain length was significant in

opposing directions. In other words, early-stage release of VCM increases as residual sodium increases, and total cumulative VCM released is greater for a shorter initial chain length within the limitations of this study.

3.4 DISCUSSION

In this chapter the impact of various processing parameters on the chain length and chemistry of the precipitated CPP was assessed. Subsequently, the ability of this precipitated CPP to modify therapeutic release characteristics was measured *in vitro* with VCM-loaded matrices.

The precipitation reaction is attributed to a compromise between repulsive electrostatic and solvation repulsions, and the van der Waals attractive forces (Silva *et al*., 2008; Dias Filho *et al*., 2005; Bhuiyan *et al*., 2002; Hribar *et al*., 2000). Consequently, there are many variables that may influence precipitation of the CPP, and it is important to note that the chemical processes during precipitation are essentially molecular level processes. Good mixing on both bulk and molecular scales will allow for a larger supersaturation ratio and a greater drive towards a precipitation reaction (Madras *et al*., 2005; Doremus, 1958; Perez *et al*., 2008). Therefore, the factors that influence such mixing should be of greatest interest in precipitation of CPP. In this chapter single-variable analyses of nine different variables were studied initially and, therefore, the lack of a 9-variable interaction study may serve as one potential limitation. However, the variables with greatest impact were studied in a multi-variable interaction study and may largely overcome this study limitation.

Variables such as reactant order, reactant Ca/P ratio, and impeller speed that were expected to impact the bulk and local mixing did indeed have a significant impact on the chain length of the resulting precipitates. For example, the addition of $NaPP_{(aq)}$ to a $CaCl_2$ salt bath, an increase in Ca/P ratio at mix of reactants (when using 10% reactant concentration for both reagents), and an increase in impeller speed were largely detrimental to the chain length of the collected precipitate. One existing theory on the interaction of calcium with polyphosphate is that, at small Ca/P ratios, the calcium ions will be located in "cage-like" sites (site 1) (Dias Filho *et al*., 2005). Upon saturation of site 1 the calcium ions may cross-link between adjacent chains (site 2) and allow for the polyphosphates to precipitate out of solution. It may be possible, then, that with an overwhelming amount of calcium present upon first addition of some NaPP, the ionic exchange between sodium and calcium becomes quicker and less random (Masson *et al*., 1997), and the system has less time to be stabilized by chelation. There is an almost immediate saturation of site 1 along the polyphosphate chains with quick filling of site 2 following shortly thereafter. Any additional calcium present at this point could lead to increased interaction with surrounding water, and some compensatory chain scission (Silva *et al*., 2008; Dvinskikh *et al*., 1998; Crutchfield *et al*., 1965).

Hydrolysis works against the polymerization of CPP. Therefore, variables that impact the rate of hydrolysis, such as precipitate collection time, $NaPP_{(aq)}$ concentration, and buffering were expected to challenge the capacity to increase chain length. By increasing the precipitate collection time from 2 mins to 40 mins, the precipitates were exposed to

hydrolysis reactions for a greater period of time. Solvation of the phosphate through aqueous exposure served to relieve the unfavorable bridging angle for the metal phosphate and allow available calcium ions to affect the electrostatic repulsion of the phosphate groups (Ma *et al*., 1994; Dvinskikh *et al*., 1998). Change in solvation behaviour may also explain why diluting the precursor $NaPP_{(aq)}$ solution by 100x also resulted in a significant drop in chain length. A significantly greater dilution likely increased the solvation layer around the NaPP, made it more difficult for calcium-site binding to occur (Crutchfield *et al*., 1965), lowered the dielectric constant of the solution (Willot *et al*., 2002; Gavish *et al*., 2012), and allowed the polyphosphate chains to extend (Strauss *et al*., 1953-II). This extension would subsequently increase the electrostatic repulsion along the chains (Ma *et al*., 1994), weaken the P-O-P linkages and increase the susceptibility of the chains to random chain-scission. In other words, water essentially served as an additional glass modifier (Dvinskikh *et al*., 1998) and assisted in the preferential attack by calcium ions on the middle chain linkages (Crutchfield *et al*., 1965) to reduce CPP chain length. However, as shown by the *multi-variable assessment*, a dilution of only 10X at this same 1.0 Ca/P molar ratio at mix resulted in a significant increase in chain length. This differing impact on chain length with dependence on degree of NaPP reagent dilution suggests there may be a limiting NaPP concentration beyond which this variable-outcome interaction changes. A dilution of only 10X may have allowed the phosphate chains to become disentangled enough to allow greater ease of calcium ion attachment at sites 1 or 2 (Dvinskikh *et al*., 1998; Crutchfield *et al*., 1965; Ma *et al*., 1994). It is important to note, however, that NaPP concentration was not found to have a significant impact on chain length when Ca/P molar ratio at mix was only 0.5.

Furthermore, although it is well accepted that the hydrolysis rates of phosphates decrease with increasing pH (Huffman *et al*., 1960; Ma *et al*., 1995), this may not be the case in the presence of divalent metal cations, as was observed here. It has previously been reported that the hydrolysis of polyphosphates is generally most rapid at neutral pH when divalent cations are present (Ma *et al*., 1995; Dick *et al*., 1987). This could be due to the closer approach of the water dipole towards the dissolved polyphosphate with calcium present. Therefore, by buffering and raising the pH of the solution closer to neutral conditions, the system is less stable and scission of the chain occurs. A previous report that lowering the dielectric constant by introducing a solvent other than water (e.g. TMA) may lead to loss of charge density and a greater likelihood for OH- attack (Gupta *et al*., 1995) further supports the observations of chain scission with the buffering reported here.

Pearson correlation analysis confirmed that the molar Ca/P ratio and residual sodium of collected precipitates was generally moderate –to- strong (for single and multi-variable analysis, respectively) and opposing. In other words, a precipitate with a higher molar Ca/P ratio often had lower residual sodium content. One of the strongest design variables to show this correlation was NaPP reactant concentration prior to $CaCl_2$ addition. The ability of sodium to compete with calcium for positions on the polyphosphate chain significantly decreases as the NaPP concentration is reduced. This is evidenced by the increasing Ca/P molar ratio of the precipitate and simultaneous decrease in residual sodium as NaPP concentration decreases from 10, 5.0, or 1.0% to 0.1% NaPP. That the drop in NaPP concentration from 10 to 5%, 10 to 1% and 5 to 1% shows no correlation between Ca/P molar ratio and residual sodium in single-variable analysis could indicate

the step-wise change required in NaPP concentration to observe any such relationship (i.e. need a 100X dilution). This 100X dilution may encourage greater attachment of calcium ions to the chain as a result of phosphate extension and its highly charged nature. A greater Ca/P molar ratio would result even as residual sodium is reduced. Meanwhile, the lack of correlation between Ca/P molar ratio and residual sodium levels in the precipitates dried under different conditions may indicate some energy- (i.e. temperature-) dependent chain scission or development of different phases.

As anticipated, variables associated with processes following initial collection of precipitate, such as the pre-drying technique and final drying protocol, had less of an impact on the chain length of the resultant CPP precipitate. Based on the chain length, Ca/P ratio, and residual sodium levels observed for precipitates processed with different drying protocols, pre-drying with ethanol and freeze-drying were chosen for further optimization studies.

The correlation between chain length and VCM loading was found to be strong and negative, with greater chain length resulting in a significantly reduced VCM loading efficiency. Although supported by ANOVA analysis, it is important to recognize that this correlation is limited to only three discrete sample groups (i.e. three different chain lengths) in this study. Further research is necessary in order to confirm if this correlation extends beyond the levels of chain length studied here. Available literature suggests that VCM loading is achieved through physical adsorption (Gbureck, 2007) and, thus, as a result of electrostatic interactions. Critical to VCM loading is the balance of electrostatic

repulsion between charged macro-ions (whether amongst phosphate units or VCM molecules, respectively) and electrostatic attraction between the phosphate chains and VCM (Netz, 2003). A prior report by Jonsson *et al* (2001-II) noted that with shorter (and more flexible) polyelectrolyte chains, any repulsion between macro-ions may be largely screened and the macro-ions may position themselves near one another as they attach to the polyelectrolyte. Correspondingly, a significant increase in chain length (and notable decrease in flexibility) could reduce any such screening and macro-ions would then need to position themselves further apart to account for more apparent repulsion between them (Jonsson *et al.*, 2001-II). As a result, a greater chain length results in a reduced loading efficiency for VCM (as the macro-ion) in the CPP-based matrices.

G2 disks made of CPP precipitated with 10% $NaPP_{(aq)}$ released significantly more calcium ions, phosphorus ions, and VCM within the first 8 hours of elution study in TBS than the other sample groups, while matrices derived from CPP precipitated at 1% $NaPP_{(aq)}$ (having significantly greater chain length but lower residual Na) released essentially the same amount as that observed for the melt-derived CPP disks. This significant difference in early stage VCM release could be a direct result of the impact of residual sodium in the precipitated CPP matrix on the degradation and subsequent loss of disk shape over time *in vitro*. In fact, the Pearson correlation analysis found that the greater the residual sodium in the glass, the greater the early stage fraction of available VCM released. Previous reports have indicated that the presence of sodium in phosphate-based glasses may increase the solubility and the overall rate of degradation of the glass (Chun *et al*., 2001; Ahmed *et al*., 2005). Though the precipitates have 6mol%

or less of residual sodium, this level could be enough to have an impact on the release of ions (as an early chemical indicator of degradation) from the CPP precipitated with 10% $NaPP_{(aq)}$ where the chain length of the matrix was much closer to that of the melt-derived CPP. The inclusion of sodium increased the dissolution and subsequent disentanglement of the molecular chains of CPP such that more VCM could be released. That the disks made of this 10% $NaPP_{(aq)}$-precipitated CPP lost shape earlier in the elution study and to a greater extent than any of the other groups further supports this theory. Drug diffusion was then further aided here by the increased surface area-to-volume ratio (due to loss of disk shape), which has previously been shown to have an impact on drug release (Reynolds *et al*., 2002). A chain length roughly six times greater than that of the melt-derived CPP likely compensated for some of the degradation challenges faced by inadvertent incorporation of sodium in the CPP precipitated with 1% $NaPP_{(aq)}$. Polymer molecular weight has previously been shown to have an impact on drug release, with a polymer of higher molecular weight (i.e. chain length) reducing drug diffusion from the matrix (Kadri, 2001).

The differences in pre-elution study chain length of the CPP samples also had a significant impact on total fraction of available VCM released after 15d. In fact, the Pearson correlation analysis found that the greater the initial chain length, the lower the amount of total available VCM released. Overall, it is important to note that the behaviour of the G2 disks was shown here to be fairly reproducible. For example, the cumulative release of VCM at 8hrs is consistently less than 11% from G2 disks fabricated using melt-derived CPP. In contrast, the release of VCM in this same period of time from disks made from CPP precipitate via 10% $NaPP_{(aq)}$ was approximately 31%.

The significantly greater early stage release of VCM from matrices made from precipitated CPP of ~2X the chain length of melt-derived CPP is a significant impediment in the design of a CPP-based local delivery system for treating osteomyelitis. Ideally, the implantable local delivery device should release the loaded antibiotic following a zero-order profile with the local concentration readily maintained between the minimum inhibitory concentration and maximum tolerated concentration of the antibiotic for a given period of time. Significant early stage release may lead to an increased risk of systemic toxicity, as well as potentially encourage antibiotic resistance development with less of the depot available for later release. Increasing chain length by a factor of ~6X mitigated the impact of residual sodium significantly, yet in the end only achieved early stage VCM release similar to that of melt-derived CPP. For the benefits of greater CPP chain length to be seen in VCM delivery, this processing strategy needs to reach even higher chain lengths and/or lower residual sodium. Future study should consider different levels of precipitation variables. However, recognizing the constraints of the current study design and considering the final application, CPP will continue to be fabricated in accordance with the traditional furnace protocol.

3.5 STUDY LIMITATIONS

Initial single-variable analysis of nine factors on CPP precipitate characteristics did not involve the study of any factor interactions. To overcome this limitation each measured output used a consistent sample reference (e.g. melt-derived CPP and previously measured CPP precipitates). In addition, subsequent optimization of the three top-ranked factors was assessed with a multi-variable design using 2^{nd} and 3^{rd} order interactions.

Precipitation involves a number of different factors and is traditionally difficult to study; studies, as done here, typically involve only a few of these factors and it is important to acknowledge that the composition-structure-property relationships described here are applicable within the constraints of this study design.

Given the importance of chain length in this study it is important to be aware of the limitations associated with its measurement using NMR – whether solid or liquid state. Solid state NMR profiles are much broader than those from liquid NMR and do not separate the species beyond the general classifications (e.g. both linear and metaphosphate Q^2 are grouped as Q^2). Liquid NMR is able to separate out the different species further and increase spectra resolution due to more rapid nuclei isotropic motions and removal of anisotropic interactions by averaging – but this does not occur naturally in solid state NMR (Andrew *et al*., 1981). To best improve the resolution of the solid state NMR, current commercial equipment (such as that used in this work) includes a magic angle spinning facility in order to impose an improved spin on the nuclei within the solid and better match liquid profile resolution (Andrew *et al*., 1981). There still remains a noticeable difference in the two types of NMR spectra, but in each case most of the phosphorus atoms can be found in the Q^2 position. In addition, although the absolute chain length value may be different in solid and liquid state, the trends observed were found to be the same relative to the measured references. This use of sample references may also largely overcome concerns over exposure of CPP to an aqueous environment during liquid NMR and potential changes to polyphosphate chains while waiting for sample measurement (Dion *et al*., 2005).

Mass losses observed using DSC/TGA was attributed to water loss. However, it is possible that other chemicals may be given off during the heating of the sample and will then contribute to this mass loss. To confirm the relative mass of water present in the sample, the broad peak in ATR-FTIR for water between 3100 and 3700cm^{-1} could be quantified (Omelon *et al*., 2008).

TBS was chosen as the media in the elution study owing to its lack of a significant concentration of either phosphorus or calcium ions. However, TBS is not very physiologically relevant. CPP may behave differently in other media, such as PBS, due to the presence of ions (e.g. phosphorus) that may slow dissolution and impact VCM release. Conditions mimicking higher acidity due to infection should also be considered. Furthermore, the use of a more physiologically relevant dynamic motion set-up (i.e. more than 2D movement on a horizontal shaker) should be considered. For example, fluid dynamics in an *in vivo* animal model may be more restricted than the elution set-up used in this study (McLaren, 2004). Overall, differences between *in vitro* and *in vivo* conditions contribute to the difficulty in translating any knowledge gained in one towards the application in the other.

3.6 CONCLUSIONS

In accordance with the primary objective of this chapter, CPP glass was successfully precipitated with significantly greater average chain length than that of the melt-derived

CPP reference. Aqueous NaPP concentration, order of reactant addition, and Ca/P molar ratio at mix of reactants were found to have a particularly strong influence on the precipitation of CPP with respect to achieving the design criteria (i.e. obtaining high chain length and maintaining basic CPP chemistry). Precipitated CPP of significantly greater chain length had a significantly lower VCM loading efficiency, did not reduce early stage release and did not increase total cumulative release of vancomycin in the elution study compared to melt-derived CPP. From a drug delivery standpoint, traditional melt-derived CPP glass is preferable to precipitation in order to maintain high initial loading of the antibiotic into the matrix, and a minimal early-stage release of antibiotic *in vitro*. However, despite not seeing a significant improvement in drug release properties, this systematic study of CPP precipitation from NaPP precursors provided valuable mechanistic data on this interesting processing strategy.

CHAPTER 4 DOPING CALCIUM POLYPHOSPHATE WITH 10 MOL% STRONTIUM – A STRATEGY TO TUNE GLASS STRUCTURE, MANIPULATE VCM RELEASE *IN VITRO* AND IMPROVE THERAPEUTIC POTENTIAL

4.1 INTRODUCTION

The introduction of various ions such as strontium into a material is one method of managing physical characteristics such as glass structure, crystallinity or degradation (Song, W. *et al*., 2011; Song, W. *et al*., 2008; Lakhkar *et al*., 2009; Lakhkar *et al*., 2011; Wang *et al*., 2010; Chen *et al*., 2008). In addition, some ions are believed to have a therapeutic impact when they are released *in situ* (Hoppe, A. *et al*., 2011). For example, there have been a number of studies evaluating strontium ion release from biomaterials for treating metabolically damaged bone (Hott, M. *et al*., 2003; Dahl, S. *et al*., 2001; Marie, P. *et al*., 2001; Buehler, J. *et al*., 2001; Takahashi, N. *et al*., 2003). Together, the ability of strontium to modify amorphous CPP degradation and tune antibiotic release while actively assisting in bone regeneration may enhance the suitability of the CPP-based local delivery system in osteomyelitis therapy.

The structure, degradation, and osteoconductivity of *crystalline* CPP have also been shown to be impacted by strontium doping (Song, W. *et al*., 2011; Qiu, K.(b) *et al*., 2006; Song, W. *et al*., 2008; Wang, Q. *et al*., 2010; Chen, Y. *et al*., 2008). However, as these earlier studies have been limited to CPP in its crystalline form, for the purposes of developing a CPP glass-based delivery system, the impact of strontium doping on *amorphous* CPP needs to be assessed. The first objective of this study was then **to determine for the *first* time the impact of strontium on the powder density, chain**

length, and transition temperatures of the *amorphous* CPP. As part of this objective, two different strontium concentrations together with two different strontium salts were evaluated. *It was hypothesized that increasing strontium doping to 10 mol% would increase the density and chain length of CPP glass while reducing the crystallization, melting, and glass transition temperatures upon heating. It was also hypothesized that the powder density, chain length, and crystallization, melting, and glass transition temperatures studied here would not be dependent on strontium salt used in fabrication.*

Owing to the importance of being able to *gel* the CPP glass in order to contain a water-soluble antibiotic in the final delivery device, the next objective was **to determine the impact of strontium doping on the gelling capacity and overall stability of the CPP glass *in vitro***. As part of this objective two different strontium concentrations and two different strontium salts were evaluated without the presence of antibiotic in the disks. *It was hypothesized here that increasing strontium doping to 10 mol% would not impact the capacity of the material to gel and form blank CPP-based G1 disks. A related hypothesis was that the structural stability of the blank CPP-based G1 disks in vitro would be improved with strontium doping, with less ion release and greater retentation of disk shape. It was further hypothesized that the structural stability of the blank CPP-based G1 disks in vitro will not be dependent on the type of strontium salt used in fabrication.*

As the delivery system was designed to include *both* therapeutic ions and an antibiotic, the third objective was **to determine the impact of strontium doping on ion and VCM release from the final *VCM-loaded* CPP glass-based local delivery matrices**. Here,

only one strontium concentration and one strontium salt were evaluated based on the results of blank G1 disk studies. *It was hypothesized that 10 mol% strontium doping would reduce the degradation of the CPP G2 matrices and release of calcium and phosphorus ions, as well as delay VCM release in vitro*.

With this therapeutically loaded delivery system, there is potential to eradicate the infection *in conjunction with* recovering bone tissue originally lost to this disease. As an early indication of its clinical feasibility, the short-term performance of the device against relevant bacteria and cell activity has to be assessed. The last objective of this chapter was therefore **to determine the impact of strontium doping on the cytocompatibility and VCM efficacy of the CPP glass-based local delivery matrices**. *It was hypothesized that doping CPP glass with 10 mol% strontium will not change the cytocompatibility or VCM efficacy of the therapeutically-loaded CPP-based G2 matrices relative to test controls*.

4.2 MATERIALS AND METHODS

4.2.1 Material Processing and Matrix Fabrication

4.2.1.1 Strontium-Doped CPP Glass

Amorphous xSrO- CPP containing 0, 5, or 10 mol% SrO (i.e. x of 0, 5, or 10) was produced by modifying the calcine-melt protocol previously presented in section 3.2.1 for undoped melt-derived CPP. As the phase diagrams for $CaO\text{-}P_2O_5$ (Hill *et al*., 1944) and $SrO\text{-}P_2O_5$ (Kreidler, E. *et al*., 1967) are very similar, the temperatures and hold duration for calcining and melting of the starting powders were not adjusted. In short, reagent grade powders of strontium phosphate ($SrHPO_4$) or strontium carbonate ($SrCO_3$),

ammonium phosphate ($NH_4H_2PO_4$), and CPMM at the requisite amounts (see equations 4.1 and 4.2, where x=0, 0.05, or 0.10) were mixed in a custom-made V-shaped rotary mixer for 1 hr and then placed in a Pt crucible to be calcined at 500°C for 10 hrs. Each of these powders was purchased from Sigma-Aldrich Canada Co. The calcined powder was then melted at 1100°C for 2hrs and quenched in distilled water to produce an amorphous frit. Following washing in 100% ethanol, the resulting frit was then milled and sieved to obtain a <45μm powder fraction.

With $SrCO_3$ as the strontium salt, the following reaction is anticipated:

$$xSrCO_3 + (0.5\text{-}x)Ca(H_2PO_4)_2{*}H_2O + 2xNH_4H_2PO_4 \rightarrow Sr_xCa_{(0.5\text{-}x)}PO_3 + xCO_2 + 2xNH_3 + 1.5H_2O$$

[Equation 4.1]

The corresponding reaction with $SrHPO_4$ as the strontium source is as follows:

$$xSrHPO_4 + (0.5\text{-}x)Ca(H_2PO_4)_2{*}H_2O + xNH_4H_2PO_4 \rightarrow Sr_xCa_{(0.5\text{-}x)}PO_3 + xNH_3 + (1.5\text{-}x)H_2O$$

[Equation 4.2]

As noted in Equations 4.1 and 4.2, $NH_4H_2PO_4$ is used to meet the stoichiometric phosphate requirements of the final CPP and encourage the reactions of the oxides in the melt (Pires *et al*., 2004; Pires *et al*., 2004-2; Schneider *et al*., 2005).

Following processing, the glass powder was assessed for its chemical and molecular nature as a function of the two study variables, strontium concentration and strontium salt.

4.2.1.2 Strontium-Doped CPP Matrices

The fabrication of blank G1 disks (i.e., no VCM loading) and, later, blank or VCM-loaded G2 disks followed the protocol previously outlined in section 3.2.1. The G1 and G2 disks were characterized for their matrix porosity and *in vitro* degradation. In addition, G2 disks were also characterized for VCM loading and release *in vitro*, their cytocompatibility and the efficacy of the released VCM against *S.aureus*.

4.2.2 Material Characterization

4.2.2.1 Strontium-Incorporated CPP Glass

As presented in section 3.2.2 the composition of the xSrO-CPP glass powder (where x=0, 5, or 10 mol%) was confirmed after dissolution in an equi-volume mix of 6N $HCl_{(aq)}$ and 15N $HNO_{3(aq)}$ at 80^0C for 12hrs followed by assessment with ICP-OES (PerkinElmer Optima8000). Calcium, phosphorus and strontium were measured at wavelengths of 317.933nm, 213.617nm, and 407.771nm, respectively. Strontium doping efficiency was calculated by determining the amount of strontium measured as a percentage of that theoretically expected.

In addition, the functional groups present, average phosphate chain length, and thermal profile of the xSrO-CPP glass powder were assessed following the methodology outlined in section 3.2.2 using ATR-FTIR, solid state ^{31}P MAS NMR, and DSC/TGA, respectively. The isotropic chemical shift (i.e. Q^2 position) and full width at half-maximum (FWHM) of the ^{31}P central chemical shift peak obtained from the solid state ^{31}P MAS NMR spectra were also reported in this chapter (see Figure 4.1).

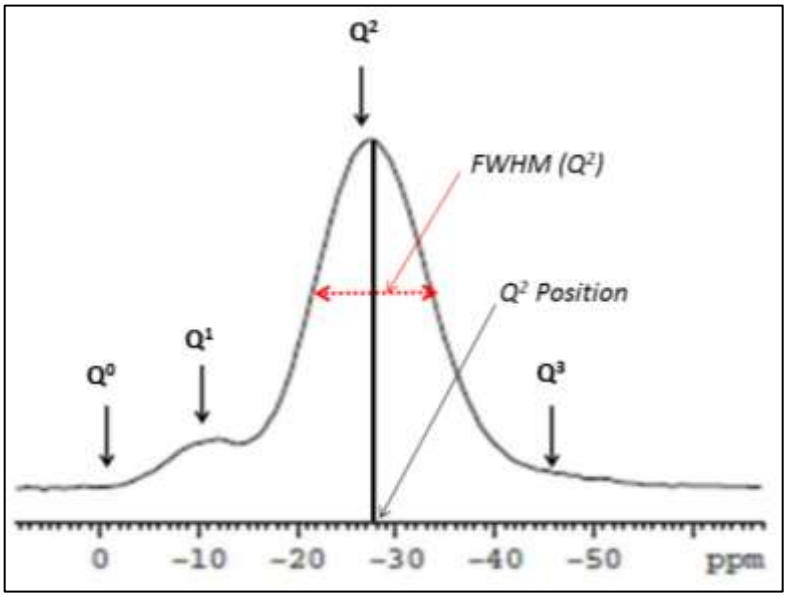

Figure 4.1: Solid state 31P MAS NMR schematic for FWHM and position determination for central Q^2 species of CPP.

The skeletal density of the glass powder was measured with a helium pycnometer (AccuPyc 1340, Micromeritics). Following calibration of the equipment using a 1.0cm^3 sample cup and calibration sphere, the sample cup was filled to 2/3 of its capacity with each glass powder sample. The mass of the sample (not including cup) was recorded and the cup returned to the pycnometer chamber. The pycnometer reports 10 density values for each sample at the end of each run and the average of these was presented here for each glass sample. The sample cup was cleaned with 70% ethanol and tissue paper (KIMTECH Sciences) after each glass powder measurement.

4.2.2.2 Strontium-Incorporated CPP Matrices

The blank G1 and blank or VCM-loaded G2 Disks were characterized for their skeletal density (ρ_t) using a helium pycnometer (AccuPyc 1340, Micromeritics) as per section

4.2.2.1, and their apparent bulk density (ρ_a) calculated upon measurement of the weight and volume of the matrices (ρ_a=disk weight/disk volume). From these skeletal density and apparent bulk density values, the %porosity was determined as per equation 4.3 (Webb, 2001; Hancock et al., 2003):

$$\%\, porosity = 1 - \frac{\rho_a}{\rho_t} \qquad \textbf{[Equation 4.3]}$$

VCM loading efficiency (L_{eff}) for the G1 powder was determined following the protocol previously outlined in section 3.2.2 (Equation 3.4). The *in vitro* elution studies of the G1 and G2 disks followed that previously presented in section 3.2.2. In addition, the pH of the media was monitored over the duration of elution studies of the disks with an Accumet® Basic AB15 Plus pH meter (Fisher Scientific). The appearance of the G1 and G2 disks at the designated time points *in vitro* was recorded with the assistance of a Nikon D3100 camera.

Scanning Electron Microscope (SEM) images of mounted and Au/Pd sputter coated G2 disk samples (n=1) (Figure 4.2) under intact and sectioned conditions were taken using an Hitachi S-4700 and recorded at an accelerating voltage of 15kV, with images captured at 80X and 1500X (i.e. 1.5kX) magnification. G2 disks were carefully sectioned by hand using a flat-edge blade.

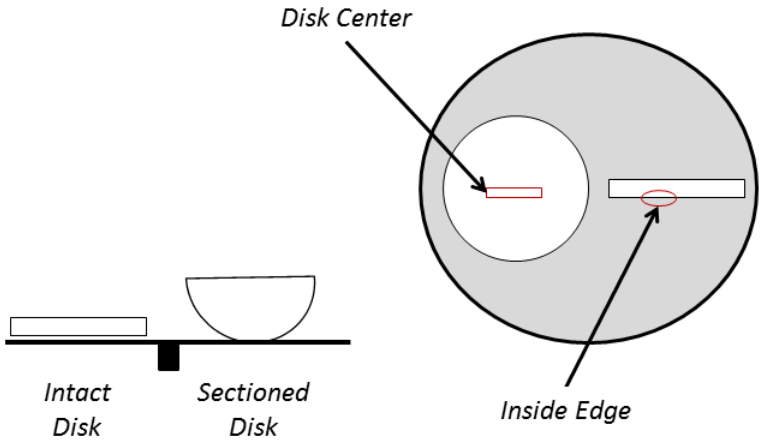

Figure 4.2: Schematic of SEM pin with intact and sectioned disks for imaging.

4.2.2.3 Functional Assays with Strontium-Doped CPP G2 Matrices

The G2 Disks (blank and VCM-loaded) underwent *in vitro* biological evaluation using a cytocompatibility-based MTT assay (in accordance with ISO standard 10993-5, 2009) and microbiological activity assay (in accordance with Clinical Laboratory Standards Institute standard M07-A8, 2009) via the use of elution extracts. G2 disks were prepared as outlined in section 3.2.2 and added to 15mL 0.1M TBS for a period of 24hr undisturbed at 37^0C on a horizontally rotating plate at 90rpm. TBS was chosen as the extract media for consistency with prior elution studies (as per section 4.2.2.2) and to best mitigate any change in pH. After 24hr, the elution extracts were collected and filtered using sterile 0.20µm filters (Sarstedt, Canada). Ion and VCM release was measured as previously reported in section 3.2.2.

4.2.2.3.1 *In Vitro* Cytocompatability (MTT)

Immortalized rat fibroblasts (NIH-3T3) (American Type Culture Collection, Manassas, VA) at passages 15–20 were used for these experiments. The cells were grown in 75 cm^2 tissue culture flasks in Dulbecco's Modified Eagle's Medium (DMEM) (Sigma) supplemented with 5% heat-inactivated fetal calf serum (FCS) (Sigma). Cells were passaged twice weekly at 70-80% confluence, using 1mL of 0.25% trypsin-EDTA (Sigma) to detach cells, and re-suspended with 19mL of fresh 5%FCS-DMEM (i.e. total flask volume is 20mL). Flasks were maintained in a humidified atmosphere at 37^0C and 10% CO_2. Fibroblasts for subsequent studies were harvested at 70-80% confluence, detached using trypsin-EDTA, counted using a haemocytometer, then diluted and suspended at a concentration of $3x10^4$ cells/mL.

NIH-3T3 cells were seeded at a density of $3x10^4$ cells/mL in a 96-well plate at a well volume of 200µL per well (CoStar, Corning, Canada). Sterile-filtered dimethyl sulfoxide (DMSO) (Sigma) was used as a negative control, 0.1M TBS used as a positive reagent control, and cells with only culture media used as a positive cell control. The 96-well plate was incubated for 24hr in a cell culture incubator at 37^0C (10% CO_2/95% air atmosphere). After 24hr, half of the wells had 20µL of the sterile-filtered sample added to the existing 200µL of DMEM, while the remainder of the wells had 10µL of sample and 10µL of 0.1M TBS added to each well in their respective plate (corresponding to an additional 50% dilution) (Kehoe *et al*., 2012). The plates were then incubated for another 24hr at 37^0C (10% CO_2/95% air atmosphere). Analysis of each extract was performed in triplicate. A 5mg/mL solution of MTT reagent (M2128, Sigma Aldrich Canada) was

prepared in phosphate-buffered saline (PBS), vortexed and sterile-filtered (0.20μm); each well was exposed to the prepared MTT at an amount equal to 10% of the culture media volume (i.e. 22μL) before being returned to the incubator for a further 3h. Viable cells will reduce yellow water-soluble MTT (3-(4,5-dimethylthiazol-2-yl)-2,5-diphenyltetrazoliumbromid) to a blue-violet insoluble formazan. After incubation, a solubilization solution of DMSO (Sigma) was added to each well at a volume equal to the original culture media volume. Each well was gently stirred on a horizontally rotating shaker under aluminum foil in order to enhance dissolution of the formazan crystals. Subsequently, the absorbance of each well was spectrophotometrically measured at a wavelength of 570nm on a multi-detection microplate reader (Synergy HT, BIO-TEK). The photometric colour intensity measured following dissolving formazan in a solubilisation agent correlates to the number of viable cells. Cell positive control wells were assumed to have 100% metabolic activity corresponding to cell viability of 100%. To note any impact of TBS alone (i.e. extract media) on cell viability, the absorbance of the cell positive and positive reagent control samples were compared. Next, the percentage of cell viability for cells exposed to experimental extracts was calculated relative to the positive reagent control. These steps are standard practice when performing an indirect extract test of cell viability. Here a control of TBS meets the ISO standard 10933-12 definition of test blank (i.e. positive reagent control) that is necessary to mitigate any effects owing to extract conditions alone.

4.2.2.3.2 *In Vitro* Micro-dilution Assay with Staphylococcus Aureus

As per the Clinical Laboratory Standards Institute (CLSI) protocol (M07-A8, 2009), a micro-dilution assay was performed to determine VCM activity of the xSrO-CPP extracts. For this assay the MIC of eluted VCM in 24hr extracts was compared with that of stock VCM. Mueller-Hinton agar plates were streaked with *Staphylococcus aureus* (lab stain 6538) and incubated at 37^0C overnight. The resulting bacteria spores were added to 10mL of Mueller Hinton broth and broth volume adjusted until an absorbance reading of 0.08-0.1 was obtained at an absorbance of 625nm in clear analysis tubes on a spectrophotometer (Spectronic® 20D+, Thermo Scientific). In accordance with CLSI, this absorbance corresponds to $1\text{-}2x10^8$ colony forming units/mL of broth (M07-A8, 2009). However, earlier work in our lab has found the concentration at this absorbance to be closer to $4\text{-}5x10^7$ CFU/mL for *S.aureus*. The positive control for this study was Mueller-Hinton broth containing bacterial culture, while the negative control was Mueller-Hinton broth alone.

The stock VCM solution was prepared at 1mg/mL in 0.1M TBS and subsequently adjusted to 64µg VCM/mL with Mueller Hinton broth. A similar initial adjustment was prepared with elution extracts (of known VCM concentration). From this point a nine step two-fold serial dilution was performed on stock VCM and elution extracts by transferring 0.5mL of the initial VCM/broth mixture (i.e. 64µg VCM/mL) to the next tube and adding 0.5mL of the prepared bacterial culture, giving a 32µg VCM/mL concentration for the first sample. This dilution series was continued until a final concentration of 0.125µg VCM/mL was obtained. All samples and controls, once prepared, were incubated at 37°C for 24hrs. The MIC was then determined as the lowest

concentration able to inhibit the growth of bacterium as characterized by a lack of turbidity (i.e. cloudiness of the sample).

4.2.3 Statistics

A power analysis was initially performed in order to estimate the required sample size for detection of reasonable departures from the null hypothesis. Based on preliminary studies a minimum sample size of 5 for the analysis of the strontium glass powder was found to be sufficient for a power greater than 98%. Elution studies designed to match prior work sought a power greater than 98% and required a sample size of 6.

Differences in means of study outcomes were analyzed using Minitab15.0, a statistics software program, and either a one-way ANOVA (for VCM loading efficiency, VCM elution, and strontium ion release *in vitro*) or a two-way ANOVA (for remaining outputs) was used with a significance value of $p=0.05$. In addition, a post-hoc pairwise Tukey analysis was performed. Lastly, study outcomes were compared with Pearson correlation to determine any significantly related trends ($p<0.05$).

4.3 RESULTS

4.3.1 Strontium-Doped CPP Glass

Glasses with 0 mol% Sr are designated “0SrO-CPP”, those with 5 mol% Sr “5SrO-CPP”, and those with 10 mol% Sr “10SrO-CPP”, while those fabricated with $SrCO_3$ or $SrHPO_4$ are indicated with “carbonate” or “phosphate”, respectively. The processing protocol

used in this research enabled Sr doping efficiencies of ~98%, with no significant dependence on Sr concentration or salt (Table 4.1).

Table 4.1: Doping efficiency, Ca/P ratio, and density of xSrO-CPP glass powder.

Sample Group	Sr Doping Efficiency (%)	Ca/P Ratio (mol/mol)	True Density (g/cm³)
0SrO CPP Glass	--	0.50±0.00^{A}	2.65±0.01^{C}
5SrO CPP (Carbonate) Glass	97.76±1.71^{A}	0.46±0.00^{B}	2.70±0.01^{B}
5SrO CPP (Phosphate) Glass	98.21±1.21^{A}	0.46±0.01^{B}	2.70±0.01^{B}
10SrO CPP (Carbonate) Glass	97.90±1.12^{A}	0.41±0.01^{C}	2.75±0.01^{A}
10SrO CPP (Phosphate) Glass	98.13±0.73^{A}	0.39±0.01^{D}	2.76±0.01^{A}

Note: Means that do not share a letter are significantly different.

There was some dependence of glass powder density on strontium concentration, with this density increasing with Sr doping; there was no dependence on strontium salt used for doping. A two-way ANOVA found that there was no significant interaction between strontium concentration and salt for the measured glass powder densities ($p>0.05$). As the theoretical density of SrO (4.7g/cm^3) is greater than that for CaO (3.4g/cm^3), it was anticipated that strontium-incorporated CPP would have a greater density then undoped CPP (Hesaraki, S. *et al*., 2010). The Ca/P ratios of the glasses were all within 2-3% of the expected Ca/P molar ratio (e.g. 0.45 for 5SrO-CPP and 0.40 for 10SrO-CPP).

ATR-FTIR spectra of the three CPP glasses (with 0, 5, 10 mol% SrO) each closely matched those previously reported for the un-doped polymorph (Figure 4.3), indicating that the arrangement of bonds within the polymeric CPP are maintained (Jackson *et al*., 2005).

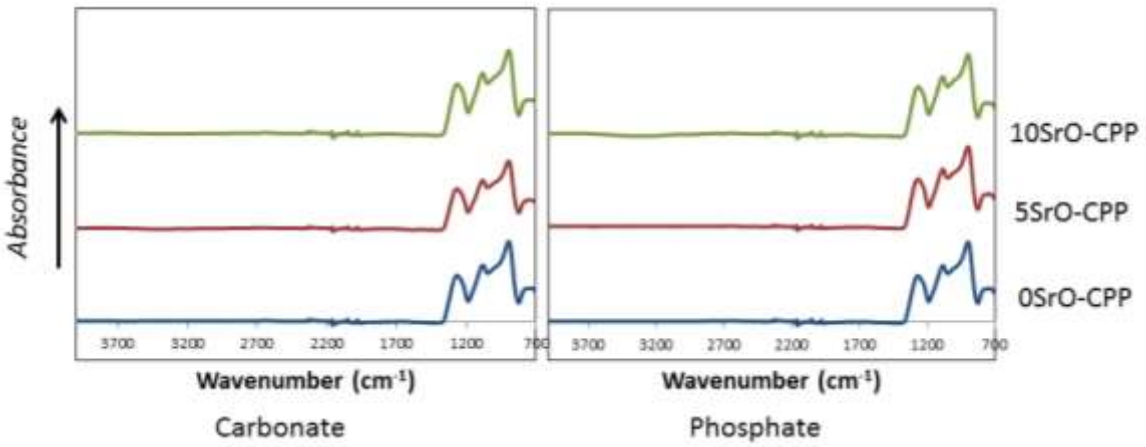

Figure 4.3: ATR-FTIR spectrum of xSrO-CPP glass powder. Spectra shown is the average of the scans for measured samples (n=4).

Neither strontium concentration nor salt used in this study were found to have a significant impact on the FTIR spectra of the CPP glass.

In contrast, changes in the NMR spectra (Figure 4.4) – while subtle – were found to be significantly dependent on strontium concentration within the study design, with changes in chain length (as determined by peak areas), Q^2 position, and Q^2 FWHM observed (Figure 4.5).

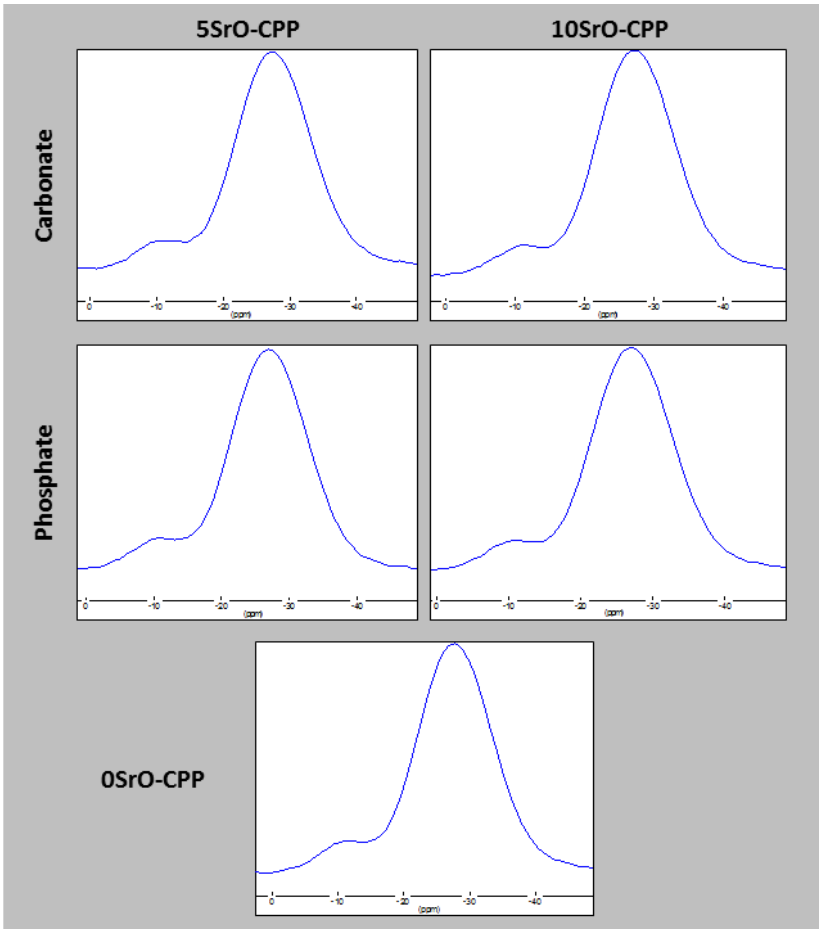

Figure 4.4: Solid state ^{31}P MAS NMR profile of xSrO-CPP glass powder.

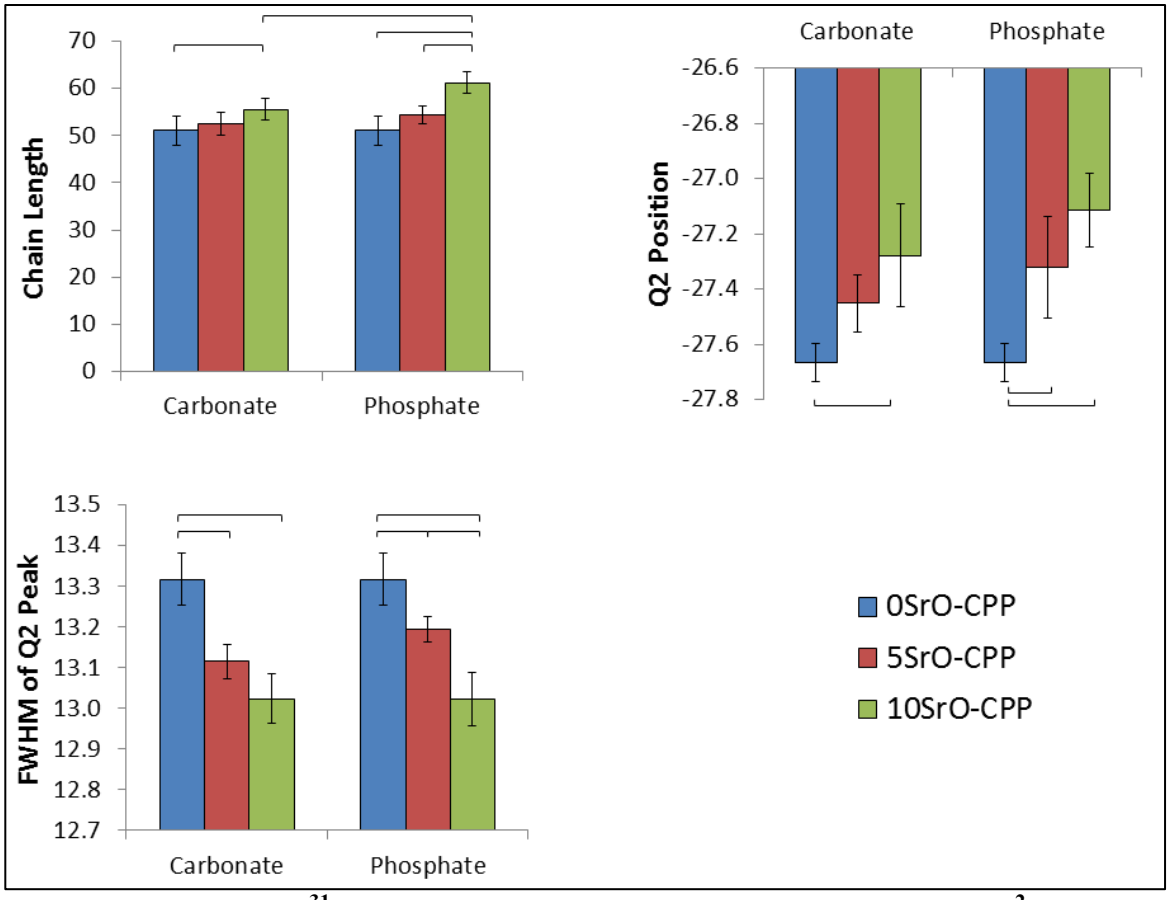

Figure 4.5: Solid state ^{31}P MAS NMR (top left) Chain length, (top right) Q^2 position, and (bottom left) FWHM of Q^2 peak of xSrO-CPP. Data reported as average values while error bars represent one standard deviation (n=5). Horizontal bars represent significant difference ($p<0.05$).

^{31}P NMR chemical shifts are very sensitive to both the composition of the phosphate glasses and the polymerization of phosphate tetrahedral (Fletcher, J. *et al*., 1993; Brow, R. *et al*., 1991) and can reveal much about the structure of the glass. In this study, the NMR spectra of the strontium-incorporated CPP and undoped CPP glasses were dominated by the Q^2 peak, with correspondingly very small peaks for Q^1 and Q^3 tetrahedra. As the level of strontium doping increased from 0 to 10 mol%, the chain length of the glass significantly increased ($p<0.05$). Only with 10 mol% Sr doping was the type of strontium salt used for doping found to significantly impact chain length

($p<0.05$), with 10SrO-CPP glass from strontium phosphate having significantly greater chain length than that obtained using strontium carbonate. In addition, the Q^2 position became significantly more positive ($p<0.05$), and the FWHM of Q^2 significantly smaller ($p<0.05$) with the addition of 10 mol% SrO. A two-way ANOVA found that the interaction between strontium concentration and strontium salt was significant for chain length ($p = 0.032$), but not Q^2 position or FWHM of the Q^2 peak ($p>0.05$). It is important to note that the error associated with NMR is 2-5% and, as a result, the FWHM and Q^2 position analysis for the strontium-doped CPP should be considered in this context. A study of greater strontium doping concentrations is recommended in order to confirm these NMR observations.

Strontium doping was found to have a significant impact on the glass transition, crystallization, and melting temperatures of the CPP glass (Figure 4.6).

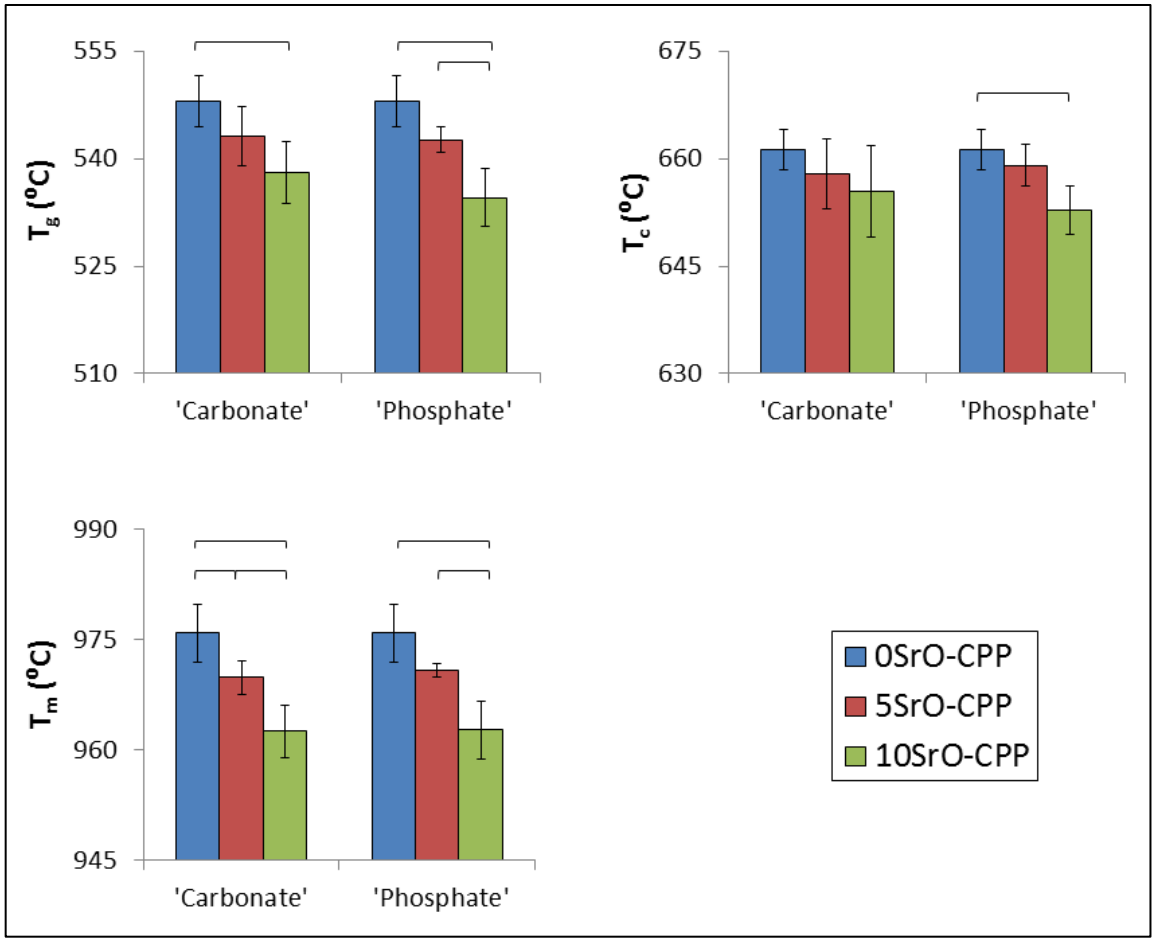

Figure 4.6: (Top left) Glass transition temperature, (top right) Crystallization temperature, and (bottom left) Melting temperature of xSrO-CPP. Data reported as average values while error bars represent one standard deviation (n=6). Horizontal bars represent significant difference ($p<0.05$).

Adding 10 mol% Sr to CPP glass resulted in a significant decrease in glass transition and melting temperatures (with no dependence on strontium salt). However, only phosphate-based Sr doping at 10 mol% resulted in a significant decrease in crystallization temperature. A two-way ANOVA found that the interaction between strontium concentration and strontium salt was not significant for any of the transition temperatures ($p>0.05$). The Pearson correlation between powder density and each of the reported transition temperatures (correlation: -0.965 to -0.985, $p<0.01$), as well as between chain

length and both glass transition and crystallization temperatures (correlation: -0.921 to -0.937, $p<0.05$) was found to be significant and strongly opposing. As either powder density or chain length of the glass increased, the aforementioned transition temperatures decreased. As transition temperatures is typically influenced by the flexibility of the chains, it is interesting that increasing chain length (which should reduce chain flexibility) is correlated so strongly with the decrease in these temperatures. However, as will be discussed later, structural glass theories could indicate the greater role strontium ion itself has on transition temperatures.

4.3.2 Strontium-Doped CPP Matrices

To load VCM into this CPP-based delivery system, the glass must be able to gel and entrap this antibiotic by physical adsorption during the drug loading (G1) stage. As shown in Figure 4.7, there is no significant dependence of strontium concentration or strontium salt on the ability to produce G1 disks or on their measured porosity.

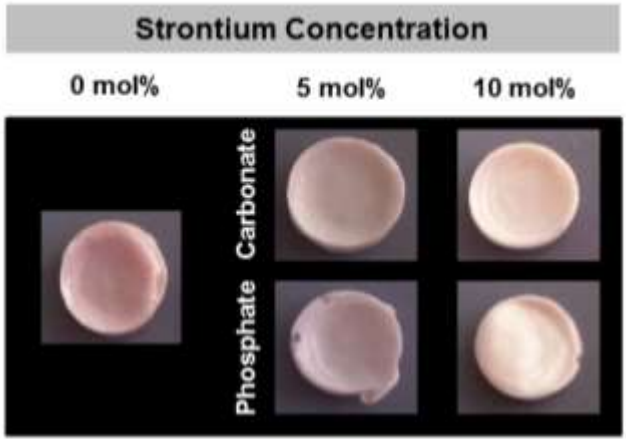

Sample Group	Disk Porosity (%)
0SrO CPP G1	30.97 ± 5.67[A]
5SrO CPP (Carbonate) G1	31.42 ± 6.66[A]
5SrO CPP (Phosphate) G1	31.51 ± 3.22[A]
10SrO CPP (Carbonate) G1	31.52 ± 4.40[A]
10SrO CPP (Phosphate) G1	31.75 ± 3.77[A]

Note: Means that do not share a letter are significantly different ($p<0.05$)

Figure 4.7: (Top) Images of xSrO-CPP G1 disks of varying strontium concentrations and from different strontium salt reagents, and (bottom) G1 disk porosity.

Strontium doping was shown, however, to alter the structural stability of the disks *in vitro* over a 7d period in 0.1M TBS (Figure 4.8 and 4.9).

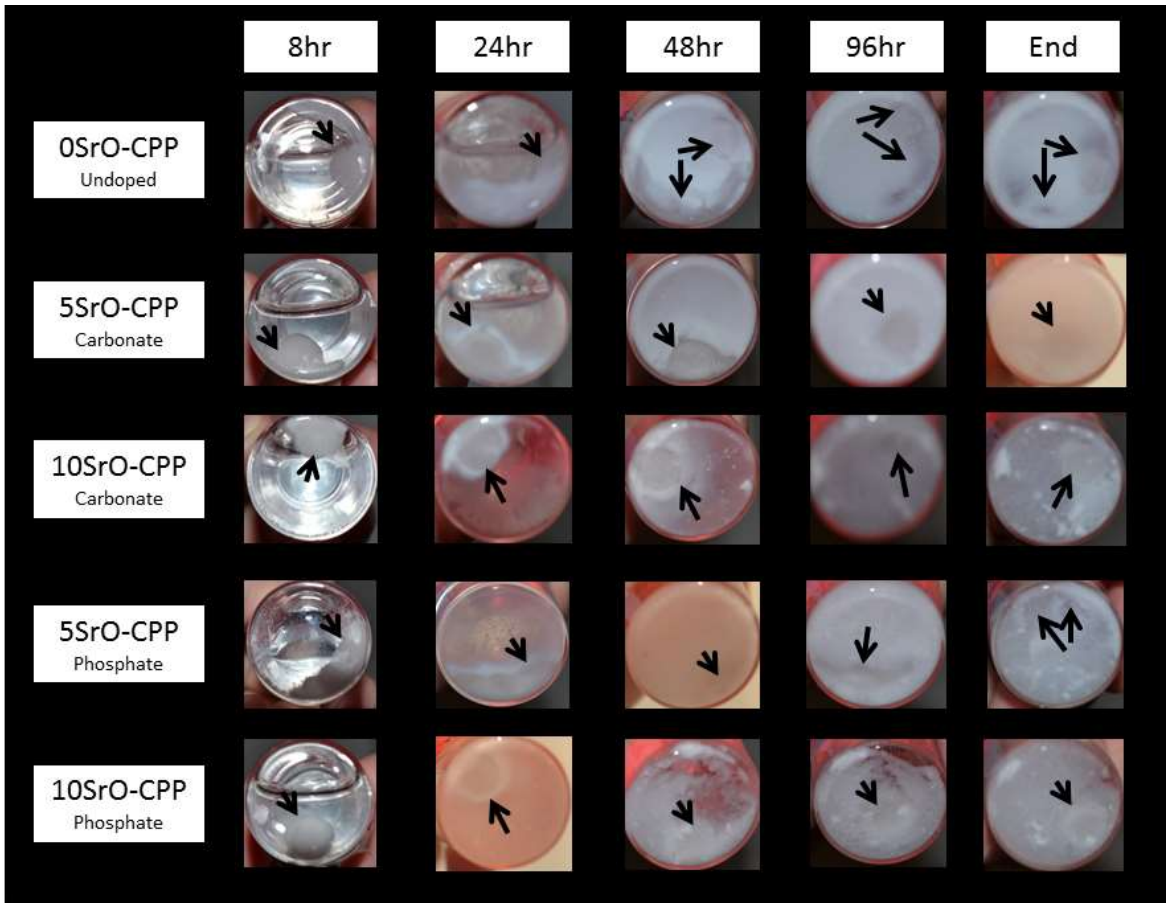

Figure 4.8: xSrO-CPP G1 disks at select time points in 0.1M TBS *in vitro*. Black arrow indicates disk location at bottom of vial (and multiple arrows indicate disk spread).

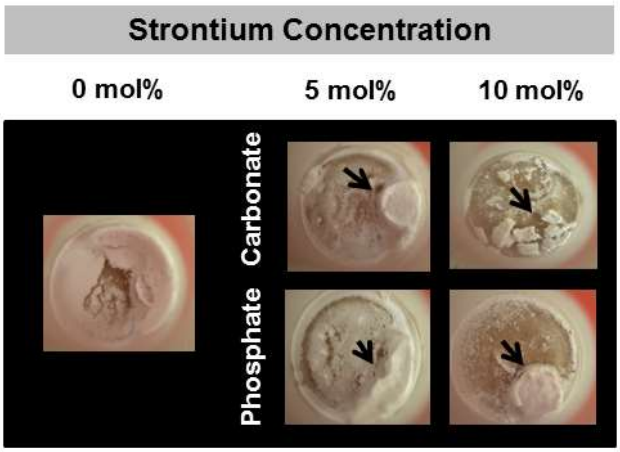

Figure 4.9: Dried xSrO-CPP G1 disks after 7d in 0.1M TBS and media removal. Black arrow indicates disk location at bottom of vial.

Adding 10 mol% SrO to the CPP-based glass using either strontium salt reagent appeared to improve the structural stability of the disks slightly during elution compared to the 0SrO-CPP disks (see Figure 4.8), as disk shape was maintained over the week spent in elution media at 37°C. However, it was not until the media had been removed at the end of the *in vitro* study and the G1 disks allowed to dry that there was a noticeable dependence on strontium salt. The strontium phosphate reagent yielded 10SrO-CPP G1 disks better able to handle hydration-dehydration compared to strontium carbonate reagent-based disks.

Ion release is a good indication of the progress of the chemical reactions involved in CPP degradation. In this elution study there was little significant difference in the fraction of available calcium, strontium or phosphorus ion content released from the different G1 sample groups over 7d (Figure 4.10). There was also little significant difference in the pH of the elution media (Figure 4.11).

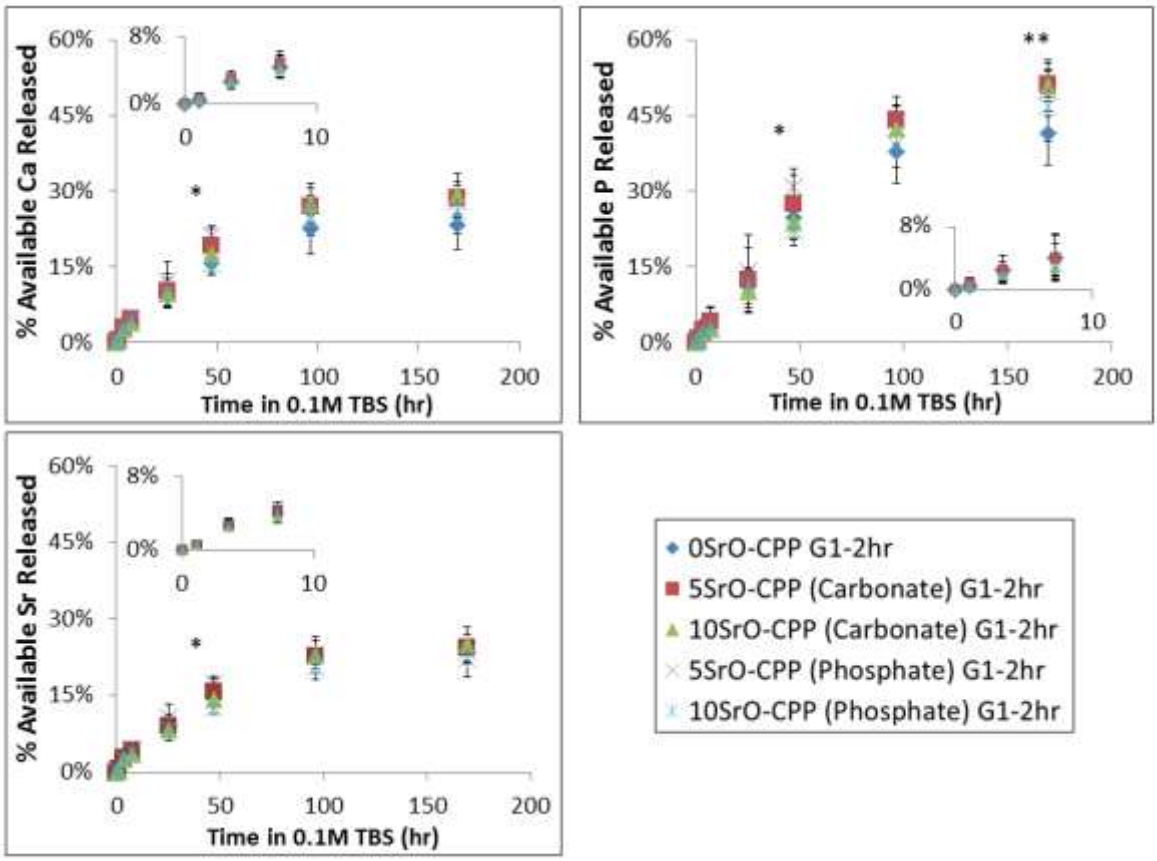

Figure 4.10: Release of (left) calcium and (right) phosphorus ions from xSrO-CPP G1 disks in 0.1M TBS (insert shows first 8hrs of release). Data reported as average values while error bars represent one standard deviation (n=6). 5SrO-CPP (phosphate) released significantly more % ion than 10SrO-CPP (phosphate) (*), while 0SrO-CPP released significantly less % ion than 5SrO-CPP (carbonate) (**) at indicated time points ($p<0.05$).

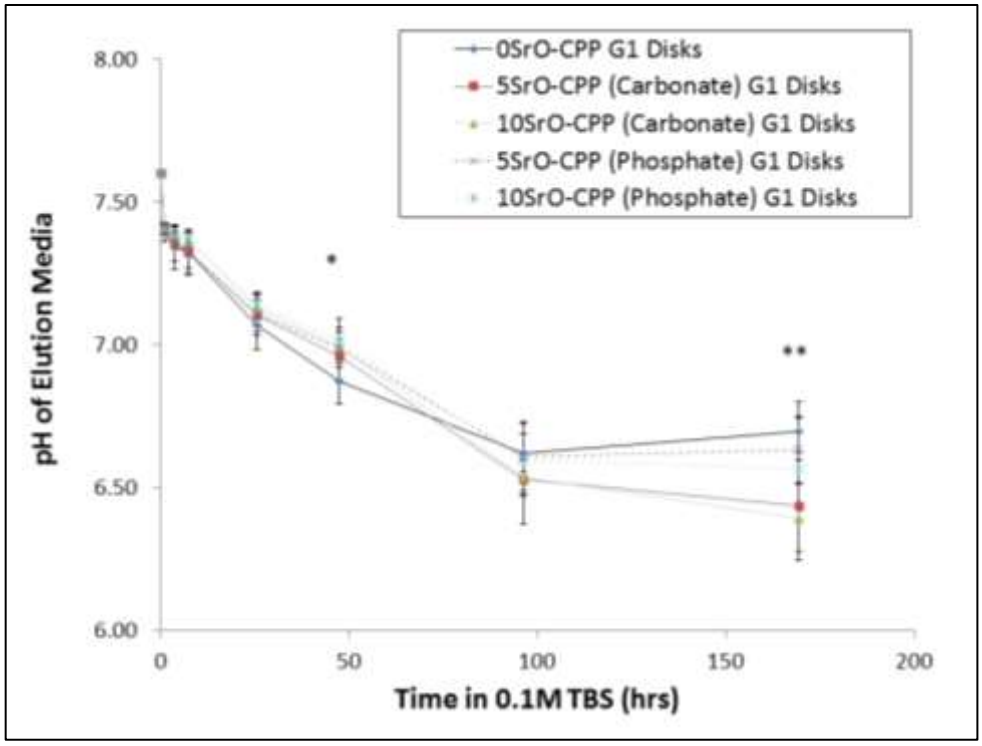

Figure 4.11: pH of elution media with xSrO-CPP G1 disks. Data reported as average values while error bars represent one standard deviation (n=6). 0SrO had a significantly lower pH than 5SrO- and 10SrO-CPP (phosphate) (*), while 0SrO had a significantly greater pH than 5SrO- and 10SrO-CPP (carbonate) (**) at indicated time points ($p<0.05$).

Only at the 47hr time point was there some dependence of calcium, phosphorus, and strontium ion release as well as elution media pH on strontium concentration, with 10SrO-CPP (phosphate) G1 disks releasing significantly fewer calcium, strontium and phosphorus ions than 5SrO-CPP (phosphate) G1 disks ($p< 0.05$). At this time point the media pH with 0SrO-CPP disks was also significantly lower than that observed with either phosphate-based or the 10SrO-carbonate-based disks ($p<0.05$).

For phosphorus ion release and pH the 169hr time point was also significant. Here, 0SrO-CPP G1 disks released significantly less total phosphorous and had a significantly

higher pH ($p<0.05$) than either G1 disk made from carbonate derived strontium-incorporated CPP G1 disks. In addition, a two-way ANOVA found that the interaction between strontium concentration and strontium salt was not significant for G1 ion release or pH measurements ($p>0.05$). Lastly, the Pearson correlation between glass chain length and the release of ions *in vitro* was not found to be significant ($p>0.05$). However, the Pearson correlation between calcium and strontium ion release from G1 disks was consistently strong, positive and significant during elution study (correlation: >0.95, $p<0.05$): the greater the amount of calcium released, the more strontium that was also released.

Owing to some concern over the stability of carbonate-based 10SrO-CPP disks after two stages of gelling and drying, as well as more moles of impurities needing to be released per mole of starting strontium carbonate (e.g. H_2O), the G2 disks were fabricated with phosphate-based xSrO-CPP glass powder only. In addition, for subsequent G2 disk studies only 10% doping of strontium was evaluated given the enhanced disk stability observed in G1 disk studies.

As found with G1 disk production, Sr doping did not impact G2 disk production steps, where compaction of G1 glass powders and a secondary gelling step is required (Figure 4.12). In addition, doping CPP with 10mol% Sr did not significantly impact VCM loading efficiency of G1 powder (L_{eff}) or final G2 matrix porosity (Table 4.2). Loading efficiency of the G1 powder fabricated in this study matched that previously reported (Dion *et al*., 2005).

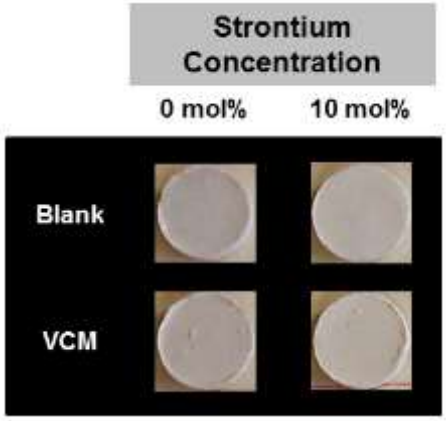

Figure 4.12: xSrO-CPP G2 disks.

Table 4.2: xSrO-CPP G1 powder VCM Loading Efficiency and G2 disk porosity

Matrix Composition	G1 Powder VCM Loading Efficiency(%)	G2 Disk Porosity (%)
Blank 0SrO-CPP (Phosphate) G2	-	30.63 ± 7.02^{A}
Blank 10SrO-CPP (Phosphate) G2	-	38.89 ± 5.37^{A}
VCM 0SrO-CPP (Phosphate) G2	94.53 ± 2.72^{A}	35.48 ± 3.27^{A}
VCM 10SrO-CPP (Phosphate) G2	96.03 ± 3.63^{A}	34.02 ± 2.91^{A}

Note: Means that do not share a letter are significantly different ($p<0.05$)

Figure 4.13 shows SEM images of the surface of an intact disk at the centre and of the "inside edge" of a freshly sectioned disk.

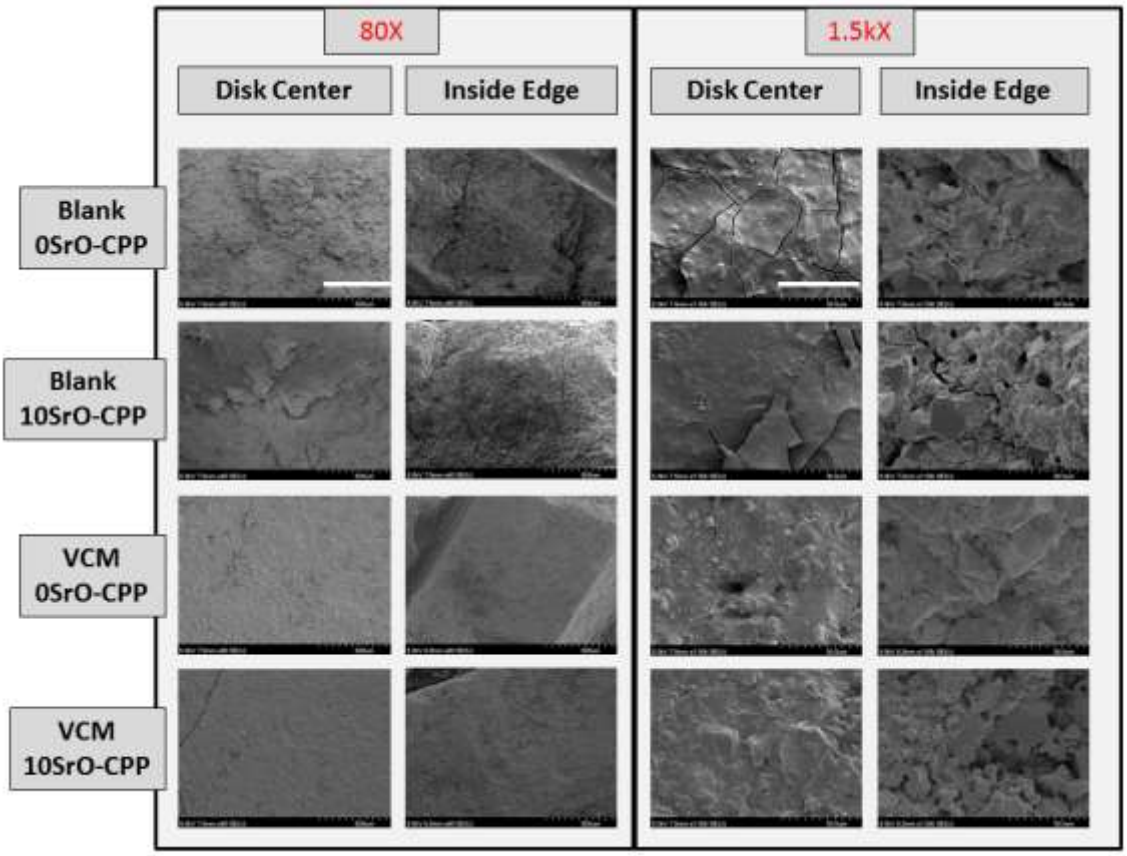

Figure 4.13: SEM Images of xSrO-CPP G2 disks with (left) 80X magnification (500µm scale bar), and (right) 1500X magnification (30µm Scale Bar).

Although sample size for SEM imaging was small and placed a significant limitation on any conclusions, these images still give some insight into the potential impact of strontium and VCM doping on final G2 disk macrostructure. For example, VCM-loaded G2 disks appeared to have a slightly smoother external surface at the disk center and inside edge compared to blanks. Strontium doping also resulted in a slightly smoother external surface for the blank disks, although VCM loading appears to overwhelm any differences that might emerge; strontium doping did not similarly impact VCM-loaded disks.

In the *short-term* (e.g. 24hrs) period spent *in vitro* the loading of CPP G2 disks with VCM seemed to improve disk stability (Figure 4.14). However, strontium doping appeared to have a greater impact on the *long-term* structural stability of the disks *in vitro* (Figure 4.14). All disks expanded significantly upwards without the assistance of vertical constraints to guide this directionality (Figure 4.15).

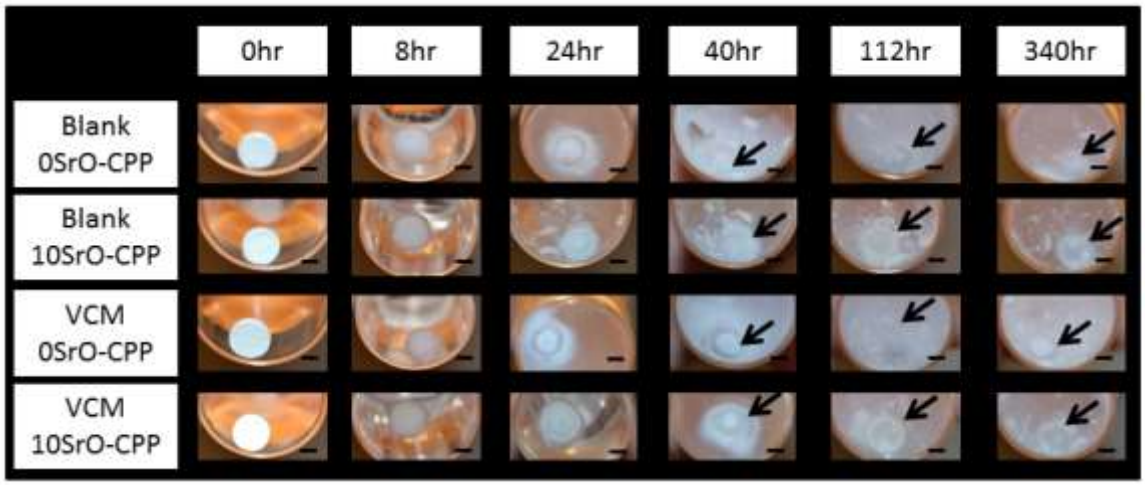

Figure 4.14: xSrO-CPP maintained in 0.1M TBS at 37^{0}C and observed at several time points. Arrows indicate matrices in media. Scale bars in each image represent 4mm.

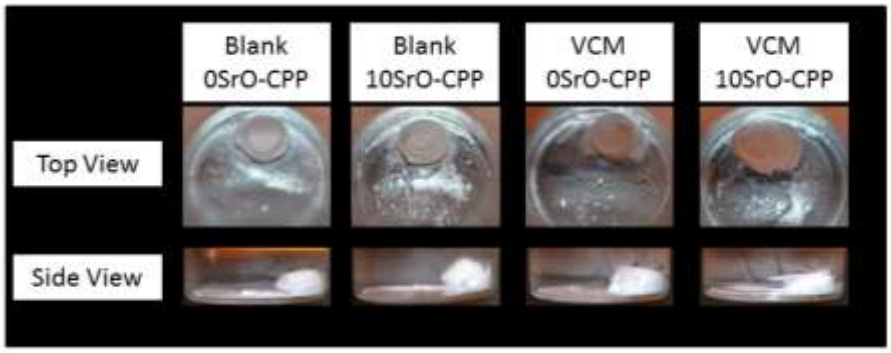

Figure 4.15: (Top) Top-view and (bottom) Side-view images of xSrO-CPP G2 disks following a two-week elution study and after media removal.

Corresponding reductions in ion release or media pH drop, both of which serve as good indications of the progress of chemical reactions involved in CPP degradation, were not consistently observed with 10 mol% Sr doping of the matrices, however (Figure 4.16 – 4.18). The table that follows (Table 4.3) indicates the significant pairs at given time points for pH, and calcium and phosphorus ion release.

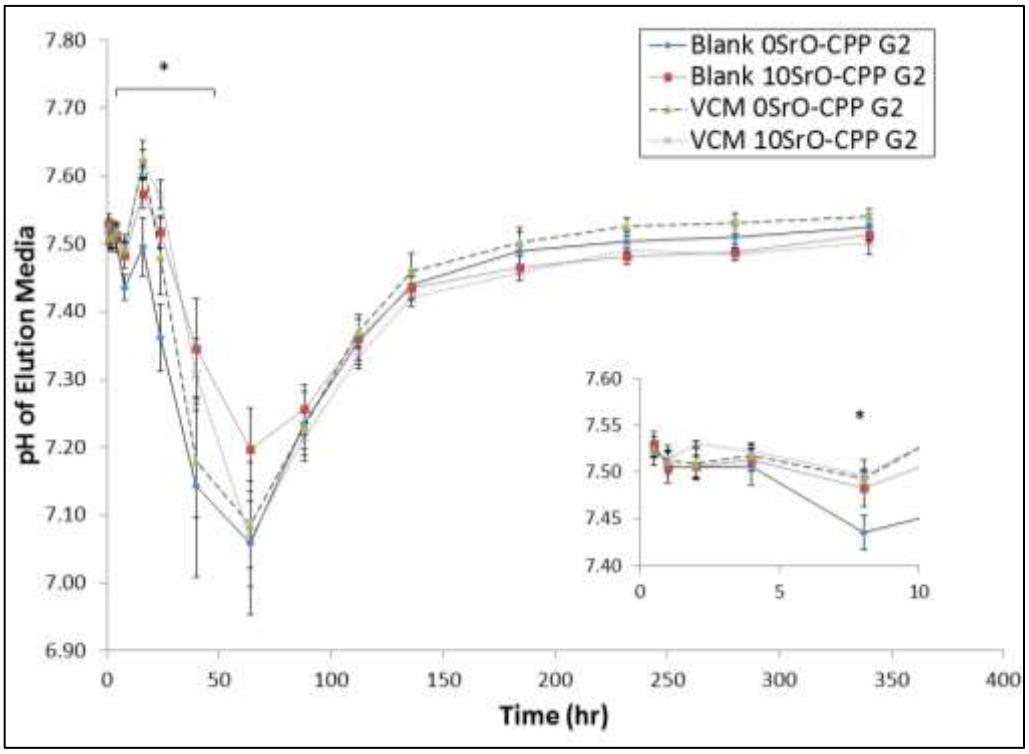

Figure 4.16: pH of elution media with xSrO-CPP G2 matrices (insert shows first 8hrs of release). Data reported as average values while error bars represent one standard deviation (n=6). Blank 10SrO-CPP extracts had a significantly higher pH than blank 0SrO-CPP (*) at indicated time points ($p<0.05$).

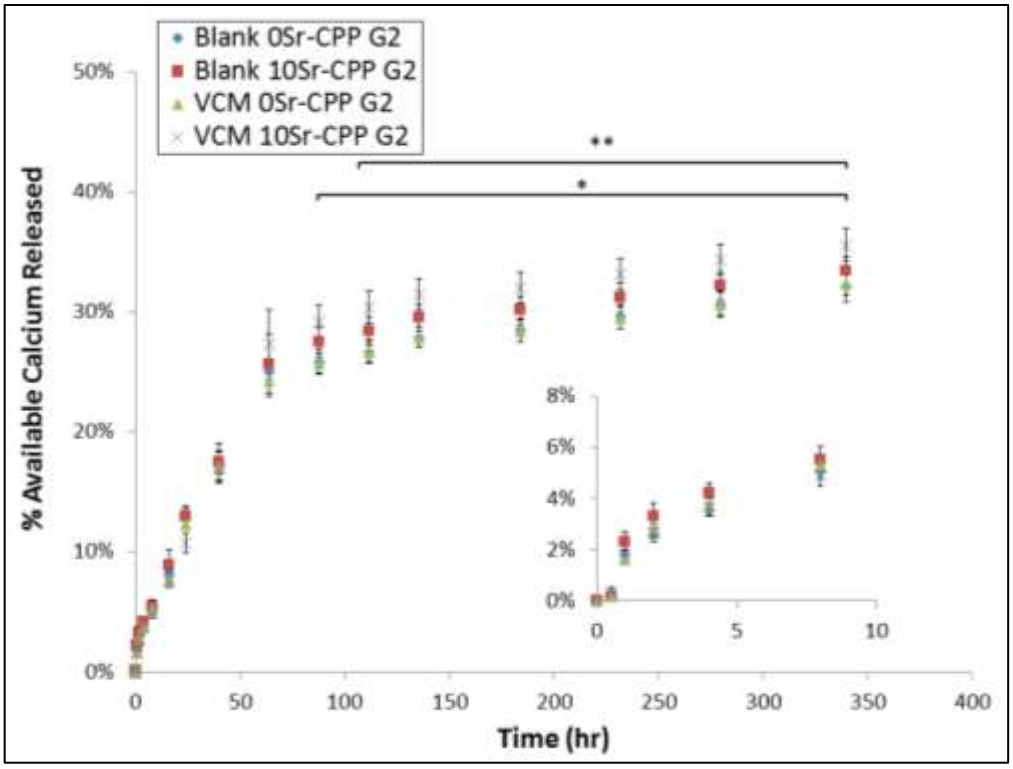

Figure 4.17: Cumulative calcium ion release from xSrO-CPP G2 matrices (insert shows first 8hrs of release). Data reported as average values while error bars represent one standard deviation (n=6). VCM 10SrO-CPP released significantly more % available calcium than VCM 0SrO-CPP (*) and blank 10SrO-CPP (**) at indicated time points ($p<0.05$).

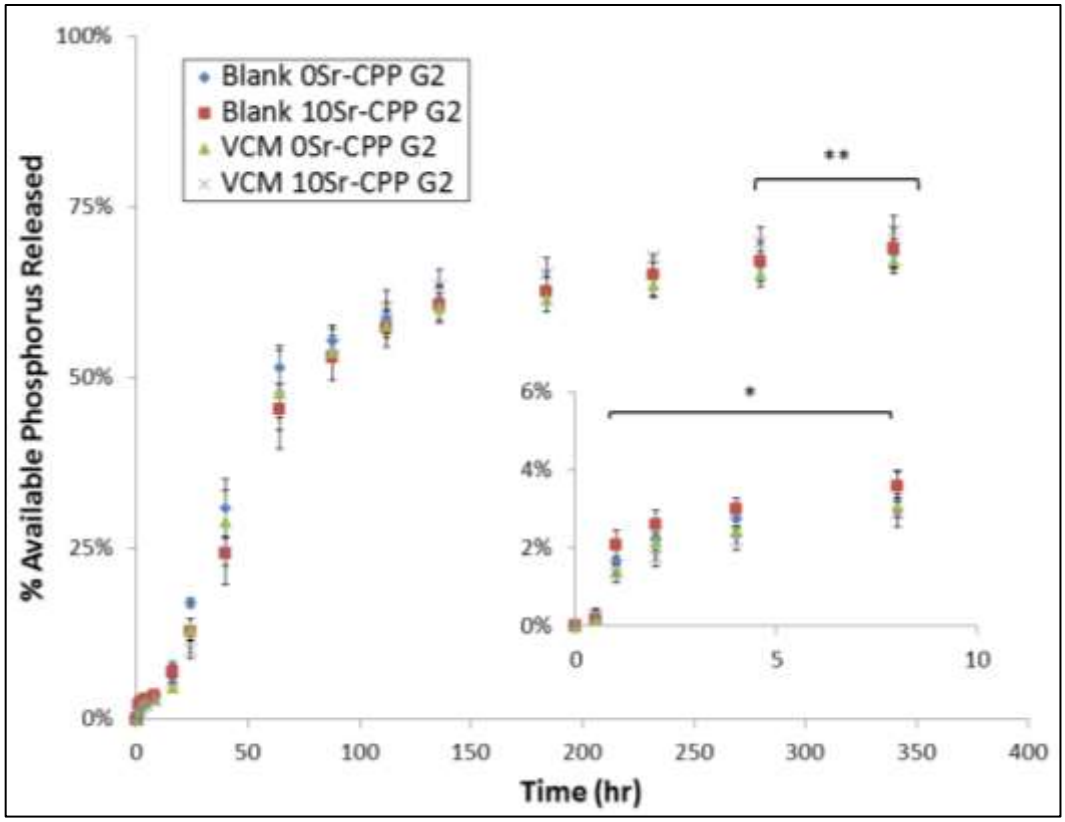

Figure 4.18: Cumulative phosphorus ion release from xSrO-CPP-based G2 matrices (insert shows first 8hrs). Data reported as average values while error bars represent one standard deviation (n=6). VCM 10SrO-CPP released significantly less % available phosphorous than blank 10SrO-CPP (*), and significantly more % available phosphorous than VCM 0SrO-CPP (**) at indicated time points ($p<0.05$).

Table 4.3: xSrO-CPP G2 disk elution study results with significant pairs indicated (p<0.05) (n=6).

Time	2hr	4hr	8hr	16hr	24hr	40hr	64hr	88hr	112hr	136hr	184hr	232hr	280hr	340hr
pH of Elution Media														
Blank 0SrO-CPP	7.51^{B} (0.01)	7.51 (0.02)	7.44^{B} (0.02)	7.50^{C} (0.04)	7.36^{C} (0.05)	7.14^{C} (0.13)	7.06 (0.06)	7.24 (0.05)	7.36 (0.03)	7.44^{A,B} (0.02)	7.49^{A,B} (0.03)	7.50^{B} (0.02)	7.51^{A,B} (0.02)	7.52^{A,B} (0.02)
Blank 10SrO-CPP	7.51^{B} (0.01)	7.51 (0.01)	7.48^{A} (0.02)	7.57^{B} (0.02)	7.52^{A,B} (0.02)	7.35^{A} (0.07)	7.20 (0.06)	7.26 (0.04)	7.36 (0.03)	7.44^{A,B} (0.02)	7.47^{B} (0.02)	7.48^{C} (0.01)	7.49^{B,C} (0.01)	7.51^{B} (0.01)
VCM 0SrO-CPP	7.51^{B} (0.02)	7.52 (0.01)	7.49^{A} (0.01)	7.63^{A} (0.03)	7.48^{B} (0.06)	7.18^{B,C} (0.08)	7.09 (0.06)	7.23 (0.05)	7.37 (0.02)	7.46^{A} (0.03)	7.50^{A} (0.02)	7.53^{A} (0.01)	7.53^{A} (0.02)	7.54^{A} (0.01)
VCM 10SrO-CPP	7.53^{A} (0.00)	7.52 (0.01)	7.50^{A} (0.02)	7.62^{A,B} (0.02)	7.57^{A} (0.02)	7.31^{A,B} (0.05)	7.07 (0.11)	7.21 (0.02)	7.33 (0.02)	7.42^{B} (0.01)	7.46^{B} (0.01)	7.49^{B,C} (0.01)	7.49^{C} (0.01)	7.50^{B} (0.02)
% Available Calcium Released														
Blank 0SrO-CPP	2.58^{B} (0.26)	3.57^{B} (0.24)	5.03^{A,B} (0.25)	8.14^{A,B} (0.33)	12.81^{A} (0.79)	17.11 (1.22)	25.04^{A} (1.08)	25.85^{B} (0.98)	26.70^{B} (0.99)	27.92^{B} (0.92)	28.48^{B} (0.96)	29.58^{B} (0.98)	30.65^{B} (1.09)	32.13^{B} (1.29)
Blank 10SrO-CPP	3.30^{A} (0.50)	4.21^{A} (0.38)	5.52^{A} (0.50)	8.94^{A} (1.29)	12.98^{A} (0.84)	17.55 (1.50)	25.69^{A} (2.45)	27.64^{A,B} (1.49)	28.52^{B} (1.47)	29.65^{B} (1.39)	30.28^{B} (1.43)	31.35^{B} (1.47)	32.31^{B} (1.43)	33.56^{B} (1.42)
VCM 0SrO-CPP	2.48^{A,B} (0.41)	3.76^{A,B} (0.21)	5.31^{A,B} (0.16)	7.73^{A,B} (0.64)	12.37^{A} (0.44)	17.12 (1.32)	24.26^{A} (1.30)	25.76^{B} (0.82)	26.68^{B} (0.86)	27.89^{B} (0.86)	28.39^{B} (0.93)	29.52^{B} (0.94)	30.66^{B} (0.97)	32.40^{B} (1.04)
VCM 10SrO-CPP	2.65^{B} (0.36)	3.66^{B} (0.37)	4.91^{B} (0.44)	7.57^{B} (0.25)	10.81^{B} (0.82)	17.00 (0.46)	27.29^{A} (2.85)	29.17^{A} (1.38)	30.40^{A} (1.36)	31.45^{A} (1.29)	32.03^{A} (1.29)	33.14^{A} (1.28)	34.34^{A} (1.26)	35.57^{A} (1.32)
% Available Phosphorus Released														
Blank 0SrO-CPP	2.22^{A,B} (0.11)	2.76^{A,B} (0.23)	3.58^{A} (0.41)	7.54^{A} (0.64)	17.05^{A} (0.74)	30.99^{A} (4.30)	51.58 (2.52)	55.47 (2.29)	58.78 (2.29)	61.52 (1.99)	62.88 (1.98)	65.00^{A,B} (1.95)	66.57^{A,B} (2.01)	68.39^{A,B} (2.12)
Blank 10SrO-CPP	2.61^{A} (0.34)	2.99^{A} (0.30)	3.59^{A} (0.36)	6.88^{A,B} (1.58)	12.90^{B} (0.82)	24.27^{B} (4.47)	45.46 (5.88)	52.98 (3.27)	57.35 (2.76)	60.79 (2.66)	62.64 (2.86)	65.14^{A,B} (3.02)	67.06^{A,B} (2.91)	69.07^{A,B} (2.94)
VCM 0SrO-CPP	2.15^{B,C} (0.24)	2.43^{B,C} (0.13)	3.07^{A,B} (0.30)	4.74^{C} (0.67)	13.19^{B} (1.62)	29.05^{A,B} (4.56)	47.89 (3.62)	53.94 (1.67)	57.83 (1.88)	60.39 (1.88)	61.66 (1.96)	63.80^{B} (1.97)	65.40^{B} (1.98)	67.29^{B} (1.97)
VCM 10SrO-CPP	1.77^{C} (0.24)	2.21^{C} (0.26)	2.91^{B} (0.37)	5.57^{B,C} (0.18)	10.24^{C} (1.27)	24.54^{B} (1.98)	48.67 (6.18)	54.73 (2.42)	60.25 (2.57)	63.56 (2.36)	65.30 (2.42)	67.73^{A} (2.31)	69.88^{A} (2.15)	71.65^{A} (2.12)

Note1: Values reported as mean (standard deviation)

Note2: Grey columns show no significant dependence on strontium addition or VCM loading with two-way ANOVA (p>0.05)

Note3: Means that do not share a letter are significantly different at the given time point (p<0.05).

After roughly 88hrs (~4d) into the G2 disk study, extract pH began to recover and stabilized towards the initial pH of the buffer solution for all samples (Figure 4.16). In addition, the two-way ANOVA interaction between the two study variables (strontium doping and VCM loading) was found to be significant ($p<0.05$) for the fraction of available calcium released at most elution time points. For example, the VCM 10SrO-CPP G2 disks released significantly more available calcium than VCM 0SrO-CPP disks after 88hr ($p<0.05$), and than *blank* 10SrO-CPP disks after 112hrs ($p<0.05$).

In contrast to calcium ion release, phosphorus ion release was not significantly dependent on either strontium doping or VCM loading for most of the elution study (with a few exceptions). A two-way ANOVA confirmed that the interaction between strontium doping and VCM loading was significant ($p<0.05$) for the fraction of available phosphorus released at only a few time points. For example, for the first 8 hrs in media blank 10SrO-CPP G2 disks released significantly more phosphorus than those of VCM-loaded 10SrO-CPP ($p<0.05$), while after 280hrs VCM 10SrO-CPP G2 disks released significantly more phosphorus than those of VCM 0SrO-CPP ($p<0.05$).

Similar to calcium ion release, strontium ion release was dependent on VCM doping towards the end of the elution study (Figure 4.19).

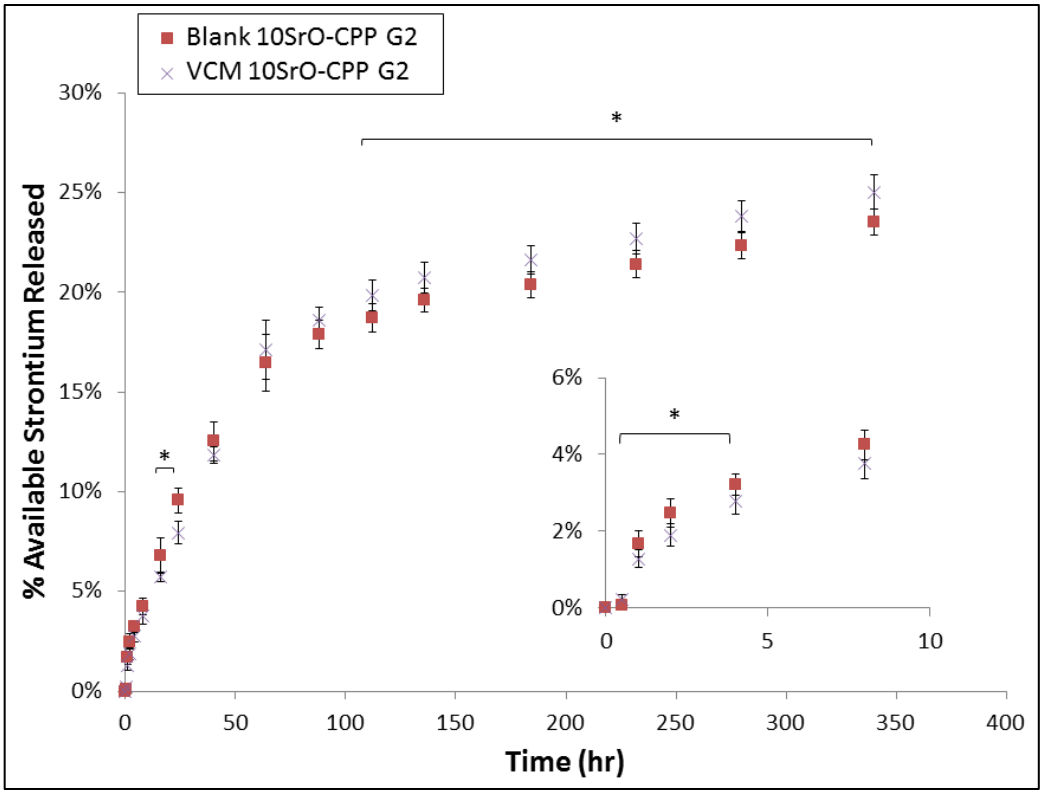

Figure 4.19: Cumulative strontium ion release from xSrO-CPP-based G2 matrices (insert shows first 8hrs of release). Data reported as average values while error bars represent one standard deviation (n=6). VCM loading has a significant impact on % available strontium released (*) at indicated time points ($p<0.05$).

VCM 10SrO-CPP G2 disks released a significantly greater fraction of available strontium ions than the blank disks after 112hrs ($p<0.05$). As additional evidence, the cation-to-phosphorus ion ratios in the collected media confirm the aforementioned impact of strontium addition and VCM loading on G2 degradation (Appendix A: Figure A5). As the elution study progressed, the proportion of phosphorous ion released increased relative to that of the cations, with phosphorous ions predominantly being released after 24 hr. As phosphorous makes up the backbone of the CPP structure it is not surprising that we visually observe some loss of matrix integrity after 24hrs (and an increase in presence of disk debris). In addition, there is a noteable drop in fraction of available ion

released after 4d for calcium, phosphorus, and strontium. This plateau may be attributed to debris that has not been accounted for and/or the formation of more stables phases within or on the surfaces of the CPP disks. The remnant G2 disk cation-to-phosphorus ion ratios presented in Appendix A (Figure A6) provide some support to the latter theory (as the ratios are higher than the stoichiometric ratio of ~0.5).

Strontium doping of these matrices was found to have an impact on VCM release at later elution study time points, similar to that observed with calcium ion release (Figure 4.20). After 88hrs 10SrO-CPP matrices released significantly more cumulative VCM than 0SrO-CPP ($p<0.05$), although after 112hrs very little additional VCM is released from either set of disks.

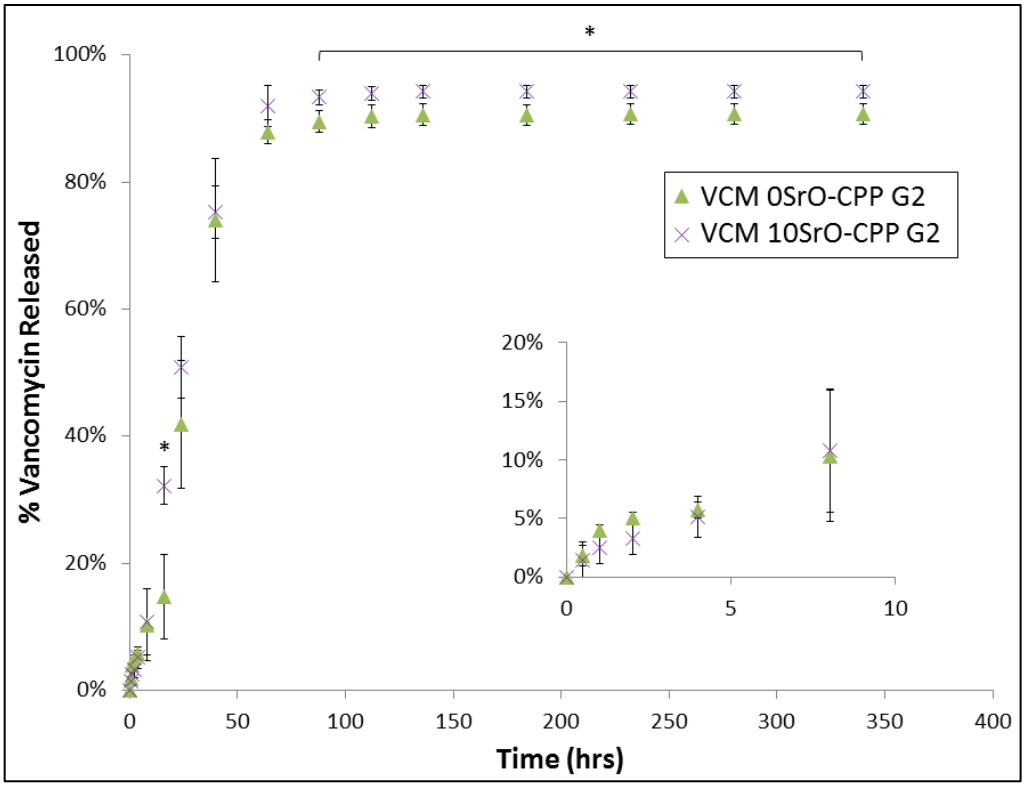

Figure 4.20: Cumulative VCM release from xSrO-CPP G2 matrices in 0.1M TBS (insert shows first 8hrs of release). Data reported as average values while error bars represent one standard deviation (n=6). Strontium doping has a significant impact on % available VCM released (*) at indicated time points ($p<0.05$).

4.3.3 Functional Assays with Strontium-Doped CPP G2 Matrices

Overall, the fraction of available ions (i.e. calcium, phosphorus, and strontium) and VCM released after leaving the elution set-up undisturbed for 24hr (Figure 4.21) was comparable to that reported previously using multiple time point media extractions (as reported in section 4.3.2).

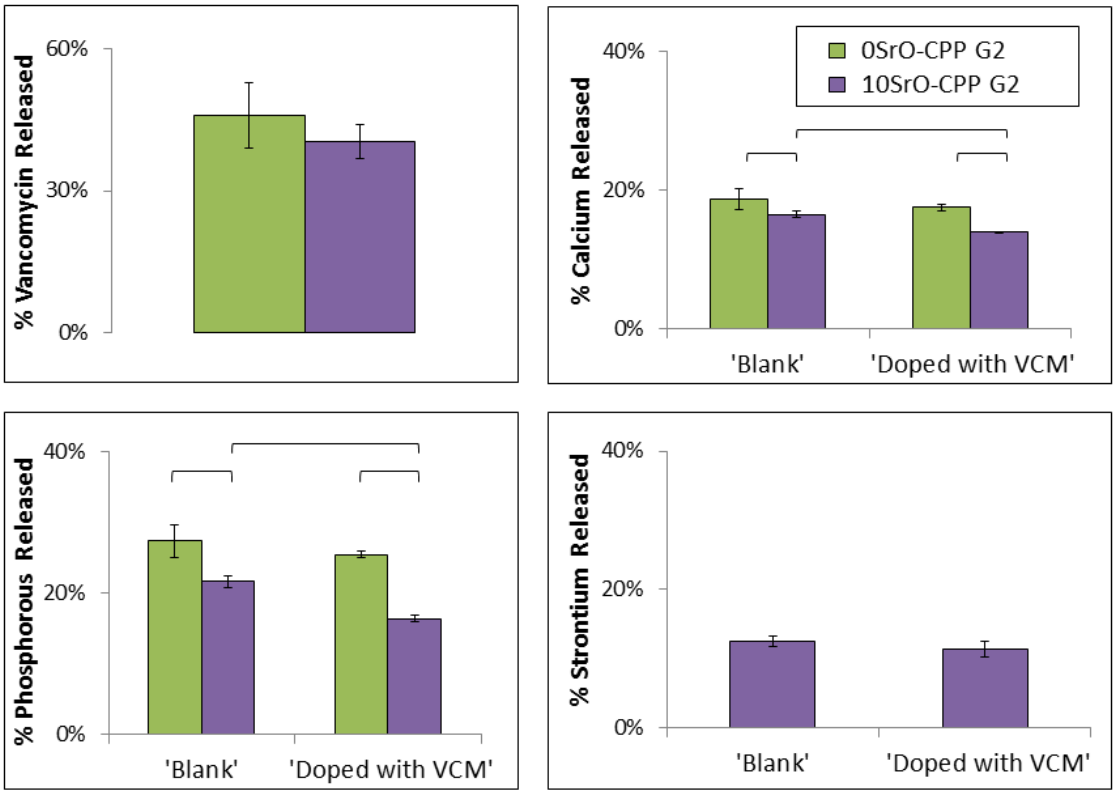

Figure 4.21: Fraction of (top left) Available VCM released, (top right) Available calcium released, (bottom left) Available phosphorus released, and (bottom right) Available strontium released from G2 matrices after 24hrs. Data reported as average values while error bars represent one standard deviation (n=3). Horizontal bars represent significant difference ($p<0.05$).

The standard MTT cytotoxicity test is based on the measurement of cell viability via metabolic activity (ISO 10993-5, 2009). As shown in Figure 4.22 the addition of extracts containing strontium and/or VCM to the culture media (at both full concentration and diluted 50%) did not significantly impact cell cytocompatibility compared to undoped, blank matrices (all relative to the TBS control).

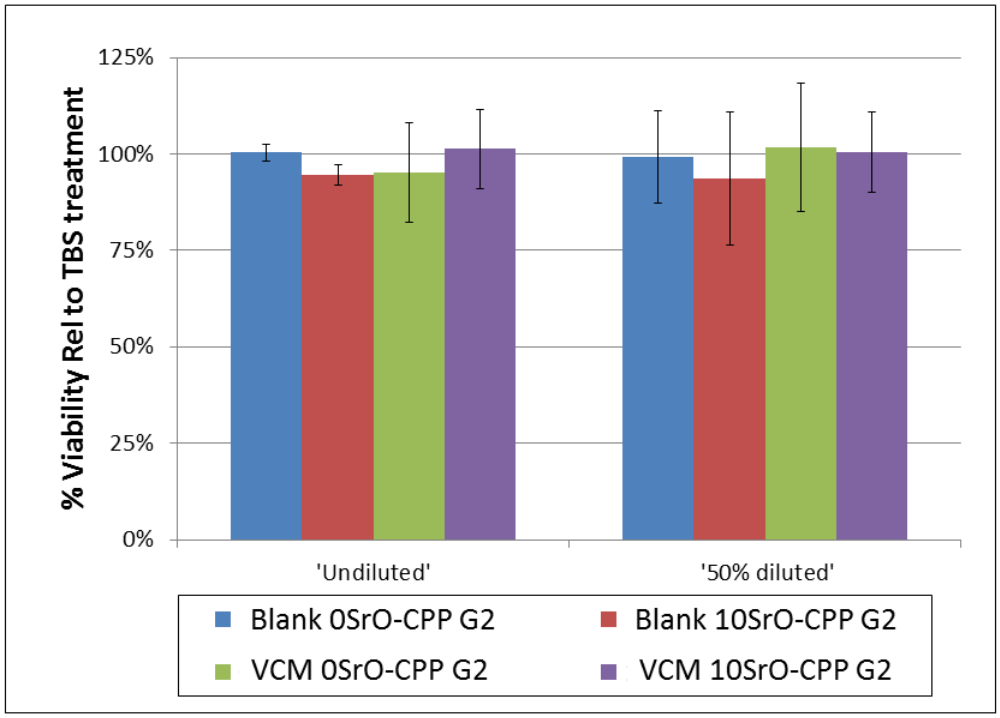

Figure 4.22: Cell viability following indirect 24hr exposure to elution extract relative to 0.1M TBS-only treatment. Data reported as average values while error bars represent one standard deviation (n=3). There is no significant difference to report ($p<0.05$).

Notably, the cell control (i.e. cells + DMEM only) had a cytocompatibility only ~10% greater than the positive reagent control (i.e. cells + 0.1M TBS only) – indicative of no significant cytotoxicity introduced by the buffer solution itself.

The micro-dilution assay confirmed that VCM activity was maintained after loading into the xSrO-CPP glass powder and subsequent G2 disk fabrication when compared to the stock VCM solution, with a significantly decreased turbidity for *S.aureus* at the standardized minimum inhibitory concentration of 1-2µg/mL. Previous studies have also demonstrated the relatively benign nature of the G2 matrix fabrication process (Dion *et al*., 2005; Petrone *et al*., 2008).

4.4 DISCUSSION

For the *first time* a strontium-incorporated CPP glass that has been fabricated by modifying the calcine-melt protocol for un-doped CPP is reported. To date strontium-doped CPP reported fabrication has consisted of adding a strontium salt at phosphoric acid flux stage and precipitating out a strontium-doped CPMM prior to a calcine and melt (Chen, Y. *et al*., 2008; Chen, Y. *et al*., 2008-b; Qiu, K.(b) *et al*., 2006; Song, W. *et al*., 2009). To simplify this protocol – and recalling the multitude of factors that influence the properties of CPP precipitates and will likely make ion doping less controllable - the strontium salt reagent was mixed with CPMM in powder form and then the mixture was calcined and melted. The production of other phosphate glasses has commonly employed such a simplified protocol with the use of carbonate-based salts; here, the goal was to apply the simplified protocol with consideration of *two* different strontium salts, strontium carbonate and strontium phosphate (Gao *et al*., 2004; Gao *et al*., 2004-b; Lakhkar *et al*., 2010; Neel *et al*., 2008; Pires *et al*., 2004; Gentleman *et al*., 2010).

Adding 10 mol% strontium to the CPP increased the density and chain length of the glass without nominally changing the arrangement of bonds in the polymeric structure (e.g. P-O-P or PO_2). Despite some indication by ATR-FTIR that there was little change to the next-nearest neighbour environment around the phosphate network with strontium doping (e.g. P-vs-P, P-vs-cation), further examination of the ^{31}P MAS NMR spectra seemed to suggest otherwise. Changing the next-nearest neighbour environment by substituting some of the calcium for strontium should still alter the glass structure enough for

differences to be visible in the NMR spectrum (Brow, R. *et al*., 1991) and in the performance of the glass (Brow, R. 2000). It is well accepted that a change in field strength (equation 1.1) or ionic potential (i.e. Z = charge/radius) of the cation has a significant impact on both the position and breadth of the peaks in the ^{31}P spectra (Brow, R. *et al*., 1991). Decreasing the ionic potential and electronegativity by adding strontium increases the electron density on phosphorus such that the "effective" electronegativity of oxygen is reduced (with respect to phosphorus) and the shielding at phosphorus is decreased (i.e. shift more positive) (Delahaye, F. *et al*., 1999; Brow, R. *et al*., 1991). In addition, observed decreases in FWHM of the Q^2 peak with strontium concentration may be indicative of reduced glass disorder (Brow, R. *et al*., 1991); there is less heterogeneity in the amorphous PO_2 environment as more strontium is incorporated and the phosphate chains are lengthened, which in turn gives rise to a narrowed Q^2 band (Pemberton, J. *et al*., 1991).

Thermal analysis further revealed that doping CPP glass with 10 mol% Sr resulted in a significant decrease in the glass transition and melting temperatures measured (compared to undoped CPP). To better understand the ease of glass formation and driving force for crystallization and melting as a result of cation substitution, there are several classification systems that could be considered. Currently, the most commonly used system to classify metal cations is Dietzel's field strength (Equation 1.1, Section1.3.1). This system measures the electrostatic energy between the metal cations and the neighbouring oxygen anions. As the field strength is lower for strontium (0.28) than calcium (0.33) (Sales *et al*., 1998), doping CPP with strontium narrows the distribution of

phosphate anions in the glass (as previously indicated in the NMR analysis) and further weakens the glass network (i.e. more open structure). This in turn leads to greater resistance to glass formation upon cooling (Sales *et al*., 1998; Avramov *et al*., 2005)). The ordering of free energy of formations for cations in simple phosphate glass is another system (Sales, B. *et al*, 1998). This scheme is largely similar to Dietzel's classification using field strength and orders strontium similar to calcium ions with respect to ease of glass formation. As strontium ion has a higher free energy of formation than calcium ion in simple phosphate glass, doping CPP with 10 mol% strontium is again predicted to increase resistance to glass formation (i.e. reduce T_g) upon cooling and provide a larger driving force for crystallization. In other words, the activation energy of crystal growth is reduced upon doping CPP with strontium (Lahl *et al*., 2000). Therefore, despite a greater chain length upon doping CPP with 10 mol% strontium, the presence of strontium ion itself appears to contribute more to the reported transition temperatures of the glass powders.

In this study there was no significant dependence of strontium doping on G1 or G2 disk fabrication or measured porosity. However, doping CPP with 10 mol% strontium resulted in noticeable differences in G1 and G2 disk structural stability *in vitro*. To explain these observations it is perhaps most revealing that the fraction of strontium released is less than that for calcium. It is important to recall that erosion involves hydration of the matrices, dissolution of the chains (with chain relaxation) and network breakage (Maderuelo *et al*., 2011; Ahola *et al*., 2014); the presence of strontium may impact any or all of these steps. With a lower field strength than calcium the presence of

strontium should increase the "openness" of the glass structure and improve aqueous media access. However, owing to the greater phosphate chain ionization of the CPP-based glass with strontium doping (Jia *et al*., 2009), the water dipole is less able to approach the phosphate chain and hydration that does occur is accompanied by stronger electrostatic interactions in the hydrated layer compared to undoped CPP. Altogether, by slowing the development of a hydration layer the subsequent dissolution of strontium-doped CPP glass is impeded. Strontium itself may also become trapped in this hydrated layer. Recalling that the measured fraction of available strontium released from the disks was less than that for calcium, it is likely that it was the impact of strontium doping on hydration and not dissolution that primarily delayed the erosion of the strontium-doped disks. For example, with a lower bonding strength the Sr-O bond should be more readily broken in dissolution (Gentleman *et al*., 2010; Akamatsu *et al*., 2005); if dissolution was the primary player in the CPP disk erosion the proportion of available strontium released should be equivalent or greater than that of calcium. Altogether, with a higher starting phosphate chain length, decreased structural disorder, and greater phosphate chain ionization of the CPP-based glass, strontium doping will significantly impact disk hydration such that the phosphate chain relaxation and dissolution of the matrices is noticeably delayed. After approximately 4 days spent *in vitro* the differences in CPP *dissolution* due to strontium doping begin to make a more noteable contribution to disk stability, as evidenced by the plateauing of available ions released and the slightly greater release of VCM from strontium-doped G2 disks compared to undoped. As mentioned previously, the presence of more stable phases within the CPP disks may have led to the observed decrease in the fraction of available ion released after 4 days (i.e. "plateauing").

The steps involved in the fabrication of strontium- and VCM-loaded CPP G2 disks did not have a detrimental impact on the cytocompatibility or antibiotic efficacy of the disks. These results are not surprising given the early success of fabricating antibiotic-loaded CPP matrices; both antibiotic stability and efficacy have previously been confirmed (Dion *et al*., 2005; Petrone *et al*., 2008; Kim *et al*., 2008). It is possible that, if degradation had been more significantly reduced (and media pH change further minimized), doping amorphous CPP with strontium may have *improved* the viability of the NIH 3T3 cells. In fact, Qiu, K(b) *et al* (2006) observed in their MTT test that the viability of osteoblastic cells on 10 mol% strontium-doped *crystalline* CPP after 1 day was greater than that for undoped CPP. The greater degradation of amorphous CPP compared to crystalline CPP (Qiu, K(a) *et al* (2006), as well as differences in test set-up, may account for the differences observed on the impact of strontium doping on cell viability in this study and that by Qiu, K(b) *et al* (2006). Together the functional assays performed in this study and the preceding conclusions obtained through glass study and disk elution provide further support towards the development of a therapeutically loaded local delivery system.

4.5 STUDY LIMITATIONS

It is important to acknowledge that this chapter considers two strontium levels (5, 10mol%) and two salts during characterization of the CPP-based glass and G1 disks, while further analysis of G2 disks is limited to one level of both strontium (10 mol%) and VCM (7.5mg/150mg CPP). Trends and other study observations reported are applicable

within these study constraints. The upper limit of 10mol% strontium was chosen owing to prior degradation and osteocompatibility studies of crystalline strontium-doped CPP (Qiu, K(b) et al., 2006; Song et al., 2008; Chen, Y. et al., 2008). However, in future analysis of these matrices the addition of strontium may be increased to further benefit from its impact on structural integrity and degradation *in vitro*.

In addition to the limitations mentioned in chapter 3 (section 3.5) for NMR, DSC/TGA, and elution measurements, this chapter also needs to address possible limitations resulting from density measurement. For example, in determining the apparent density of the disks an envelope volume was assumed. Although disk processing introduced few surface flaws, particularly in the case of G2 disks, the 5-10% standard deviation reported for disk porosity may be partly attributed to their presence.

The cell functionality tests were performed to confirm that the novel addition of strontium to the CPP glass did not interact in any way to impede the efficacy of the loaded VCM or cytocompatibility of the disks. To that end disks were added to TBS to match the prior *in vitro* study conditions. Future testing should consider the short- and long-term needs for osteomyelitis therapy. For example, further MTT testing should consider using culture media for extract collection or a direct-contact set-up; either suggestion could significantly reduce extract dilution. In addition, MTT and micro-dilution tests should be performed at several time points in order to assess disk performance throughout treatment with this local delivery system.

With disks as the basis for a local delivery system there may be a significant modality limitation. In more complex and irregular bone defects disks will not pack well such that any contact with the surrounding tissue will be poor and controlled release properties may be compromised. The next chapter will address this limitation by considering a novel bead design.

4.6 CONCLUSIONS

Doping CPP with 10 mol% strontium increased the density and chain length while decreasing the structural disorder and transition temperatures of the CPP glass. In addition, the presence of up to 10 mol% strontium was not found to significantly impact the gelling mechanism required for therapeutic loading and subsequent fabrication of the local delivery matrices (G2 disks). There was essentially no significant dependence of available calcium and phosphorus ion release during *in vitro* degradation on the G1 disk composition. For G2 disks strontium doping also did not significantly alter the release of phosphorus ions, but did significantly increase the release of calcium and VCM from the matrices *in vitro* compared to that from un-doped matrices after ~4d in the elution media. Still, improved structural integrity of both the G1- and G2-based matrices *in vitro* with 10 mol% strontium doping was observed overall and was likely a result of a decrease in glass disorder and increased electrostatic interaction in the hydrated portion of the disk, as evidenced by a lower fraction of available strontium ions released compared to calcium ions. This study has provided further evidence that strontium doping of the CPP glass used for this local delivery device may serve to manipulate antibiotic release while potentially providing a source of therapeutic ions for enhanced bone regeneration.

CHAPTER 5 DEVELOPMENT OF A COLD ISOSTATIC PRESSING DESIGN – A STRATEGY TO INCREASE MATRIX STRUCTURAL STABILITY, MODIFY VANCOMYCIN RELEASE AND ENHANCE CLINICAL FEASIBILITY

5.1 INTRODUCTION

One of the greatest challenges in designing drug delivery systems is determining how to best load the drug without de-activating it and, simultaneously, maintain all necessary carrier characteristics for optimal elution. Previous studies reported in Chapters 3 and 4 have addressed the influence of phosphate chain length and ion incorporation on drug release from CPP. The current chapter describes the use of cold isostatic pressing to address the geometrical constraints of the CPP-based system, while further modifying its physical properties, in order to improve its overall clinical feasibility.

For several years our research group has sought to exploit the unique gelling characteristics of CPP glass, in conjunction with secondary processing methods, in order to achieve more robust therapeutic loading and subsequently increase sustainability of release. For example, a low temperature gelling and drying ("G1") protocol developed by Dion *et al*. (2005) demonstrated reduced VCM burst release from the gelled amorphous CPP disks along with an extended release period compared to un-gelled disks. However, despite observed greater sample densities with gelling, tensile properties remained poor; non-uniform distribution of the VCM further contributed to appreciable – albeit reduced – burst release. To improve upon these G1 studies, a subsequent G2 protocol was developed by Petrone *et al* (2008) and involved comminution of G1 disks and subsequent uniaxial compaction of the drug-loaded particulate, followed by a second gelling and

drying step. The resulting G2 disks were found to have very limited burst release along with an extended release profile overall, characteristics that were thought to be largely attributed to a more uniformly distributed therapeutic load and marginal increases in matrix density. To better address the geometrical requirements of the delivery system and potentially improve drug release management further, secondary processing involving CIP is considered here. Several papers have previously shown that CIP can be applied to calcium phosphate materials in order to develop a therapeutically loaded controlled release system (Tadic *et al*., 2004; Gautier *et al*., 2000a; Gautier *et al*., 2000b; Makarov *et al*., 2014; Del Valle *et al*., 2011).

The complexity of device shape that is possible increases significantly with the use of CIP during device fabrication and, as a result, devices can be fabricated to better fit the given application. The shape of the device is a critical factor in therapeutic delivery, with changes in the surface area of the matrix directly reflected in the drug release rate (Maderuelo *et al*., 2011; Dash *et al*., 1998). The shape of the carrier will also impact how well the device fits the dead space that is left following debridement of the infected tissue and assists in wound healing (Ahola *et al*., 2014; Li *et al*., 2010). For example, when beads are packed in a cavity they can contribute to cell migration and extracellular matrix growth through the vacancies that were formed (Hong *et al*., 2011; Paul *et al*., 1999; Bhattacharya *et al*., 2013). In considering these carrier requirements and the clinical interest in Septopal® and Osteoset® beads, the design of a bead-shaped delivery system is of greatest interest in this study. The previously reported material-based disadvantages associated with these beads for osteomyelitis therapy and bone recovery (see Chapter 1)

provide the motivation here for pursuing an amorphous CPP-based CIP bead local delivery system. In this chapter the application of CIP in the design of spherical VCM-loaded CPP beads is detailed. The first objective of this CIP study was **to reproducibly form therapeutically loaded CPP beads using a novel cold isostatic pressing and gelling protocol.** *It was hypothesized that after removal from the CIP molds and subsequent gelling, the beads will maintain their uniform and spherical shape.*

Isostatic pressing is adept at compressing ceramic mixtures and increasing the degree of contact, and therefore density, of the resulting matrix at a given pressure (Ani, 2006; Itoh *et al*., 1994). Device density and porosity are two additional factors to be considered in therapeutic delivery (Columbo *et al*., 1995; Pastorino *et al*., 2015; Canal *et al*., 2013; Bhattacharya *et al*., 2013; Maderuelo *et al*., 2011). With the absence of die-wall fraction and the greater area over which pressure is applied, CIP provides more uniform pressure distribution within the compact than uniaxial die compaction (Eksi *et al*., 2002). Dimensional control is critical in minimizing device heterogeneities, such as a high degree of non-uniform densification, and further controlling release (Glass *et al*., 1997; Dion *et al*., 2005b). In addition, by enhancing fluid exchange and with increasing surface area, a greater porosity will increase both drug delivery and availability (Pastorino *et al*., 2015). To manipulate the densification of the ceramic powder during CIP, different particle size distributions may be utilized (Eksi *et al*., 2002; Harun *et al*., 2010; Glass *et al*., 1997). However, whether a finer particle size will impact densification significantly depends on the pressure used and mechanism(s) primarily involved in densification (Fell *et al*., 1971). For example, Fell *et al* (1971) observed that particle rearrangement during

densification was more important for small particles; as particles get smaller it is theoretically possible to obtain zero porosity in the matrix. In addition, independent reports by Cooper *et al*. (1962) and Hardman *et al* (1972) provide evidence that the final stages of compaction are more influenced by the nature of the material itself rather than the particle size and shape. A second objective for this CIP study, then, was **to determine the impact of strontium doping and G1 CPP glass particle size on the porosity and gelling ability of the CPP CIP beads.** *It was hypothesized that a smaller overall G1 CPP glass particle size would reduce the porosity of the CPP-based beads but not impact the ability of the beads to gel. Doping CPP with 10 mol% strontium was not expected to impact the porosity or gelling ability of the CPP-based beads.*

Following the characterization of CIP bead porosity, the third study objective was **to determine the impact of strontium doping and G1 CPP glass particle size on ion release (degradation) in conjunction with VCM release from the CPP CIP bead-based local delivery system *in vitro***. *It was hypothesized that a smaller overall particle size would delay VCM release and slow CIP bead degradation, while doping CPP with 10 mol% strontium would further delay bead degradation and VCM release in vitro.*

A consideration of the device geometry is especially important when making comparisons between delivery systems for which some level of diffusion-controlled drug release is expected. For example, cylindrical tablets of similar aspect ratio have closely-matched antibiotic release profiles (Siepmann *et al*., 2000). However, in comparing the drug release of *differently shaped* devices the surface area (SA)-to-volume ratio has been

shown to be of greater significance than surface area alone in normalizing drug release for differences in device shape and size (Skoug *et al*., 1991; Reynolds *et al*., 2002). Provided a number of study variables (e.g. material, drug) are kept constant, Reynolds *et al*., (2002) reported that roughly equivalent surface area-to-volume ratios for different tablet shapes resulted in similar release profiles. Thus, while the aspect ratio is relevant in comparing the relative release from cylindrical devices, the surface area-to-volume ratio is likely of more value in comparing drug release from tablets of varying shapes (Reynolds *et al*., 2002). Maintaining this ratio should allow for better comparison between the compaction strategies for G2 and CIP matrices. The third objective of this study was **to compare the release of VCM from the CPP G2 disk- and CIP bead-based local delivery systems**. *It was hypothesized that CIP beads will extend the period of measurable VCM release beyond that achieved with G2 disks in vitro.*

Several studies have reported on the promotion of osteoblast precursor differentiation into mature osteoblasts and bone nodule formation in the presence of strontium ions (Bonnelye *et al*., 2008; Chattopadhyay *et al*., 2007; Canalis *et al*., 1996). After addressing the potential improvements in matrix stability and VCM release with manipulating geometrical design, the final objective of this study was **to assess the clinical feasibility of the newly designed therapeutically loaded CPP CIP beads for supporting bone tissue recovery using an *in vitro* model**. *It was hypothesized that doping CPP with 10 mol% strontium would improve pre-osteoblastic cell response to bead extracts, while VCM loading would not negatively impact this same response relative to the study controls*.

5.2 MATERIALS & METHODS

5.2.1 Fabricating Cold Isostatically Pressed CPP Beads

As shown in Figure 5.1, the CIP beads under development were designed to match the surface area-to-volume ratio of the G2 disks previously described.

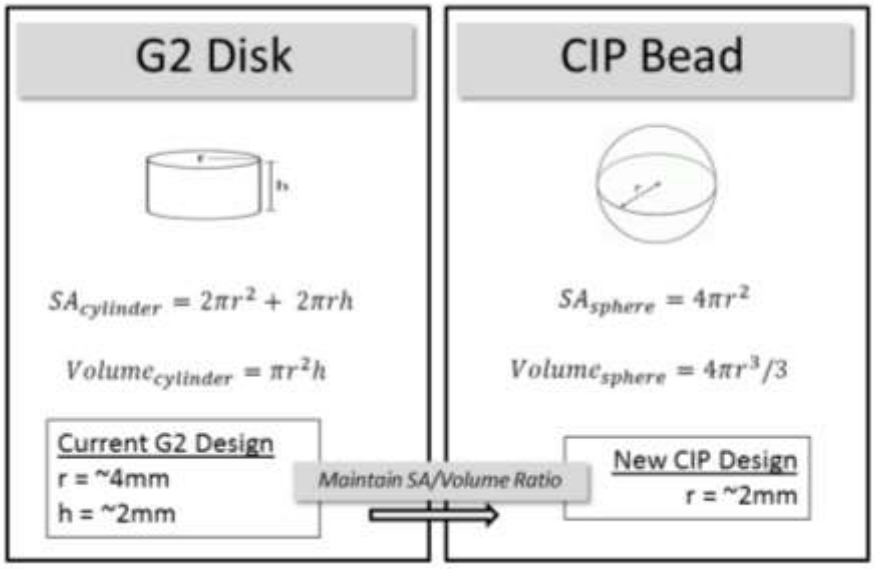

Figure 5.1: Designing CIP beads based on surface area-to-volume ratio of existing G2 disks.

Based on this geometrical analysis, the new bead radius should be roughly 2mm in order to maintain this surface area-to-volume ratio.

Amorphous xSrO-CPP (x=0 or 10 mol%) was processed in accordance with section 4.2.1, while the protocol for VCM loading and fabrication of G1 disks as described in section 3.2.2 was observed. G1 matrices were then milled (Fritsch Planetary Mill) and sieved (Laboratory Test Sieves, Fisher Scientific) to obtain <45µm and 45-212µm G1 particle size distributions. Approximately 85mg of the G1 powder was placed in each

custom-fabricated, spherical ~5mm diameter cavity created using a polyvinylsiloxane mold (Figure 5.2). Molds were then vacuum bagged to protect the powder from the liquid during wet-bag CIP.

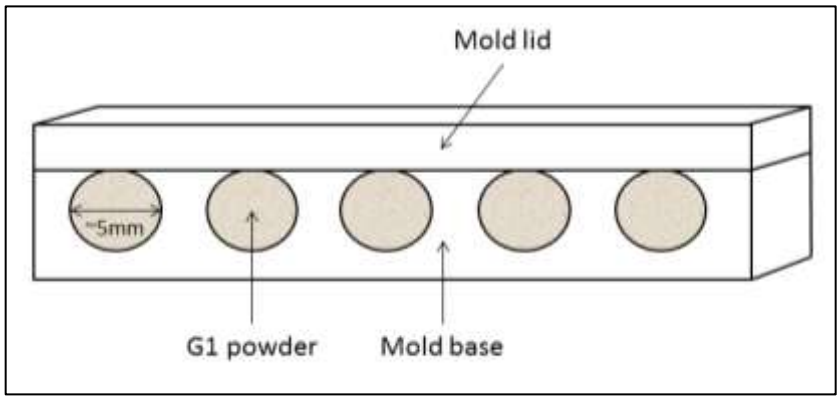

Figure 5.2: Cut-away side view schematic of bead molds for CIP.

Vacuum bagged molds were added to a perforated basket, the basket lowered into the CIP chamber (Avure Technologies), and (after closing the necessary valves) the pump enabled to achieve a compaction pressure of 113MPa. This pressure was held for 5 minutes prior to disabling the pump and releasing the vent valve (corresponding to a drop of ~1ksi/5seconds). The beads were subsequently removed from the molds and gelled in open-ended containers under high humidity at 37^0C for 3hrs; open-ended containers increased bead exposure to humidity. A preliminary investigation revealed that beads only began to lose their shape after ~5hrs under humid conditions; a 3 hr gelling time was therefore chosen to match G2 fabrication conditions. Following gelling, beads were dried outside of the high humidity at 37^0C for ~48hrs. It is important to note that the compaction pressure of 113MPa and dwell of 5min were chosen in CIP to match that previously applied in the uniaxial pressing of G2 disks.

5.2.2 CPP Bead Characterization

5.2.2.1 Physical Properties of CPP Beads

The average of four bead diameter measurements was reported per bead prior to (d_1) and after gelling (d_2). The change in bead diameter relative to the original mold diameter (d_0) was calculated as $[d_1-d_0]/d_0$ x 100%. Similarly, the shrinkage resulting from gelling was calculated as $[d_2-d_1]/d_1$ x 100%. The density and porosity of the un-gelled and gelled beads were measured in accordance with Section 4.2.2. VCM loading efficiency (L_{eff}) for the G1 powder prior to CIP was determined following the protocol previously outlined in Section 3.2.2 (Equation 3.4).

To compare the bead surface and cross-section to that of the G2 disks discussed in Chapter 4, and owing to time constraints, only beads made of <45μm G1 powder were evaluated. SEM images of mounted and Au/Pd sputter coated beads (n=1), under intact and sectioned conditions (Figure 5.3), were obtained using an Hitachi S-4700 and recorded at an accelerating voltage of 15kV, with images captured at 80X and 350X magnification. Beads were carefully sectioned by hand using a flat-edge blade.

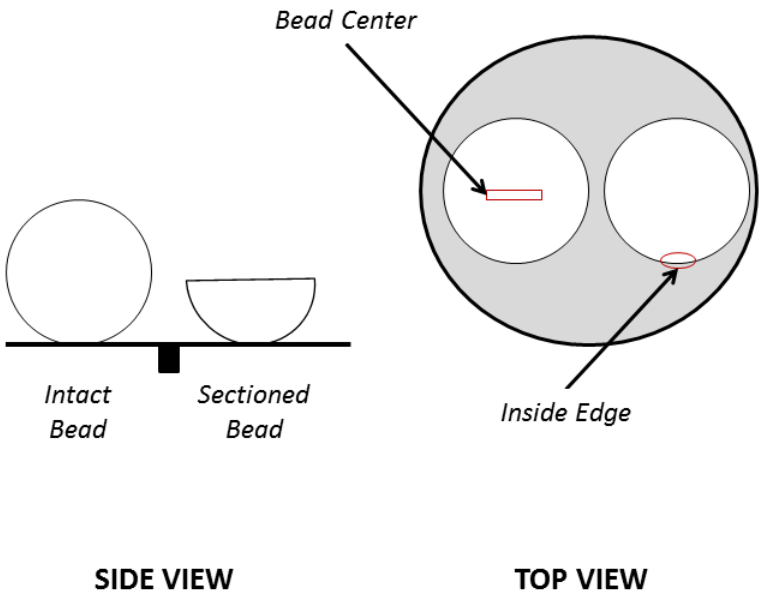

Figure 5.3: Schematic of SEM pin prepared for imaging.

5.2.2.2 Bead Degradation and Drug Release In Vitro

For *in vitro* elution studies, the CIP beads were added to 15mL polypropylene tubes containing 15mL 0.1M TBS and rotated at roughly 30^0 at a speed of 30rpm (one bead per tube). This set-up and speed were chosen to maintain flow across the beads without invoking too rapid a loss of shape or settling of the bead across the bottom of a vial (due to bead movement). At set time points over a span of three weeks, 7mL of elution media was removed for measurement of VCM, calcium, strontium, and phosphate ion release. A fresh 7mL of 0.1M TBS was then added to each bead to maintain the elution volume. VCM and ion release were analyzed using UV-Vis spectrophotometer and ICP-OES, respectively, at wavelengths previously reported in section 3.2.2. Adjustments were made for the concentrations present at the previous time point and taking into consideration the dilution of the sample upon addition of fresh TBS at each time point. Media pH was also monitored over the duration of the elution studies of the disks with an

Accumet® Basic AB15 Plus pH meter (Fisher Scientific). Images of the beads were captured with a Nikon D3100 camera. At the completion of the elution study the beads were removed from the buffer solution, dried at 37°C, and sectioned by hand using a flat-edge blade before also being imaged with the Nikon D3100 camera.

5.2.2.3 Functional Assessment of CPP Beads

5.2.2.3.1 *In Vitro* Cytocompatability (MTT)

The subset of strontium-doped CIP beads (either <45µm or 45-212µm G1 particles) that demonstrated the most sustained release of VCM was chosen for further study with functional assays. This group subsequently underwent a 24hr *in vitro* MTT assay (as per section 4.2.3) in order to confirm that the change in compaction strategy and matrix geometry did not significantly alter the cytocompatibility previously established using extracts from strontium- doped and VCM-loaded G2 disks. It is important to note that the beads, as done with the G2 disks, were added to scintillation vials containing 15mL 0.1M TBS and placed on a horizontally rotating plate (90rpm, 37°C) for 24hr. After filtering the 24hr extracts with sterile 0.20µm filters (Sarstedt, Canada), they were assessed for calcium, phosphorus, strontium and VCM release in accordance with section 5.2.2.2 before preceeding to the MTT assay.

5.2.2.3.2 Pre-Osteoblastic Cell Functionality Assays

For this functional assay, an *in vitro* cell culture system was utilized in order to investigate the effects of ion and VCM release on the distinct stages of cell response that most resemble respective stages of osteogenesis, specifically cell differentiation of pre-

osteoblastic cells and osteoid mineralization by terminally differentiated osteoblasts (Ehara *et al*., 2003).

A 12-day cell activity study was performed using newborn C57B/6 rat calvaria-derived MC3T3-E1 cells (ATCC® CRL-2593). MC3T3-E1 cells report a time-dependent and sequential expression of osteoblast characteristics analogous to *in vivo* bone formation and provides a useful model for examination of each stage of bone development (Quarles *et al*., 1992). The cells were maintained in $75cm^2$ tissue culture flasks with alpha modified minimum essential medium (α-MEM) (GIBCO) supplemented with 10% fetal bovine serum (FBS) (Sigma) within a humidified 5% CO_2 balanced air incubator at 37^0C. Cells were passaged twice weekly at 70-80% confluence using 1.5mL of 0.25% trypsin-EDTA (Sigma) to detach cells, and re-suspended in 13.5mL of fresh culture media. Media was changed once between passages (i.e. total media changes was every other day). Cells at passage 25-26 were removed from the flasks with 0.25% Trypsin-EDTA, re-suspended in the culture media, counted using a haemocytometer, diluted with further media (as needed) and seeded at a density of $3x10^4$cells/mL in each required well of a 24-well plate. After incubating for 24hrs, media was exchanged for differentiation-encouraging medium containing 10mM sodium β-Glycerophosphate (BGP) (G9422, Sigma), 50µg/mL ascorbic acid (AA) (Sigma), and 100U/mL Penicillin/Streptomycin (GIBCO). When MC3T3-E1 cells are grown in the presence of FBS and ascorbic acid they more readily differentiate into osteoblasts and can produce extensive collagenous extra-cellular matrix (Sudo *et al*., 1983; Quarles *et al*., 1992). The addition of BGP to the media encourages mineralization (Beck *et al*., 1998; Quarles *et al*., 1992). The presence

of both AA and BGP *in vitro* is reportedly essential for the full differentiation and mineralization processes of the MC3T3-E1 cells to occur (Quarles *et al*., 1992). In the absence of AA and BGP the MC3T3-E1 cells have been shown to attain growth arrest by day 10 with low levels of ALP, and fail to express a fully differentiated osteoblast phenotype (Quarles *et al*., 1992). As a result, the change to a differentiation media does not simply accentuates cell processes, but is necessary to better model external cues provided to the cells *in vivo* and increase reproducibility of study outcomes. The change to differentiation media was considered t=0 or "0hr" for this functional cell assay.

In parallel with this activity assay, fresh CIP beads were added to 0.1M TBS in a second elution study (set-up similar to that described in Section 5.2.2.2). Collection time points of 4hr, 24hr, 48hr, 96hr, 6d, 8d, and 10d were chosen to coincide with cell culture media exchanges, with consideration as well to maintenance of "sink" conditions for the elution extracts. In addition to reporting the fraction of available ion and VCM released and extract pH (measured in accordance with section 5.2.2.2), the *real-time* ion and VCM concentrations in the elution extracts were also described. Samples were sterile-filtered (0.20µm filters) (Sarstedt, Canada) before being added to the cell-seeded wells at 10 vol% of the differentiation medium volume such that the cells see roughly $1/10^{th}$ the reported *real-time* extract ion and VCM concentration. The positive control for this test was differentiation media only, while a positive reagent control consisted of differentiation media and 10% 0.1M TBS. Figure 5.4 shows the plate layout for this cell study.

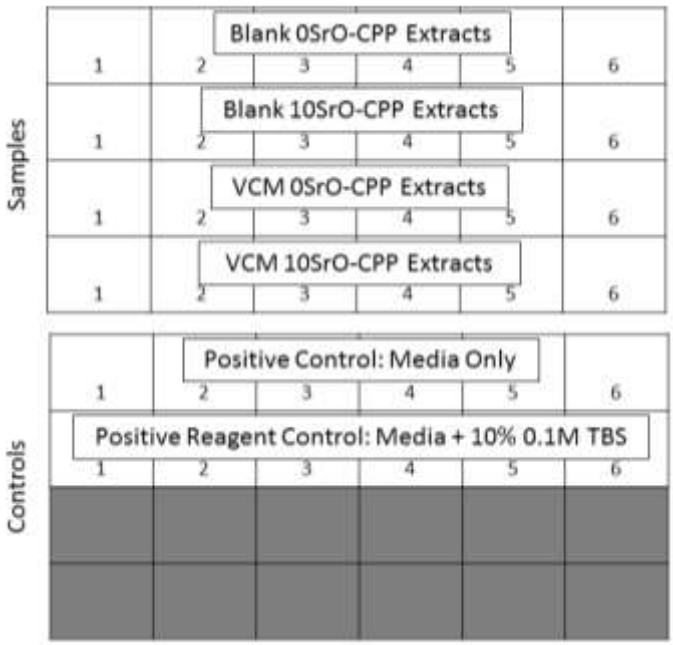

Figure 5.4: Plate layout for (top) samples, (bottom) controls (n=6).

To quantitatively assess MC3T3-E1 cell differentiation, alkaline phosphate (ALP) activity was evaluated (Sigma APF-1kt) at 3, 6, and 12d, with separate cell-seeded 24-well plates prepared for each time point; ALP activity is a characteristic marker of early osteogenic differentiation (Pati *et al*., 2013). At these time points media was removed from the wells, cells were rinsed with chilled PBS, and 1mL 0.1% Triton X-100 buffer was added to each well (see Appendix B for buffer recipe). The plates were then placed on ice on a horizontal shaker (300rpm) for 30min to assist in cell lysis. Cell lysates were collected with the aid of a cell scrapper and added to 1.5mL labelled Eppendorf tubes, which were subsequently frozen at -80^{0}C for later analysis. Prior to performing the ALP assay, tubes were thawed at 37^{0}C on a horizontal shaker for 30minutes and centrifuged for 15minutes at 14.5x1000rpm. The collected protein supernatant was used in both the ALP assay and a corresponding BCA assay to measure total protein. For the ALP assay 20µL of the protein supernatant for each sample and control was added to each of 3 wells

in a white fluorescence plate. 20µL of the 0.1% Triton buffer was added to 3 wells to serve as a negative control for the ALP assay. A serial dilution of the supplied control enzyme served as the test standard curve for each plate. The fluorescence plates were incubated at 65^0C for 15min and allowed to cool to room temperature before the kit-provided reagents (i.e. dilution buffer, fluorescent assay buffer, and diluted substrate solution) were added. The plates were subsequently placed on a horizontally rotating plate (100rpm) for 1hr under aluminum foil prior to reading at 360nm excitation and 440nm emission (1 filter, S=25) using a multi-detection microplate reader (Synergy HT, BIO-TEK).

To normalize ALP values, the total cell protein was concurrently measured using the protein supernatant collected at 3, 6, and 12d and a commercial kit (QuantiPro BCA Assay kit, Sigma). The bicinchoninic acid (BCA) assay relies on the formation of a Cu^{2+} protein complex under alkaline conditions, followed by a reduction of Cu^{2+} to Cu^{1+} that is proportional to the amount of protein present (QuantiPro BCA Technical Report, Sigma). Cu^{1+} forms a purple-blue complex with BCA that can be subsequently measured. A serial dilution of the provided protein standard with diluted 0.1% Triton X-100 buffer served as the standard curve (0 – 30µg/mL). As there was 10% glycerol in the 0.1% Triton X-100 buffer and glycerol content >1% is incompatible with the BCA assay, the collected protein supernatants and the buffer itself were diluted 20X prior to the addition of kit reagents. 100µL of the unknown samples or controls was added to each of 3 wells in a 96-well plate. An equal volume of BCA working reagent (i.e. 100µL) was added to each well before the plate was added to a horizontally rotating shaker (100rpm) at 60^0C for

1hr. After 1hr plates were cooled to room temperature before being measured for absorbance at 562nm using a multi-detection microplate reader (Synergy HT, BIO-TEK).

Mineralization was also assessed in this study as an additional indicator of osteoblast activity. To observe any mineralization at 6d and 12d, a staining protocol using 40mM Alizarin Red solution (ARS) (Sigma) and 0.2% SF Yellowish solution ("SFYS", Sigma) was employed (protocol adapted from Lee et al., 2004). At the designated time points the media was removed, the wells rinsed with chilled PBS, and the cells subsequently fixed with 10% neutral formalin solution (Sigma) for 30min. Cells were then rinsed 3X with dH_2O and 0.5mL ARS added for 5min under aluminum foil prior to rinsing several more times with dH_2O until the rinse was completely clear. Plates were imaged using a light microscope and Nikon Imaging software, with four images taken per well at a magnification of 10X. Any calcium deposits attributed to the mineralization process were stained brown with increasing red-ish colour as bone nodules progressively grew (Lee *et al*., 2004). Next, cells were stained with 0.5mL of SFYS for 5min. As before, the wells were rinsed with dH_2O until the run-off was clear. With SFYS, the collagen fibers of the extracellular matrix are stained green (Lee *et al*., 2004). Following imaging of these dual-stained wells, the dH_2O was removed from the well and 0.5mL of a 10% cetylpyridinium chloride solution (CPC) was added for 30min to de-stain each well for ARS quantification (Hessle *et al*. 2002; Ripoll *et al*., 2009). The CPC was then extracted from each well, added to a 96-well plate and measured for absorbance at 540nm using a multi-detection microplate reader (Synergy HT, BIO-TEK). The ARS stain has a strong peak at ~540nm while SFYS stain has a peak at ~620nm, indicating that any interference

from SFYS should be minimal. Blank wells (without cells) were stained with dye and rinsed in a similar matter to account for any staining owing to the walls of the well and not the cells. A standard curve was prepared by performing a serial dilution of the ARS with CPC solution. As with the ALP assay the mineralization OD540 reading was normalized to total protein for each sample subset.

5.2.3 Statistics

A power analysis was initially performed on the samples used for this study in order to estimate the required sample size for detection of reasonable departures from the null hypothesis. Physical characterization and elution studies designed to match prior work sought a power greater than 98% and required a sample size of 6. Similarly, a sample size of 6 was chosen for the cell activity assays.

Differences in means of study outcomes were analyzed using Minitab15.0, a statistics software program, and either a two-way analysis of variance (for VCM loading efficiency, VCM elution, strontium ion release and cell study outcomes *in vitro*) or a 3-factor modified general linear model (for porosity measurement, as well as calcium and phosphorus ion release *in vitro*) was used with a significance value of $p=0.05$. In addition a post-hoc pairwise Tukey analysis was performed. Lastly, study outcomes were compared with Pearson correlation to determine any significantly related trends ($p<0.05$).

5.3 RESULTS

5.3.1 Physical Properties of CPP Beads

Freshly compacted beads were readily removed from the molds. Bead shape and diameter uniformity did not appear to be impacted by either strontium doping, VCM loading or G1 particle size (Figure 5.5, Table 5.1).

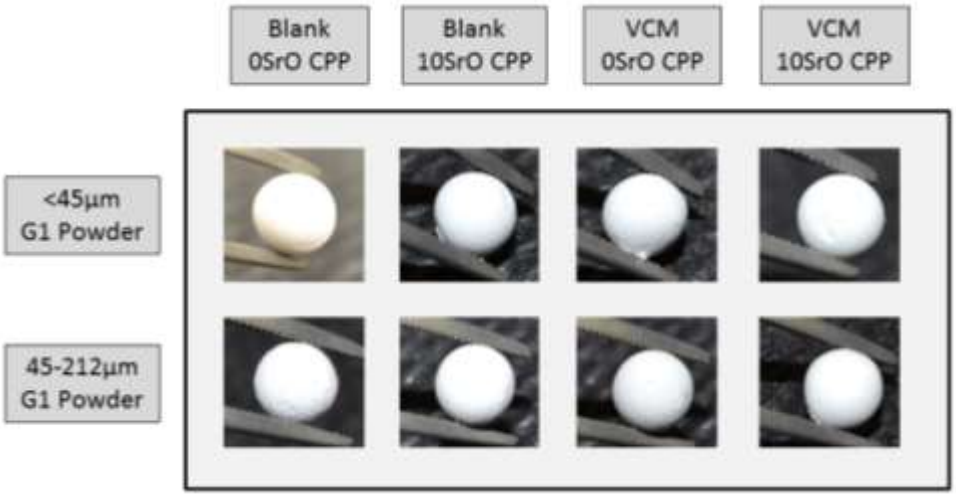

Figure 5.5: Freshly compacted and un-gelled CPP beads.

Table 5.1: CPP bead diameter following CIP and gelling.

Sample Group (G1 Particle Size)	Ungelled Bead Diameter (mm)	Gelled Bead Diameter (mm)
Blank 0SrO CPP (<45µm)	4.27±0.03	4.09±0.02
Blank 0SrO CPP (45-212µm)	4.26±0.04	4.12±0.06
Blank 10SrO CPP (<45µm)	4.26±0.06	4.07±0.04
Blank 10SrO CPP (45-212µm)	4.25±0.07	4.08±0.08
VCM 0SrO CPP (<45µm)	4.21±0.09	4.06±0.10
VCM 0SrO CPP (45-212µm)	4.24±0.05	4.16±0.05
VCM 10SrO CPP (<45µm)	4.19±0.06	4.12±0.07
VCM 10SrO CPP (45-212µm)	4.25±0.04	4.17±0.04

There was a consistent 11-12% decrease in bead diameter following CIP compared to the initial mold diameter. In addition, gelling resulted in a further 2-4% reduction in diameter for each sample group. Overall, the final beads obtained here were within 0.2mm (or 5%) of the desired 4mm bead diameter (see Figure 5.1). There was no significant dependence of bead diameter on 10 mol% strontium addition to CPP, VCM loading, or G1 particle size. The loading efficiency of the G1 powder used in CIP was 97.71 ± 2.20% and 94.81 ± 1.33% for un-doped and strontium-doped CPP, respectively (values similar to that reported in Table 4.2 of section 4.3.2 for the G1 powder batch of the earlier study).

VCM loading of G1 powder and gelling after CIP did induce noticeable changes in bead porosity (Figure 5.6).

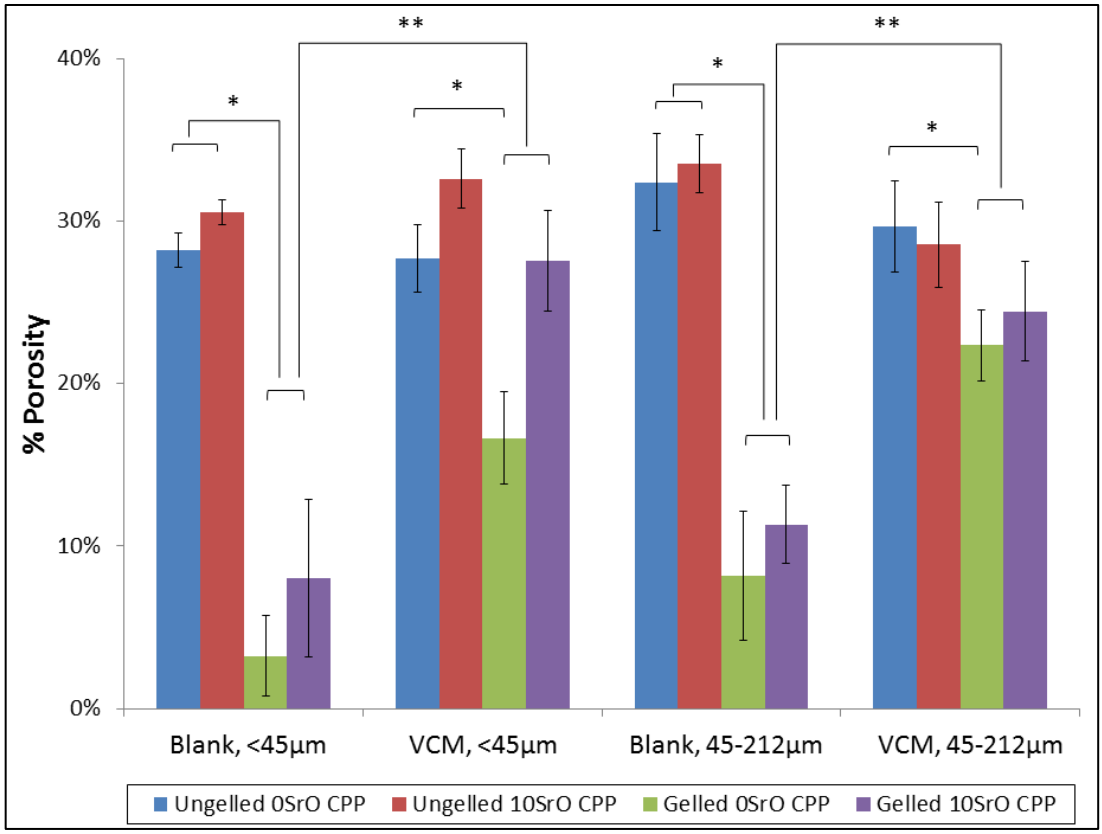

Figure 5.6: Porosity of CPP beads. Data reported as average values while error bars represent one standard deviation (n=6). Gelling significantly reduced porosity (*), while VCM loading significantly increased porosity (**) ($p<0.05$).

Gelling resulted in a significant decrease in bead porosity for most sample groups, while loading CPP with VCM significantly diminished the capacity of gelling to decrease bead porosity ($p<0.05$). Neither strontium doping nor G1 particle size was found to have a consistently significant impact on bead porosity.

SEM images of the respective bead surfaces are shown in Figures 5.7 and 5.8.

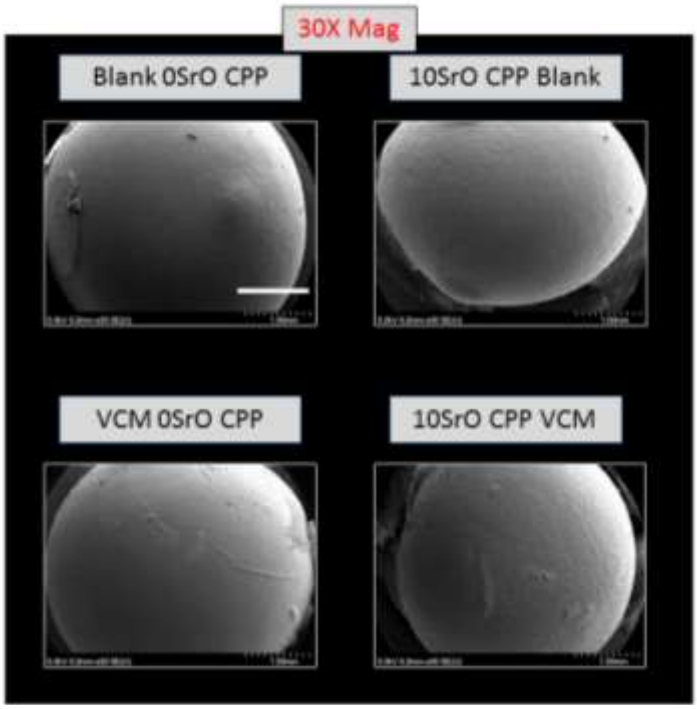

Figure 5.7: CPP beads of <45µm G1 powder at 30X magnification (scale bar: 1mm).

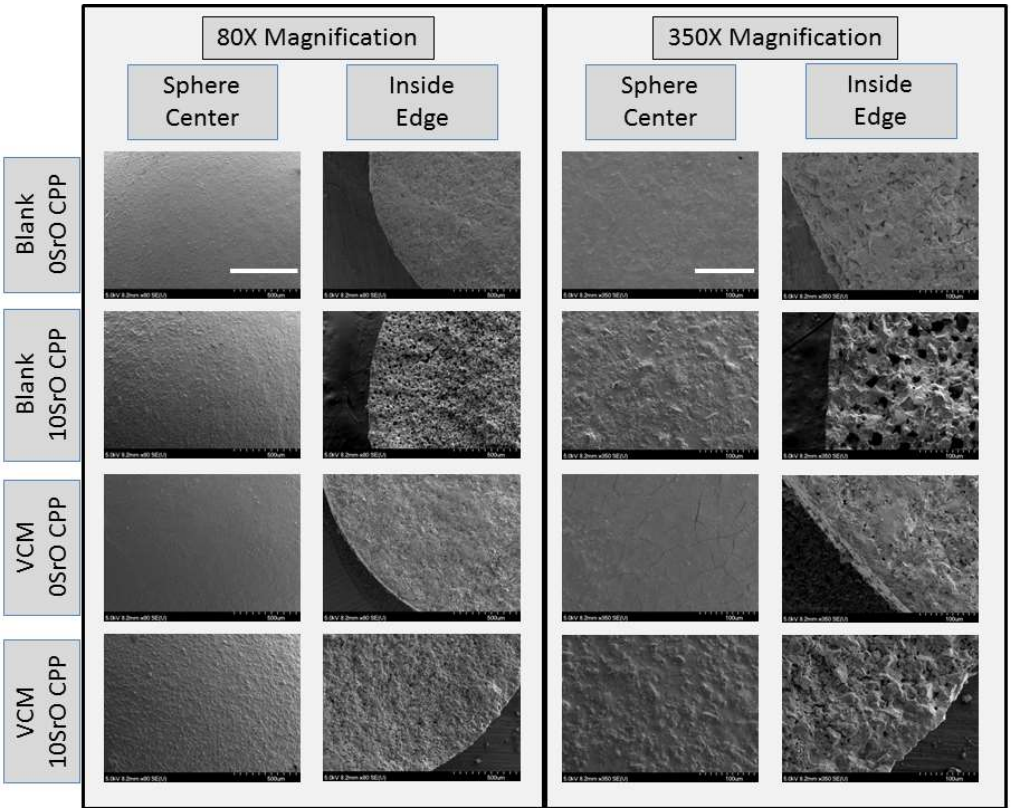

Figure 5.8: Sectioned CPP beads (<45µm G1 powder) at (left) 80X magnification (scale bar: 500µm) and (right) 350X magnification (scale bar: 100µm).

Overall, beads derived from undoped CPP appeared to have a smoother outer surface and smaller internal pores compared to their strontium-doped counterparts. A thin outer layer that appeared denser compared to the bead center was also present and was particularly noticeable for the VCM-loaded beads.

5.3.2 Bead Degradation and Drug Release *In Vitro*

Observing CIP beads in elution media for a period of roughly three weeks revealed noticeable differences in the structural stability of the different sample groups (Figures 5.9 - 5.12). For example, doping CPP glass with 10 mol% strontium visibly and significantly decreased any apparent bulk degradation of the blank CIP beads (independent of G1 particle size). VCM loading noticeably improved this structural stability even more so with no dependence on the G1 particle size used or strontium doping.

<45um

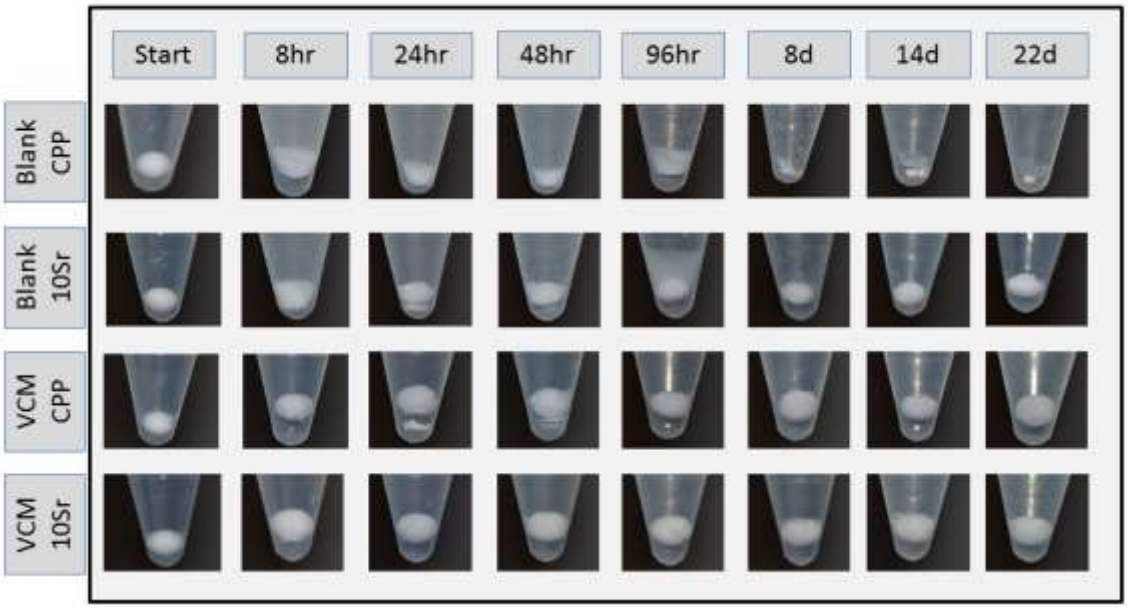

Figure 5.9: CPP beads fabricated using <45µm G1 particles in 0.1M TBS over 22d.

45-212um

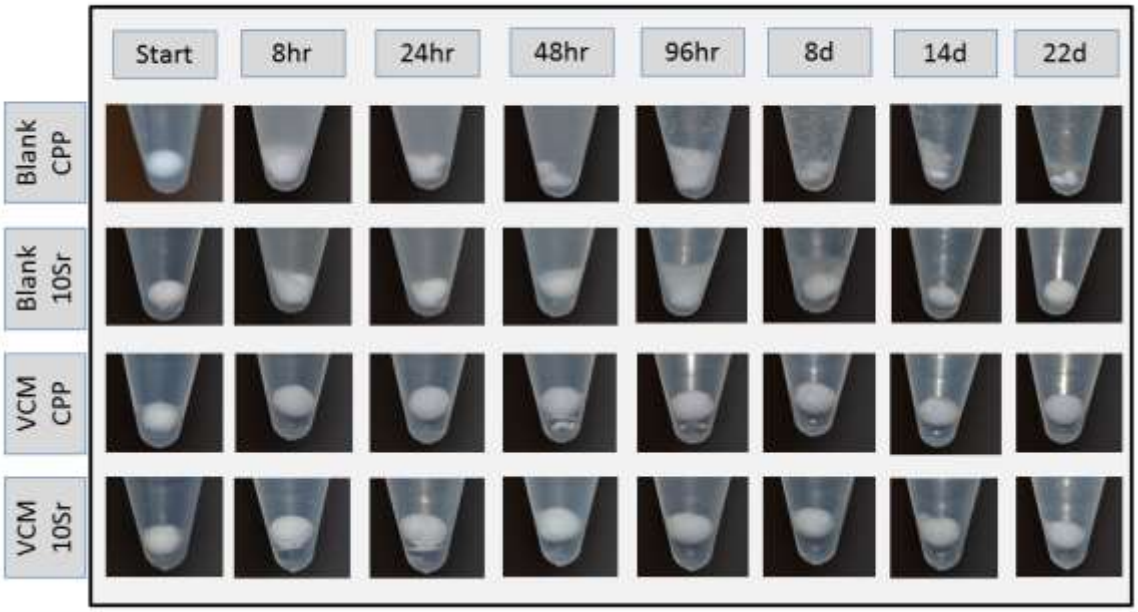

Figure 5.10: CPP beads fabricated using 45-212µm G1 particles in 0.1M TBS over 22d.

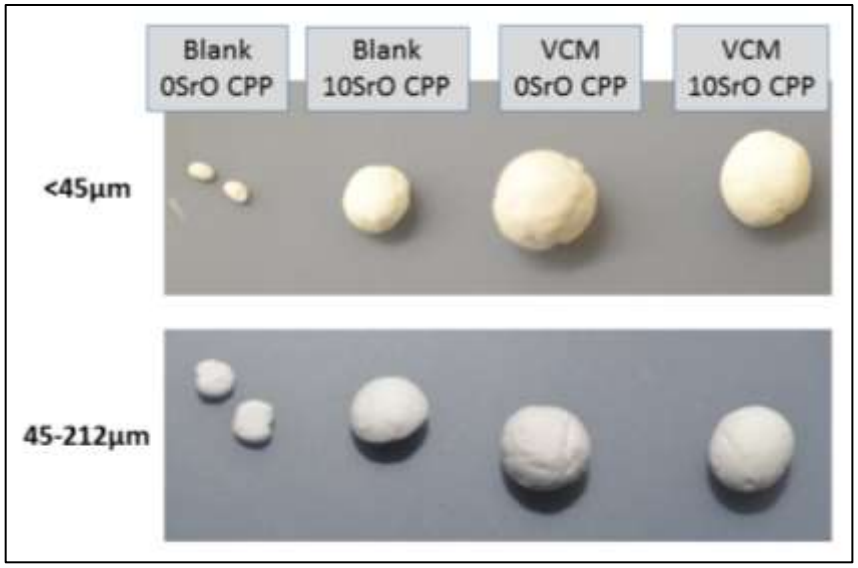

Figure 5.11: CPP beads (top) of <45µm G1 particles, and (bottom) of 45-212µm G1 particles after 22d in 0.1M TBS elution media.

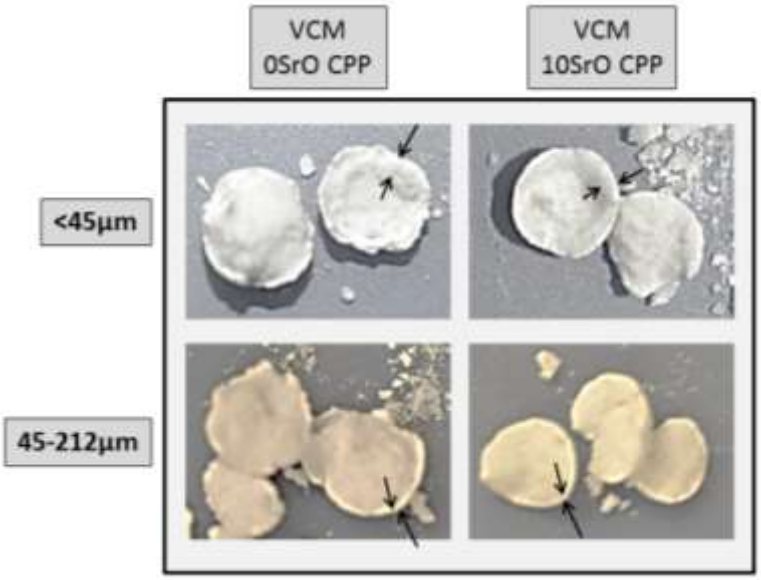

Figure 5.12: CPP beads (top) of <45µm G1 particles, and (bottom) of 45-212µm G1 particles after 22d in 0.1M TBS elution media and sectioned. Arrows indicate presence of an outer shell layer.

In addition, there was a noticeable increase in the diameter of the VCM-loaded beads made of <45µm G1 particles (likely as a result of bead swelling), while their counterparts

of larger G1 particle size roughly maintained their size throughout the 22d study (Figure 5.11). Sectioning of the remaining VCM-loaded CPP beads following completion of the elution study further confirmed the presence of an outer shell layer (see arrows in Figure 5.12). Blank CPP beads of either particle size began to disintegrate by 24hr into the study and were largely loose powder by 8d. The addition of 10 mol% strontium appeared to improve the structural stability of the blank beads, with these beads still present after 22d despite a significant amount of debris collected in the media during the course of the study. All beads gradually lost their spherical shape and became more oval-shaped as the *in vitro* study progressed, likely as a result of the dynamics of the study set-up.

Structural differences noted for the CIP beads correlated well with the release of ions and VCM (Figure 5.13 – 5.16). The table that follows (Table 5.2) indicates the significant pairs at given time points of elution study for the fraction of available ion and VCM released.

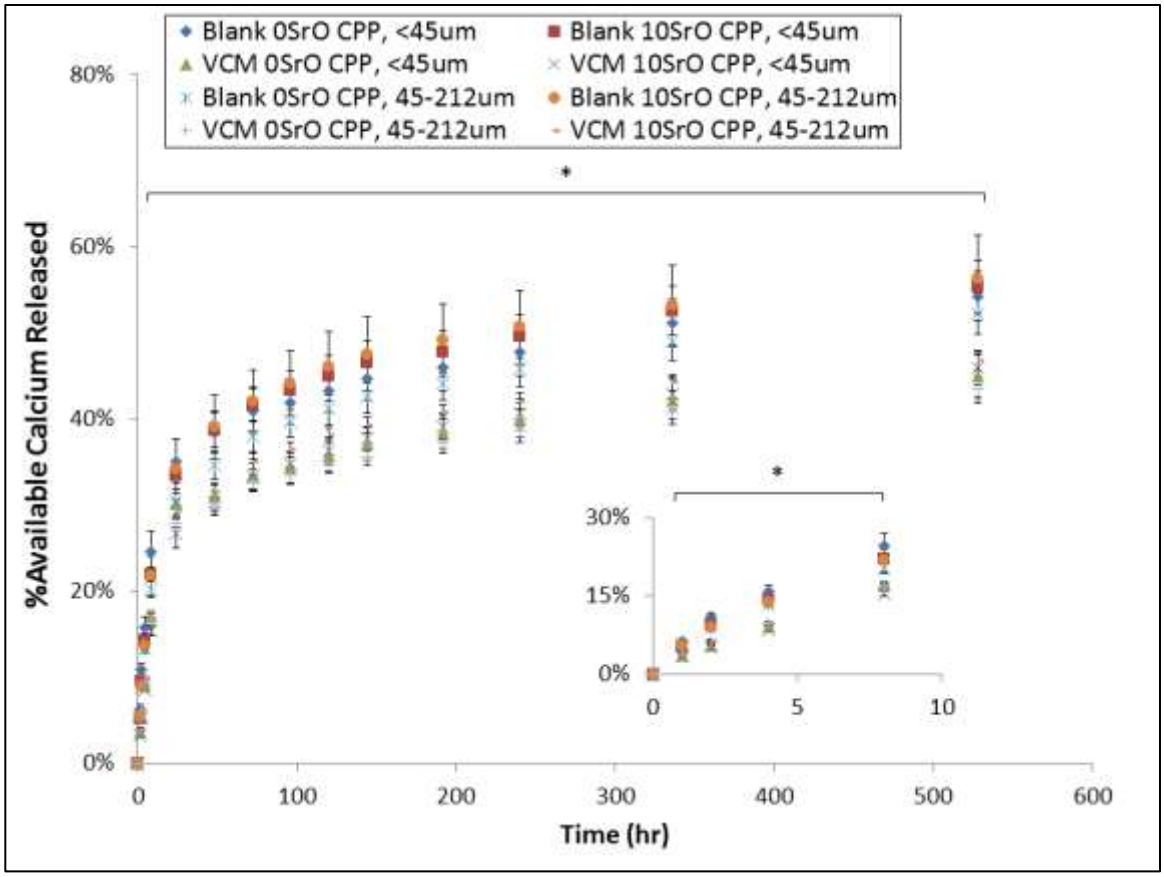

Figure 5.13: Fraction of available calcium released from CPP beads. Data reported as average values while error bars represent one standard deviation (n=6). VCM-loaded beads released significantly more % available calcium than blank beads (*) ($p<0.05$).

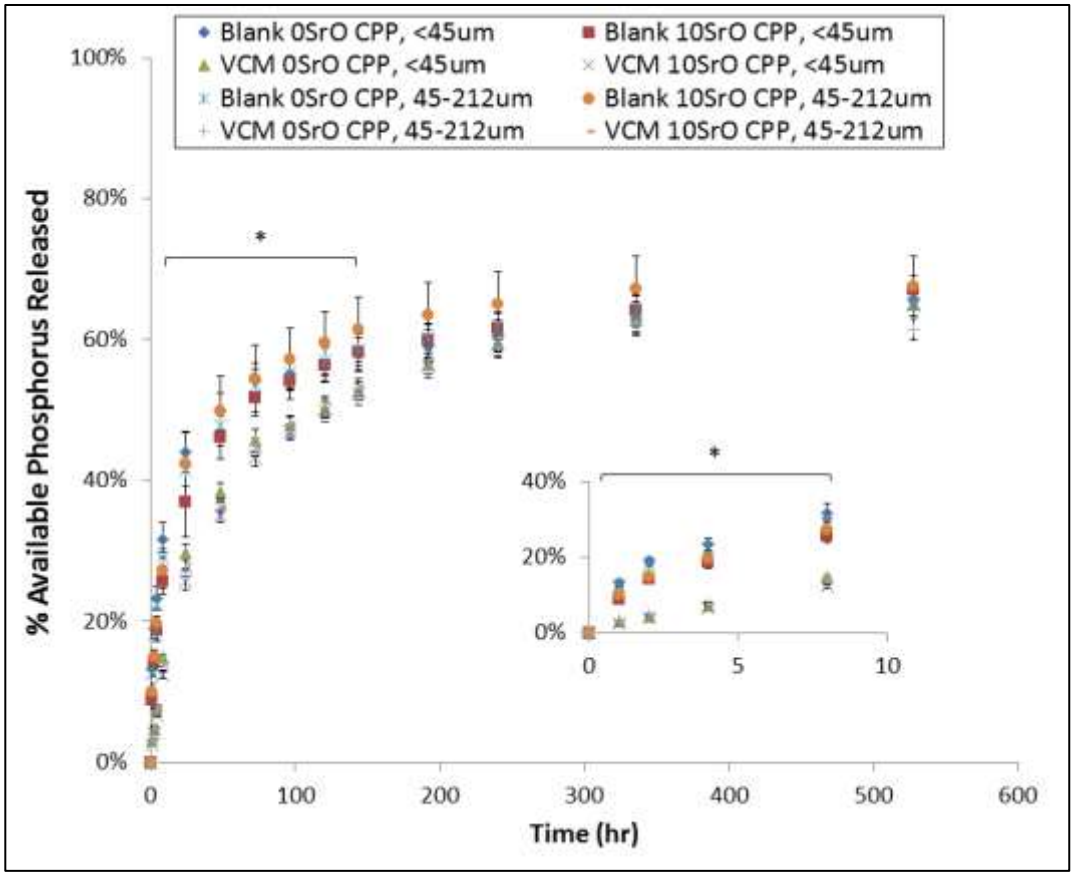

Figure 5.14: Fraction of available phosphorus released from CPP beads. Data reported as average values while error bars represent one standard deviation (n=6). VCM-loaded beads released significantly less % available phosphorus than blank beads (*) at indicated time points ($p<0.05$).

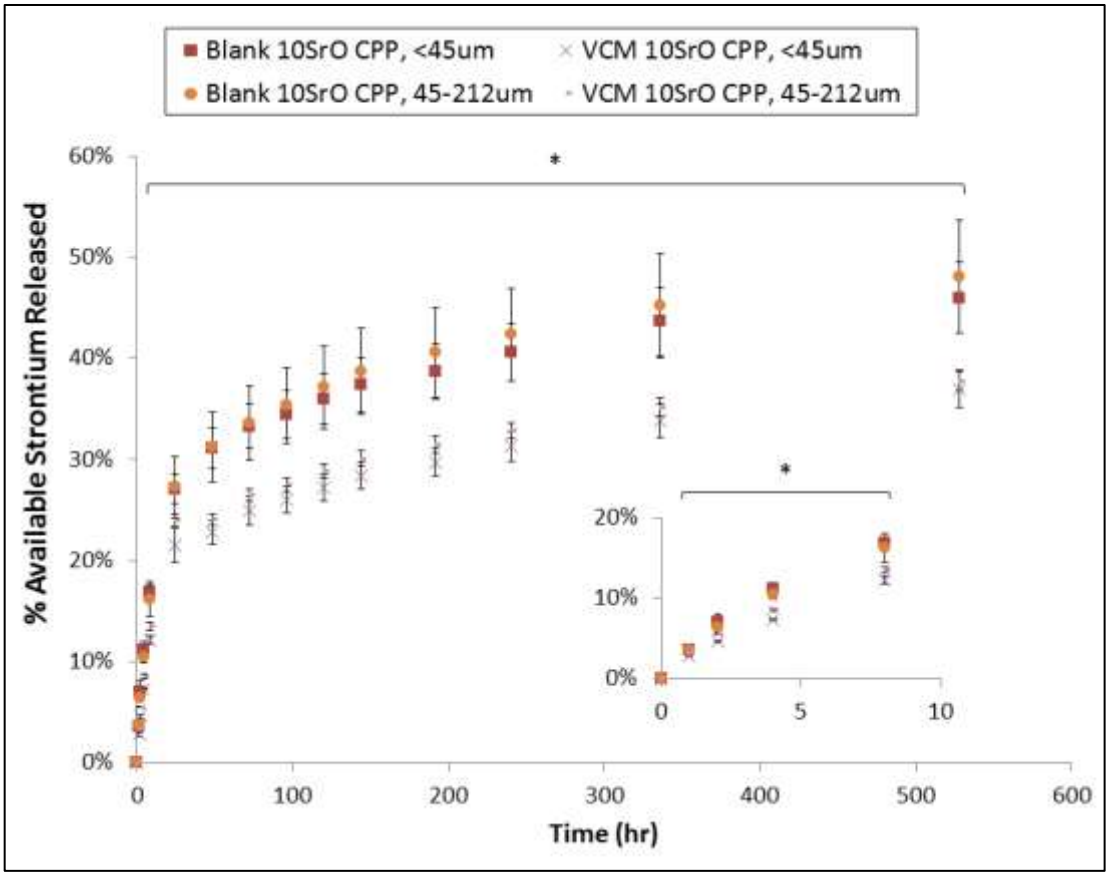

Figure 5.15: Fraction of available strontium released from CPP beads. Data reported as average values while error bars represent one standard deviation (n=6). VCM-loaded beads released significantly less % available strontium than blank beads (*) ($p<0.05$).

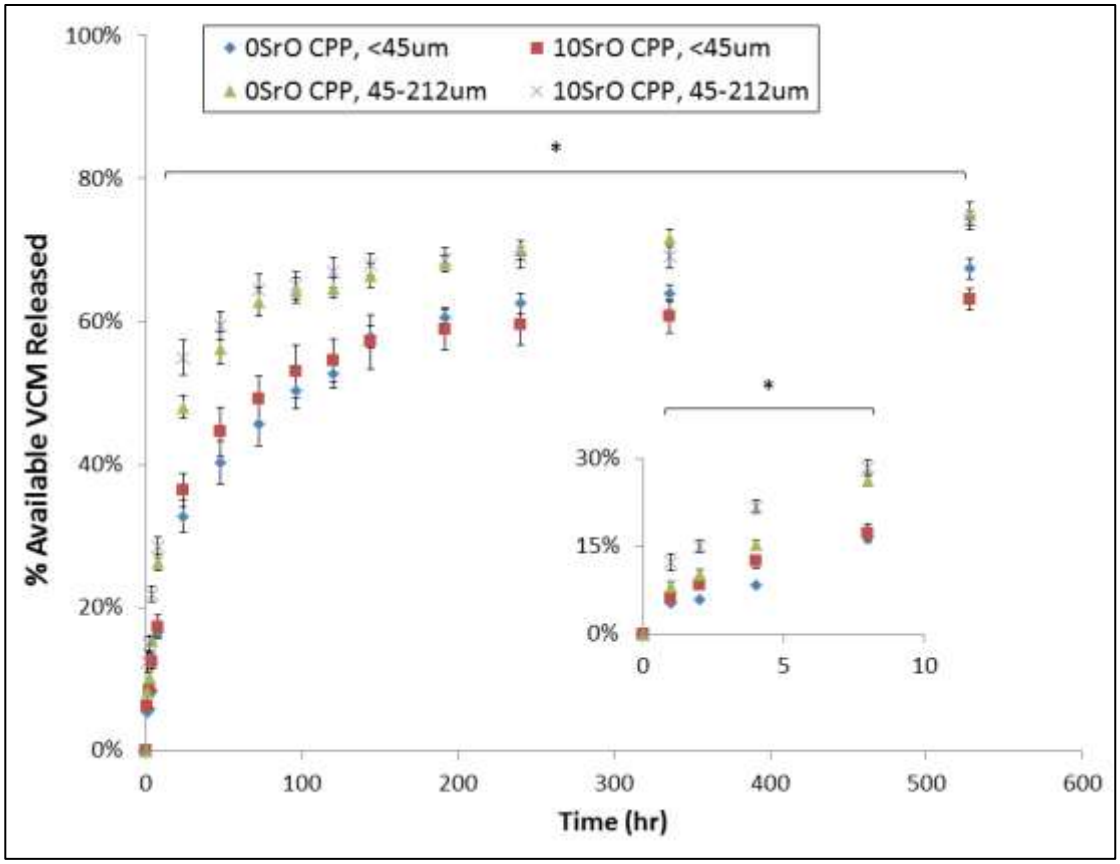

Figure 5.16: Fraction of available VCM released from CPP beads. Data reported as average values while error bars represent one standard deviation (n=6). Beads of larger particle size released significantly more % available VCM than those of smaller size (*) ($p<0.05$).

Table 5.2: Fraction of available ion and VCM released with relative significance indicated ($p<0.05$) (n=6).

Time	4hr	8hr	24hr	48hr	72hr	144hr	192hr	240hr	336hr	528hr
% Available Calcium Released										
Blank 0SrO-CPP (<45µm)	15.72^{A} (1.25)	24.57^{A} (2.41)	35.09^{A} (2.57)	38.46^{A} (2.50)	$40.98^{A,B}$ (2.50)	$44.74^{A,B}$ (2.55)	$45.90^{A,B}$ (2.60)	$47.72^{A,B}$ (2.68)	51.12^{A} (2.77)	54.20^{A} (2.87)
Blank 10SrO-CPP (<45µm)	14.20^{B} (0.89)	21.94^{B} (0.87)	$33.39^{A,B}$ (1.50)	38.71^{A} (1.94)	$41.67^{A,B}$ (2.05)	$46.56^{A,B}$ (2.43)	$47.81^{A,B}$ (2.43)	$49.54^{A,B}$ (2.51)	52.56^{A} (2.88)	55.33^{A} (3.11)
VCM 0SrO-CPP (<45µm)	$9.04^{C,D}$ (0.56)	17.05^{C} (0.70)	$30.19^{B,C}$ (1.27)	$31.08^{B,C}$ (1.45)	33.50^{D} (1.77)	37.12^{D} (1.89)	38.46^{D} (1.91)	39.89^{D} (2.04)	42.19^{C} (2.30)	44.92^{B} (2.51)
VCM 10SrO-CPP (<45µm)	8.50^{D} (0.10)	15.33^{C} (0.49)	26.65^{D} (1.71)	30.26^{C} (1.42)	33.43^{D} (1.54)	37.73^{D} (1.42)	39.13^{D} (1.52)	40.60^{D} (1.65)	42.92^{C} (1.87)	45.98^{B} (1.96)
Blank 0SrO-CPP (45-212µm)	13.33^{B} (0.45)	20.20^{B} (0.89)	$30.41^{B,C}$ (1.45)	34.63^{B} (1.67)	$37.98^{B,C}$ (1.86)	$42.59^{B,C}$ (1.97)	$44.14^{B,C}$ (2.03)	$45.84^{B,C}$ (2.10)	$48.96^{A,B}$ (2.22)	52.24^{A} (2.43)
Blank 10SrO-CPP (45-212µm)	13.70^{B} (0.63)	21.78^{B} (2.20)	34.18^{A} (3.59)	39.05^{A} (3.68)	41.99^{A} (3.75)	47.51^{A} (4.25)	49.14^{A} (4.18)	50.64^{A} (4.24)	53.23^{A} (4.62)	56.35^{A} (4.95)
VCM 0SrO-CPP (45-212µm)	$9.69^{C,D}$ (0.38)	16.48^{C} (0.41)	$27.95^{C,D}$ (0.64)	30.10^{C} (0.88)	32.52^{D} (1.02)	35.65^{D} (1.07)	37.16^{D} (1.15)	38.57^{D} (1.30)	40.82^{C} (1.43)	43.42^{B} (1.50)
VCM 10SrO-CPP (45-212µm)	9.86^{C} (0.24)	16.90^{C} (0.49)	$29.26^{C,D}$ (0.61)	$31.57^{B,C}$ (0.67)	$35.08^{C,D}$ (0.88)	$39.29^{C,D}$ (0.90)	$40.77^{C,D}$ (0.89)	$42.09^{C,D}$ (0.88)	$44.24^{B,C}$ (0.93)	46.72^{B} (1.00)
% Available Phosphorus Released										
Blank 0SrO-CPP (<45µm)	23.34^{A} (1.72)	31.60^{A} (2.44)	44.08^{A} (2.92)	49.84^{A} (2.63)	54.09^{A} (2.51)	57.85^{A} (2.34)	$59.13^{B,C}$ (2.25)	60.63^{B} (2.25)	$63.06^{A,B}$ (2.27)	$65.75^{A,B}$ (2.41)
Blank 10SrO-CPP (<45µm)	18.67^{B} (1.44)	25.78^{C} (2.00)	36.94^{B} (5.00)	46.12^{A} (3.04)	51.67^{A} (2.53)	58.19^{A} (2.50)	$59.94^{A,B,C}$ (2.40)	$61.60^{A,B}$ (2.36)	$64.12^{A,B}$ (2.33)	67.12^{A} (2.03)
VCM 0SrO-CPP (<45µm)	7.51^{C} (0.49)	14.99^{D} (0.41)	29.77^{C} (1.16)	38.50^{B} (1.20)	45.72^{B} (1.56)	52.71^{B} (1.30)	$56.51^{B,C}$ (1.45)	59.34^{B} (1.59)	62.83^{B} (1.68)	$65.00^{A,B,C}$ (1.69)
VCM 10SrO-CPP (<45µm)	6.68^{C} (0.15)	12.33^{D} (0.51)	25.68^{C} (1.22)	35.01^{B} (0.95)	43.25^{B} (1.23)	52.50^{B} (1.13)	$56.25^{B,C}$ (1.18)	59.49^{B} (1.27)	$63.33^{A,B}$ (1.41)	$64.90^{A,B,C}$ (1.62)
Blank 0SrO-CPP (45-212µm)	22.45^{A} (0.54)	$29.12^{A,B}$ (1.20)	$41.40^{A,B}$ (2.19)	47.90^{A} (2.34)	53.51^{A} (2.32)	58.55^{A} (2.17)	$60.32^{A,B}$ (1.88)	$61.82^{A,B}$ (1.90)	$64.18^{A,B}$ (2.06)	$65.15^{A,B,C}$ (1.92)
Blank 10SrO-CPP (45-212µm)	19.70^{B} (1.10)	$27.23^{B,C}$ (2.49)	42.31^{A} (4.57)	49.88^{A} (4.87)	54.50^{A} (4.74)	61.42^{A} (4.64)	63.49^{A} (4.55)	64.99^{A} (4.56)	67.28^{A} (4.59)	67.57^{A} (4.32)

Table 5.2 Continued…

Time	4hr	8hr	24hr	48hr	72hr	144hr	192hr	240hr	336hr	528hr
VCM 0SrO-CPP (45-212µm)	7.82^{C} (0.39)	14.04^{D} (0.38)	26.96^{C} (0.67)	36.71^{B} (0.74)	44.44^{B} (0.96)	51.76^{B} (1.03)	55.88^{C} (1.24)	58.67^{B} (1.30)	62.10^{B} (1.49)	61.46^{C} (1.47)
VCM 10SrO-CPP (45-212µm)	7.82^{C} (0.29)	13.80^{D} (0.62)	28.05^{C} (0.83)	36.19^{B} (0.82)	44.76^{B} (1.27)	53.52^{B} (0.92)	$57.26^{B,C}$ (0.76)	60.24^{B} (0.80)	$63.95^{A,B}$ (0.86)	$62.71^{B,C}$ (0.84)
% Available Strontium Released										
Blank 10SrO-CPP (<45µm)	11.11^{A} (0.84)	16.83^{A} (0.74)	27.05^{A} (1.43)	31.10^{A} (2.03)	33.28^{A} (2.21)	37.37^{A} (2.66)	38.72^{A} (2.68)	40.63^{A} (2.85)	43.67^{A} (3.36)	46.01^{A} (3.45)
VCM 10SrO-CPP (<45µm)	7.30^{C} (0.11)	12.16^{B} (0.43)	21.53^{B} (1.66)	22.78^{B} (1.22)	24.98^{B} (1.43)	28.36^{B} (1.32)	29.74^{B} (1.41)	31.30^{B} (1.51)	33.88^{B} (1.67)	36.96^{B} (1.83)
Blank 10SrO-CPP (45-212µm)	10.43^{A} (0.60)	16.19^{A} (1.74)	27.27^{A} (3.01)	31.18^{A} (3.44)	33.62^{A} (3.68)	38.74^{A} (4.30)	40.55^{A} (4.40)	42.34^{A} (4.60)	45.23^{A} (5.17)	48.11^{A} (5.54)
VCM 10SrO-CPP (45-212µm)	8.55^{B} (0.20)	13.48^{B} (0.39)	23.98^{B} (0.54)	24.08^{B} (0.51)	26.47^{B} (0.62)	30.07^{B} (0.78)	31.47^{B} (0.78)	32.83^{B} (0.81)	35.21^{B} (0.89)	37.77^{B} (0.95)
% Available VCM Released										
VCM 0SrO-CPP (<45µm)	8.37^{D} (0.24)	16.67^{C} (0.68)	32.76^{D} (2.29)	40.27^{B} (2.99)	45.58^{B} (2.98)	57.97^{B} (1.54)	60.64^{B} (1.38)	62.57^{B} (1.39)	63.92^{B} (1.18)	67.42^{B} (1.40)
VCM 10SrO-CPP (<45µm)	12.44^{C} (1.11)	17.32^{C} (1.66)	36.45^{C} (2.39)	44.58^{B} (3.45)	49.20^{B} (3.21)	57.17^{B} (3.85)	58.88^{B} (2.79)	59.64^{B} (2.84)	60.80^{C} (2.34)	63.15^{C} (1.54)
VCM 0SrO-CPP (45-212µm)	15.39^{B} (0.67)	26.35^{B} (1.15)	48.06^{B} (1.59)	56.28^{A} (2.24)	62.83^{A} (1.98)	66.47^{A} (1.69)	68.23^{A} (1.17)	70.07^{A} (1.33)	71.72^{A} (1.19)	75.09^{A} (1.60)
VCM 10SrO-CPP (45-212µm)	21.86^{A} (1.10)	28.51^{A} (1.41)	54.96^{A} (2.39)	59.38^{A} (2.04)	64.47^{A} (2.20)	67.95^{A} (1.56)	68.64^{A} (1.73)	69.00^{A} (1.56)	69.15^{A} (1.72)	74.26^{A} (1.33)

Note1: Values reported as mean (standard deviation)

Note2: Means that do not share a letter are significantly different at the given time point ($p<0.05$).

Therapeutically loading CPP with VCM significantly reduced bead degradation. For example, throughout the 22d elution study VCM-loaded CPP beads released significantly less calcium and strontium than blank CPP beads. A similar impact of VCM loading was seen with respect to decreasing phosphorus ion release for the first 10 days of elution. Further evidence that VCM loading provided structural support to the beads and delayed degradation *in vitro* was given in the cation-to-phosphorus ratio measured in the collected elution media (Appendix A: Figure A7). The proportion of phosphorus ions released relative to cations remained relatively constant for the blanks over time, while that for the VCM-loaded beads decreases until 24hr into the study, after which consistent ratios are released. As the VCM-loaded beads released very little debris even after 24hrs, it is possible that there are still a significant fraction of crosslinks being maintained between the cations and phosphate chains.

Of the study variables studied, G1 particle size had the most significant impact on VCM release. Here, beads derived from 45-212μm G1 particles released significantly more VCM than those made from <45μm throughout the 22d elution study. In contrast, the impact of strontium doping was only observed in the first 24hrs, with 10SrO-CPP releasing significantly more VCM than 0SrO-CPP beads, and at the end of the study, where the opposite trend was observed. As a further observation, bead porosity did not correlate significantly with the fraction of available VCM released.

Doping CPP with strontium only had a significant impact on the ion release for blank (i.e. no VCM added) beads. In addition, for ion release from samples the two-way interaction

between strontium doping and particle size was significant. For example, for beads of smaller G1 particle size, blank strontium-doped CPP beads released significantly fewer calcium and phosphorus ions than blank undoped CPP beads for the first 8 hrs. In contrast, more calcium was released from blank strontium-doped beads of larger particle size G1 between 8hrs and 10d compared to blank undoped beads during the elution period between 8hrs and 10d. The cumulative fraction of ion release from the beads noticeably began to plateau after 2-3d *in vitro*. As noted for the G2 disk ion release in chapter 4, this plateauing may be attributed to the debris not accounted for in sample collection and/or the formation of more stable phases within or on the surfaces of the CPP beads. The remnant bead cation-to-phosphorus ion ratios presented in Appendix A (Figure A8) provide some support to the latter theory (as higher than stoichiometric CPP ratio of ~0.5).

The Pearson correlation was strong, positive and significant between each of the pairings of fraction of ion released (i.e. Ca vs P, Ca vs Sr, P vs Sr) (correlation: >0.90, $p<0.001$). For example, the greater the amount of calcium ion released, the more phosphorus ion that was concurrently released. In addition, the Pearson correlation between bead porosity and fraction of available ions released was found to be of medium – to – high strength, in the same dirrection and significant (correlation: >0.60, $p<0.001$) throughout the study. In other words, a bead of greater porosity had greater ion release *in vitro*.

5.3.3 Biocompatibility and Bioactivity of the CPP Beads

5.3.3.1 In Vitro Cytocompatability (MTT)

An undisturbed 24hr elution study only re-affirmed the aforementioned trend for VCM release, with strontium doping significantly increasing the fraction of VCM released from the bead ($p<0.05$) (Figure 5.17). However, this re-affirmation did not extend to ion release. For example, in the undisturbed study the fraction of available ion released in was significantly lower than that observed in the prior elution study ($p<0.05$). In addition, the significant differences in ion release observed previously between sample groups were not observed in this subsequent undisturbed 24hr study. As VCM release was similar, these differences in ion release likely owe more to the undisturbed nature of the test and gradual development of electrostatic interaction between ions in the hydrated portion of the bead such that it is stabilized against erosion. The additional changes to the protocol in order to match that used for collection of G2 extracts for the MTT assay (in Chapter 3) (e.g. horizontally rotating beads) likely did not contribute as much as reduced frequency in extract collection.

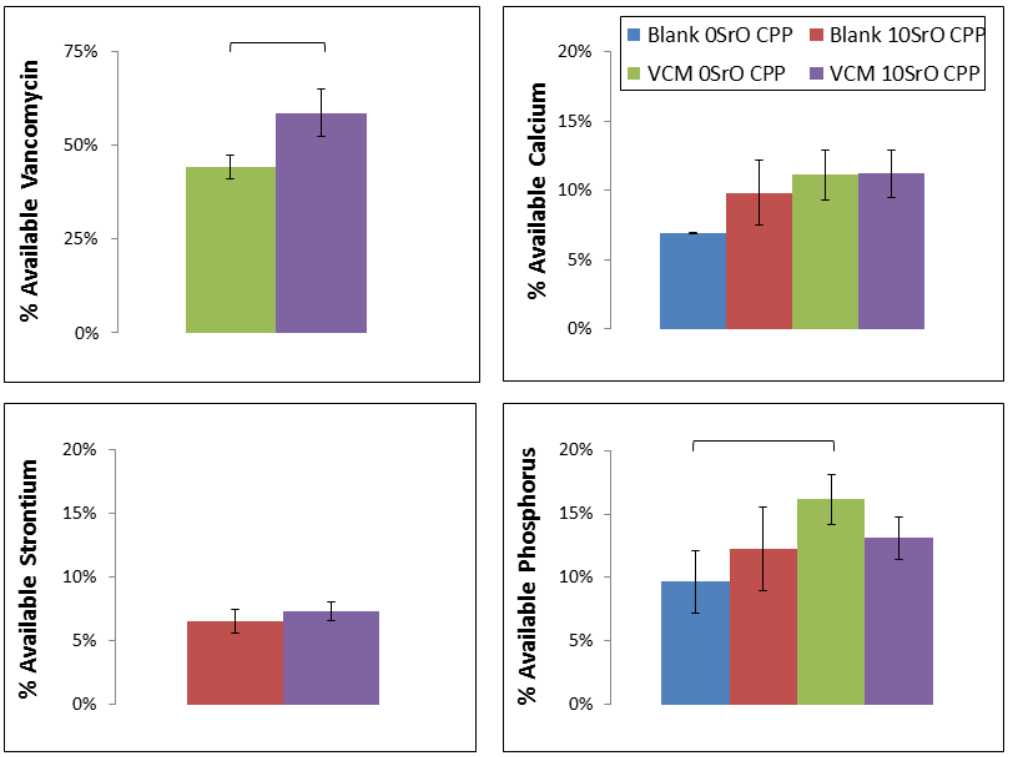

Figure 5.17: Fraction of available (top left) VCM, (top right) calcium ion, (bottom left) strontium ion, and (bottom right) phosphorus ion released from CPP beads after 24hrs. Data reported as average values while error bars represent one standard deviation (n=3). Horizontal bars represent significant difference ($p<0.05$).

As shown in Figure 5.18, the addition of extracts to the culture media (at both full concentration and diluted 50%) did not significantly impact cell cytocompatibility compared to undoped, blank matrices or relative to the TBS control. As anticipated, these CIP beads possessed similar cytocompatibility to that obtained with extracts from G2 disks. While verification of VCM activity was not performed here, other studies have previously confirmed that there is no denaturation of VCM or decrease in efficacy following isostatic compression of VCM within different matrices at pressures as high as 2.5GPa (Gautier *et al*., 2000b; Makarov *et al*., 2014).

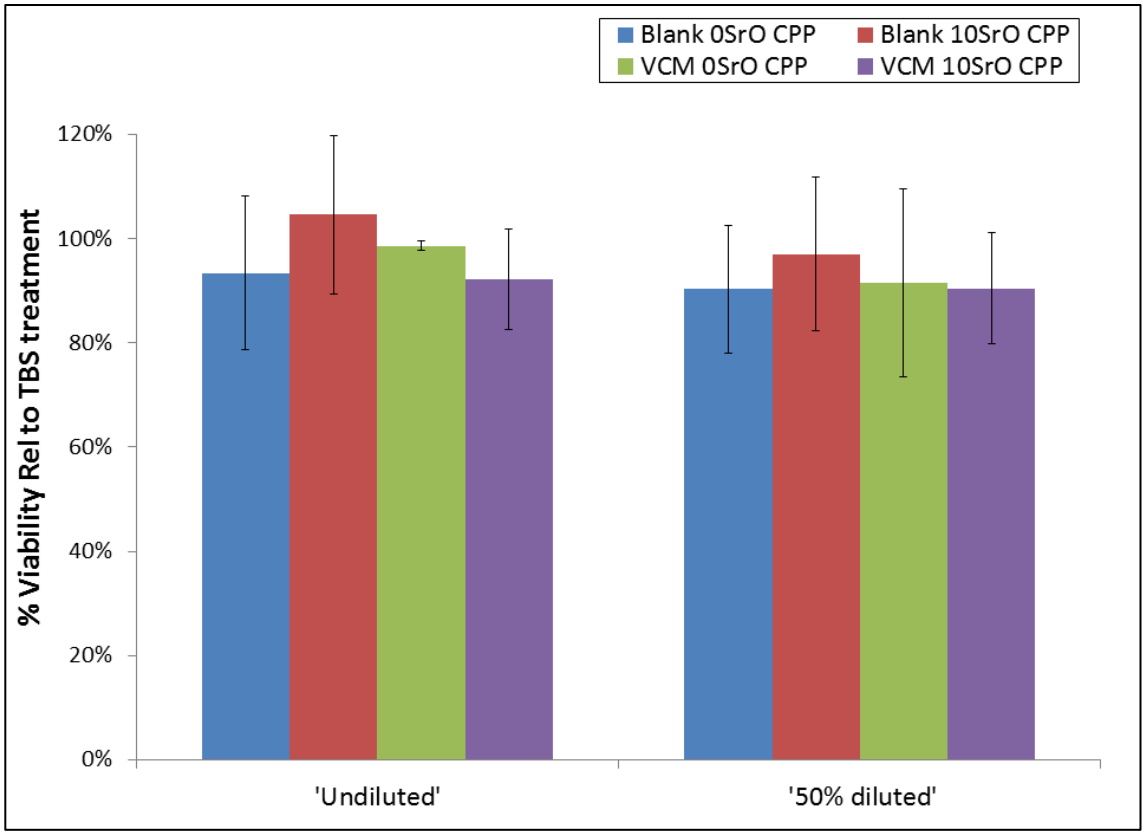

Figure 5.18: Viability of NIH-3T3 cells following indirect 24hr elution extract exposure from CPP beads relative to 0.1M TBS treatment. Data reported as average values while error bars represent one standard deviation (n=3). There was no significant difference reported ($p<0.05$).

5.3.3.2 Pre-Osteoblastic Cell Functionality Assays

Although the elution *set-up* here was similar to the 22d study, the delay in extract collection to match culture media changes may have once again contributed to the 5-10% lower ion release in these extracts compared to that reported in the 22d CIP elution study (Figure 5.19, Table 5.3). The infrequent sample collection likely led to the gradual development of electrostatic interaction between released ions in the hydrated portion of the beads such that they became more resistant to erosion; this was similarly noted for the 24hr undisturbed samples for MTT study. As shown in Figure 5.20, while the fraction of available calcium is notably lower (and slower to plateau) in the cell study extracts, the

VCM release is roughly similar. Over time the differences in calcium ion release between the two studies is reduced.

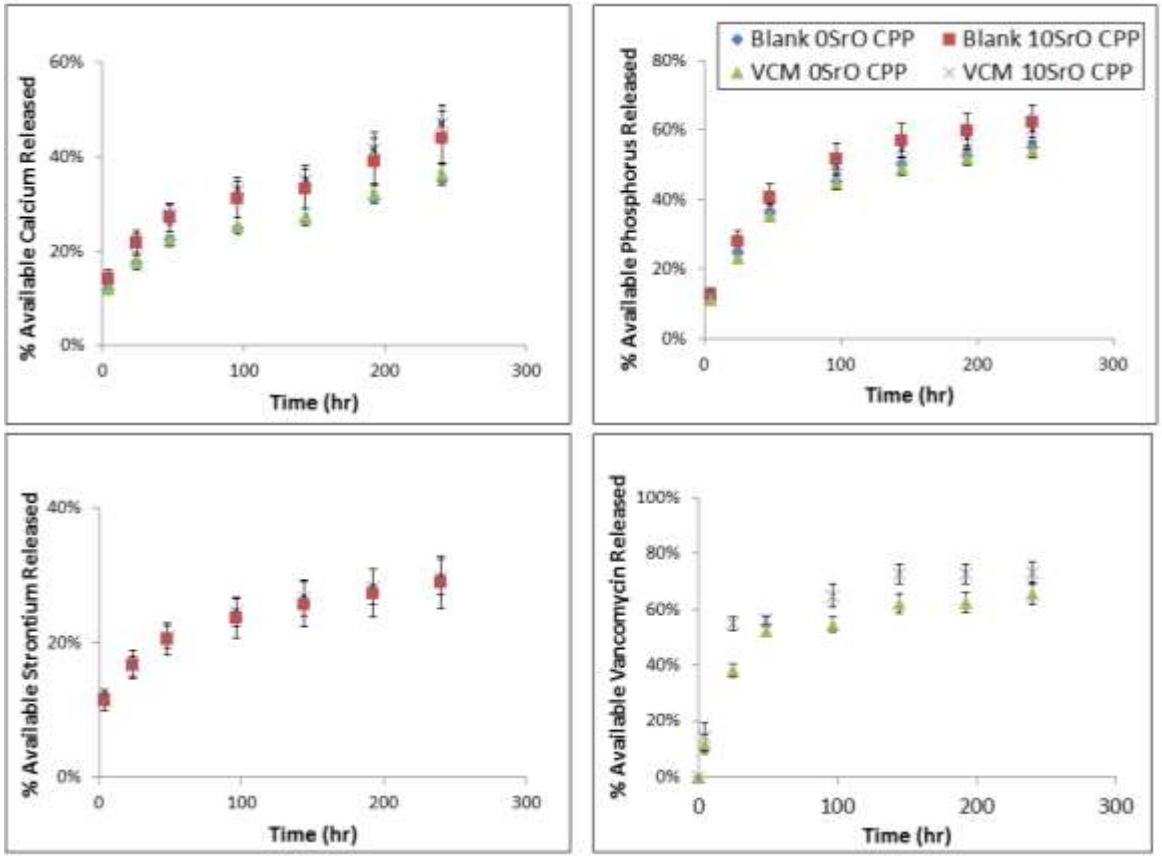

Figure 5.19: Ions and VCM released in 10d elution study of CIP beads for cell study. Data reported as average values while error bars represent one standard deviation (n=6).

Table 5.3: Fraction of available ion and VCM released with significance indicated.

Time	4hr	24hr	48hr	96hr	144hr	192hr	240hr
% Available Calcium Released							
Blank 0SrO CPP	11.81 (0.55)^{B}	17.59 (0.58)^{B}	22.47 (0.86)^{B}	24.84 (0.59)^{B}	26.52 (0.51)^{B}	31.08 (0.41)^{B}	35.04 (0.40)^{B}
Blank 10SrO CPP	14.19 (1.91)^{A}	21.68 (2.64)^{A}	27.06 (3.10)^{A}	30.99 (3.76)^{A}	33.13 (4.16)^{A}	38.94 (4.95)^{A}	43.92 (5.64)^{A}
VCM 0SrO CPP	12.12 (0.77)^{B}	17.71 (1.85)^{B}	22.53 (1.58)^{B}	25.36 (1.80)^{B}	27.14 (1.88)^{B}	32.14 (2.17)^{B}	36.31 (2.44)^{B}
VCM 10SrO CPP	14.41 (1.16)^{A}	21.50 (1.90)^{A}	27.70 (2.00)^{A}	32.98 (2.63)^{A}	35.07 (3.05)^{A}	41.60 (3.61)^{A}	46.95 (3.97)^{A}
% Available Phosphorus Released							
Blank 0SrO CPP	11.52 (0.88)^{A,B}	25.01 (1.31)^{A,B}	36.85 (1.91)^{A,B}	45.33 (2.06)^{B}	50.10 (2.03)^{B,C}	52.66 (1.67)^{B}	55.00 (1.75)^{B}
Blank 10SrO CPP	12.42 (1.78)^{A,B}	27.92 (3.28)^{A}	40.59 (3.84)^{A}	51.49 (4.58)^{A}	57.07 (4.89)^{A}	59.69 (4.94)^{A}	62.10 (5.15)^{A}
VCM 0SrO CPP	11.12 (0.79)^{B}	23.14 (1.79)^{B}	35.16 (1.77)^{B}	44.78 (2.04)^{B}	48.89 (1.97)^{C}	51.88 (1.95)^{B}	54.07 (2.02)^{B}
VCM 10SrO CPP	13.42 (1.10)^{A}	26.15 (1.91)^{A,B}	37.43 (1.85)^{A,B}	50.23 (1.97)^{A}	54.88 (2.47)^{A,B}	58.21 (2.68)^{A}	60.54 (2.68)^{A}
% Available Strontium Released							
Blank 10SrO CPP	11.43 (1.57)^{A}	16.75 (2.05)^{A}	20.49 (2.34)^{A}	23.61 (2.92)^{A}	25.64 (3.35)^{A}	27.30 (3.59)^{A}	28.86 (3.85)^{A}
VCM 10SrO CPP	11.63 (0.86)^{A}	16.57 (1.46)^{A}	20.86 (1.69)^{A}	24.55 (2.17)^{A}	26.53 (2.64)^{A}	28.19 (2.67)^{A}	29.69 (2.71)^{A}
% Available Vancomycin Released							
VCM 0SrO CPP	11.67 (3.20)^{A}	38.11 (2.42)^{B}	52.22 (1.53)^{B}	54.73 (2.60)^{B}	62.07 (3.70)^{B}	62.67 (3.53)^{B}	65.51 (3.88)^{B}
VCM 10SrO CPP	14.34 (5.01)^{A}	54.86 (2.57)^{A}	56.23 (1.46)^{A}	64.91 (4.20)^{A}	72.53 (3.60)^{A}	72.53 (3.60)^{A}	73.03 (4.10)^{A}

Note1: Values reported as mean (standard deviation)

Note2: Means that do not share a letter are significantly different at given time point ($p<0.05$)

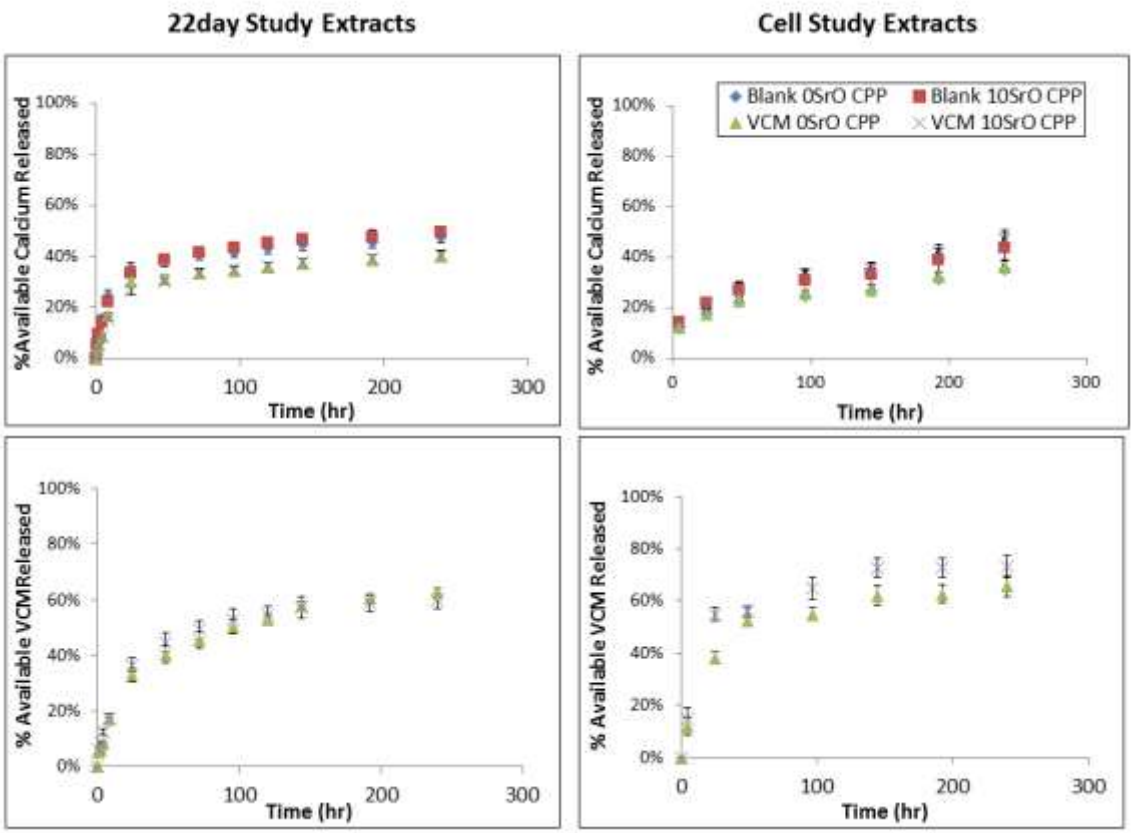

Figure 5.20: Fraction of available calcium ion and VCM released in (left) 22day study and (right) cell study extracts from CIP beads in 0.1M TBS. Data reported as average values while error bars represent one standard deviation (n=6).

Figures 5.21 – 5.25 describe the changes in eluent pH, as well as the eluent ion and VCM concentration at the given time points for this study; these are "real time" measurements. The table that follows (Table 5.4) indicates the significant pairs at given time points for media pH, as well as ion and VCM concentration in the eluents.

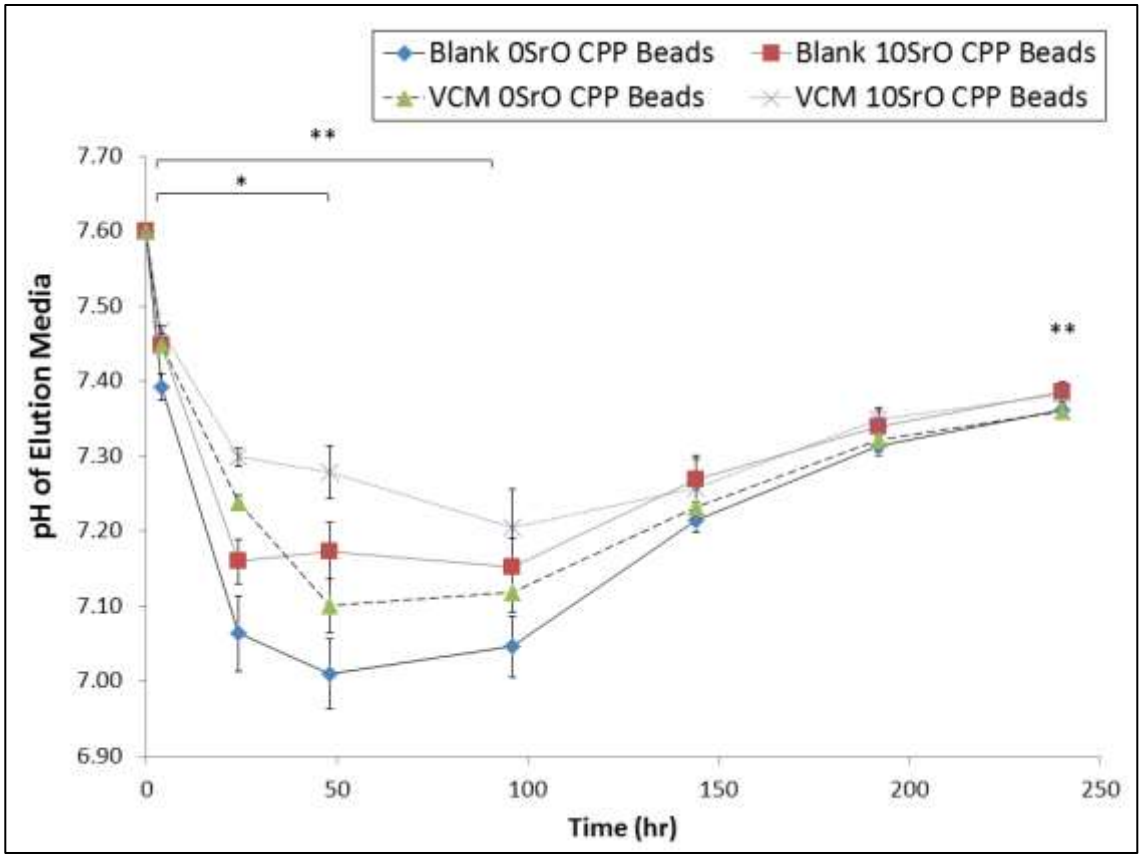

Figure 5.21: pH of elution media with CPP beads. Data reported as average values while error bars represent one standard deviation (n=6). VCM-loaded beads have a significantly higher pH than blank beads (*), while strontium-doped beads have a significantly higher pH than undoped beads (**) at indicated time points ($p<0.05$).

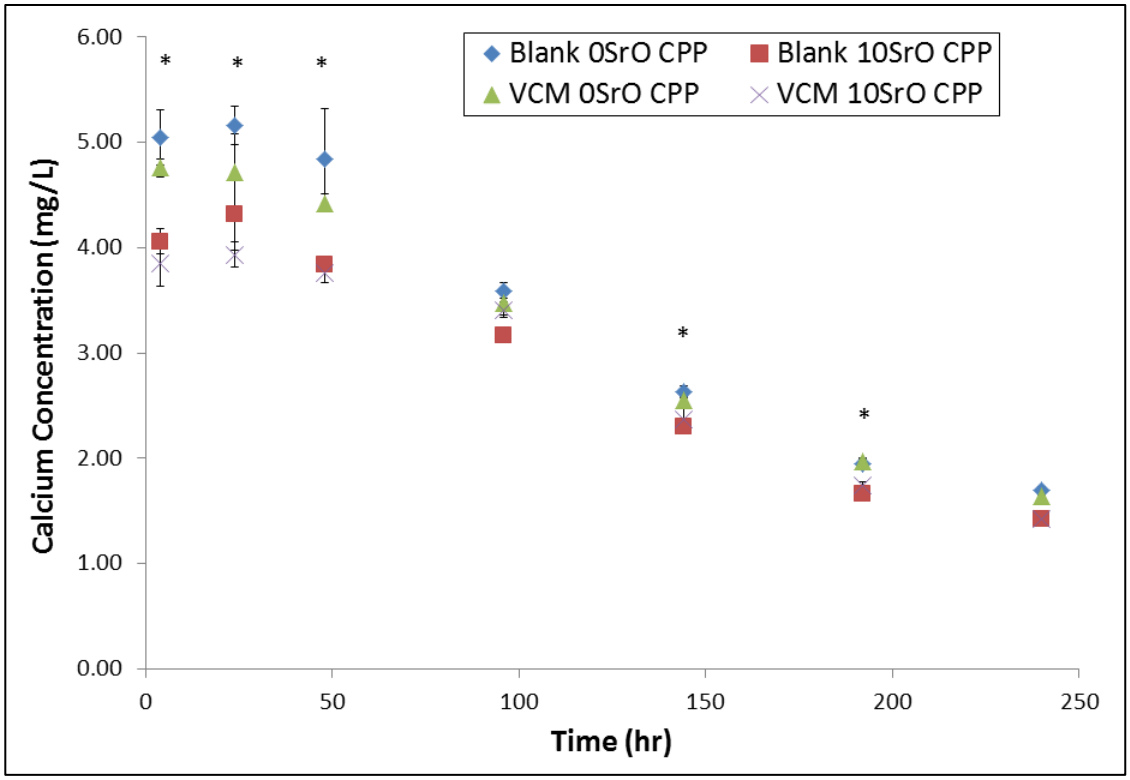

Figure 5.22: Calcium ion concentration in eluent over 10d elution study of CIP beads for cell study. Data reported as average values while error bars represent one standard deviation (n=6). Strontium-doped bead extracts had a significantly lower calcium concentration than those from undoped beads (*) at indicated time points ($p<0.05$).

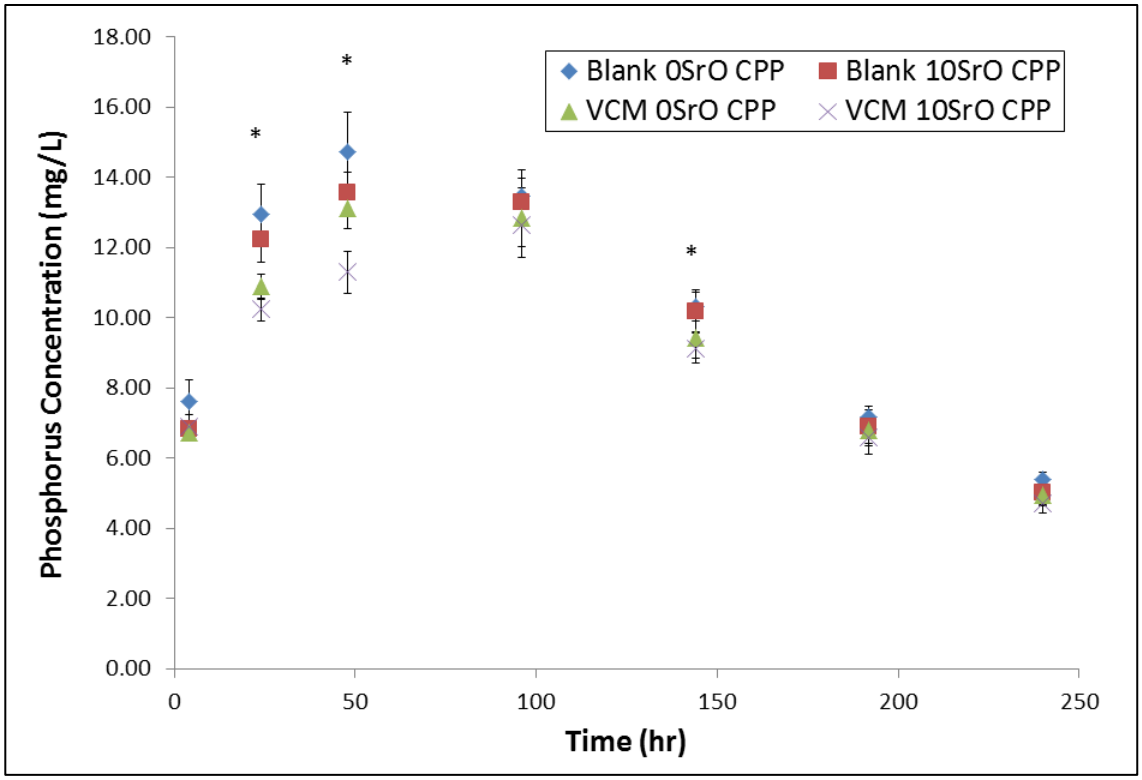

Figure 5.23: Phosphorus ion concentration in eluent over 10d elution study of CIP beads for cell study. Data reported as average values while error bars represent one standard deviation (n=6). VCM-loaded bead extracts had a significantly lower phosphorus concentration than those from blank beads at indicated time points (*) ($p<0.05$).

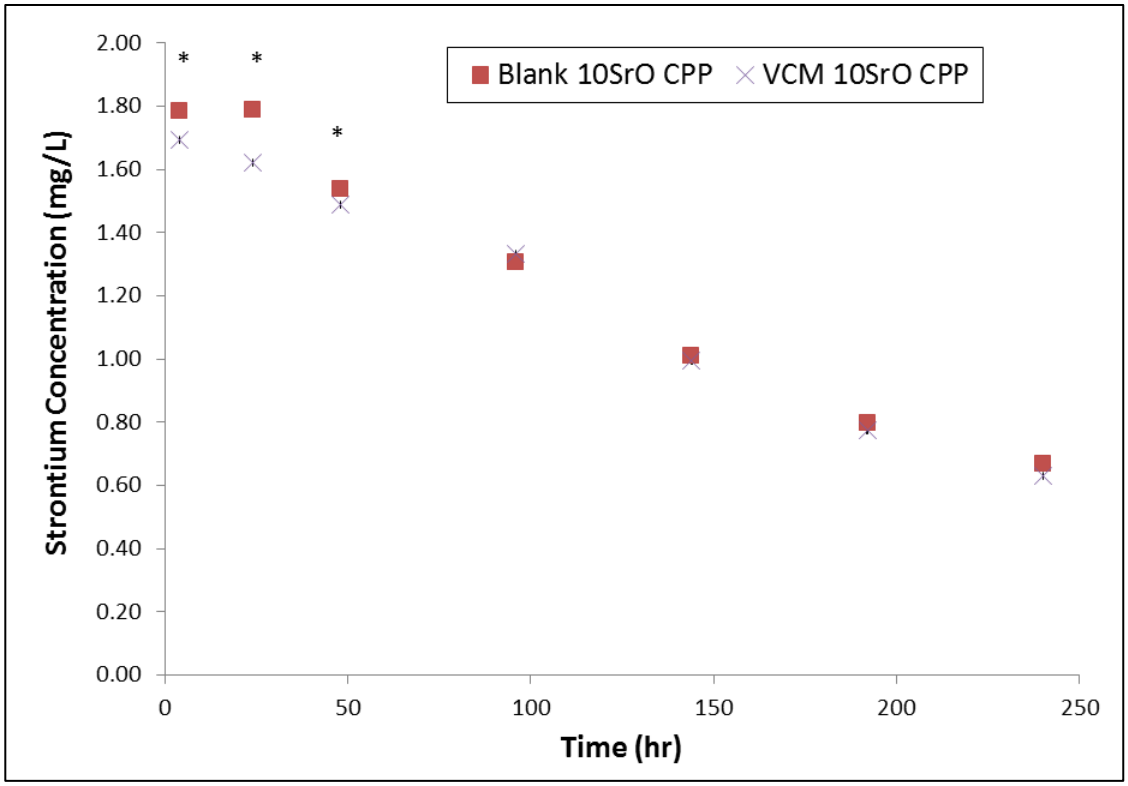

Figure 5.24: Strontium ion concentration in eluent over 10d elution study of CIP beads for cell study. Data reported as average values while error bars represent one standard deviation (n=6). VCM-loaded bead extracts had a significantly lower strontium concentration than those from blank beads (*) at indicated time points ($p<0.05$).

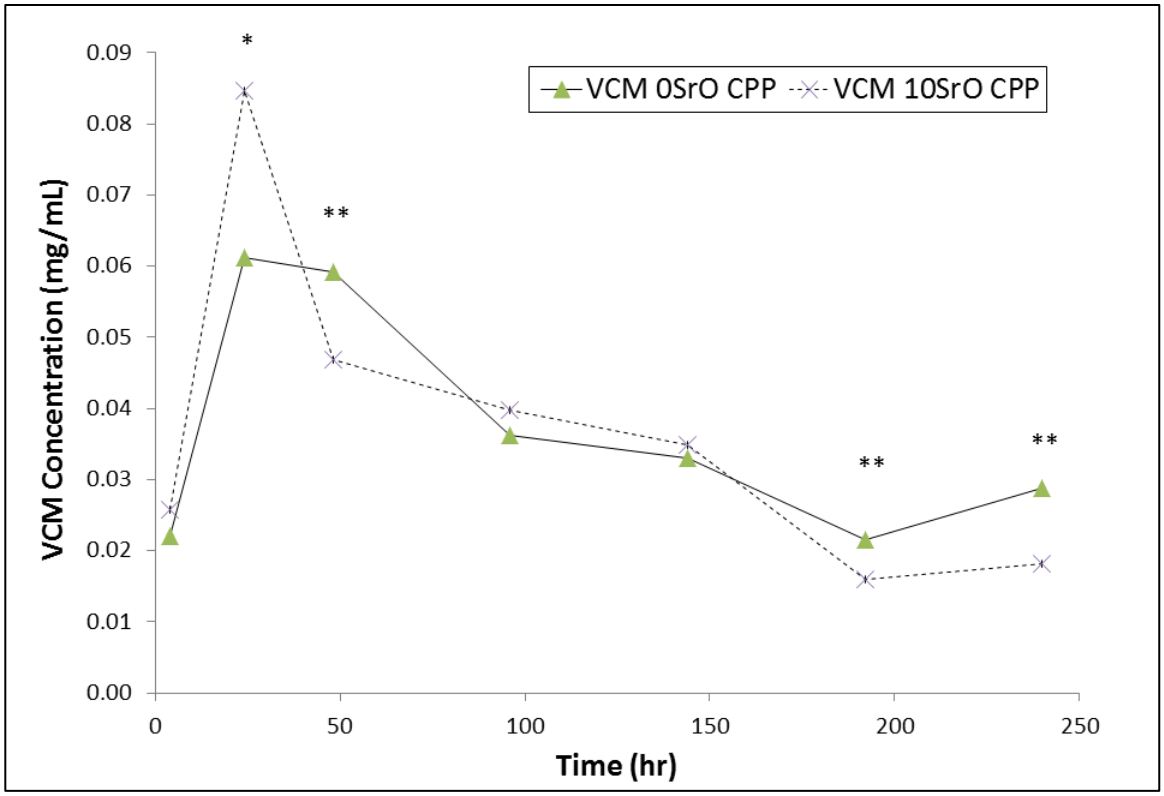

Figure 5.25: VCM concentration in eluent over 10d elution study of CIP beads for cell study. Data reported as average values while error bars represent one standard deviation (n=6). Strontium-doped bead extracts had significantly higher (*) or lower (**) VCM concentration than those from undoped beads at indicated time points ($p<0.05$).

The pH of the collected extracts continued to drop until at least 48hrs into the *in vitro* study for all beads. However, at no collection time point did this pH fall below 7.0. After 96hrs, all extracts showed a trend towards pH stabilization and a return to the starting media pH. Given these findings, no adjustment was made to the extract pH prior to addition to the cell culture wells.

Table 5.4: Reported pH and fraction of available ion and VCM released with relative significance indicated ($p<0.05$) (n=6).

Time	4hr	24hr	48hr	96hr	144hr	192hr	240hr
pH of Elution Media							
Blank 0SrO CPP	7.39 (0.02)^{C}	7.06 (0.05)^{D}	7.01 (0.05)^{D}	7.05 (0.04)^{C}	7.22 (0.02)^{B}	7.31 (0.01)^{B}	7.36 (0.01)^{B}
Blank 10SrO CPP	7.45 (0.01)^{B}	7.16 (0.03)^{C}	7.17 (0.04)^{B}	7.15 (0.04)^{A,B}	7.27 (0.03)^{A}	7.34 (0.02)^{A,B}	7.39 (0.01)^{A}
VCM 0SrO CPP	7.45 (0.01)^{B}	7.24 (0.01)^{B}	7.10 (0.04)^{C}	7.12 (0.03)^{B}	7.23 (0.02)^{A,B}	7.32 (0.02)^{A,B}	7.36 (0.01)^{B}
VCM 10SrO CPP	7.47 (0.01)^{A}	7.30 (0.01)^{A}	7.28 (0.04)^{A}	7.21 (0.05)^{A}	7.26 (0.04)^{A,B}	7.35 (0.02)^{A}	7.38 (0.00)^{A}
Eluent Calcium Ion Concentration (mg/L)							
Blank 0SrO CPP	5.05 (0.26)^{A}	5.16 (0.18)^{A}	4.84 (0.48)^{A}	3.59 (0.07)^{A}	2.63 (0.05)^{A}	1.95 (0.06)^{A}	1.69 (0.04)^{A}
Blank 10SrO CPP	4.06 (0.12)^{B}	4.31 (0.34)^{B,C}	3.84 (0.05)^{C}	3.17 (0.05)^{C}	2.30 (0.07)^{B}	1.66 (0.05)^{C}	1.42 (0.05)^{A}
VCM 0SrO CPP	4.76 (0.09)^{A}	4.72 (0.36)^{A,B}	4.42 (0.09)^{B}	3.47 (0.11)^{A,B}	2.55 (0.04)^{A}	1.97 (0.03)^{A}	1.64 (0.03)^{A}
VCM 10SrO CPP	3.84 (0.21)^{B}	3.93 (0.12)^{C}	3.76 (0.09)^{C}	3.41 (0.08)^{B}	2.37 (0.10)^{B}	1.74 (0.04)^{B}	1.43 (0.03)^{A}
Eluent Phosphorus Ion Concentration (mg/L)							
Blank 0SrO CPP	7.61 (0.65)^{A}	12.96 (0.85)^{A}	14.74 (1.12)^{A}	13.46 (0.75)^{A}	10.33 (0.41)^{A}	7.19 (0.31)^{A}	5.39 (0.22)^{A}
Blank 10SrO CPP	6.85 (0.19)^{B}	12.25 (0.67)^{A}	13.58 (0.57)^{A,B}	13.30 (0.67)^{A}	10.19 (0.60)^{A,B}	6.90 (0.48)^{A}	5.01 (0.33)^{A,B}
VCM 0SrO CPP	6.75 (0.19)^{B}	10.89 (0.35)^{B}	13.14 (0.59)^{B}	12.87 (0.84)^{A}	9.43 (0.59)^{B,C}	6.79 (0.42)^{A}	4.95 (0.30)^{A,B}
VCM 10SrO CPP	6.92 (0.34)^{B}	10.25 (0.32)^{B}	11.31 (0.60)^{C}	12.66 (0.92)^{A}	9.14 (0.43)^{C}	6.59 (0.48)^{A}	4.72 (0.28)^{B}
Eluent Strontium Ion Concentration (mg/L)							
Blank 10SrO CPP	1.79 (0.06)^{A}	1.79 (0.16)^{A}	1.54 (0.04)^{A}	1.31 (0.05)^{A}	1.01 (0.05)^{A}	0.80 (0.06)^{A}	0.67 (0.04)^{A}
VCM 10SrO CPP	1.70 (0.06)^{B}	1.62 (0.05)^{B}	1.49 (0.02)^{B}	1.33 (0.05)^{A}	1.00 (0.06)^{A}	0.77 (0.02)^{A}	0.63 (0.01)^{A}
Eluent Vancomycin Concentration (mg/mL)							
VCM 0SrO CPP	0.02 (0.01)^{A}	0.06 (0.00)^{B}	0.06 (0.00)^{A}	0.04 (0.01)^{A}	0.03 (0.01)^{A}	0.02 (0.00)^{A}	0.03 (0.00)^{A}
VCM 10SrO CPP	0.03 (0.01)^{A}	0.08 (0.01)^{A}	0.05 (0.01)^{B}	0.04 (0.00)^{A}	0.03 (0.00)^{A}	0.02 (0.00)^{B}	0.02 (0.00)^{B}

Note1: Values reported as mean (standard deviation)

Note2: Means that do not share a letter are significantly different at given time point ($p<0.05$).

For much of the elution study, the concentration of calcium ions present in the eluent was significantly greater for undoped CPP beads, not surprising given that with doped CPP strontium addition replaces 10% of the available calcium. By comparison, VCM loading of the CPP beads resulted in a significantly reduced phosphorus ion concentration in the eluent at a few time points, while significantly reducing strontium concentration for the first 48hrs of the study ($p<0.05$). After 48hrs, any differences in ion and VCM concentrations in the eluents of the sample groups were noticeably reduced. It is important to note, however, that the total cation concentration (i.e. calcium and strontium) added to the cells from the strontium-doped beads was still significantly greater than that from the undoped beads. Differences in cell activity in response to extract addition may then, as a result, be influenced more by how the added therapeutic components manipulate degradation of the bead and release of all osteo-promotive ions.

BCA total protein assay results are shown in Figure 5.26, the ALP activity results in Figure 5.27, and the mineralization staining and de-staining results in Figures 5.28-5.29.

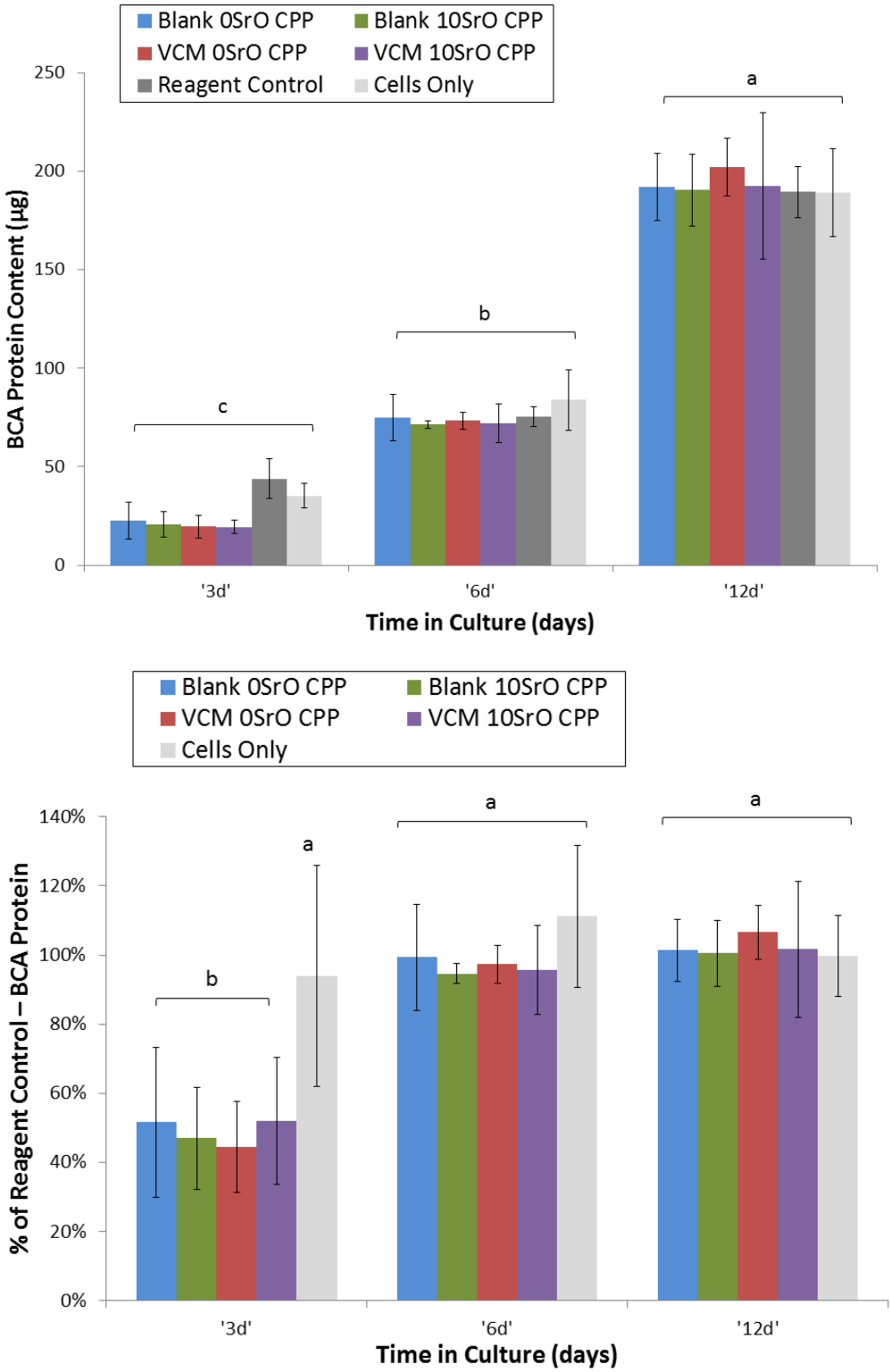

Figure 5.26: (Top) BCA protein of MC3T3-E1 cells and (bottom) relative fraction of BCA content detected. Data reported as average values while error bars represent one standard deviation (n=6). Means that do not share a letter are significantly different ($p<0.05$).

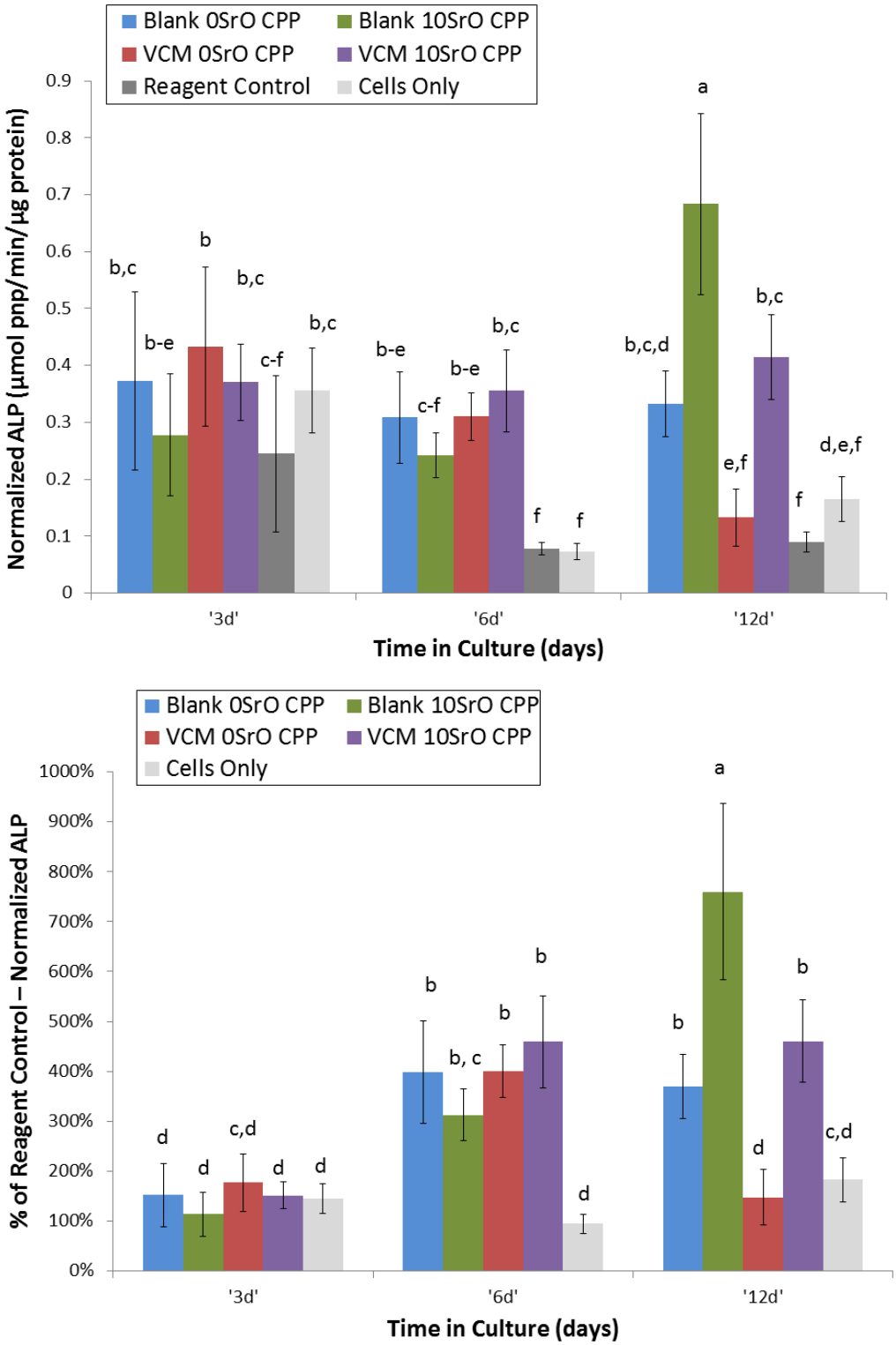

Figure 5.27: (Top) ALP of MC3T3-E1 cells normalized to total protein and (bottom) relative fraction of normalized ALP detected. Data reported as average values while error bars represent one standard deviation (n=6). Means that do not share a letter are significantly different ($p<0.05$).

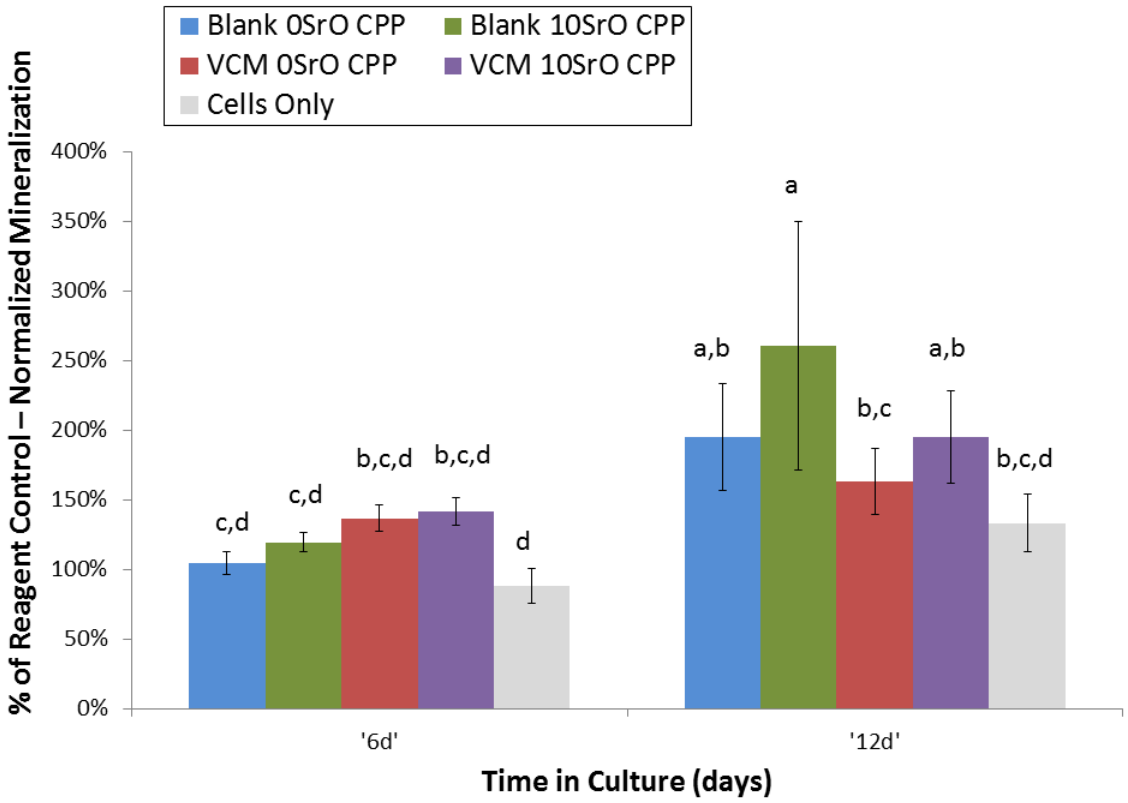

Figure 5.28: Degree of mineralization normalized to total protein and reported relative to reagent control. Data reported as average values while error bars represent one standard deviation (n=6). Means that do not share a letter are significantly different ($p<0.05$). Due to potential differences in staining efficiency on different days, the degree of mineralization was reported relative to the reagent control for that days staining. The next figure (5.29) helps qualify mineralization progression.

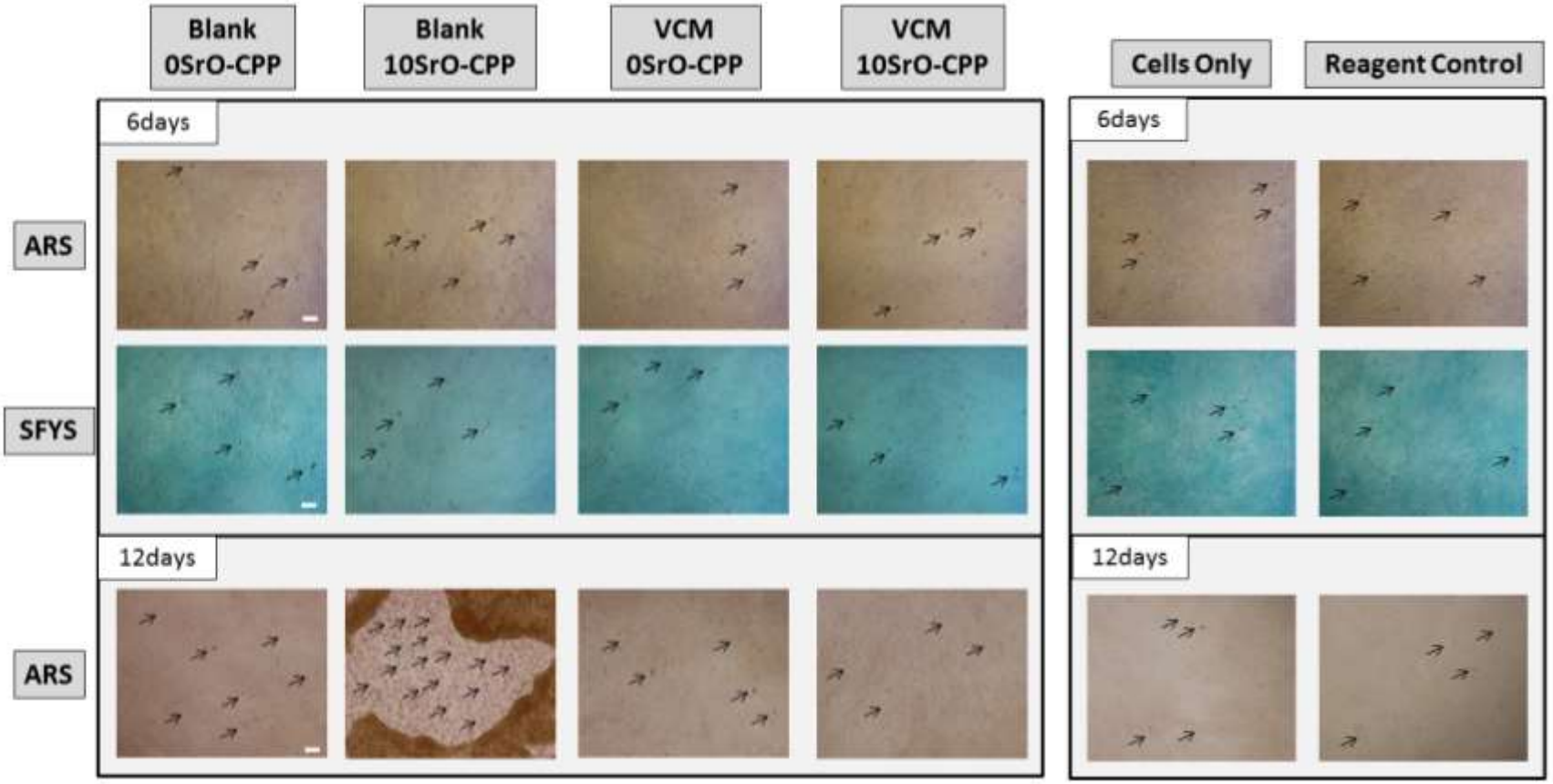

Figure 5.29: Microscopic images of MC3T3-E1 cells at 10X magnification after staining for mineralization. Black arrows indicate some of the detectable deposits of calcium. Scale bars represent 100μm.

The amount of protein increased significantly from 3d to 6d and again from 6d to 12d for each sample group and reagent control ($p<0.05$); no significant differences were noted, however, between sample groups at each time point. The protein detected with the cells-only control was significantly closer to that found with the reagent control (i.e. 0.1M TBS extract added to cells). From this data and light microscope observation, the cells overall appeared to be healthy and active with confluency in the culture wells reached at approximately day 4.

ALP activity for sample groups was either comparable to or significantly greater than that observed for the controls. For example, the ALP activity of extracts from Blank 10SrO CPP beads at day 6 and VCM 0SrO CPP beads at day 12 was comparable to that of the reagent control. The remaining sample groups had as much as 4-7X the ALP activity of the reagent control at day 6 and 12 ($p<0.05$). In addition, at day 12 there was a significant dependence on strontium and VCM doping of the bead. For example, extracts from strontium-doped beads had significantly *increased* ALP activity while extracts from VCM-doped beads had a significantly *decreased* ALP activity compared to eluents lacking either strontium or VCM, respectively ($p<0.05$). Pearson correlation analysis confirmed these observations. Strontium concentration in the extracts correlated strongly, positively and significantly (correlation: 0.755, $p<0.001$) with 12d ALP activity, while VCM correlation was of medium strength, opposing and significant (correlation: -0.655, $p<0.01$) for 12d ALP activity. In other words, the more strontium and less VCM added to the cells, the greater the ALP activity of the cells

For blank samples the degree of mineralization increased significantly from day 6 to day 12 ($p<0.05$) with more calcium deposits formed and, subsequently, more alizarin red de-staining measured with a UV-Vis spectrophotometer at 562nm. At 12d the extracts from blank strontium-doped beads also had significantly greater degrees of mineralization than the controls ($p<0.05$). Sample extracts with VCM present had a degree of mineralization comparable to the cell-only control. Pearson correlation analysis further confirmed that strontium concentration in the extract correlated with medium strength, positively, and significantly (correlation: 0.430, $p<0.05$) with 12d degree of mineralization, while VCM correlated with similar strength and significance as strontium but in the opposing direction (correlation: -0.438, $p<0.05$) for the same measurement. In other words, the more strontium and less VCM added to the cells, the greater degree of mineralization that was observed at 12d.

5.4 DISCUSSION

5.4.1 Physical and Degradation Characteristics of the CIP-Derived Beads

By and large, the capacity to predictably and reproducibly fabricate CPP beads of clinical relevance using a cold isostatic pressing approach was demonstrated. Gelling of the CIP beads – possible due to the hygroscopic nature of CPP glass - led to a significant drop in bead porosity for all beads.

In this study the significant impact of VCM on CPP matrix porosity was observed and reported on for the *first* time. This study found that loading CPP with VCM limited the degree to which gelling was able to reduce bead porosity (compared to the un-gelled

state). In contrast, earlier studies by Dion *et al* (2005) and Petrone *et al* (2008) on the fabrication of G1 and G2 CPP disks, respectively, found that VCM incorporation did not significantly influence disk gelling or porosity. It is possible that fabricating matrices with CIP magnifies the impact of VCM loading on the physical characteristics of the gelled matrix by improving dimensional uniformity. As a result, the impact of VCM loading on the inter-particle fusion processes during gelling is then more apparent. VCM is a very large molecule and the challenges of doping a calcium phosphate with VCM is often attributed to the steric hindrance near the carboxylic functional group (Stigter *et al*., 2004; Pacheco *et al*., 2014; Ooya *et al*., 2002; Kriwet *et al*., 1996). Thus, VCM may not chemically bind with CPP, but instead may be electrostatically interacting with it and further balancing some of the phosphate charge; a phosphate structure that was once considered "nearly neutral" in the presence of only calcium ion may be given additional "pseudo positive charge" by the VCM molecule. The doping of CPP with VCM may then increase the ionization of the phosphate chains. Moisture will be unable to approach the phosphate chains as closely with VCM present and gelling will not proceed as quickly. The development of a thin outer, *gelled* shell on the VCM-loaded beads gives some credence to this theory (SEM results in Figure 5.8).

An improvement in matrix structural stability with the addition of 10 mol% strontium to CPP appeared even more significant in the *in vitro* study of the beads (particularly those lacking VCM) than previously observed for the G2 disks (in Chapter 4). To explain the observed differences in disk structural stability *in vitro* it is perhaps most revealing that, as with G2 disks, the fraction of strontium released from the beads is less than that for

calcium. The likely differences in hydration and dissolution of CPP with the larger strontium ion substituted in for some calcium ion will contribute to the observed decrease in matrix erosion *in vitro*.

The *long-term* impact of VCM loading on enhanced matrix structural stability and reduced ion release *in vitro* has also not been observed until now (for G2 disks VCM impact was much less dramatic and *short-term*). This could, like the impact of VCM on CPP gelling and resultant porosity, be a result of the reduced access of water dipole to the phosphate chain when VCM is present. In addition, owing to the size of VCM, the addition of this macro-ion to CPP may hinder the ability of the hydrated phosphate chains in the gel layer to progressively relax, disentangle from the partially hydrated chains still attached to the surface, and leach into solution.

The external shell observed on the VCM-loaded beads after gelling may also protect this matrix against erosion and further retard drug release (Lapidus *et al*., 1968). Typically when matrices are added to aqueous media they will absorb water and undergo some swelling as amorphous regions are penetrated by the moisture and both secondary and tertiary structures stabilized by van der Waal's forces and hydrogen bonds are disrupted (Lao *et al.*, 2011; Maderuelo *et al*., 2011; Jimenez-Kairuz *et al*., 2005). In fact, the hydration of the matrices is often accompanied by the formation of several distinct fronts that subsequently disappear as dissolution continues: (1) the erosion front (which separates the matrix and dissolution media), (2) diffusion front (which separates the region where drug is soluble and where it is not), and (3) swelling front (which separates

hydrated matrix from the untouched core) (Madeurello *et al.*, 2011). Here, the presence of an external shell (as well as reduced porosity) is slowing the access of water into the bead and significantly reducing the swelling of the beads relative to G2 disks. By slowing the development of the hydrated layer the release of ions *in vitro* is delayed when VCM is present. In contrast, the G2 disks are more exposed to the aqueous environment and the impact of VCM on structural stability is only observed in the first few hours of *in vitro* study (i.e. a *short-term* impact*)*.

The impact of *strontium* on VCM release *in vitro* was only observed in the first 24hrs, with strontium-doped CPP beads releasing significantly more VCM than undoped beads. This *short-term* impact may also be due to aforementioned differences in gelling related to the ability of water to approach the phosphate chains. For example, SEM analysis (Figure 5.8) suggests that beads containing strontium may not have been gelled as well as the undoped beads, as evident by greater apparent surface roughness and larger pores (both evidence of less hydration).

While G1 particle size had little significant impact on *ion release* from VCM-loaded beads, it did impact *VCM release*. Beads derived from the larger particle size released significantly more VCM than those obtained using <45 μm particulate. When powders are molded under pressure the compaction process occurs with two non-exclusive stages: (1) rearrangement of the particles, and (2) elastic and plastic deformation of the particles or fracture (Koizumi *et al*., 1991; Eksi *et al*., 2002). Densification and the related drop in porosity occur as a result of these continued events with increased pressure and number

of contacts (or "coordination number") developing over time within the matrix. As G1 particle size was not found to have a significant impact on densification and % porosity prior to gelling, it is likely that the compaction process (using the given protocol in section 5.2) is dominated by deformation and/or fracture. In stage two the applied pressure is transmitted more uniformly from the outside towards the bead center, with densification occurring in that same radial direction. As larger particles will fracture much more readily than smaller ones (Bazant *et al*., 1990; List *et al*., 2006), when stage two begins to dominate the smaller particles will be more likely to experience deformation (and an increase in contact between particles), while larger particles will experience more fracture and a small degree of particle rearrangement. Such differences could then lead to beads derived from smaller G1 particles having a narrower pore size distribution (Yan *et al*., 2011) and outer regions of slightly greater density; overall, the % porosity would still be similar to that seen with beads of larger G1 particles. The VCM is then more readily released from beads of larger G1 particles as they have a greater effective surface area at the outer regions of the bead.

5.4.2 Comparing CIP Beads and G2 Disks

Given the significantly reduced porosity and increased distance to the matrix center, one could expect that aqueous media access to the matrix core is more limited for the beads relative to the G2 disks. These differences contribute to degradation occurring more by surface erosion for the beads and by bulk erosion for the disks. Improved dimensional uniformity of CIP beads may have also impacted their *in vitro* degradation relative to the G2 disks. Owing to such differences, it is possible that the drug release mechanism(s)

that dominate will differ between the G2 disks and CIP beads. Mathematical modelling can be employed to compare VCM release from the different CPP matrix geometries. Initially, one could use a simple semi-empirical equation (equation 5.1) presented by Peppas *et al* (1997; 2014) to analyze the first 60% of drug release data under sink conditions:

$$\frac{M_t}{M_\infty} = kt^n \qquad \textbf{[Equation 5.1]}$$

Here, M_t/M_∞ is the fractional release of the drug, t is the release time, k is a structural and geometrical release rate constant, and n is the diffusional release exponent indicative of drug release mechanism (Arifin *et al*., 2006). This power-law equation is commonly depicted as a superposition of Fickian diffusion and "Case-II transport" (i.e. relaxation-controlled mechanism) processes (Arifin *et al*., 2006; Yasir *et al*., 2010). Relaxational changes include swelling, degradation, microcavity formation, and rearrangement of chain segments (Peppas *et al*., 1994). Different values of n exist for cylindrical and spherical geometrics; for cylindrical disks n is 0.45 for Fickian diffusion and 1.0 for "Case-II transport", while for spherical beads these values are 0.43 and 0.85, respectively (Arifin *et al*., 2006; Santos *et al*., 2004). By fitting the release data to Equation 5.1, the semi-empirical diffusional exponent (n) was determined for each of the sample groups and is reported in Table 5.5. The fractional VCM release was also plotted as a function of $t^{1/2}$ in a Higuchi plot (Figure 5.30) to give an indication of the relative contribution of the diffusion-based and relaxation-based release mechanisms (Higuchi *et al*., 1963; Siepmann *et al*., 2011). Linear regions in a Higuchi plot correspond to Fickian diffusion

-dominated release, while non-linear segments are more indicative of anomalous transport.

Table 5.5: Semi-empirical analysis of different matrix systems and likely VCM release mechanisms

System	Diffusional exponent (n)	R^2	Drug Release Mechanism
G2-0SrO CPP (<45μm)	0.68	0.92	Anomalous Transport
G2-10SrO CPP (<45μm)	0.91	0.96	Anomalous Transport
CIP-0SrO CPP (<45μm)	0.51	0.97	Diffusion-based
CIP-10SrO CPP (<45μm)	0.45	0.97	Diffusion-based
CIP-0SrO CPP (45-212μm)	0.54	0.98	Diffusion-based
CIP-10SrO CPP (45-212μm)	0.44	0.98	Diffusion-based

Strontium doping of the CPP G2 disks increased the contribution of relaxational mechanisms (i.e. higher "n"). In addition, the Higuchi plot for the strontium-incorporated G2 disks show an earlier deviation from the first linear trend than the undoped disks. Overall, with no significant impact on *disk* gelling, the impact of strontium on VCM release is attributed to the relative movement of the different hydration fronts (Appendix A, Figure A9). In fact, owing to the openness of the strontium-doped CPP glass network compared to the undoped glass, the relative movement of the swelling front to the diffusion front is likely greater. As a result, strontium-doped disks were less reliant on a diffusion-based mechanism than undoped disks. Additional support for this theory comes from earlier discussion in chapter 4 where the impact of doping CPP with strontium on slowing disk erosion was attributed to the increased degree of electrostatic interactions within the hydrated layer (which here, in turn, impeded movement of diffusion front).

As beads exhibit a 10-20% lower porosity than disks, water transport into the bead construct appears more limiting than any chain relaxation. The lower diffusional exponents for the CIP-based systems compared to the G2 disks indicate a largely diffusion-based mechanism of drug release. This corresponds to the slower rate of erosion and reduced swelling observed for the VCM-loaded beads compared to G2 disks during elution study.

It is also interesting to note that while strontium doping *increased* deviation from Fickian behaviour for the G2 disks, it very slightly *decreased* this same deviation for the CIP beads relative to the undoped matrices. Hydration will be a challenge in both, but for the *strontium-doped beads* the reduced gelling and lower porosity may compound upon this limited hydration and lead to these noted differences in VCM release. Firstly, with a more limited rate of hydration there may not be as distinct a separation of the swelling and diffusion fronts (as expected with the disks). As a result, any chain relaxation may occur almost simultaneously with VCM release. In addition, as hydration soon continues beyond the gelled portion of the beads, the more open glass network of strontium-doped CPP may contribute to the *slightly* quicker release of VCM compared to undoped beads. The release from strontium-doped beads may then be more diffusion-dependent.

Subsequent discussion and analysis of CIP beads will be limited to those derived from <45μm G1 particulate given that VCM release was significantly less controlled from

beads produced from 45-212µm G1 particulate and the desire to compare more directly to G2 disks also made from this smaller particle size.

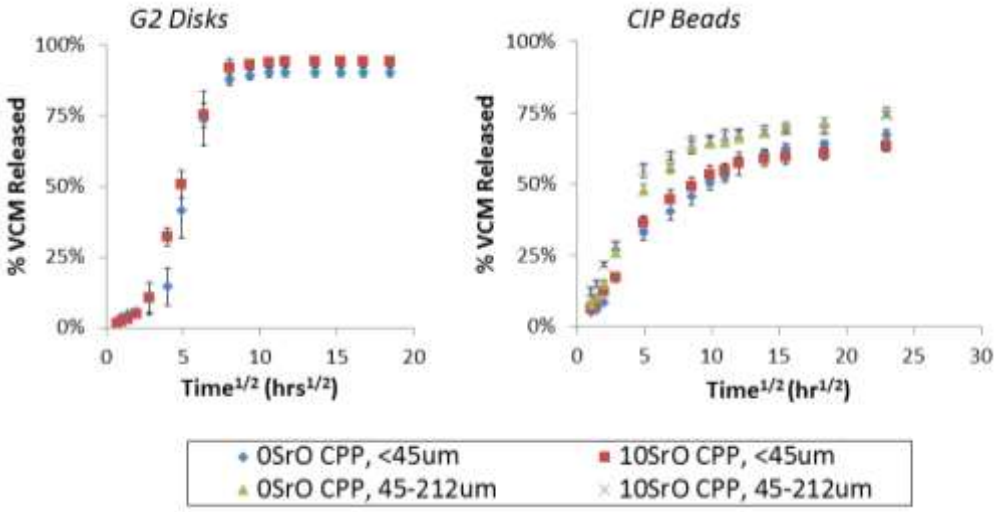

Figure 5.30: VCM drug release from xSrO-CPP (left) G2 disks and (right) CIP beads. Data reported as average values while error bars represent one standard deviation (n=6).

Acknowledging the limitations associated with comparing ion and drug release measured using slightly different elution protocols, Figure 5.31 is intended solely to illustrate relative feasibility of using either matrix design for therapeutic agent delivery. The strontium release profiles for the G2 and CIP matrices (both <45µm G1 and results normalized per 100mg) are similar after ~48hrs, while the impact of matrix shape and fabrication on reaching and maintaining steady VCM levels is more significant. As shown in Figure 5.32 the CIP beads are better able to reach and subsequently maintain steady antibiotic levels throughout the 3-week study. In contrast, the G2 disks reached VCM levels 3-5X higher than that seen with the CIP beads at 24hr, 2d, and 3d, with near zero levels by 6d into elution study. The potential of CPP-based CIP beads for providing

more controlled and therapeutically relevant local delivery of VCM and strontium in osteomyelitis therapy is significant. As a result, *in vitro* functional assessment with cell culture was performed with the fresh extracts of CIP beads.

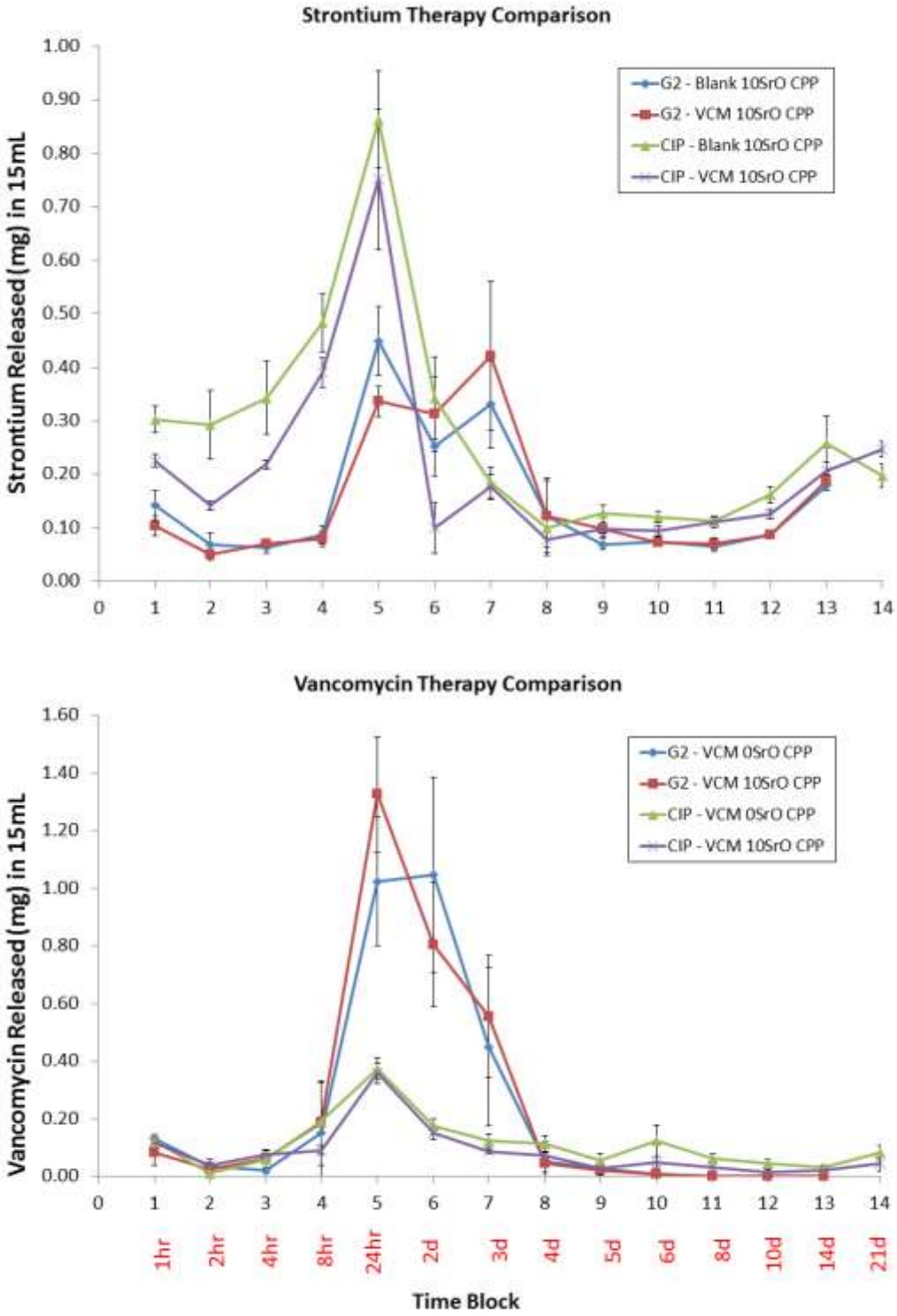

Figure 5.31: (Top) Strontium and (bottom) VCM released at each time point per 100mg matrix. Data reported as average values while error bars represent one standard deviation (n=6).

5.4.3 Functionality Assays

The enhanced *differentiation* capacity of the strontium-doped bead extracts may largely be attributed to the additional presence of strontium in the media, as loading beads with strontium resulted in a statistically significant but only small decrease in extract calcium concentration compared to undoped beads. Pearson correlation confirmed that ALP activity increased with strontium concentration. However, as this correlation was only of medium strength it is likely that *total* cation concentration in the extracts also plays a role in the observed differentiation.

In contrast to strontium doping, the *differentiation* capacity of the VCM-loaded bead extracts is reduced, though still comparable (e.g. VCM-CPP) or greater (e.g. VCM-10SrO-CPP) than either control group after 6d. It is possible that the reduced phosphorus concentration in the media is responsible for the reduced ALP activity of the cells compared to that of cells not exposed to VCM-loaded extracts. Phosphate species, such as BGP and orthophosphates, have previously been found to encourage ALP activity (Kawazoe *et al*., 2004; Omelon *et al*., 2014; Ariganello *et al*., 2014).

Based on the ARS and SFYS staining observed in this study, little difference could be seen in the *maturation* and *mineralization* of the sample groups at 6d. A few calcium deposits were visible in the fields of view in each sample, while the layering of the cells and collagen development progressed only slightly more so for sample extracts with no VCM present than those with VCM or the study controls. The presence of strontium ions in the extract does not noticeably impact cell layering which was stained at 6d. Areas of greater cell layering and more collagen staining are where the few calcium deposits are

found. Studies by others have observed that MC3T3-E1 cells grow first in a monolayer with a shape similar to that of fibroblasts, before matrix maturation (i.e. multiple cell layers appear and the extracellular matrix consisting largely of collagen is laid down) and subsequent matrix mineralization (i.e. calcium deposits and eventually nodules develop) occurs (Lee, 2004; Quarles *et al*., 1992; Franceschi *et al*., 1992).

The number of calcium deposits increased between 6d and 12d for all samples, but particularly so for samples without VCM present and, in fact, several-fold for those with strontium (but no VCM) present. The degree of mineralization reported following de-staining supported this observed increase in calcium deposition between 6 and 12d. At 12d a significant number of the cells cultured with sample extracts containing strontium had also changed shape, appearing more spherical. In contrast, cells cultured for 12d with other sample extracts and controls largely maintained their original fibroblast-like shape. Additionally, neither the number of calcium deposits nor the degree of mineralization increased significantly between 6d and 12d for the controls. Lastly, at 12d there was also a noticeably white opaque precipitate in the wells for extract samples with strontium, regardless of whether VCM was present or not. This precipitate was not observed in any of the wells at 11d so it may be that the other sample wells will soon see a precipitate as well. Studies by others have noted the formation of this "membrane" (Lee *et al*., 2004; El-Ghannam *et al*., 1997) and consider it to be cross-linked collagen fibers originating from the extracellular matrix of the MC3T3-E1 cells.

From the *in vitro* pre-osteoblastic cell functionality results it would appear that strontium doping improves the agonistic potential of the CPP matrices by both manipulating matrix dissolution and releasing strontium ions into the media.

5.5 STUDY LIMITATIONS

In this chapter the study design is once again limited to two levels of strontium addition (0 or 10mol%) and two levels of VCM addition (0 or 7.5mg/150mg CPP); reported data should be appreciated for these design constraints. In addition, cell functionality assays involved quantification of total protein and ALP activity, with staining of calcium deposits and collagen presence over 12d. While the impact of different bead extracts on early pre-osteoblastic cell differentiation was observed, more substantive differences in mineralization due to the presence of strontium, for example, may have been observed at later time points. Future studies should consider additional weeks of cell activity study. The concerns regarding matrix hydration and limited ion release may also be addressed in future studies by collecting a greater volume of extract at each time point. Such a small change in elution set-up may allow for a more significant impact of strontium and VCM loading of CPP on cell activity. Lastly, it is important to acknowledge the artificial nature of any *in vitro* assay and the difficulty in fully translating these study results to *in vivo* expectations. However, *in vitro* studies are important for comparison purposes and the aforementioned changes in study design may further support the clinical feasibility of this CPP-based delivery system.

In addition to the limitations mentioned in Chapters 3 and 4 (section 3.5 and 4.5, respectively) for NMR, DSC/TGA, and density, this chapter also needs to address possible limitations resulting from the new elution study set-up for beads. Owing to concerns of bead movement over the bottom of vials (on horizontally rotating plate), beads were added to 15mL tubes and rotated at an angle for the 22d study. Modelling of G2 disks and CIP beads reaffirmed elution study observations that the various release mechanisms contribute to each matrix system differently. However, it is important to recognize that many factors contribute to VCM release from these matrices and the general approach of modelling applied here is more for comparative discussion.

5.6 CONCLUSIONS

In this chapter an evaluation of a novel CIP bead design for localized osteomyelitis therapy was investigated. CPP beads were successfully fabricated with no significant impact of strontium loading or G1 particle size on the bead diameter or porosity. Gelling produced an expected drop in bead porosity (compared to the un-gelled state). Unexpected and novel to this system is the greater bead porosity as well as apparent improvement in bead structural stability and reduced release of ions *in vitro* with VCM loading of CPP. Furthermore, while the G1 particle size used for CIP had little significant impact on ion release from VCM-loaded beads, it was found to have the greatest influence on VCM release, with the larger particle size releasing significantly more VCM over the 3-week elution period. The cytocompatibility of extracts derived from these beads was confirmed using a standard MTT assay. Subsequent pre-osteoblast functionality assays demonstrated the capacity for these strontium-doped beads to

enhance osteoblast differentiation, as evident by substantive increases to early (ALP expression) and later (mineralization) markers for differentiation during the 12d study.

A comparison of G2 disk and CIP beads *in vitro* revealed that drug release mechanisms contribute to each matrix system differently. The therapeutic release from the CIP beads was more readily controlled with a greater contribution from diffusion-based mechanisms and detectable levels of release out to the 3-week time point reported.

CHAPTER 6 THESIS CONCLUSIONS AND FUTURE DIRECTIONS

With conventional systemic routes of therapy currently unable to adequately address osteomyelitis treatment, local therapeutic delivery systems that achieve elevated antibiotic concentrations at the site of infection while limiting systemic side effects have taken on a greater clinical focus. More appealing still is the capacity to promote healing and bone regeneration while ensuring full eradication of the infection. To this end, the overall aim of this research was to develop a clinically relevant, CPP-based local delivery system for the treatment of osteomyelitis and restoration of any bone lost to the disease. The results from a series of developmental studies to achieve this aim are summarized here in conjunction with the specific objectives and corresponding hypotheses guiding this work. This chapter concludes with recommendations for future study of this CPP-based local delivery system.

6.1 CONCLUSIONS

As chain length was expected to be a key driver of CPP glass properties and the performance of CPP-based VCM delivery systems *in vitro*, a precipitation protocol to achieve CPP glass of preferably greater chain length than that possible by standard melt-derived methods was pursued. In the first part of this study the impact of nine different processing variables, including drying protocol, aqueous NaPP concentration, buffer conditions, order of reactant addition, aqueous solution mixing time, reaction temperature, Ca/P mix ratio of reactants, and impeller speed on the molecular nature of precipitated CPP was first assessed using single-variable analysis. Subsequently, the

three processing variables having the greatest capacity to primarily increase chain length while secondarily maintaining low residual sodium levels and Ca/P molar stoichiometry were further studied in a multi-variable design. Degradation and VCM release from matrices made from precipitated CPP and melt-derived CPP were then compared in a short-term *in vitro* study.

Objective 1.1	To compare the molecular nature of precipitated CPP to that of the conventional melt-derived CPP glass.

Hypothesis 1.1a	*A precipitation strategy can be optimized to create a CPP with significantly greater chain length than that achieved through the conventional melt approach*

CPP glass was successfully precipitated with a significantly greater average chain length than that of the melt-derived CPP reference. Analysis of the chemistry of the collected samples revealed a strong and negative relationship between the residual sodium and Ca/P molar ratio of the precipitates – the higher the residual sodium the lower the Ca/O molar ratio. However, most precipitated samples were still within 10% of the stoichiometric Ca/P molar ratio of CPP of 0.50. Further structural analysis confirmed that a polymeric phosphate-based structure was achieved during CPP precipitation.

All variables studied in CPP precipitation were found to have an impact on CPP chain length during single-variable analysis. However, manipulating aqueous NaPP concentration, order of reactant addition, or Ca/P molar ratio at mix of reactants

separately had the greatest ability to increase amorphous CPP chain length. Optimization of these variables in the subsequent multi-variable study resulted in a precipitate with a 6-fold increase in chain length compared to melt-derived CPP.

Objective 1.2	To compare the *in vitro* elution of VCM from the CPP glass matrices achieved using CPP obtained from either a conventional melt approach or by the new precipitation protocol

Hypothesis 1.2a	*An increase in chain length resulting from this alternative precipitation protocol will enhance the sustained delivery of VCM from the CPP-based G2 matrices*

Precipitated CPP of significantly greater chain length demonstrated a significantly lower VCM loading efficiency compared to melt-derived CPP glass. When included in the fabrication of G2 disks, this precipitated CPP did not reduce early stage (i.e. burst) release or increase the total cumulative release period for measurable VCM release compared to melt-derived CPP G2 disks. The presence of residual sodium was considered largely responsible for the greater degradation and early-stage release from the precipitated CPP G2 disks. Increasing precipitated CPP chain length from 2 to 6X that of melt-derived CPP, while maintaining a residual sodium level below 5 mol%, managed to slightly mitigate this impact of sodium. However, from a drug delivery standpoint, traditional melt-derived CPP glass is still preferable to precipitation in order to maintain high initial loading of the antibiotic into the matrix and minimal early-stage

release of antibiotic *in vitro*. Subsequent studies presented in this thesis therefore made use only of a melt-derived protocol for stock CPP glass processing.

A second thrust of this thesis project was to examine the impact of strontium doping at levels up to 10 mol% on CPP glass structure and degradation, and a corresponding capacity to tune antibiotic release. Strontium was of particular interest given the potential of this ion to actively assist in bone regeneration. Blank and VCM-loaded matrices obtained after one (G1) and two (G2) stages of gelling were evaluated *in vitro* for degradation and release of therapeutic components. 24hr degradation extracts from the G2 disks were also assessed for their cytocompatibility and antibacterial efficacy compared to study-relevant controls.

Objective 2.1	To determine the impact of strontium on the powder density, chain length, and crystallization, melting and glass transition temperatures of the CPP glass

Hypothesis 2.1a	*Increasing strontium doping to 10 mol% will increase the density and chain length of CPP glass while reducing the crystallization, melting, and glass transition temperatures upon heating*

Adding 10 mol% strontium to the CPP glass increased its powder density and chain length without nominally changing the arrangement of bonds in the polymeric structure (e.g. P-O-P or PO_2). However, changes in the next-nearest neighbour environment by substituting some of the calcium for strontium, as revealed by NMR analysis, suggested

that the distribution of phosphate environments was more homogeneous and the short-range structural order greater for the glass. Furthermore, adding 10 mol% strontium was also found to decrease the glass transition temperature, melting temperature, and crystallization temperature of the CPP glass.

Hypothesis 2.1b	*The powder density, chain length, and crystallization, melting, and glass transition temperatures of the strontium-doped CPP glass will not be dependent on the type of strontium salt used in fabrication*

There was largely no dependence of the measured characteristics of strontium-loaded CPP glass on the type of strontium salt used in fabrication – whether strontium phosphate or strontium carbonate.

Objective 2.2	To determine the impact of strontium doping on the gelling capacity and overall stability of CPP glass *in vitro*

Hypothesis 2.2a	*The addition of 10mol% strontium to CPP will not impact the ability of this material to gel and form blank CPP-based G1 disks*

The addition of up to 10 mol% strontium did not significantly affect the ability of the matrices to gel – a requisite for drug loading in this system – and subsequently form disk-like shapes.

Hypothesis 2.2b	*The structural stability of the blank CPP-based G1 disks in vitro will be improved with strontium doping, with less ion release and greater retention of disk shape*

Adding up to 10 mol% strontium noticeably improved the structural stability of the G1 disks over the 7d in 0.1M TBS at 37°C, with visible retention of the matrix shape even after one week. The fraction of available calcium and phosphorus ion released was not dependent on the G1 disk composition over this period; however, the fraction of available strontium released from the doped disks was lower than that for calcium. This could indicate the potential role strontium may be serving to impact the hydration and erosion of CPP.

Hypothesis 2.2c	*The structural stability of the blank CPP-based G1 disks in vitro will not be dependent on the type of strontium salt used in fabrication*

There was no noticeable dependence of disk structural stability *in vitro* on the salt used for strontium doping. However, following elution and upon drying, the disks derived from strontium carbonate-based CPP glass easily broke apart. This observation, and consideration of the need for an additional gelling and drying step (G2) in forming the final local delivery device, prompted a decision to pursue only phosphate-based strontium-loaded glass for G2 disk fabrication.

Objective 2.3	To determine the impact of strontium doping on ion and VCM release from the CPP glass-based local delivery system

Hypothesis 2.3a	*10 mol% strontium doping will reduce the degradation of the CPP G2 matrices and release of calcium and phosphorus ions, as well as delay VCM release from the CPP-based G2 matrices in vitro*

As observed with G1 disks, adding strontium into the CPP-based G2 disks did not significantly impact the ability to fabricate the disks or the porosity of the fabricated G2 disks. Strontium doping did not significantly alter the release of available phosphorus ions but did significantly *increase* the release of available calcium and VCM from the matrices *in vitro* compared to that from un-doped matrices after ~4d in the elution media. Furthermore, the addition of VCM in the CPP-based G2 disks significantly increased the available strontium released after ~4d.

Similar to G1 disks, the fraction of strontium ions released from the strontium-loaded G2 disks was lower than that for calcium. This provided further support for the role strontium is playing to stabilize the disks.

Objective 2.4	To determine the impact of strontium doping on the cytocompatibility and VCM efficacy of the CPP glass based local delivery system

Hypothesis 2.4a	*10mol% strontium doping will not change the cytocompatibility or vancomycin efficacy of the CPP-based G2 matrices relative to undoped matrices*

There was no significant dependence of cell viability on strontium or VCM doping. In addition, the MIC of the VCM released from strontium-doped and undoped G2 disks was comparable to that of freshly prepared stock VCM solution when assessed with a micro-dilution assay using *S.aureus* bacteria.

As a third and final development stream, cold isostatic pressing was deployed as an alternative secondary processing strategy during the G2 phase to achieve VCM-loaded and strontium-doped CPP-based beads, with an eye to increasing matrix structural stability, modifying VCM release and enhancing clinical relevance. Here, the impact of G1 particle size and strontium doping of CPP on bead porosity, degradation and VCM release *in vitro* was first measured. Subsequent assessment with cell functionality assays was performed to provide additional evidence for clinical feasibility of the CPP bead-based local delivery system.

Objective 3.1	To reproducibly form therapeutically loaded CPP beads using a novel cold isostatic pressing and gelling protocol

Hypothesis 3.1a	*After removal from the CIP molds and subsequent gelling the beads will maintain their uniform and spherical shape*

The capacity to predictably and reproducibly fabricate CPP beads of clinical relevance using a cold isostatic pressing approach was demonstrated.

Objective 3.2	To determine the impact of strontium doping and G1 CPP glass particle size on the porosity and gelling ability of the CPP CIP beads

Hypothesis 3.2a	*A smaller overall G1 CPP glass particle size will reduce the porosity of the CPP-based beads but not impact the ability of the beads to gel*

Hypothesis 3.2b	*10 mol% strontium doping will not impact the porosity or gelling ability of the CPP-based beads*

CPP bead diameter and porosity showed no significant dependence on strontium doping or G1 particle size. Gelling realized an expected drop in bead porosity (compared to the un-gelled state). Strontium-doped beads appeared slightly less gelled with a rougher outer surface and larger pores in cross-section than undoped beads. Unexpectedly, loading CPP with VCM reduced the degree to which gelling was able to reduce porosity.

Objective 3.3	To determine the impact of strontium doping and G1 CPP glass particle size on ion and VCM release from the CPP CIP bead-based local delivery system *in vitro*

Hypothesis 3.3a	*A smaller overall G1 CPP glass particle size will delay VCM release and slow CIP bead degradation*

Hypothesis 3.3b	*10 mol% strontium doping will delay CPP CIP bead degradation and VCM release in vitro*

The doping of CPP with 10 mol% strontium again led to a noticeable improvement in matrix structural stability in vitro. As observed with the earlier *in vitro* disk studies the fraction of strontium released from the beads was lower than that for calcium.

In addition, while G1 particle size used for CIP had little significant impact on ion release from VCM-loaded beads, it was found to significantly impact VCM release, with the larger particle size releasing significantly more VCM over the 3-week elution period. This difference in VCM release may be attributed to the how the two different G1 glass particle sizes impact VCM distribution within the beads.

Unexpected and novel to this system is the apparent long-term improvement in bead structural stability and reduced ion release *in vitro* with VCM loading. This observation may be a result of the large size of VCM as well as the nature of its electrostatic interaction with CPP.

Objective 3.4	To compare the release of VCM from the CPP G2 disk- and CPP CIP bead-based local delivery systems

Hypothesis 3.4a	*CIP beads will extend the period of measurable VCM release beyond that achieved with G2 disks in vitro*

A comparison of G2 disk and CIP beads *in vitro* revealed systems that had different dominant mechanisms involved in VCM release. While VCM release from G2 disks exhibited anomalous transport mechanisms, release from the CIP beads was more diffusion-based. Overall, VCM release from CIP beads was more controlled than the disks with detectable levels of release out to at least the 3-week time point reported.

Objective 3.5	To assess the clinical feasibility of the newly designed therapeutically loaded CPP CIP beads for supporting bone tissue recovery using an *in vitro* model

Hypothesis 3.5a	*10 mol% strontium doping will improve pre-osteoblastic cell response to bead extracts, while VCM loading will not negatively impact this same response relative to the study controls*

The cytocompatibility of extracts derived from these beads was confirmed using a standard MTT assay. Subsequent pre-osteoblast functionality assays demonstrated the capacity for these strontium-doped beads to enhance osteoblast differentiation, as evident by substantive increases to early (ALP expression) and later (mineralization) markers for differentiation during the 12d study. VCM-loaded beads were found to have similar expression of these markers relative to the study controls.

The ultimate goal of this thesis work was to design a therapeutically loaded CPP-based delivery system capable of both treating the infection by releasing an antibiotic in a

controllable manner and providing therapeutic ions capable of supporting subsequent bone regeneration. The improved structural stability and VCM release from the matrices by applying CIP, modifying matrix geometry and doping with strontium, together with the agonistic potential displayed in the pre-osteoblast functionality assays, provide evidence for an enhanced clinical feasibility of the therapeutically-loaded CPP bead-based local delivery system.

6.2 FUTURE DIRECTIONS

This thesis presents for the *first time* the impact of different processing parameters, including precipitation variables and strontium doping, on the structural characteristics of amorphous CPP glass and subsequent *in vitro* degradation. The high novelty in this project lies with the use of cold isostatic pressing in conjunction with structural and chemical modification of CPP glass to improve the geometric versatility, therapeutic component release, and clinical feasibility of the CPP-based delivery system for osteomyelitis therapy and bone recovery. This work has established novel protocols for adding strontium to melt-derived CPP and for cold isostatic pressing of the bead-based matrices. Future studies should consider the addition of greater strontium concentrations, the interaction of VCM and other drugs with CPP, further study of CIP bead properties and predictive modeling thereof, as well as additional *in vitro* and *in vivo* studies on the CPP-based beads.

Strontium was found to have a significant impact on glass properties and matrix hydration. A recommendation for future study is the development of a SrO-CaO-P_2O_5

phase diagram. This phase diagram will prove particularly useful should the crystallization of CPP be considered another approach for tuning delivery from the matrices. In addition, greater strontium doping of these CPP-based matrices may reduce the degradation and release of ions even further compared to undoped matrices; with reduced degradation, VCM release may prove more controllable. Additional strontium should also allow for any impact of strontium on the polyphosphate structure (observed using ATR-FTIR and NMR analyses) and matrix gelling (in relation to porosity and observations by DSC/TGA analysis) to be more visible and significant compared to undoped CPP glass. In this regard, ^{87}Sr NMR may confirm the degree of network distortion before *and after* gelling of the CPP-based glass.

The addition of other cations to CPP glass should also be considered. For example, silver ions have previously demonstrated antibacterial efficacy against a broad spectrum of pathogens including *S.aureus* and *Staphylococcus epidermidis* (Hetrick *et al*., 2006; Mourino *et al*., 2010; Eqald *et al*., 2011). In the 1920s the FDA accepted colloidal silver as being effective for wound management and, more recently, clinicians have begun to incorporate varying levels of silver in wound dressings (Chopra, 2007; Ewald *et al*., 2011). Silver ions have not previously been added to amorphous CPP, but owing to its monovalent nature and lower field strength compared to calcium, it should impact CPP glass properties and degradation. Altogether, how other ions may complement the CPP-based delivery system – with respect to impact on glass properties and therapeutic release, as well as interaction with other components – will be interesting to study in the future.

This thesis reports for the *first time* the impact of antibiotic loading on improving the structural stability of CPP-based matrices *in vitro*. Additional analytical methods, including ^{13}C NMR, immunofluorescence, and DSC/TGA, are recommended in future study of the CIP beads to confirm the molecular nature of the loaded antibiotic, antibiotic distribution within the matrices, and nature of any water present, respectively, following gelling and after different stages of i*n vitro* bead hydration. Different drugs, including gentamicin and cefuroxime, should also be considered in conjunction with CIP. Observing how other drugs - of smaller size and containing different functional groups - interact with CPP within the beads may further reveal how VCM itself interacts with CPP. For example, it will be interesting to observe how much of the observed impact of VCM on *in vitro* bead stability is due to antibiotic size, charge, and other properties. To that end, it would also be very interesting to study the release of antibiotics from the beads in media of different pH; antibiotic charge is largely pH dependent (Vijan *et al*., 2009).

In this study the compaction pressure and device surface area-to-volume ratio for the CIP beads were designed to match that of the G2 disks. Future study should consider modeling the impact of different compaction pressures on ungelled bead porosity. A compaction curve (i.e. relative density as a function of pressure) can then be built to more fully understand the mechanisms guiding bead compaction (Kong *et al*., 2000). Following this, it would be useful to know how much gelling is impacted by the preceding densification achieved in CIP. An analysis of density and porosity distribution

within the bead (compared to the G2 disks) should be performed. NMR, XRD, and EDX analysis of the bead cross-section may further confirm any potential impact of gelling on bead structure and chemistry. Next, although the current design is not indicated for load-bearing applications, to extend clinical feasibility of these beads to load-bearing they need to be assessed for mechanical requirements. Beads should then be added to a defect model and mechanical testing performed.

In vitro modelling of bead hydration is recommended in order to more fully understand the speed and manner in which the beads erode. One possible model involves adding the different beads to colour-dyed media and removing the beads at given time points in order to measure the depth of media perfusion and any changes to hydration layer and outer gelled shell. Additional considerations in *in vitro* modelling of beads include studying the impact of collecting a different extract volume (other than 7mL). Such a small change in elution set-up should change the degree of electrostatic interactions in the hydrated portion of the bead and manipulate how much total therapeutic is released.

To meet clinical demands, an additional consideration in bead fabrication using CIP is scale-up. For example, future studies should consider improving the design of CIP molds to allow for greater yield while maintaining bead uniformity and dimensional control.

While the impact of different bead extracts on early osteoblastic cell differentiation was observed in this 12d study, more substantive differences in mineralization due to the presence of strontium, for example, may have been observed at later time points. Future

study should consider additional weeks of cell activity study. Other morphological and biochemical techniques for measuring the progression of osteoblast differentiation should also be considered. For example, the relative expression of additional bone matrix proteins (including bone sialoprotein and osteocalcin) will provide more information on the role of the bead extracts in differentiation (Cooper *et al*., 1998). Lastly, future study may consider the use of tissue culture plate inserts for increasing the exposure of cells to bead extracts (Obadia *et al*., 2011). The test is still considered "indirect", however, by adding the beads to culture media (in these inserts) there is no dilution of the extracts and there, potentially, will be a more immediate response of the cells to the therapeutic components. An existing concern with these inserts is how to best mitigate media pH changes owing to bead degradation. More frequent media changes and/or smaller bead diameter may largely overcome this challenge.

The beads released detectable levels of VCM for at least 3 weeks in the study reported here. In future studies the measurement of microbiological activity in response to this eluted antibiotic at intermittent time points is recommended in order to confirm antibiotic efficacy. Additional bactericidal analysis, such as with a disk-diffusion susceptibility test on agar (Clinical Laboratory Standards Institute standard M02-A8), may also be necessary to support the potential of the CPP-based delivery device for infection eradication.

Following further *in vitro* examination of the clinical feasibility of the CPP bead-based delivery system, an *in vivo* infection model is also recommended. For example, rabbit

long bone models are the most popular in literature for studying treatment of osteomyelitis, but other small animals may also be considered (Norden, 1988).

BIBLIOGRAPHY

Abulfotooh, M. Osteomyelitis: Historical review. Pan Arab J Orth Trauma. 7: 95-109, 2003.

Ahmed I, Lewis MP, Nazhat SN, Knowles JC. Quantification of anion and cation release from a range of ternary phosphate-based glasses with fixed 45 mol% P_2O_5. J Biomater Appl 2005;20:65-80.

Ahola, N. In vitro Studies of Bioabsorbable and Antibiotic-Releasing Composites for the Treatment of Osteomyelitis. Tampere University of Technology (2014 PhD Thesis).

Akamatsu, T.; Kasuga, T.; Nogami, M. Formation of metaphosphate hydrogels and their proton conductivities. J Non-Cryst Solids 2005; 351: 691-696.

Ambrose, C.; Gogola, G.; Clyburn, T.; Raymond, A.; Peng, A.; Mikos, A. Antibiotic Microspheres: Preliminary Testing for Potential Treatment of Osteomyelitis. Clin Orth Rel Res 2003; 415: 279 – 285.

Amjad Z, Zuhl RW. The Influence of Polymer Architecture on Inhibition of Amorphous Calcium Phosphate Precipitation. Phosphorus Research Bulletin 2002;13:51-57.

Ammann, P. Strontium ranelate: A novel mode of action leading to renewed bone quality. Osteoporos Int 2005; 16: S11 – S15.

Ammann, P.; Shen, V.; Robin, B.; Mauras, Y.; Bonjour, J.; Rizzoli, R. Strontium Ranelate Improves Bone Resistance by Increasing Bone Mass and Improving Architecture in Intact Female Rats. J Bone Miner Res 2004; 18: 2012 – 2020.

Andrew, E. Magic angle spinning in solid state n.m.r. spectroscopy. Phil Trans R Soc Lond A 1981; 299: 505 – 520.

Ani, S. Physical Behaviour of Powder Ceramic Part Using Cold Isostatic pressing Processes. M.Engg Thesis, 2006.

Antoci Jr, V., Adams, C. S., Hickok, N. J., Shapiro, I. M., & Parvizi, J. Antibiotics for local delivery systems cause skeletal cell toxicity in vitro. Clin Orth Rel Res, 2007; 462: 200-206.

Arifin, D.; Lee, L.; Wang, C. Mathematical modeling and simulation of drug release from microspheres: Implications to drug delivery systems. Adv Drug Del Rev 2006; 58: 1274-1325.

Ariganello, M.; Omelon, S.; Variola, F.; Wazen, R.; Moffatt, P.; Nanci, A. Osteogenic Cell Cultures Cannot Utilize Exogenous Sources of Synthetic Polyphospahte for Mineralization. J Cell Biochem 2014; 115: 2089-2102.

Arruebo, M., Vilaboa, N., Santamaria, J. Drug delivery from internally implanted biomedical devices used in traumatology and in orthopaedic surgery. Expert Opin Drug Deliv 2010; 7: 589 – 603.

Ascherl, R.; Stemberger, A.; Lechner, F.; Plaumann, L.; Rupp, G.; Machka, K.; Erhardt, W.; Sorg, K.; Blumel, G. Treatment of chronic osteomyelitis with a collagen-antibiotic compound—preliminary report. Unfallchirurgie 1986; 12: 125-127.

Ataka, K.; Yotsuyanagi, T.; Osawa, M. Potential-Dependent Reorientation of Water Molecules at an Electrode-Electrolyte Interface Studies by Surface-Enhanced Infrared Absorption Spectroscopy. J Phys Chem 1996; 100: 10664-10672.

Avramov, I.; Vassilev, T.; Penkov, I. The glass transition temperature of silicate and borate glasses. J Non Crys Sol 2005; 351: 472-476.

Baksh, D., Davies, J., Kim, S. Three-dimensional matrices of CPPs support bone growth in vitro and in vivo. J Mater Sci: Mater Med 1998; 9: 743-748.

Balamurugan, A., Mabrouk, K., Pina, S., Bousmina, M., Ferreira, J. Melt-Derived Condensed Polymorphic Calcium Phosphate as Bone Substitute Material: An In Vitro Study. J Amer Ceram Soc 2011; 94: 3023-3029.

Bamberger, D. Diagnosis and Treatment of Osteomyelitis. Comp Ther. 26: 89 – 95, 2000.

Baradari, H.; Damia, C.; Dutreih=Colas, M.; Laborde, E.; Pecout, N.; Champion, E.; Chulia, D.; Viana, M. Calcium phosphate porous pellets as drug delivery systems: Effect of drug carrier composition on drug loading and in vitro release. J Europ Ceram Soc 2012; 32: 2679-2690.

Beck, G.; Sullivan, E.; Moran, E.; Zerler, B. Relationship Between Alkaline Phosphatase Levels, Osteopontin Expression, and Minrealization in Differentiating MC3T3-E1 Osteoblasts. J Cell Biol 1998; 68: 269-280.

Bénet N, Muhr H, Plasari E, Rousseaux J. New technologies for the precipitation of solid particles with controlled properties. Powder Technol 2002;128:93-98.

Bhargava, H.; Srivastava, D. Degradation of Graham's salt in presence of water-miscible organic solvents. J Phys Chem 1970; 74: 36-39.

Bhattacharya, R.; Kundu, B.; Nandi, S.; Basu, D. Systematic approach to treat chronic osteomyelitis through localized drug delivery system: Bench to bed side. Mater Sci Eng C 2013; 33: 3986-3993.

Bhuiyan L, Vlachy V, Outhwaite C. Understanding polyelectrolyte solutions: macroion condensation with emphasis on the presence of neutral co-solutes. Int Rev Phys Chem 2002;21:1-36.

Bonnelye, E.; Chabadel, A.; Saltel, F.; Jurdic, P. Dual effect of strontium ranelate: Stimulation of osteoblast differentiation and inhibition of osteoclast formation and resorption in vitro. Bone 2008; 42: 129 – 138.

Bostman, O.; Hirvensalo, E.; Makinen, J.; Rokkanen, P. Foreign-body reactions to fracture fixation implants of biodegradable synthetic polymers. J Bone Joint Surg 1990; 72B: 592-596.

Brady, R.; Leid, J.; Costerton, J.; Shirtliff, M. Osteomyelitis: Clinical Overview and Mechanisms of Infection Persistence. Clin Microbio Newsletter. 28: 65 – 72, 2006.

Brouillet, M.; Gautier, H.; Miegeville, A.; Bouler, J.; Merle, C.; Caillon, J. Inactivation of Staphylococcus aureus in Calcium Phosphate Biomaterials via Isostatic Compression. J Biomed Mater Res Part B: Appl Biomater 2009; 91B; 348-353.

Brow, R. Review: the structure of simple phosphate glasses. J Non-Cryst Solids 2000; 263: 1-28.

Brow, R. K., Phifer, C. C., Turner, G. L., Kirkpatrick, R. J. Cation effects on 31P MAS NMR chemical shifts of metaphosphate glasses. J Amer Ceram Soc 1991; 74: 1287-1290.

Brown, E.; MacLEOD, R. Extracellular Calcium Sensing and Extracellular Calcium Signaling. Physio Rev. 81: 239 – 297, 2001.

Buchholz, H.; Elson, R.; Heiner, K. Antibiotic-loaded Acrylic Cement: Current Concepts. Clin Orth Rel Res 1984; 96-108.

Buehler J, Chappuis P, Saffar JL, Tsouderos Y, Vignery A. Strontium ranelate inhibits bone resorption while maintaining bone formation in alveolar bone in monkeys. Bone 2001; 29:176–9.

Calhoun, J.H. et al. Treatment of diabetic foot infections: Wagner classification, therapy, and outcome. Foot Ankle 1988; 9:101-106.

Callis, C.; Van Wazer, J.; Arvan, P. The Inorganic Phosphates as Polyelectrolytes. Chem Rev 1954: 54: 777-796.

Camire, C., Nevsten, P., Lidgren, L., McCarthy, I. The effect of crystallinity on strength development of alpha-TCP bone substitutes. J Biomed Mater Res B Appl Biomater 2006; 79: 159-165.

Canal, C.; Pastorino, D.; Mestres, G.; Schuler, P.; Ginebra, M. Relevance of microstructure for the early antibiotic release of fresh and pre-set calcium phosphate cements. Acta Biomater 2013; 9:8403-8412.

Canalis, E.; Hott, M.; Deloffre, P.; Tsouderos, Y.; Marie, P. The Divalent Strontium Salt S12911 Enhances Bone Cell Replication and Bone Formation In Vitro. Bone 1996; 18: 517-523.

Caputo GM, Cavanagh PR, Ulbrecht JS, Gibbons GW, Karchmer AW. Assessment and management of foot disease in patients with diabetes. N Engl J Med 1994; 331: 854–60.

Carstensen, J., Ertell, C. Physical and Chemical Properties of CPs for Solid State Pharmaceutical Formulations. Drug Dev Ind Pharm 1990; 16: 1121-1133.

Caverzasio, J. Strontium ranelate promotes osteoblastic cell replication through at least two different mechanisms. Bone 2008; 42: 1131 – 1136.

Chang, W.; Colangeli, M.; Colangeli, S.; Di Bella, C.; Gozzi, E.; Donati, D. Adult osteomyelitis: Debridement versus debridement plus Osteoset T® pellets. Acta Orthop Belg 2007; 73: 238-244.

Chattopadhyay, N.; Quinn, S.; Kifor, O.; Ye, C.; Brown, E. The calcium-sensing receptor (CaR) is involved in strontium ranelate-induced osteoblast proliferation. Biochem Pharmacol 2007; 74: 438-447.

Chen J, Zheng C, Chen GA. Interaction of macro-and micromixing on particle size distribution in reactive precipitation. Chemical Engineering Science 1996;51:1957-1966.

Chen, F., Wang, K., Liu, C. Crystalline structure and its effects on the degradation of linear CPP bone substitute. Appl Surf Sci 2008; 255: 270-272.

Chen, Y., Feng, T., Shi, G., Ding, Y., Yu, X., Zhang, X., Zhang, Z., Wan, C. Interaction of endothelial cells with biodegradable strontium-doped CPP for bone tissue engineering. Appl Surf Sci 2008b; 255: 331-335.

Chen, Y.; Shi, G.; Ding, Y.; Yu, X.; Zhang, X.; Zhao, C.; Wan, C. In vitro study on the influence of strontium-doped calcium polyphosphate on the angiogenesis-related behaviors of HUVECs. J Mater Sci: Mater Med 2008; 19: 2655-2662.

Chevalier, J.; Gremillard, L. Ceramics for medical applications: A picture for the next 20 years. J Eur Ceram Soc 2009; 29: 1245 – 1255.

Cho, S.; Song, H.; Koo, K.; Jeong, S.; Park, Y. Antibiotic-impregnated cement beads in the treatment of chronic osteomyelitis. Bull Hosp Jt Dis 1997; 56: 140-144.

Chopra, I. The increasing use of silver-based products as antimicrobial agents: a useful development or a cause for concern? J Antimicrob Chemother 2007; 60: 447-448.

Christoffersen, J., Christoffersen, M., Kolthoff, N., Barenholdt, O. Effects of Strontium Ions on growth and dissolution of hydroxyapatite and on Bone Mineral Detection. Bone 1997; 20:47-54.

Chun, S., Jeong, J., Kim, K., Kim, S. Biodegradation Study of Amorphous and Crystalline Calcium Metaphosphate in the SBF and Tris-Buffer Solution. Key Engg Mat 2001; 192-195: 131-134.

Chun, S., Tadjiev, T., Kim, K., Lee, J., Kim, S. Biodegradation and Characterization of Phase Separated $NaCa(PO_3)_3$ and $KCa(PO_3)_3$ from Pure $Ca(PO_3)_2$. Key Engg Mat 2006; 309-311: 211-214.

Cierny, G., Mader, J., Penninck, J. A Clinical Staging System for Adult Osteomyelitis. Clin Orthop Relat Res 2003; September: 7-23.

Clement, J., Manero, J., Planell, J., Avila, G., Martinez, S. Analysis of the structural changes of a phosphate glass during its dissolution in SBF. J Mater Sci Mater Med 1999; 10: 729-732.

CLSI Standard. Methods for dilution antimicrobial susceptibility tests for bacteria that grow aerobically; Approved standard - Sixth edition. Wayne, PA: NCCLS, 2003. NCCLS document no. M07-A8, 2009.

CLSI Standard. Performance standards for antimicrobial disk susceptibility tests; Approved standard - Eighth edition. Wayne, PA: NCCLS, 2003. CLSI document no. M02-A8.

Columbo, P.; Bettini, R.; Massimo, G.; Catellani, P.; Santi, P.; Peppas, N. Drug Diffusion Front Movement is Important in Drug Release Control from Swellable Matrix Tablets. J Pharm Sci, 1995: 84: 991-997.

Comeau, P., Frei, H., Yang, C., Fernlund, G., Rossi, F. In vivo evaluation of calcium polyphosphate for bone regeneration. J Biomater App 2010; 10 pg.

Cooper, A. R., & Eaton, L. E. Compaction behavior of several ceramic powders. J Amer Ceram Soc 1962; 45: 97-101.

Cooper, L.; Yliheikkila, P. Generalizations Regarding the Process and Phenomenon of Osseointegration. Part II. In Vitro Studies. Int J Oral Maxillofac Implants 1998; 13: 163-174.

Crutchfield M, Irani R. A P31 Nuclear Magnetic Resonance Study of Complexing between Li , Ca, and Mg2 Ions and the Lower Condensed Phosphate Polyanions1. J Am Chem Soc 1965;87:2815-2820.

Dahl, S.; Allain, P.; Marie, P.; Boivin, G.; Ammann, P.; Tsouderos, Y.; Delmas, P.; Christiansen, C. Incorporation and Distribution of Strontium in Bone. Bone 2001; 28: 446 – 453.

Dash, A.; Cudworth, G. Therapeutic Applications of Implantable Drug Delivery Systems. Journal of Pharmacological and Toxicological Methods 1998; 40: 1-12.

Del Valle, G. Amador, A. Gaudin, A. F. Miegeville, C. Jacqueline, G. Potel, H. Gautier, J. Caillon, J. M. Bouler, P. Weiss, and V. Le Mabecque. Biomaterials Applications for Nanomedicine, Ch.9: Complete healing of severe experimental osseous infections using a

calcium-deficient apatite as a drug-delivery system. INTECH Open Access Publisher, 2011.

Delahaye, F., Montagne, L., Palavit, G., Baillif, P., Touray, J. Dissolution of (50-x)Na_2O-xCaO-50P_2O_5 metaphosphate glasses in different saline solutions: mechanism and kinetic control. Glastech ber Glass Sci Technol 1999; 72: 161-166.

Dias Filho FA, Carlos LD, Messadeq Y, Ribeiro SJ. Spectroscopic study and local coordination of polyphosphate colloidal systems. Langmuir 2005;21:1776-1783.

Dick R, Tabatabai M. Factors affecting hydrolysis of polyphosphates in soils. Soil Sci 1987;143:97-104.

Ding, Y., Chen, Y., Qin, Y., Shi, G., Yu, X., Wan, C. Effect of polymerization degree of CPP on its microstructure and in vitro degradation performance. J Mater Sci Mater Med 2008; 19: 1291-1295.

Ding, Y.; Wang, J.; Chen, Y.; Shi, G.; Yu, X.; Wan, C. Immersion behaviour of calcium polyphosphate in simulated body fluid. Appl Surf Sci 2008b; 255: 534 – 537.

Dion A, Langman M, Hall G, Filiaggi M. Vancomycin release behaviour from amorphous calcium polyphosphate matrices intended for osteomyelitis treatment. Biomaterials 2005b 12;26:7276-7285.

Dion, A., Berno, B., Hall, G., Filiaggi, M. The effect of processing on the structural characteristics of vancomycin-loaded amorphous CP matrices. Biomater 2005a; 26: 4486-4494.

Doremus R. Precipitation kinetics of ionic salts from solution. J Phys Chem 1958;62:1068-1075.

Drago, L.; Romano, D.; De Vecchi, F. Bioactive glass BAG-S53P4 for the adjunctive treatment of chronic osteomyelitis of the long bones: an in vitro and prospective clinical study. BMC Infect Dis 2013: 13: 584-591.

Dvinskikh S, Murin I, Privalov A, Pronkin A, Rössler E, Vieth H. Microscopic structure of the glassy ionic conductor< i> x</i>· LiF (1−< i> x</i>)· LiPO< sub> 3</sub> from NMR data. J Non Cryst Solids 1998;240:79-90.

Edin, M.; Miclau, T.; Lester, G.; Lindsey, R.; Dahners, L. Effect of Cefazolin and Vancomycin on Osteoblastis in Vitro. Clin Orth Rel Res 1996; 333: 245-251.

Ehara, A.; Ogata, K.; Imazato, S.; Ebisu, S.; Nakano, T.; Umakoshi, Y. Effects of alpha-TCP and TetCP on MC3T3-E1 proliferation, differentiation and mineralization. Biomater 2003; 24: 831-836.

Eksi, A.; Saritas, S. Effects of Powder Hardness and Particle Size on the Densification of Cold Isostatically Pressed Powders. Turkish J Engg Env Sci 2002. 26: 377-384.

El-Ghannam, A.; Ducheyne, P.; Shapiro, I. Porous bioactive glass and hydroxyapatite ceramic affect bone cell function in vitro along different time lines. J Biomed Mater Res 1997; 36: 167-180.

Ellison, C.; Ennis, B.; Hamad, M.; Lyon, R. Measuring the distribution of density and tabletting force in pharmaceutical tablets by chemical imaging. J Pharm Biomed Analysis 2008; 48: 1-7.

Evans, R.; Nelson, C. Gentamicin-impregnated polymethylmethacrylate beads compared with systemic antibiotic therapy in the treatment of chronic osteomyelitis. Clin Orth Rel Res. 1993.

Ewald, A., Hosel, D., Patel, S., Grover, L., Barralet, J., Gbureck, U. Silver-doped Calcium Phosphate Cements with Antimicrobial Activity. Acta Biomater 2011; Jul 2011.

Faber, C.; Hoogendoorn, R.; Stallmann, H.; Lyaruu, D.; van Nieuw Amerongen, A.; Wuisman, P. In vivo comparison of Dhvar-5 and gentamicin in an MRSA osteomyelitis prevention model. J Antimicrob Chemother 2004; 54: 1078-1084.

Fell, J.; Newton, J. Effect of Particle Size and Speed of Compaction on Density Changes in Tablets of Crystalline and Spray-Dried Lactose. J Pharm Sci 1971; 60: 1866-1869.

Ferguson JF, Jenkins D, Eastman J. Calcium phosphate precipitation at slightly alkaline pH values. Journal (Water Pollution Control Federation) 1973:620-631.

Filiaggi, M., Djogbenou, N., Hall, G. A Processing Approach to Tuning the Drug Delivery Characteristics of Calcium Polyphosphate Matrices. Bioceram Develop Applic 2011; 1-4.

Fletcher, J., Kirkpatrick, J.R., Howell, D., Risbud, S. 31 P Magic-angle spinning nuclear magnetic resonance spectroscopy of calcium phosphate glasses. *Journal of the Chemical Society, Faraday Transactions* 1993; 89: 3297-3299.

Franceschi, R.; Iyer, B. Relationship Between Collagen Synthesis and Expression of the Osteoblast Phenotype in MC3T3-E1 Cells. J Bone Mineral Res 1992; 7: 235-246.

Freiberg, S.; Zhu, X. Review: Polymer microspheres for controlled drug release. Int J Pharm 2004; 282: 1-18.

Fu, Y.; Kao, W. Drug release kinetics and transport mechanisms of non-degradable and degradable polymeric delivery systems. Expert Opin Drug Deliv 2010; 7: 429-444.

Gao, H.; Tan, T.; Wang, D. Dissolution mechanism and release kinetics of phosphate controlled release glasses in aqueous medium. J control rel 2004; 96: 29-36.

Gao, H.; Tan, T.; Wang, D. Effect of composition on the release kinetics of phosphate controlled release glasses in aqueous medium. J control rel 2004; 96: 21-28.

Garcia-Lechu, K.; Bouza, E. Treatment recommendations and strategies for the management of bone and joint infections. Expert Opin Pharmacother. 10: 35 – 55, 2009.

Garvin, K.; Miyang, J.; Robinson, D.; Giger, D.; Novak, J.; Radio, S.; Nebraska, O. Polylactide/Polyglycolide Antibiotic Implants in the Treatment of Osteomyelitis. J Bone Joint Surg 1994; 76-A: 1500-1506.

Gautier, H.; Caillon, J.; Le Ray, A.; Daculsi, G.; Merle, C. Influence of isostatic compression on the stability of vancomycin loaded with a calcium phosphate-implantable drug delivery device. J Biomed Mater Res 2000b; 52: 308-314.

Gautier, H.; Merle, C.; Auget, J.; Daculsi, G. Isostatic compression, a new process for incorporating vancomycin into biphasic calcium phosphate: comparison with a classical method. Biomater 2000a; 21: 243-249.

Gavish N, Promislow K. Dependence of the dielectric constant of electrolyte solutions on ionic concentration. arXiv preprint arXiv:1208.5169 2012.

Gbureck, U.; Vorndran, E.; Muller, F. Barralet, J. Low temperature direct 3D printed bioceramics and biocomposites as drug release matrices. J Control Rel 2007; 122: 173 – 180.

Gentleman, E.; Fredholm, Y.; Jell, G.; Lotfibakhshaiesh, N.; O'Donnell, M.;Hill, R.; Stevens, M. The effects of strontium-substituted bioactive glasses on osteoblasts and osteoclasts in vitro. *Biomater* 2010; 31: 3949-3956.

Gentry, L. Management of Osteomyelitis. Int J Antimicrob Agents. 9: 37 – 42, 1997.

Ginebra, M., Traykova, T., Planell, J. Calcium phosphate cements as bone drug delivery systems: A review. J Control Release 2006; 113: 102 – 110.

Gitelis, S., Brebach, G. The treatment of chronic osteomyelitis with a biodegradable antibiotic-impregnated implant. J Orthop Surg 2002; 10: 53-60.

Giuliano, R.; Verpooten, V.; De Broe, M. Renal Cortical Kinetics of Gentamicin after Implantation of Gentamicin-Polymethylmethacrylate Beads in Rats. Antimicrob Agents and Chemother 1986; Sept. 385-389.

Glass, S.; Ewsuk, K. Ceramic Powder Compaction. MRS Bulletin; December 1997.

Gomes, D.; Pereira, M.; Bettencourt, A. Osteomyelitis: an overview of antimicrobial therapy. Brazilian J Pharm Sci 2013; 49:13-27.

Gomez, F., Vast, P., Llewellyn, P., Rouquerol, F. Dehydroxylation mechanisms of polyphosphate glasses in relation to temperature and pressure. J Non-Crystalline Solids 1997; 222: 415-421.

Grynpas MD, Pilliar RM, Kandel RA, Renlund R, Filiaggi M, Dumitriu M. Porous calcium polyphosphate scaffolds for bone substitute applications in vivo studies. Biomater. 23:2063–70, 2002.

Guo, L., Li, H., Gao, X. Phase transformations and structure characterization of CPP during sintering process. J Mater Sci 2004; 39: 7041-7047.

Gupta R, Rayeeny S, Das S, Bhargava H. A comparative study of the catalytic action of water-miscible organic solvents on the hydrolytic degradation of long-chain polyphosphates. Polym Degrad Stab 1995;50:183-188.

Haas, D.; McAndrew, M. Bacterial Osteomyelitis in Adults: Evolving Considerations in Diagnosis and Treatment. Am J Med. 101: 550-561, 1996.

Haleem, A.; Rouse, M.; Lewallen, D.; Hanssen, A.; Steckelberg, J.; Patel, R. Gentamicin and Vancomycin Do Not Impair Experimental Fracture Healing. Clin Orth Rel Res 2004; 427: 22 – 24.

Hamanishi, C.; Kitamoto, K.; Tanaka, S.; Otsuka, M.; Doi, Y.; Kitahashi, T. A Self-Setting TTCP-DCPD Apatite Cement for Release of Vancomycin. J Biomed Mater Res (Appl Biomater) 1996; 33: 139-143.

Hancock, B.; Colvin, J.; Mullarney, M.; Zinchuk, A. The Relative Densities of Pharmaceutical Powders, Blends, Dry Granulations, and Immediate-Release Tablets. Pharm Tech 2003; April: 64-80.

Hardman, J. S., & Lilley, B. A. Mechanisms of compaction of powdered materials. Proc Royal Soc (Br)A. Math Physical Sci 1973;333: 183-199.

Harun, M., Halim, M., Yazid, H., Selamat, Z., Sattar, M., Jalil, M. Preparation of SiC-Based Composites by Cold Isostatic Press. Intl Conf Adv Mat Nano 2010; 323-327.

Hasegawa, M.; Sudo, A.; Komlex, V.; Barinov, S.; Uchida, A. High Release of Antibiotic from a Novel Hydroxyapatite with Bimodal Pore Size Distribution. J Biomed Mater Res Part B: Appl Biomater 2004; 70B: 332-339.

Heijink, A.; Yaszemski, M.; Patel, R.; Rouse, M.; Lewallen, D.; Hanssen, A. Local Antibiotic Delivery with OsteoSet®, DBW®, and Collagraft®. Clin Orth Rel Res 2006; 451: 29-33.

Hesaraki, S., Alizadeh, M., Nazarian, H., Sharifi, D. Physico-chemical and in vitro biological evaluation of strontium/calcium silicophosphate glass. J Mater Sci: Mater Med 2010; 21: 695-705.

Hessle, L.; Johnson, K.; Anderson, H.; Narisawa, S.; Sali, A.; Goding, J.; Terkeltaub, R.; Millan, J. Tissue-nonspecific alkaline phosphatase and plasma cell membrane glycoprotein-1 are central antagonistic regulators of bone mineralization. PNAS 2002; 99: 9445-9449.

Hetrick, E., Schoenfisch, M. Reducing implant-related infections: active release strategies. Chem Soc Rev 2006; 35: 780-789.

Higuchi, T. Mechanism of Sustained-Action Medication: Theoretical Analysis of Rate of Release of Solid Drugs Dispersed in Solid Matrices. J Pharm Sci 1963: 1145-1149.

Hill, W.; Faust, G.; Reynolds, D. The binary system P_2O_5-2CaO-P_2O_5. Amer J Sci 1944; 242: 457-477.

Holcombe, S.; Schneider, R.; Bramlage, L.; Embertson, R. Use of antibiotic-impregnated polymethyl methacrylate in horses with open or infected fractures or joints: 19 cases (1987-1995). J Am Vet Med Assoc 1997; 211: 889-893.

Hong, M.; Son, J.; Kim, K.; Han, M.; Oh, D.; Lee, Y. Drug-loaded porous spherical hydroxyapatite granules for bone regeneration. J Mater Sci: Mater Med 2011; 22:349-355.

Hoppe, U. A structural model for phosphate glasses. J Non-Cryst Solids 1996; 195: 138-147.

Hoppe, A., Guldal, N., Boccaccini, A. Review – A review of the biological response to ionic dissolution products from bioactive glasses and glass-ceramics. Biomater 2011; 32: 2757-2774.

Hott, M.; Deloffre, P.; Tsouderos, Y.; Marie, P. S12911-2 reduces bone loss induced by short-term immobilization in rats. Bone 2003; 33: 115 – 123.

Hribar B, Vlachy V. Clustering of macroions in solutions of highly asymmetric electrolytes. Biophys J 2000;78:694-698.

Huffman, E.; Fleming, J. Calcium Polyphosphate – Rate and Mechanism of Its Hydrolytic Degradation. J Physical Chem 1960; 64: 240-244.

Ipsen, T.; Jergensen, P.; Damholt, V.; Torholm, C. Gentamicin-collagen sponge for local applications. 10 cases of chronic osteomyelitis followed for 1 year. Acta Orthop Scand 1991; 62: 592-594.

ISO Standard. 10993-5: 2009, Biological evaluation of medical devices. *Tests for in vitro cytotoxicity* (1999).

Itoh, H.; Wakisaka, Y.; Ohnuma, Y.; Kuboki, Y. A New Porous Hydoxyapatite Ceramic Prepared by Cold Isostatic Pressing and Sintering Synthesized Flaky Powder. Dental Mat J 1994; 13: 25-35.

Itokazu, M.; Kumazawa, S.; Wada, E.; Wenyi, Y. Sustained release of Adriamycin from implanted hydroxyapatite blocks for the treatment of experimental osteogenic sarcoma in mice. Cancer Letters 1996; 107: 11-18.

Jackson, L.; Kariuki, B.; Smith, M.; Barralet, J.; Wright, A. Synthesis and structure of a calcium polyphosphate with a unique criss-cross arrangement of helical phosphate chains. Chem mater 2005; 17: 4642-4646.

Jarcho, M. Calcium Phosphate Ceramics as Hard Tissue Prosthetics. Clin Orthop Relat Res 1981; 259-278.

Jeyanthi, R.; Thanoo, B.; Metha, R.; DeLuca, P. Effect of solvent removal technique on the matrix characteristics of polylactide/glycolide microspheres for peptide delivery. J Control Rel 1996; 38: 235-244.

Jia, P.; Zhao, J. Single chain contraction and re-expansion of polystyrene sulfonate: A study on its re-entrant condensation at single molecular level. J Chem Phys 2009; 131: 1-4.

Jia, W.; Luo, S.; Zhang, C.; Wang, J. In vitro and in vivo efficacies of teicoplanin-loaded calcium sulfate for treatment of chronic methicillin-resistant Staphylococcus aureus osteomyelitis. Antimicrob Agents Chemother 2010; 54: 170-176.

Jimenez-Kairuz, A.; Llabot, J.; Allemandi, D.; Manzo, R. Swellable drug-polyelectrolyte matrices (SDPM) Characterization and delivery properties. Int J Pharm 2005; 288: 87-99.

Jones, J. Review of bioactive glass: From Hench to hybrids. Acta Biomat 2013; 9: 4457-4486.

Jonsson, M.; Linse, P. Polyelectrolyte-macroion complexation. II. Effect of chain flexibility. J Chem Phys 2001; 115: 10975-10985.

Kadri, Balaji Venkataramanappa. Mechanism of drug release from matrix tablets involving moving boundaries. Department of Pharmaceutical Sciences, University of Toronto. 2001, Thesis, p.14-15.

Kanchana, P., Sekar, C. Influence of strontium on the synthesis and surface properties of biphasic CP bioceramics. J Appl Biomater Biomech 2010; 8: 153-158.

Kandel, R., Grynpas, M., Pilliar, R., Lee, J., Wang, J., Waldman, S., Zalzal, P., Hurtig, M., CIHR-Bioengineering of Skeletal Tissues Team. Repair of osteochondral defects with biphasic cartilage-calcium polyphosphate constructs in a Sheep model. Biomater 2006; 27: 4120-4131.

Kasuga, T., Wakita, T., Nogami, M., Sakurai, M., Watanabe, M., Abe, Y. Hydrogelation of Calcium Metaphosphate Glass. Chem Letters 2001; 30: 820-821.

Kawanabe, K.; Okada, Y.; Matsusue, Y.; Iida, H.; Nakamura, T. Treatment of osteomyelitis with antibiotic-soaked porous glass ceramic. J Bone Joint Surg 1998; 80-B: 527-530.

Kawazoe, Y.; Shiba, T.; Nakamura, R.; Mizuno, A.; Tsutsumi, K.; Uematsu, T.; Yamaoka, M.; Shindoh, M.; Kohga, T. Induction of Calcification in MC3T3-E1 Cells by Inorganic Polyphosphate. J Dent Res 2004; 83: 613-618.

Kehoe, S.; Langman, M.; Werner-Zwanziger, U.; Abraham, R.; Boyd, D. Mixture designs to asses composition-structure-property relationships in SiO2-CaO-ZnO-La2O3-TiO2-MgO-SrO-Na2O glasses: Potential materials for embolization. J Biomater Appl 2013; 28: 416-433.

Kim, Y., Hall, G., Filiaggi, M. Calcium polyphosphate as an anti-cancer drug delivery system. IADR, 2008. Toronto, ON.

Kind M. Colloidal aspects of precipitation processes. Chemical engineering science 2002;57:4287-4293.

Klemm, K. Gentamicin-PMMA-beads in treating bone and soft tissue infections. Zentrulbl Chir 1979; 104: 934-942.

Klemm, K. The use of antibiotic-containing bead chains in the treatment of chronic bone infections. Clin Microbiol Infect 2001; 7: 28-31

Klemm, K. The use of antibiotic-containing bead chains in the treatment of chronic bone infections. Clin Microbiol Infect 2001; 7: 28-31.

Kluin, O.; van der Mei, H.; Busscher, H.; Neut, D. Biodegradable vs non-biodegradable antibiotic delivery devices in the treatment of osteomyelitis. Expert Opin Drug Deliv 2013; 10: 341-351.

Kluin, Otto S., van der Mei, H.; Busscher, H.; Neut, D. Biodegradable vs non-biodegradable antibiotic delivery devices in the treatment of osteomyelitis. Expert Opin Drug Del 2013*;* 10: 341-351.

Koizumi, M.; Nishihara, M., eds. Text: Isostatic Pressing – Technology and Applications. Springer Science & Business Media, London & New York. Ch.1: Fundamentals of Isostatic Pressing Technology, pages: 7-30, 1991.

Kong, C.; Lannutti, J. Localized Densification during the Compaction of Alumina Granules: The State I-II Transition. J Am Ceram Soc 2000; 83: 685-690.

Kreidler, E.;Hummel, F. Phase relations in the system SrO-P2O5 and the influence of water vapor on the formation of Sr4P2O9. Inorg Chem 1967; 6: 884-891.

Kriwet, B.; Kissel, T. Interactions between bioadhesive poly(acrylic acid) and calcium ions. Int J Pharm 1996: 127: 135-145.

Kulaev IS, Vagabov V, Kulakovskaya T. The biochemistry of inorganic polyphosphates. : John Wiley & Sons; 2005.

Lahl, N.; Singh, K.; Singheiser, L.; Hilpert, K.; Bahadur, D. Crystallization kinetics in $AO\text{-}Al_2O_3\text{-}SiO_2\text{-}B_2O_3$ glasses (A=Ba, Ca, Mg). J Mater Sci 2000; 35: 3089-3096.

Lakhkar, N.; Neel, A.; Salih, V.;Knowles, J. Strontium oxide doped quaternary glasses: effect on structure, degradation and cytocompatibility. J Mater Sci: Mater Medic 2009; 20: 1339-1346.

Lakhkar, N.; Neel, E.; Salih, V.;Knowles, J. Titanium and strontium-doped phosphate glasses as vehicles for strontium ion delivery to cells. J Biomater App 2011; 25: 877-893.

Lamberti, G.; Galdi, I.; Barba, A. Controlled release from hydrogel-based solid matrices. A model accounting for water up-take, swelling and erosion. Int J Pharm 2011; 407: 78-86.

Lambotte, J.; Thomazeau, H.; Cathelineau, G.; Lancien, G.; Minet, J.; Langlais, F. Tricalcium phosphate, an antibiotic carrier: a study focused on experimental osteomyelitis in rabbits. Chirurgie 1998; 12: 572.

Lao, L.; Peppas, N.; Boey, F.; Venkatraman, S. Modeling of drug release from bulk-degrading polymers. Int J Pharm 2011; 418: 28-41.

Lapidus, H.; Lordi, N. Drug Release from Compressed Hydrophilic Matrices. J Pharm Sci 1968; 57: 1292-1301.

Larsen RM. Intramedullary pressure with particular reference to massive bone diaphyseal bone necrosis. Annals Surg 1934; 108:127.

Lee, C.; Singla, A.; Lee, Y. Review: Biomedical applications of collagen. Int J Pharm 2001; 221: 1-22.

Lee, Y., Seol, Y., Lim, Y., Kim, S., Han, S., Rhyu, I., Baek, S., Heo, S., Choi, J., Klokkevold, P., Chung, C. Tissue-engineered growth of bone by marrow cell transplantation using porous Ca metaphosphate matrices. J Biomed Mater Res 2000; 54: 216-223.

Lee, Y.; Song, J.; Lee, S.; Kim, K.; Choi, S.; Kim, C.; LeGeros, R.; Kim, K. Proliferation, differentiation, and calcification of preosteoblast-like MC3T3-E1 cells cultured onto noncrystalline calcium phosphate glass. J Biomed Mater Res 2004; 69A: 188-195.

Lew, D.; Waldvogel, F. Osteomyelitis – Current Concepts. Massachusetts Med Soc 1997; 336: 999 – 1007.

Lew, D.; Waldvogel, F. Osteomyelitis. The Lance 2004; 364: 369-379.

Li, B.; Brown, K.; Wenke, J.; Guelcher, S. Sustained release of vancomycin from polyurethane scaffolds inhibits infection of bone wounds in a rat femoral segmental defect model. J Controlled Rel 2010; 145: 221-230.

Li, C.; Paris, O.; Siegel, S.; Roschger, P.; Paschalis, E.; Klaushofer, K.; Fratzl, P. Strontium is incorporated into mineral crystals only in newly formed bone during strontium ranelate treatment. J Bone Min Res 2010; 25: 968 – 975.

Lindfors, N.; Hyvonen, P.; Nyyssonen, M. Bioactive glass S53P4 as bone graft substitute in treatment of osteomyelitis. Bone 2010; 47: 212-218.

List, E., Frenzel, J., & Vollstaedt, H. A new system for single particle strength testing of grinding powders. Industrial diamond review 2006;1: 42.

Liu, S.; Wen-Neng, S.; Lin, S.; Chan, E. In vivo release of vancomycin from biodegradable beads. J Biomed Mater Res 2002; 63: 807-813.

Lucke, M., Wildemann, B., Sadoni, S., Surke, C., Schiller, R., Stemberger, A., Raschke, M., Haas, N., Schmidmaier, G. Systemic versus local applications of gentamicin in prophylaxis of implant-related osteomyelitis in a rat model. Bone 2005; 36: 770-778.

Lucke, M.; Schmidmaier, G.; Sadoni, S.; Wildemann, B.; Schiller, R.; Haas, N.; Raschke, M. Gentamicin coating of metallic implants reduces implant-related osteomyelitis in rats. Bone 2003; 32: 521 – 531.

Ma B, Meredith C, Schaefer III HF. Pyrophosphate structures and reactions: evaluation of electrostatic effects on the pyrophosphates with and without alkali cations. J Phys Chem 1994;98: 8216-8223.

Ma B, Meredith C, Schaefer III HF. The quest for a metaphosphate intermediate. the mechanisms for hydrolysis of pyrophosphates with and without catalysis. J Phys Chem 1995;99:3815-3822.

Mader, J., Shirtliff, M., Bergquist, S., Calhoun, J. Antimicrobial Treatment of Chronic Osteomyelitic. Clin Orthop Relat Res 1999; 360: 47 – 65.

Maderuelo, C.; Zarzuelo, A.; Lanao, J. Review – Critical factors in the release of drugs from sustained release hydrophilic matrices. J Controlled Rel 2011; 154: 2-19.

Madras G, McCoy BJ. Mixing effects on particle precipitation. Ind Eng Chem Res 2005;44:5267-5274.

Maier, G.; Roth, K.; Andereya, S.; Birnbaum, K.; Niedhart, C.; Luhmann, M.; Ohnsorge, J.; Maus, U. In Vitro Elution Characteristics of Gentamicin and Vancomycin from Synthetic Bone Graft Substitutes. Open Orth J 2013; 7: 624-629.

Makarov, C.; Cohen, V.; Raz-Pasteur, A.; Gotman, I. In vitro elution of vancomycin from biodegradable osteoconductive calcium phosphate-polycaprolactone composite beads for treatment of osteomyelitis. European J Pharm Sci 2014; 62: 49-56.

Makarov, C.; Gotman, I.; Radin, S.; Ducheyne, P.; Gutmanas, E. Vancomycin release from bioresorbable calcium phosphate-polymer composites with high ceramic volume fractions. J Mater Scie 2010; 45: 6320-6324.

Makinen, T.; Veiranto, M.; Lankinen, P.; Moritz, N.; Jalava, J.; Tormala, P.; Aro, H. J In vitro and in vivo release of ciprofloxacin from osteoconductive bone defect filler. Antimicrob Chemother 2005; 56: 1063-1068.

Manning, G. Limiting Laws and Counterion Condensation in Polyelectrolyte Solutions I. Colligative Properties. J Chem Phys 1969; 51: 924-933.

Marie, P. Strontium as therapy for osteoporosis. Curr Opin Pharm 2005; 5: 633 – 636.

Marie, P. Strontium ranelate: a novel mode of action optimizing bone formation and resorption. Osteoporos Int 2005-b; 16: S7 – S10.

Marie, P. Strontium ranelate: A physiological approach for optimizing bone formation and resorption. Bone 2006; 38: S10 – S14.

Marie, P. Strontium ranelate: New insights into its dual mode of action. Bone. 40: S5 – S8, 2007.

Marie, P.; Ammann, P.; Boivin, G.; Rey, C. Mechanisms of Action and Therapeutic Potential of Strontium in Bone. Calcif Tissue Int 2001; 69: 121 – 129.

Masson NC, de Souza EF, Galembeck F. Calcium and iron (III) polyphosphate gel formation and aging. Colloids Surf Physicochem Eng Aspects 1997;121:247-255.

Mast, N.; Horwitz, D. Osteomyelitis: A Review of Current Literature and Concepts. Op Tech Ortho. 12: 232-241, 2005.

McAndrew, J.; Efrimescu, C.; Sheehan, E.; Niall, D. Through the looking glass; bioactive glass S53P4 (BonAlive®) in the treatment of chronic osteomyelitis. Ir J Med Sci 2013; 183: 509-511.

McFadden, J. Vascularized partial first metatarsal transfer for the treatment of phalangeal osteomyelitis. J Reconst Micro Surg 1998; 14: 309-312.

McHugh, S., Collins, C., Corrigan, M., Hill, A., Humphreys, H. The role of topical antibiotics used as prophylaxis in surgical site infection prevention. Journal of Antimicrobial Chemotherapy 2011. February.

McKee, M.; Wild, L.; Schemitsch, E.; Waddell, J. The use of an antibiotic-impregnated, osteoconductive, bioabsorbable bone substitute in the treatment of infected long bone defects: early results of a prospective trial. J Orthop Trauma 2002; 16: 622-627.

McLaren, A. Alternative Materials to Acrylic Bone Cement for Delivery of Depot Antibiotics in Orthopaedic Infections. Clin Orthop Relat Res 2004; 101-106.

McPherson, E.; Dipane, M.; Sherif, S. Dissolvable Antibiotic Beads in Treatment of Periprosthetic Joint Infection and Revision Arthroplasty – The Use of Synthetic Pure Calcium Sulfate (Stimulan®) Impregnated with Vancomycin & Tobramycin. Joint Implant Surg Res Foundation 2013; 32-43.

Mehrotra R. Synthesis and properties of simple and complex polymetaphosphate glasses of alkali metals. Pure Appl Chem 1988;60(8):1349-1356.

Mehta, S.; Humphrey, J.; Schenkman, D.; Seaber, A.; Vail, T. Gentamicin distribution from a collagen carrier. J Orth Res 1996;. 14: 749-754.

Montastruc L, Azzaro-Pantel C, Biscans B, Cabassud M, Domenech S. A thermochemical approach for calcium phosphate precipitation modeling in a pellet reactor. Chem Eng J 2003;94:41-50.

Mourino, V., Boccaccini, A. Bone tissue engineering therapeutics: controlled drug delivery in three-dimensional scaffolds. J.R. Soc Interface 2010; 7: 209 – 227.

Nandi, S.; Kundu, B.; Ghosh, S.; Mandal, T.; Datta, S.; De, D.; Basu, D. Cefuroxime-impregnated calcium phosphates as an implantable delivery system in experimental osteomyelitis. Cera Int. 2009; 35: 1367-1376.

Nandi, S.; Mukherjee, P.; Roy, S.; Kundu, B.; De, D.; Basu, D. Local antibiotic delivery systems for the treatment of osteomyelitis – A review. Mat Sci Eng: C. 29: 2478 – 2485, 2009.

National Centre for Biotechnology Information, U.S. National Library of Medicine. PubChem Open Chemistry Database: Compound Summary for CID 15969, Vancomycin.

Neel, E.; Chrzanowski, W.; Pickup, D.; O'Dell, L.; Mordan, N.; Newport, R.; Smith, M.; Knowles, J. Structure and properties of strontium-doped phosphate-based glasses. J Royal Soc Interface 2008: 1-12.

Nelson, C.; Evans, R.; Blaha, J. A comparison of gentamicin-impregnated polymethylmethacrylate bead implantation to conventional parenteral antibiotic therapy in infected total hip and knee arthroplasty. Clin Orthop 1993; 295: 96-101.

Nelson, C.; McLaren, S.; Skinner, R.; Smeltzer, M.; Thomas, J.; Olsen, K. The treatment of experimental osteomyelitis by surgical debridement and the implantation of calcium sulfate tobramycin pellets. J Orth Res 2002; 20: 643-647.

Netz, R.; Andelman, D. Neutral and charged polymers at interfaces. Phys Rep 2003; 380: 1-95.

Neut, D.; Van de Belt, H.; Van Horn, J. Residual gentamicin-release from antibiotic-loaded polymethylmethacrylate beads after 5 years of implantation. Biomater 2003; 24: 1829-1831.

Norden, C. Lessons Learned from Animal Models of Osteomyelitis. Rev Infectious Diseases 1988; 10: 103-110.

Obadia, L.; Julien, M.; Quillard, S.; Rouillon, T.; Pilet, P.; Guicheux, J.; Bujoli, B.; Bouler, J. Na-doped β-tricalcium phosphate: physic-chemical and in vitro biological properties. J Mater Sci: Mater Med 2011; 22: 593-600.

Oberacker, R. Chapter 1: Powder Compaction by Dry Pressing. Editor: Riedel, R.; Chen, I. Ceramics Science and Technology, Synthesis and Processing – Vol.3. John Wiley & Sons, 2011; Page 3-38.

Omdahl, J.; DeLuca, H. Rachitogenic Activity of Dietary Strontium. I. Inhibition of intestinal calcium absorption and 1,25-dihydroxycholecalciferol synthesis. J Biol chem. 247: 5520 – 5526, 1972.

Omelon, S.; Baer, A.; Coyle, T.; Pilliar, R.; Kandel, R.; Grynpas, M. Polymeric crystallization and condensation of calcium polyphosphate glass. Mater Res Bul 2008; 43: 68-80.

Omelon, S.; Georgiou, J.; Variola, F.; Dean, M. Colocation and role of polyphosphates and alkaline phosphatase in apatite biomineralization of elasmobranch tesserae. Acta Biomater 2014; 10: 3899-3910.

Ooya, T.; Eguchi, M.; Ozaki, A.; Yui, N. Carboxyethylester-polyrotaxanes as a new calcium chelating polymer: synthesis, calcium binding and mechanism of trypsin inhibition. Int J Pharm 2002; 242: 47-54.

Otsuka, M.; Matsuda, Y.; Suw, Y.; Fox, J.; Higuchi, W. A Novel Skeletal Drug-Delivery System Using Self-Setting Calcium Phosphate Cement. 4. Effects of the Mixing Solution Volume on the Drug-Release Rate of Heterogeneous Aspirin-Loaded Cement. J Pharm Sci 1994; 83: 259-263.

Ozaki, T.; Yoshitaka, T.; Kunisada, T.; Danura, T.; Naito, N.; Inoue, H. Vancomycin-impregnated polymethylmethacrylate beads for methicillin-resistant Staphylococcus aureus (MRSA) infection: report of two cases. J Orthop Sci 1998; 3: 163-168.

Ozgur, S.; Sumer, H.; Kocoglu, G. Rickets and soil strontium. Arch Dis Child 1996; 75: 524 – 526.

Pacheco, H.; Vedantham, K.; Aniket; Young, A.; Marriott, I.; El-Ghannam, A. Tissue engineering scaffold for sequential release of vancomycin and rhBMP2 to treat bone infections. J Biomed Mater Res Part A 2014; 102A: 4213-4223.

Park, E., Lee, Y., Choi, J., Oh, S., Shin, H., Kim, K., Kim, S., Kim, S. Cellular biocompatibility and stimulatory effects of Calcium Metaphosphate on Osteoblastic differentiation of human bone marrow-derived stromal cells. Biomater 2004; 25: 3403-3411.

Parsons, B.; Strauss, E. Surgical management of chronic osteomyelitis. Amer J Surg. 188: 57S – 66S (Suppl to July 2004).

Pastorino, D.; Canal, C.; Ginebra, M. Drug delivery from injectable calcium phosphate foams by tailoring the macroporosity-drug interaction. Acta Biomater 2015; 12: 250-259.

Pati, F.; Kalita, H.; Adhijari, B.; Dhara, S. Osteoblastic cellular responses on ionically crosslinked chitosan-tripolyphosphate fibrous 3-D mesh scaffolds. J Biomed Mater Res Part A 2013; 00A: 1-12.

Paul, W.; Sharma, C. Development of porous spherical hydroxyapatite granules: application towards protein delivery. J Mater Sci: Mater Med 1999; 10: 383-388.

Pemberton, J. E., Latifzadeh, L., Fletcher, J. P., & Risbud, S. H. Raman spectroscopy of calcium phosphate glasses with varying calcium oxide modifier concentrations. Chem Mater 1991; *3*: 195-200.

Peppas, N.; Brannon-Peppas, L. Water Diffusion and Sorption in Amorphous Macromolecular Systems and Foods. J Food Engg 1994; 22: 189-210.

Peppas, N.; Colombo, P. Analysis of drug release behavior from swellable polymer carriers using the dimensionality index. J Control Rel 1997; 45: 35-40.

Peppas, N.; Duncan, R.; Wnek, G.; Hoffman, A.; Gao, G.; Kim, S.; Lee, D.; Hadjiargyrou, M.; Touitou, E.; Ainbinder, D.; Mumper, R.; Rolland, A.; Niidome, T.; Labhasetwar, V.; Liu, S.; Zhou, G.; Huang, Y.; Xie, Z.; Jing, X.; Csaba, N.; Alonso, M.; Ali, O.; Mooney, D.; Lonn, P.; Dowdy, S.; Feng, S.; Gao, J.; Lee, E.; Na, K.; Bae, Y.; Zentner, G.; Kim, H.; Yoo, H.; Nakayama, M.; Okano, T.; Liao, Z.; Chuang, E.; Hsiao, C.; Sung, H.; Cabral, H.; Kataoka, K.; Nair, P.; Discher, D.; Mitragotri, S. High cited research articles in Journal of Controlled Release: Commentaries and perspective by authors. Ch.1 Commentary on an exponential model for the analysis of drug delivery. J Control Rel 2014; 190: 31-32.

Perez M, Dumont M, Acevedo-Reyes D. Implementation of classical nucleation and growth theories for precipitation. Acta materialia 2008;56:2119-2132.

Petrone, C., Hall, G., Langman, M., Filiaggi, M. Compaction strategies for modifying the drug delivery capabilities of gelled CPP matrices. Acta Biomater 2008; 4: 408-413.

Pfanstiel R, Iler R. Magnesium Polymetaphosphate. J Am Chem Soc 1956;78:5510-5511.

Phienney, R.; Schwartz, S.; Lee, D.; Mondino, B. Collagen-shields delivery of gentamicin and vancomycin. Arch Optalmol 1988; 106: 1599-1604.

Pilliar, R., Filiaggi, M., Well, J., Grynpas, M., Kandel, R. Porous CPP scaffolds for bone substitute applications – in vitro characterization. Biomater 2001; 22: 963-972.

Pires, R.; Abrahams, I.; Nunes, T.; Hawkes, G. 31P Nuclear Magnetic Resonance and X-Ray Diffraction Studies of Na-Sr-Phosphate Glass-Ceramics. Key Eng Mater, 2004; 254: 95-98.

Pires, R.; Abrahams, I.; Nunes, T.; Hawkes, G. Non-random cation distribution in sodium–strontium–phosphate glasses. J non-cryst solids 2004; 337: 1-8.

Porter, J., Ruckh, T., Popat, K. Bone Tissue Engineering: A Review in Bone Biomimetics and Drug Delivery Strategies. Biotechnol Prog 2009; 25: 1539 – 1560.

Porter, N., Pilliar, R., Grynpas, M. Fabrication of porous CPP implants by solid freeform fabrication: A study of processing parameters and in vitro degradation characteristics. J Biomed Mater Res 2001; 56: 504-515.

Qiu, K., Zhao, X., Wan, C., Zhao, C., Chen, Y. Effect of strontium ions on the growth of ROS17/2.8 cells on porous CPP scaffolds. Biomat 2006b; 27: 1277-1286.

Qiu, K., Wan, C., Zhao, C., Chen, X., Tang, C., Chen, Y. Fabrication and characterization of porous CPP scaffolds. J Mater Sci 2006a; 41: 2429-2434.

Quarles, L. Cation Sensing Receptors in Bone: A Novel Paradigm for Regulating Bone Remodeling. J Bone Miner Res 1997; 12: 1971 – 1974.

Quarles, L.; Yohay, D.; Lever, L.; Caton, R.; Wenstrup, R. Distinct Proliferative and Differentiated Stages of Murine MC3T3-E1 Cells in Culture: An In Vitro Model of Osteoblast Development. J Bone Min Res 1992; 7: 683-692.

Reginster, J.; Felsenberg, D.; Boonen, S.; Diez-Perez, A.; Rizzoli, R.; Brandi, M.; Spector, T.; Brixen, K.; Goemaere, S.; Cormier, C.; Balogh, A.; Delmas, P.; Meunier, P. Effects of long-term strontium ranelate treatment on the risk of nonvertebral and vertebral fractures in postmenopausal osteoporosis. ArthRheum 2008; 58: 1687 – 1695.

Reynolds, P. Structure, biochemistry and mechanism of action of glycopeptide antibiotics. Europ J Clin Microbiol Infect Diseases 1989; 8: 943-950.

Reynolds, T.; Mitchell, S.; Balwinski, K. Investigation of the Effect of Tablet Surface Area/Volume on Drug Release from Hydroxypropylmethylcellulose Controlled-Release Matrix Tablets. Drug Develop Industry Pharm. 2002. 28: 457-466.

Ripoll, C.; Bunnell, B. Comparative characterization of mesenchymal stem cells from eGFP transgenic and non-transgenic mice. BMC Cell Bio 2009; 10: 1-12.

Romano, C.; Logoluso, N.; Meani, E.; Romano, D.; De Vecchi, E.; Vassena, C.; Drago, L. A comparative study of the use of bioactive glass S53P4 and antibiotic-loaded calcium-based bone substitutes in the treatment of chronic osteomyelitis. Bone Joint J 2014; 96-B: 845-850.

Rose, F.; Oreffo, R. Bone Tissue Engineering: Hope vs Hype. Biochem Biophys Res Comm 2002; 282: 1 – 7.

Sales, B.; Boatner, L.; Ramey, J. Intermediate-range order in simple metal-phosphate glasses: The effect of metal cations on the phosphate-anion distribution. J non-cryst solids 1998; 232: 107-112.

Salma K, Berzina-Cimdina L, Borodajenko N. Calcium phosphate bioceramics prepared from wet chemically precipitated powders. Processing and Application of Ceramics 2010;4:45-51.

Santos, H.; Veiga, F.; Pina, M.; Sousa, J. Compaction, compression and drug release characteristics of xanthan gum pellets of different compositions. Europ J Pharm Sci 2004; 21: 271-281.

Schneider, J.; Oliveira, S.; de Oliveira Nunes, L.; Bonk, F.; Panepucci, H. Short-range structure and cation bonding in calcium-aluminum metaphosphate glasses. Inorg chem 2005; 44: 423-430.

Schofield, S., Berno, B., Langman, M., Hall, G., and Filiaggi, M Gelled CPP Matrices Delay Antibiotic Release. J Dent Res 2006; 85: 643-647.

Schrooten, I.; Behets, G.; Cabrera, W.; Vercauteren, S.; Lamberts, L.; Verberckmoes, S.; Bervoets, A.; Dams, G.; Goodman, W.; De Broe, M.; D'Haese, P. Dose-dependent effects of strontium on bone of chronic renal failure rats. Kidney Int 2003; 63: 927 – 935.

Schrooten, I.; Carbera, W.; Goodman, W.; Dauwe, S.; Lamberts, L.; Marynissen, R.; Dorrine, W.; De Broe, M.; D'Haese, P. Strontium causes osteomalacia in chronic renal failure rats. Kidney Int 1998; 54: 448 – 456.

Schlickewei, C.; Yarar, S.; Rueger, J. Eluting antibiotic bone graft substitutes for the treatment of osteomyelitis in long bones. A review: evidence for their use? Orth Res Rev 2014; 6: 71-79.

Shinto, Y.; Uchida, A.; Korkusuz, F.; Araki, N.; Ono, K. Calcium hydroxyapatite ceramic used as a delivery system for antibiotics. J Bone Joint Surg Br 1992; 74: 600-604.

Siepmann, J.; Kranz, H.; Peppas, N.; Bodmeier, R. Calculation of the required size and shape of hydroxypropyl methylcellulose matrices to achieve desired drug release profiles. Int J Pharm 2000; 201: 151-164.

Siepmann, J.; Peppas, N. Review – Higuchi equation: Derivation, applications, use and misuse. Int J Pharm 2011; 418: 6-12.

Silva MA, Franco DF, C. de Oliveira, Luiz Fernando. New insight on the structural trends of polyphosphate coacervation processes. The Journal of Physical Chemistry A 2008;112:5385-5389.

Sinyaev, V., Shustikova, E., Levchenko, L., Sedunov, A. Synthesis and Dehydration of Amorphous Calcium Phosphate. Inorg Mater 2001; 37: 619-622.

Skoug, J.; Borin, M.; Fleishaker, J.; Cooper, A. In Vitro and in Vivo Evaluation of Whole and Half Tablets of Sustained-Release Adinazolam Mesylate. Pharm Res 1991; 8: 1482-1488.

Song, W., Tian, M., Chen, F., Tian, Y., Wan, C., Yu, X. The Study on the Degradation and Mineralization Mechanism of Ion- Doped CPP in Vitro. J Biomed Mater Res B Appl Biomater 2009; 89B: 430-438.

Song, W., Wang, Q., Wan, C., Shi, T., Markel, T., Markel, D., Blaiser, R., Ren, W. A novel alkali metals/strontium cosubstituted CPP scaffolds in bone tissue engineering. J Biomed Mater Res B Appl Biomater 2011; 98B: 255-262.

Soontornvipart, K.; Necas, A.; Dvorak, M. Review Article – Effects of Metallic Implant on the Risk of Bacterial Osteomyelitis in Small Animals. Acta Vet 2003; 72: 235 – 247.

Squali, A., Montagne, L., Vast, P., Palavit, G., Buisine, J. Thermobarometric Analysis of Physico-Chemical Transformations of Coacervates and Gels of Polyphosphates. J Thermal Anal Calorimetry 1991; 37: 1673-1678.

Stienstra, D. Introduction to Design of Structural Ceramics. Rose-Hulman Institute of Technology, 1992 (Revised 2003).

Stigter, M.; Bezemer, J.; de Groot, K.; Layrolle, P. Incorporation of different antibiotic into carbonated hydroxyapatite coatings on titanium implants, release and antibiotic efficacy. J Controlled Rel 2004; 99: 127-137.

Strauss UP, Ross PD. Counterion Binding by Polyelectrolytes. III. Stability Constants for the Binding of Univalent Cations by PO3--Groups of Polyphosphates from Electrophoresis Measurements1. J Am Chem Soc 1959;81:5295-5298.

Strauss UP, Smith EH, Wineman PL. Polyphosphates as Polyelectrolytes. I. Light Scattering and Viscosity of Sodium Polyphosphates in Electrolyte Solutions1. J Am Chem Soc 1953;75:3935-3940.

Strauss UP, Smith EH. Polyphosphates as Polyelectrolytes. II. Viscosity of Aqueous Solutions of Graham's Salts1. J Am Chem Soc 1953;75:6186-6188.

Strauss UP, Woodside D, Wineman P. Counterion Binding by Polyelectrolytes. I. Exploratory Electrophoresis, Solubility and Viscosity Studies of the Interaction between Polyphosphates and Several Univalent Cations. J Phys Chem 1957;61:1353-1356.

Sudo, H.; Kodama, H.; Amagai, Y.; Yamamoto, S.; Kasai, S. In Vitro Differentiation and Calcification in a New Clonal Osteogenic Cell Line Derived from Newborn Mouse Calvaria. J Cell Biol 1983; 96: 191-198.

Tadic, D., Welzel, T., Seidel, P., Wust, E., Dingeldein, E., Epple, M. Controlled release of gentamicin from biomimetic calcium phosphate in vitro. Comparison of four different incorporation methods. Controlled Release 2004; 35: 1001-1005.

Takahashi, N.; Sasaki, T.; Tsouderos, Y.; Suda, T. S 12911-2 Inhibits Osteoclastic Bone Resorption In Vitro. J Bone Miner Res 2003; 18: 1082 – 1087.

Tian, M.; Chen, F.; Song, W.; Song, Y.; Chen, Y.; Wan, C.; Yu, X.; Zhang, X. In vivo study of porous strontium-doped calcium polyphosphate scaffolds for bone substituted applications. J Mater Sci: Mater Med 2009; 20: 1505 – 1512.

Trostle, S.; Hendrickson, D.; Stone, W.; Klohnen, A. Use of antimicrobial-impregnated methacrylate beads for treatment of chronic, refractory septic arthritis and osteomyelitis of the digit in a bull. J Am Vet Med Assoc 1996: 208: 404 - 407.

Turner, T.; Urban, R.; Gitelis, S. Radiographic and histologic assessment of calcium sulfate in experimental animal models and clinical use as a resobable bone-graft substitute, a bone-graft expander, and a method for local antibiotic delivery. One institution's experience. J Bone Joint Surg Am 2001; 83: S8-18.

Turner, T.; Urban, R.; Hall, D.; Chye, P.; Segreti, J.; Gitelis, S. Local and systemic levels of tobramycin delivered from calcium sulfate bone graft substitute pellets. Clin Orthop Relat Res 2005; 437: 97-104.

Uckay, I.; Jugun, K.; Gamulin, A.; Wagener, J.; Hoffmeyer, P.; Lew, D. Chronic Osteomyelitis. Curr Infect Dis Rep 2012; 14: 566 – 575.

Ue, J. The effect of sodium doping on calcium polyphosphate. M.A.Sc. Thesis, 2009.

Umegaji, T.; Kanazawa, T. Degradation of Magnesium and Calcium Highpolyphosphate Coacervates. Bulletin Chem Soc (Japan) 1979; 52: 2124 – 2126.

Umegaki T, Kanazawa T. Viscosity Behavior of Coacervates of Magnesium and Calcium Highpolyphosphates. Bull Chem Soc Jpn 1975;48:1452.

Umegaki T, Nakayama Y, Kanazawa T. Thermal Change of Magnesium High Polyphosphate Coacervates. Bull Chem Soc Jpn 1976;49:2105-2107.

Van Wazer, J.R., Phosphorus and its compounds. Vol. 1.Interscience Publishers, Inc. 1958. Chapter 6: Structure and Properties of the Condensed Phosphates, p 419-441.

Varshneya, Arun K. *Fundamentals of inorganic glasses*. Elsevier, 1993. Chapter 3: Glass Formation Principles, p 29-43.

Verberckmoes, S.; Behets, G.; Oste, L.; Bervoets, A.; Lamberts, L.; Drakopoulos, M.; Somogyi, A.; Cool, P.; Dorrine, W.; De Broe, M.; D'Haese, P. Effects of Strontium on the Physicochemical Characteristics of Hydroxyapatite. Calcif Tissue Int 2004; 75: 405 – 415.

Verron, E.; Bouler, J.; Guicheux, J. Review – Controling the biological function of calcium phosphate bone substitutes with drugs. Acta Biomater 2012; 8: 3541-3551.

Vijan, L. The Interaction of Vancomycin with DNA. Revue Roumaine de Chimie, 2009; 54*:* 807-813.

Waldman, S., Grynpas, M., Pilliar, R., Kandel, R. Characterization of cartilaginous tissue formed on CPP substrates in vitro. J Biomed Mater Res 2002;62: 323-330.

Wang, C., Yan, M., Chang, H., Ding, S. Degradation Behavior of Porous Calcium Phosphates. J Med Biol Eng 2003; 23: 159-164.

Wang, F., Qiu, K., Hu, T., Wan, C., Zhou, X., Gutmann, J. Biodegradable porous calcium polyphosphate scaffolds for the threedimensional culture of dental pulp cells. Int Endod J 2006; 39: 477-483.

Wang, K., Chen, F., Liu, C., Russel, C. The effect of polymeric chain-like structure on the degradation and cellular biocompatibility of CPP. Mater Sci Eng 2008; 28: 1572-1578.

Wang, Q., Wang, Q., Wang, J., Zhang, X., Yu, X., Wan, C. Degradation Kinetics of Calcium Polyphosphate Bioceramic: an Experimental and Theoretical Study. Mater Res 2009; 12: 495-501.

Wang, Q.; Wang, Q.; Zhang, X.; Yu, X.; Wan, C. The effect of sintering temperature on the structure and degradability of strontium-doped calcium polyphosphate bioceramics. Ceramics Silikaty 2010; 54: 97 – 102.

Webb, P. Volume and density determinations for particle technologists. *Micromeritics Instrument Corp* 2, no. 16 (2001): 01.

Wetherall, K.; Pickup, D.; Newport, R.; Mountjoy, G. The structure of calcium metaphosphate glass obtained from x-ray and neutron diffraction and reverse Monte Carlo modelling. J Phys: Condens Matter 2009; 21: 1-9.

White, L.; Edwards, R.; Holt, H.; Lovering, A.; Finch, R.; Reeves, D. The in-vitro degradation at 37 C of vancomycin in serum, CAPD fluid and phosphate-buffered saline. *J Antimicrob Chemotherap* 1988; 22: 739-745.

Willot G, Gomez F, Vast P, Andries V, Martines M, Messaddeq Y, et al. Preparation of zinc sodium polyphosphates glasses from coacervates precursors. Characterisation of the obtained glasses, and their applications. Comptes Rendus Chimie 2002;5:899-906.

Wu H. Effect of Polymerization Temperature on Polymerization Degree and Structure of Calcium Polyphosphate. J Inorg Mat 2012;27:174-178.

Xie, Z.; Liu, X,.; Jia, W. Treatment of osteomyelitis and repair of bone defect by degradable bioactive borate glass releasing vancomycin. J Control Release 2009; 138: 118-126.

Yamaguchi, T.; Chattopadhyay, N.; Kifor, O.; Sanders, J.; Brown, E. Activation of p42/44 and p38 mitogen-activated protein kinases by extracellular calcium-sensing receptor agonists induces mitogenic responses in the mouse osteoblastic MC373-E1 cell line. Biochem Biophys Res Comm 2000; 279: 363 – 368.

Yamashita, Y.; Uchida, A.; Yamakawa, T.; Shinto, Y.; Araki, N.; Kato, A. Treatment of chronic osteomyelitis using calcium hydroxyapatite ceramic implants impregnated with antibiotic. Int Orth 1998; 22: 247-251.

Yan, W., Li, N., Li, Y., Liu, G., Han, B., & Xu, J. Effect of particle size on microstructure and strength of porous spinel ceramics prepared by pore-forming in situ technique. Bulletin of Materials Science 2011; 34: 1109-1112.

Yasir, M.; Bajpai, M.; Bhattacharyya, A. Evaluation of mathematical models describing drug release kinetics from theophylline S.R. floating matrix tablets. J Pharm Res 2010; 3: 2265-2269.

Yu, D.; Wong, J.; Matsuda, Y.; Fox, J.; Higuchi, W.; Otsuka, M. Self-setting Hydroxyapatite Cement: A Novel Skeletal Drug-Delivery System for Antibiotics. J Pharm Sci 1992; 81: 529 – 531.

Zauner R, Jones AG. On the influence of mixing on crystal precipitation processes—application of the segregated feed model. Chemical Engineering Science 2002;57:821-831.

Zhang, X.; Jia, W.; Gu, Y. Teicoplanin-loaded borate bioactive glass implants for treating chronic bone infection in a rabbit tibia osteomyelitis model. Biomater 2010; 31: 5865-5874.

Zhang, W., Shen, Y., Pan, H., Lin, K., Liu, X., Darvell, B., Lu, W., Chang, J., Deng, L., Wang, D., Huang, W. Effects of strontium in modified biomaterials. Acta Biomater 2011; 7: 800-808.

Ziran, B.; Smith, W.; Morgan, S. Use of Calcium-Based Demineralized Bone Matrix/Allograft for Nonunions and Posttraumatic Reconstruction of the Appendicular Skelton: Preliminary Results and Complications. J Trauma 2007; 63: 1324-1328.

APPENDIX A – ADDITIONAL RESULTS

CHAPTER 3 – CALCIUM POLYPHOSPHATE PRECIPITATION

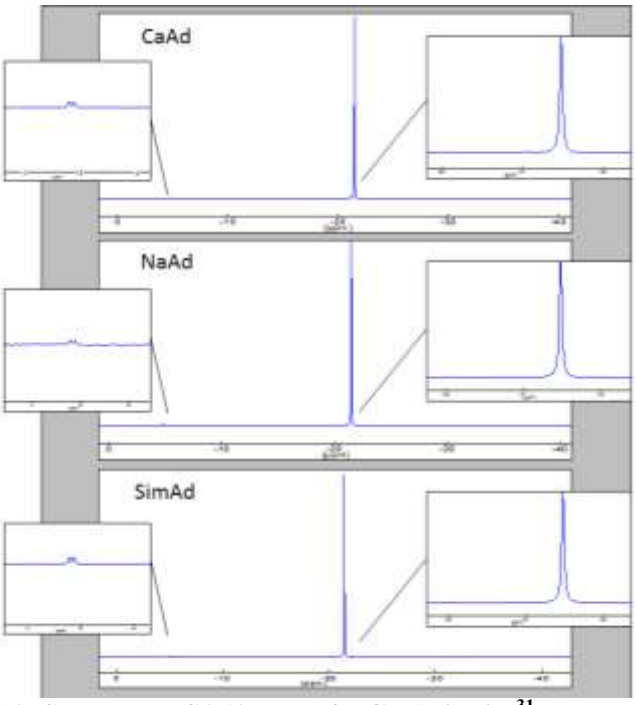

Figure A1: Sample set S1 (1NaPP-0.5CaP) liquid ^{31}P NMR profiles.

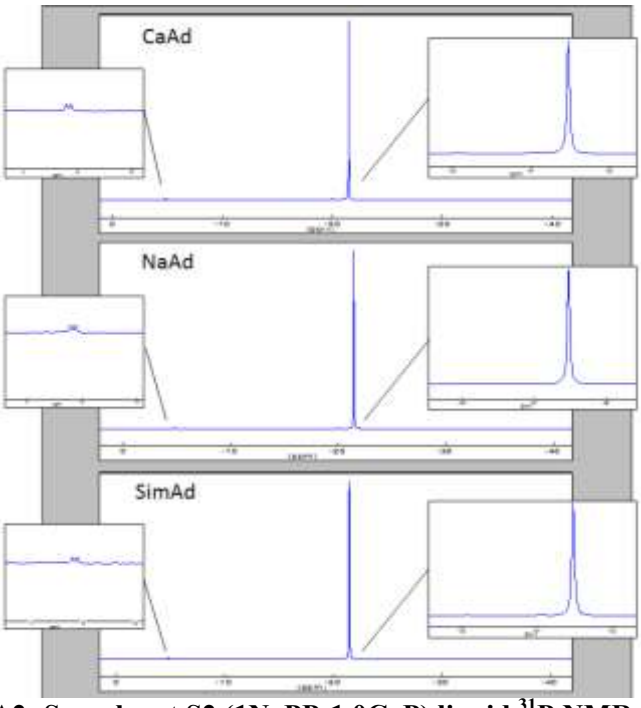

Figure A2: Sample set S2 (1NaPP-1.0CaP) liquid ^{31}P NMR profiles.

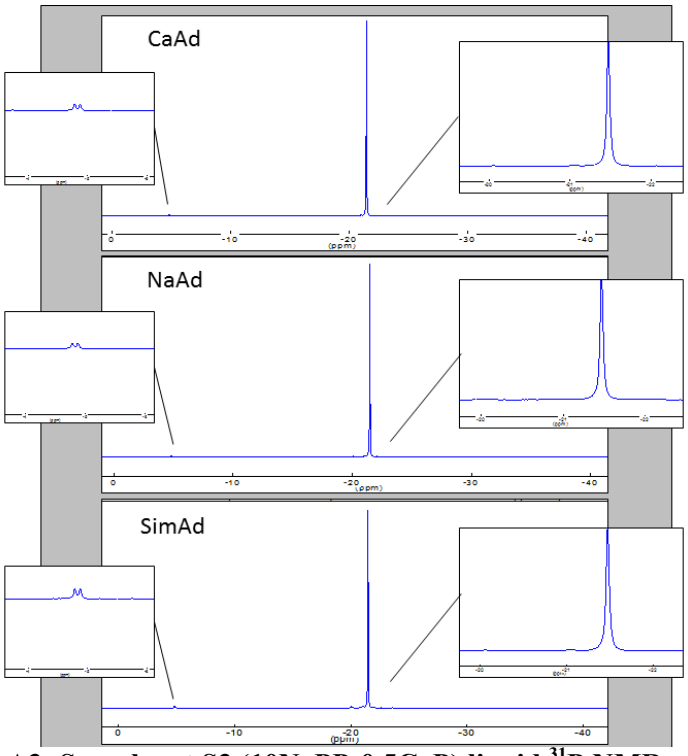

Figure A3: Sample set S3 (10NaPP-0.5CaP) liquid ^{31}P NMR profiles.

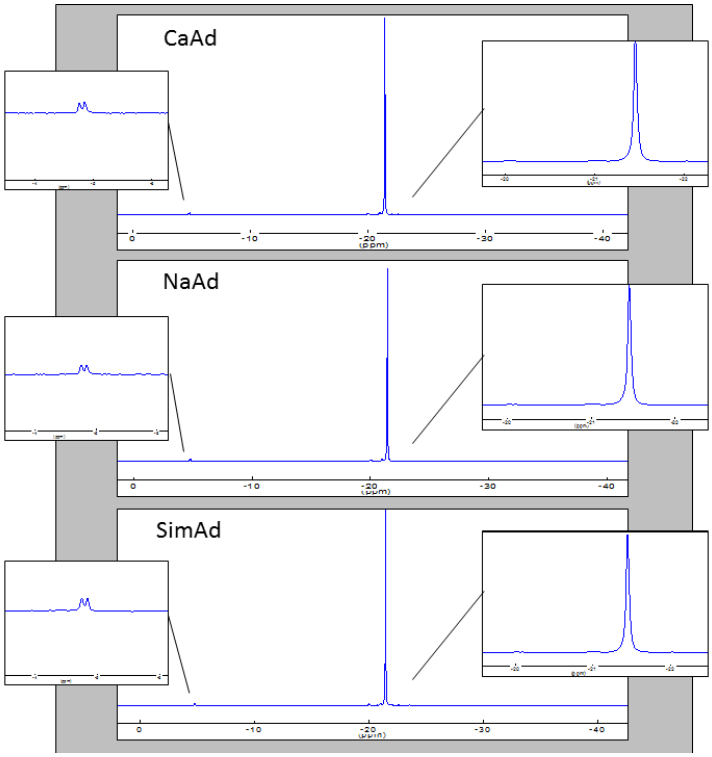

Figure A4: Sample set S4 (10NaPP-1.0CaP) liquid ^{31}P NMR profiles.

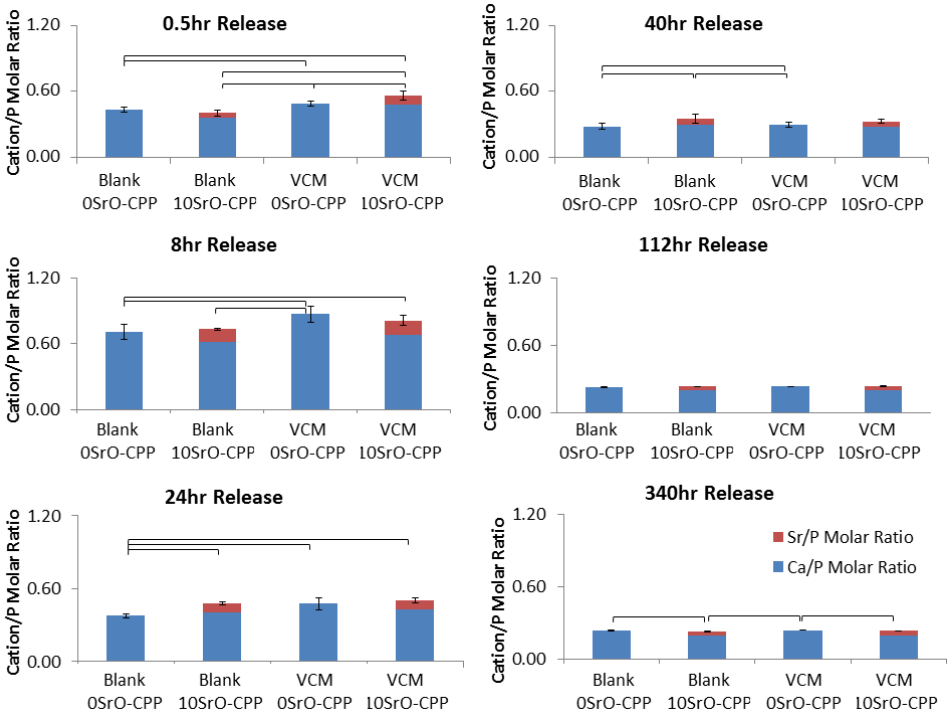

Figure A5: Cation-to-phosphorous molar ratio of G2 disk extracts. Data reported as average values while error bars represent one standard deviation (n=6). Horizontal bars represent significant difference ($p<0.05$).

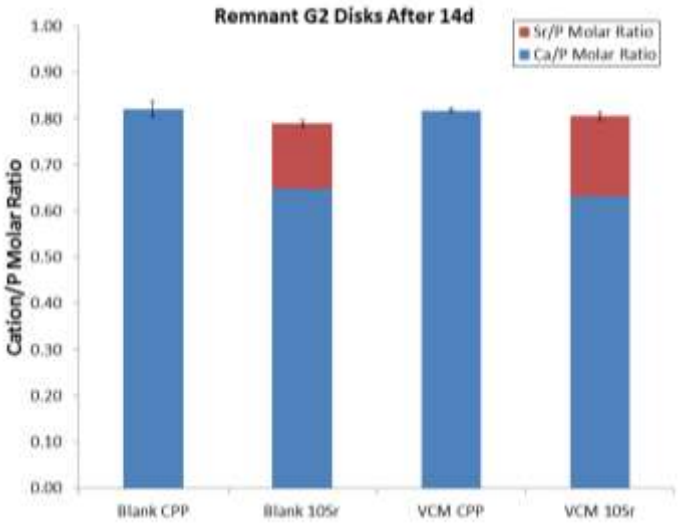

Figure A6: Cation-to-phosphorous molar ratio of remnant G2 disks after 14d study. Data reported as average values while error bars represent one standard deviation (n=6).

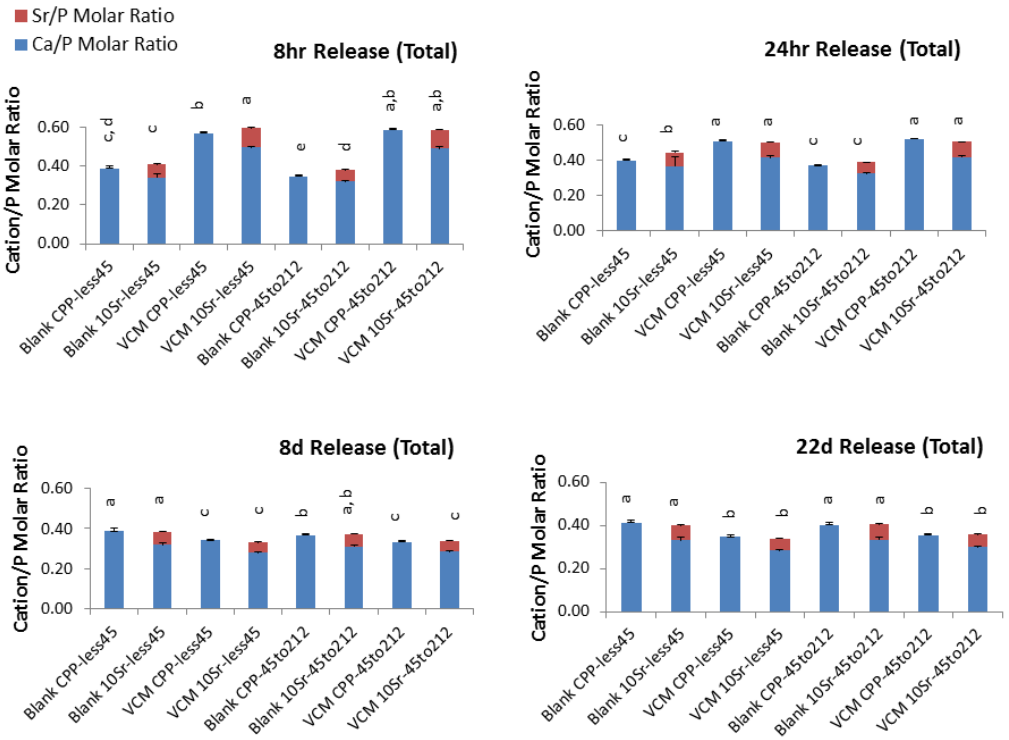

Figure A7: Cation-to-phosphorous molar ratio of bead extracts. Data reported as average values while error bars represent one standard deviation (n=6). Horizontal bars represent significant difference ($p<0.05$).

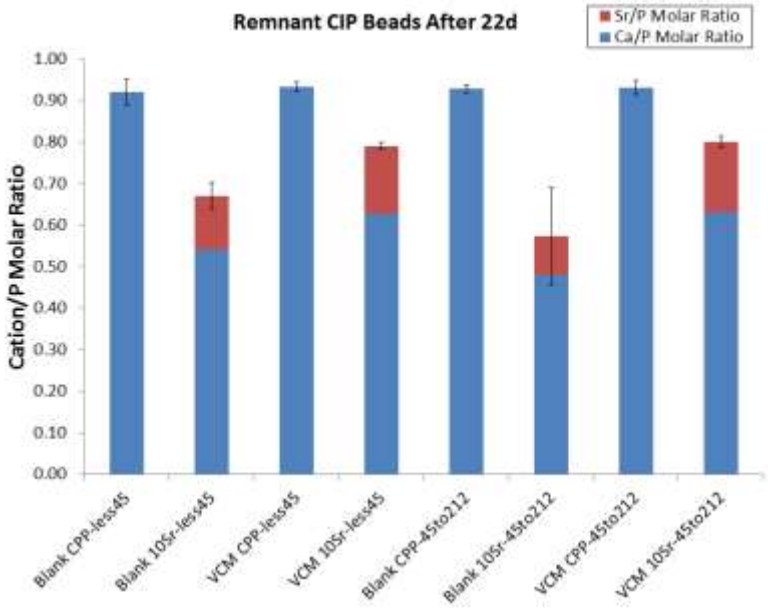

Figure A8: Cation-to-phosphorous molar ratio of remnant CIP beads after 22d study. Data reported as average values while error bars represent one standard deviation (n=6).

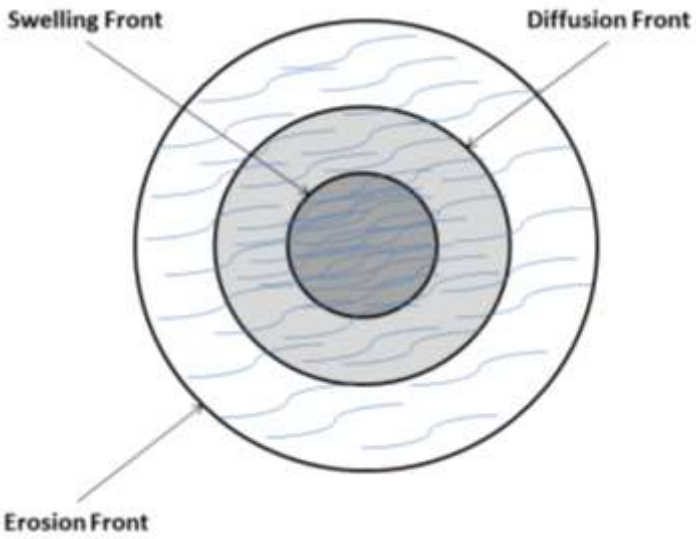

Figure A9: Schematic of matrix interaction with aqueous media (adapted from Maderuelo *et al*. (2011) and Columbo *et al*. (1995)).

APPENDIX B – REAGENT RECIPES

0.1M TBS

- To 1.0L dH2O add 3.32g Tris-base, 11.44g Tris-HCl, and 8.77g NaCl

- After powder is dissolved add 6N $HCl_{(aq)}$ drop-wise to achieve a pH of ~7.6

200mM Na_2-EDTA

- To 150mL dH_2O add 14.89g Na2-EDTA powder

- Buffer to pH ~10.0 with drop-wise addition of 10M $NaOH_{(aq)}$

- Then add mixture to 200mL volumetric flask and adjust volume with dH_2O to 200mL

0.1% Triton X-100 Buffer Solution

- To 10mL of 1M Tris-HCl of pH 8.0 add 13.75mL 5M NaCl, 50mL glycerol, 0.5mL Triton X-100

- Add mixture to 500mL volumetric flask and adjust volume with dH_2O to 500mL

- Store at -4°C

Sodium β-Glycerophosphate (Stock: 1M)

- To 100mL dH_2O add 21.60g powder (G9422, Sigma)

- After powder is dissolved, filter to sterilize, and aliquot in tubes

- Freeze tubes until needed

Ascorbic Acid (Stock: 5mg/mL)

- To 100mL dH_2O add 0.5g of Ascorbic Acid powder (A4544, Sigma)

- After powder is dissolved, filter to sterilize, and aliquot in tubes

- Freeze tubes until needed

40mM Alizarin Red Solution

- To 100mL dH_2O add 2g of Alizarin Red powder

- After powder is dissolved adjust pH to 4.3 and filter to sterilize

0.2% SF Yellowish Solution

- To 100mL dH_2O add 0.2g SF Yellowish powder

- After powder is dissolved filter to sterilize

10mM Sodium Phosphate Buffer

- To 800mL add 1.64g NaH_2PO_4-$7H_2O$, 0.47g NaH_2PO_4, and 8.77g NaCl

- After powder is dissolved adjust pH to 7.0 with 1M $NaOH_{(aq)}$

- Add mixture to 1L volumetric flask and adjust volume with dH_2O to 1L

10% Cetylpyridinium Chloride Solution

- To 100mL of 10mM Sodium Phosphate Buffer add 10g of cetylpyridinium chloride powder

- After powder is dissolved filter

APPENDIX C – ELSEVIER COPYRIGHT PERMISSION LETTER

Copyright Clearance Center RightsLink®

Home | Account Info | Help | Live Chat

Title: Calcium polyphosphate precipitation – A strategy to tune the chain length of the glass and control the subsequent release of vancomycin

Publication: Materials Chemistry and Physics

Publisher: Elsevier

Date: 1 June 2015

Logged in as:
Patricia Comeau

LOGOUT

Order Completed

Thank you very much for your order.

This is a License Agreement between Patricia A Comeau ("You") and Elsevier ("Elsevier"). The license consists of your order details, the terms and conditions provided by Elsevier, and the payment terms and conditions.

Get the printable license.

License Number	3633941015306
License date	May 21, 2015
Licensed content publisher	Elsevier
Licensed content publication	Materials Chemistry and Physics
Licensed content title	Calcium polyphosphate precipitation – A strategy to tune the chain length of the glass and control the subsequent release of vancomycin
Licensed content author	None
Licensed content date	1 June 2015
Licensed content volume number	159
Licensed content issue number	n/a
Number of pages	8
Type of Use	reuse in a thesis/dissertation
Portion	full article
Format	both print and electronic
Are you the author of this Elsevier article?	Yes
Will you be translating?	No
Order reference number	2
Title of your thesis/dissertation	Novel Fabrication of a Calcium Polyphosphate Delivery Matrix for Treatment of Osteomyelitis and Bone Regeneration
Expected completion date	Jul 2015
Estimated size (number of pages)	250
Elsevier VAT number	GB 494 6272 12
Permissions price	0.00 USD
VAT/Local Sales Tax	0.00 USD / 0.00 GBP
Total	0.00 USD

ORDER MORE... CLOSE WINDOW